



HAL
open science

Embedded GW many-body formalism within a fragment approach : developments and applications to complex systems

David Amblard

► To cite this version:

David Amblard. Embedded GW many-body formalism within a fragment approach : developments and applications to complex systems. Physics [physics]. Université Grenoble Alpes [2020-..], 2024. English. NNT : 2024GRALY028 . tel-04741314

HAL Id: tel-04741314

<https://theses.hal.science/tel-04741314v1>

Submitted on 17 Oct 2024

HAL is a multi-disciplinary open access archive for the deposit and dissemination of scientific research documents, whether they are published or not. The documents may come from teaching and research institutions in France or abroad, or from public or private research centers.

L'archive ouverte pluridisciplinaire **HAL**, est destinée au dépôt et à la diffusion de documents scientifiques de niveau recherche, publiés ou non, émanant des établissements d'enseignement et de recherche français ou étrangers, des laboratoires publics ou privés.

THÈSE

Pour obtenir le grade de

DOCTEUR DE L'UNIVERSITÉ GRENOBLE ALPES

École doctorale : PHYS - Physique

Spécialité : Physique Théorique

Unité de recherche : Institut Néel

Formalisme à N-corps GW environné dans une approche fragment : développements et applications à des systèmes complexes

Embedded GW many-body formalism within a fragment approach: developments and applications to complex systems

Présentée par :

David AMBLARD

Direction de thèse :

Xavier BLASE

DIRECTEUR DE RECHERCHE, CNRS - Délégation Alpes

Directeur de thèse

Ivan DUCHEMIN

INGENIEUR CHERCHEUR, CEA DE GRENOBLE

Co-encadrant de thèse

Rapporteurs :

FABIEN BRUNEVAL

DIRECTEUR DE RECHERCHE, CEA CENTRE DE PARIS-SACLAY

PIERRE-FRANÇOIS LOOS

DIRECTEUR DE RECHERCHE, CNRS DELEGATION OCCITANIE OUEST

Thèse soutenue publiquement le **5 juillet 2024**, devant le jury composé de :

HELENE JAMET,

PROFESSEURE DES UNIVERSITES, UNIVERSITE GRENOBLE ALPES

Présidente

FABIEN BRUNEVAL,

DIRECTEUR DE RECHERCHE, CEA CENTRE DE PARIS-SACLAY

Rapporteur

PIERRE-FRANÇOIS LOOS,

DIRECTEUR DE RECHERCHE, CNRS DELEGATION OCCITANIE OUEST

Rapporteur

PINA ROMANIELLO,

DIRECTRICE DE RECHERCHE, CNRS DELEGATION OCCITANIE OUEST

Examinatrice

CLAUDIO ATTACALITE,

DIRECTEUR DE RECHERCHE, CNRS DELEGATION PROVENCE ET CORSE

Examineur



Remerciements

Cette section est l'occasion pour moi de remercier tous ceux qui ont rendu cette thèse possible. Je voudrais tout d'abord dire un très grand merci à mes deux directeurs. La thèse est un travail collectif, et vous avez permis que tout se passe merveilleusement. Xavier, je te rassure, tu es bien plus qu'un « expert mondial du C_{60} ». Tes vastes connaissances en physique, des enjeux au sein de la communauté, nous ont permis d'aller sans cesse dans la bonne direction. Tu as toujours été là pour me guider, me conseiller. Que ce soit pour la physique, ou pour le fonctionnement de la recherche, tu m'as tant appris. Ivan, tu m'as enseigné ce qu'est réellement le HPC, ses enjeux et ses objectifs. C'est quelque chose que j'aimais avant ma thèse, et qui s'est aujourd'hui transformée en vraie passion. Que ce soit sur la partie implémentation, mathématiques, ou physique, merci à toi de m'avoir transmis une partie de tes connaissances, et d'avoir fait preuve d'une grande patience. J'ai toujours eu l'impression d'avoir été écouté. Merci à vous de m'avoir embarqué dans l'aventure **BEDEFT** et pour tous les bons moments passés ensemble. Quel dommage qu'une thèse ne dure que trois ans. . . J'espère de tout cœur que nos routes se recroiseront un jour.

Je suis également reconnaissant envers les membres de mon jury. Merci à Fabien et Titou d'avoir accepté de relire mon manuscrit et de faire le voyage jusqu'à Grenoble pour juger mon travail. Merci également à Pina, Claudio et Hélène d'avoir accepté de faire partie de mon jury, et de participer à ma soutenance. Je remercie également Roberta et Markus d'avoir été membres de mon CSI.

Je souhaite aussi remercier les collègues du groupe théorie que j'ai pu côtoyer au quotidien. Merci à Gabriele pour toutes les discussions tant sur les matériaux organiques que la culture italienne, à Marie-Bernadette pour ton soutien, à Georges pour ta bonne humeur et ton franc-parler, à Arnaud pour ton enthousiasme lors de nos repas. Merci également aux différentes personnes passées par notre *open-space* avec qui j'ai pu échanger sur de nombreux aspects et pendant de nombreuses heures : Clément, Florent, Hugo, Jesus, Lorenzo, Mauricio, Maxime. . .

Une thèse s'accompagne toujours de nombreuses démarches administratives tout au long des trois années. Je suis donc particulièrement reconnaissant envers Élodie et Mathilde d'avoir fait en sorte que tout se passe au mieux pour moi.

J'ai également eu l'occasion pendant ma thèse d'effectuer de nombreuses heures d'enseignement. Je remercie donc Vincent et Daniel de m'avoir donné la chance d'enseigner dans leur UE respective. Ceci a été très formateur pour moi.

Je souhaiterais aussi remercier Olivier Commowick pour son template L^AT_EX m'ayant grandement servi dans la rédaction de ce manuscrit, disponible au lien suivant : https://olivier.commowick.org/thesis_template.php.

D'un point de vue plus personnel, je souhaite aussi remercier Marine qui a toujours été à mes côtés pendant cette thèse. Bien que l'approximation *GW* soit à des années lumières des dunes de neige en Antarctique, tu as toujours été à l'écoute (de mes histoires peu passionnantes), compréhensive, patiente et attentionnée. Tu as été un des piliers majeurs dans la réussite de cette thèse. Merci pour tout.

Je remercie également chaleureusement la SPA du Dauphiné d'avoir eu confiance en nous, et de nous avoir confié ces quatre magnifiques et adorables chats pendant cette thèse, ainsi qu'au refuge pour chats Droit de Vivre pour tous les bons moments passés ensemble.

Enfin, je remercie l'ENS Paris-Saclay pour le CDSN qui a servi à financer cette thèse.



Artémis



Gaufre



Nina



Roucky

Contents

List of Acronyms	9
Résumé	11
Abstract	12
Introduction (version française)	13
Introduction (English version)	17
1 Theoretical background and methodology	21
Résumé	22
Summary	23
1.1 Theoretical spectroscopy	24
1.1.1 Photoemission spectroscopy	24
1.1.2 From gas phase to crystal phase	25
1.1.3 Simple models of polarization	27
1.1.3.1 Charge in front of a metallic surface and image charges	27
1.1.3.2 Charge in a dielectric cavity	29
1.2 The many-body problem	30
1.2.1 The Born-Oppenheimer approximation	30
1.3 <i>Ab initio</i> approaches	31
1.3.1 Density-Functional Theory (DFT)	31
1.3.1.1 The Hohenberg and Kohn theorems	31
1.3.1.2 The Kohn-Sham formulation	33
1.3.1.3 Exchange-correlation functionals	35
1.3.1.4 Discussion on the meaning of the Kohn-Sham single-particle energies	36
1.3.1.5 DFT in practice	38
1.3.2 The <i>GW</i> formalism	41
1.3.2.1 Green's function	41
1.3.2.2 Lehmann representation and spectral function	42
1.3.2.3 Dyson equation on G	44
1.3.2.4 The self-energy in linear response	46
1.3.2.5 Hedin's equations	48
1.3.2.6 The <i>GW</i> approximation	50
1.3.2.7 The COHSEX decomposition	52
1.3.2.8 The static COHSEX approximation	53
1.3.2.9 <i>GW</i> in practice	54
1.3.2.10 Implementation in BEDEFT	56
1.4 Objectives	62

2	Embedded <i>GW</i> formalism in a fully <i>ab initio</i> QM/QM' approach	63
	Résumé	64
	Summary	65
2.1	Introduction	66
2.2	Analytical developments	67
2.2.1	Fragment approach	67
2.2.2	Constrained compression of $\mathbf{X}_g^{(1)}(\omega)$	69
2.2.3	Minimization problem for $\tilde{\mathbf{X}}_g^{(1)}(\omega)$	71
2.2.4	Minimal effective polarization basis set $\{\gamma\}$	74
2.3	Application to organic molecules	75
2.3.1	Technical details	75
2.3.2	Validity of the fragment approach	77
2.3.3	Validation of the compression method for \mathbf{X}_g	78
2.3.4	Large scale environments: the C ₆₀ crystal and surface structures	84
2.3.5	Computational details: CPU and memory requirements	90
2.4	Conclusion	90
3	Static versus dynamically embedded <i>GW</i> formalism	93
	Résumé	94
	Summary	95
3.1	Introduction	96
3.2	The different types of embedding	97
3.2.1	The fully dynamical approach	97
3.2.2	The Δ COHSEX approach	98
3.2.3	The QM _{GW} /QM _{COHSEX} approach	99
3.2.3.1	Embedding generalities	99
3.2.3.2	Static Coulomb-Hole plus Screened-Exchange (COHSEX) from a simple pole model	100
3.2.3.3	Folding of the static COHSEX environment	102
3.3	Application to dense phase of C ₆₀	104
3.3.1	Technical details	104
3.3.2	Polarization basis set for dynamical susceptibilities	105
3.3.3	Discussion on P_n^{COH} and P_n^{SEX}	106
3.3.4	C ₆₀ infinite surface at the G_0W_0 level	107
3.3.5	Assessment of the adiabatic approximation for the environment	109
3.3.6	The QM _{GW} /QM _{GW} /QM _{COHSEX} approach	114
3.4	A water molecule inside a metallic nanotube	115
3.5	Conclusion	116
4	Polarization energies of point defects in hexagonal boron nitride via the fragment approach	119
	Résumé	120
	Summary	121
4.1	Introduction	122

4.2	Methodology	123
4.2.1	Fragmentation of hexagonal Boron Nitride (<i>h</i> -BN)	123
4.2.2	Environmental effects: observables of interest	125
4.2.3	Technical details	125
4.2.4	Geometries of the fragments	127
4.3	Fragmentation of the monolayer	129
4.4	Fragmentation of the multilayers	134
4.5	Point defects in the surface and bulk limit	136
4.6	Universality of the polarization energies among the different defects	139
4.7	Defect levels with respect to <i>h</i> -BN valence band edge	141
4.8	Conclusion	145
	Conclusion (version française)	149
	Conclusion (English version)	153
	Appendices	155
A	Constrained compression of the fragment susceptibility	157
A.1	Computation of $\tilde{\mathbf{X}}_g$	157
A.2	Computation of the polarization basis $\{\gamma\}$	159
A.2.1	Optimization for $N_\gamma = N_{\text{cstr}}$	159
A.2.2	Optimization problem for $\mathbf{A}_2 = \mathbf{0}$	160
B	The $\text{QM}_{\text{GW}}/\text{QM}_{\text{COHSEX}}$ approach: interchange of limit and integral	163
B.1	Introduction	163
B.2	Demonstration	163
C	Typical input file of beDef	167
D	Scientific production	173
	Bibliography	175

List of Acronyms

2D	two-dimensional
3D	three-dimensional
AC	Analytic Continuation
beDefT	Beyond Density-Functional Theory (The name of our <i>GW</i> code)
BSE	Bethe–Salpeter Equation
CBM	Conduction Band Minimum
CBS	Complete Basis Set
CD	Contour Deformation
CGF	Contracted Gaussian Function
COH	Coulomb-Hole
COHSEX	Coulomb-Hole plus Screened-Exchange
CPU	Central Processing Unit
DFT	Density-Functional Theory
DOS	Density Of States
EA	Electron Affinity
EOM	Equation of Motion
FCC	Face-Centered Cubic
GGA	Generalized Gradient Approximation
GTO	Gaussian Type Orbital
<i>h</i>-BN	hexagonal Boron Nitride
HEG	Homogeneous Electron Gas
HF	Hartree-Fock
HOMO	Highest Occupied Molecular Orbital
IP	Ionization Potential
IPES	Inverse Photoemission Spectroscopy
KS	Kohn-Sham
LDA	Local Density Approximation
LUMO	Lowest Unoccupied Molecular Orbital
MBPT	Many-Body Perturbation Theory
MM	Molecular Mechanics
MO	Molecular Orbital

PBC	Periodic Boundary Conditions
PCM	Polarizable Continuum Model
PES	Photoemission Spectroscopy
QM	Quantum Mechanics
QMC	Quantum Monte Carlo
QP	Quasiparticle
RI	Resolution of the Identity
RPA	Random-Phase Approximation
RS	Real Space
ScaLAPACK	Scalable Linear Algebra PACKage
SCF	Self-Consistent Field
SEX	Screened-Exchange
SVD	Singular Value Decomposition
VBM	Valence Band Maximum
vdW-DF	van der Waals Density Functional

Résumé

Le formalisme GW , dans le cadre des théories de perturbation à N -corps utilisant les fonctions de Green, gagne en popularité pour la description des propriétés électroniques des systèmes de la matière condensée en physique du solide, et plus récemment en chimie. Son application à des systèmes complexes d'intérêt en nanoscience, chimie, voire biologie, est freinée cependant par son coût numérique en particulier dans le cas de systèmes désordonnés, ou immergés dans un environnement ouvert (un solvant, un milieu moléculaire, une électrode, etc.) Le but de cette thèse est de développer des techniques multi-échelles, combinant des approches à N -corps de haut niveau pour le sous-système d'intérêt, avec une description simplifiée, mais tout de même totalement *ab initio*, d'un environnement électrostatique et diélectrique. Ces approches vont donc au-delà des modèles classiques paramétrés, développés en particulier dans la communauté chimie quantique, et basés sur une description continue (« polarizable continuum model ») ou discrète (QM/MM) de l'environnement.

Pour atteindre cet objectif, nous adoptons une approche en fragments de l'environnement, particulièrement adaptée aux systèmes moléculaires. La susceptibilité électronique non-interagissante devient ainsi diagonale par blocs, permettant d'abaisser la complexité algorithmique de quartique à cubique. Pour réduire le pré-facteur associé à l'obtention du potentiel écranté W (équation de Dyson), nous avons développé un algorithme de compression de l'opérateur susceptibilité. L'obtention automatique d'une base de polarisation très compacte permet de réduire fortement la taille des blocs de susceptibilité associés aux fragments de l'environnement. Cette méthode permet de calculer la réponse diélectrique de systèmes contenant des centaines de milliers d'atomes avec une excellente précision. Cette approche est présentée via l'étude de cristaux de fullerènes en volume, en surface, et en sous-surface.

Alors que le formalisme GW est dynamique par nature, avec ainsi un potentiel coulombien écranté W dépendant de la fréquence, une première étude est réalisée dans le cadre d'une approximation statique (limite basse fréquence) pour décrire l'écrantage par l'environnement. Une telle approche s'inscrit dans la continuité des modèles semi-empiriques traditionnels pour la description d'un milieu environnant polarisable. Cette thèse est donc l'occasion de mesurer la validité d'une telle approximation, qui suppose que l'environnement répond de façon instantanée à une excitation électronique, grâce à une comparaison explicite avec une description totalement dynamique de la réponse diélectrique de l'environnement. L'étude d'une surface de fullerènes, ainsi que d'une molécule d'eau dans un nanotube de carbone métallique, montrent qu'une description statique de l'environnement induit des erreurs sur l'énergie de polarisation inférieure à 10% sous condition que le « repliement » de l'environnement soit correctement effectué.

L'approche fragment est également appliquée à des cristaux covalents isolants, et en particulier au nitrure de bore hexagonal (h -BN). Nous avons illustré en particulier comment calculer les niveaux d'énergie de défauts ponctuels dans du h -BN, dans la vraie limite diluée, et donnons les lois d'échelle pour la renormalisation de ces niveaux de la monocouche vers un nombre (n) de couches. Cette étude démontre qu'à l'instar des systèmes moléculaires, la fragmentation de systèmes covalents isolants est possible, en lien sans doute avec le caractère très courte portée de la susceptibilité dans ces systèmes.

Ces développements, permettant l'extension d'approches quantiques à N -corps à des systèmes de plus en plus complexes, ont été implémentés dans le code `BEDEFT`, un code massivement parallèle pour l'étude des propriétés électroniques de systèmes de grande taille.

Abstract

The many-body perturbation theory GW formalism, based on Green's functions, is growing in popularity for the description of the electronic properties of condensed matter systems in solid-state physics, and more recently chemistry. Unfortunately, its application to complex systems of interest in nanosciences, chemistry, or even biology, is hampered by the large associated computing time cost, in particular in the case of disordered systems, or systems immersed in an opened environment (a solvent, a molecular medium, an electrode, etc.) The goal of the present PhD thesis is to focus on the development of multiscale techniques, merging high-level many-body treatments of the subsystem of interest, with a simplified but fully *ab initio* description of the electrostatic and dielectric environment. Such approaches should go beyond classical parametrized models, mainly developed in quantum chemistry community, which are based on a continuum ("polarizable continuum model") or discrete description (QM/MM) of the environment.

To reach such a goal, we adopt a divide-and-conquer fragmentation scheme for the environment, particularly suited to molecular systems. This leads to a block-diagonal non-interacting electron susceptibility, decreasing the algorithmic complexity from quartic to cubic. To reduce the prefactor, associated to the inversion of the Dyson equation for the screened Coulomb potential W , we have developed a compression algorithm for the susceptibility operator. The automatic computation of an extremely compact polarization basis set allows a large reduction of the size of the susceptibility blocks, associated to fragments in the environment. Such a method enables us to compute the dielectric response of systems made of several hundred thousand atoms, with an excellent accuracy. This approach is presented through the study of fullerene bulk, surface and subsurface crystals.

While the GW formalism is dynamical, with a frequency-dependent screened Coulomb potential W , a first study is done in a static approximation (low-frequency limit) for the screening properties of the environment. Such an approach follows the traditional semi-empirical models of a polarizable environment. This PhD thesis assesses the validity of such an approximation, which assumes an instantaneous response of the environment to an electronic excitation, thanks to an explicit comparison with a fully dynamical dielectric response of the environment. The study of a surface of fullerenes, as well as a water molecule inside a metallic carbon nanotube, show that a static description of the environment leads to errors on the polarization energy below 10%, on condition of treating the "folding" of the environment in the proper way.

The fragment approach is also applied to covalent insulator crystals, and more particularly to hexagonal boron nitride (h -BN). We explain how to compute the energy levels of point defects in h -BN, in the true dilute limit, and we give the asymptotic scaling laws for the renormalization of these energy levels, from the monolayer to a (n)-layer system. In addition to molecular systems, this study highlights the possibility to apply the fragment approach to covalent insulators, probably due to the short range behavior of the susceptibility of these latter.

All of these developments, extending many-body methods to increasingly complex systems, have been implemented in the massively parallel code `BEDEFT`, dedicated to the study of electronic properties of large scale systems.

Introduction (version française)

L'analyse des propriétés électroniques de matériaux est un enjeu majeur pour l'étude des relations entre leur structure et leurs propriétés. Ces caractéristiques semblent pouvoir permettre de mieux comprendre les raisons pour lesquelles telle ou telle combinaison d'atomes, suivant un arrangement donné, mène à un milieu conducteur ou au contraire à un isolant, à un matériau émettant ou absorbant de la lumière, à un ensemble prometteur pour le photovoltaïque, la photosynthèse, la catalyse, etc. Certes, de nouvelles techniques d'apprentissage automatique (en anglais *machine learning*) semblent pouvoir faire un lien direct entre structure et propriétés, sans avoir recours à des théories de mécanique quantique complexes. Il est cependant nécessaire que le jeu de données d'apprentissage soit basé sur des relevés expérimentaux. Toutefois, les avancées majeures durant les dernières décennies dans le domaine des simulations *ab initio* permettent d'espérer qu'une meilleure compréhension des phénomènes complexes, de la physique du solide à la chimie des solutions, en passant par la biologie, puisse être obtenue à l'aide de telles techniques numériques *ab initio*.

La théorie de perturbations à N -corps GW , représentant le formalisme central de ce manuscrit de thèse, illustre cette évolution. À l'origine développée et testée par Lars Hedin dans les années 1960 [1] pour le gaz homogène d'électrons interagissants, des implémentations *ab initio* d'une telle méthode ont émergé au milieu des années 1980 pour le calcul de structures de bandes de semi-conducteurs élémentaires. Aujourd'hui, des systèmes complexes tels des systèmes désordonnés, des défauts ponctuels, des interfaces (voir FIGURE 1), des cristaux à une ou deux dimensions, etc., contenant jusqu'à des centaines d'atomes, peuvent régulièrement être étudiés. De façon plus récente, des calculs sur des systèmes moléculaires organiques isolés en phase gaz gagnent en intérêt auprès d'une communauté de plus en plus large, faisant le lien entre physique et chimie quantique. À cet égard, le succès du formalisme GW a même été qualifié de « miracle » [2] dans la limite d'un faible nombre d'électrons. En effet, dans une telle limite où l'écrantage est réduit, l'approche GW devrait se réduire au formalisme GV , à savoir l'approche Hartree-Fock. De façon générale, l'approximation GW fait office d'approche de bas niveau (efficace d'un point de vue numérique), mais pourtant robuste, au sens où elle fournit des résultats satisfaisants pour des systèmes tant isolants que métalliques, de taille finie ou infinie. Une telle affirmation exclue de fait les systèmes « fortement corrélés ».

Ce travail doctoral cherche à repousser les limites du formalisme GW dans sa capacité à étudier des systèmes complexes. Complexité ne rime pas ici avec « corrélations fortes ». Tout au long de ces trois années, le formalisme GW a été utilisé tel quel, sans chercher par exemple à inclure des diagrammes d'ordre supérieur. La complexité réside plutôt dans la taille et le désordre des systèmes étudiés. Malheureusement, beaucoup de systèmes d'intérêt ne présentent pas de conditions aux limites périodiques, rendant invalide l'approche historique des physiciens du solide basée sur l'utilisation d'ondes planes et du théorème de Bloch. Cependant, le concept d'écrantage de moyenne à longue portée, inhérent au formalisme GW , nous semble toujours très pertinent pour des systèmes organiques désordonnés, des molécules ou encore l'ADN en solution. Face à de tels problèmes, la communauté de chimie quantique a développé des approches quantiques dites « environnées », dans lesquelles le système total est

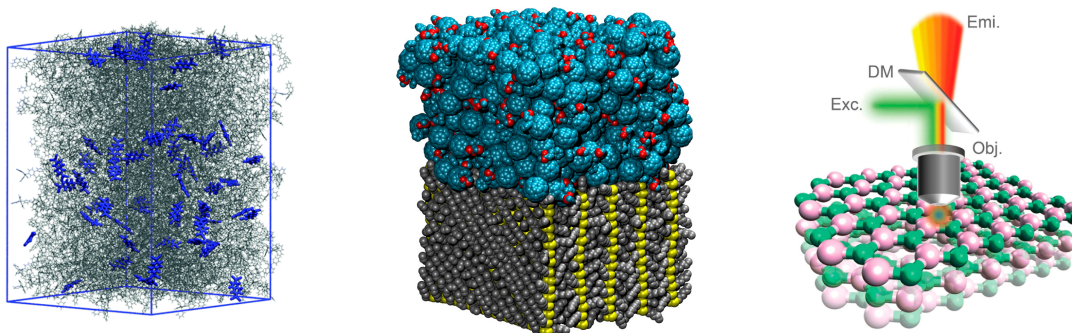


Figure 1: (Gauche) : Système amorphe de NPB (N,N' -di(1-naphthyl)- N,N' -diphényl-(1,1'-biphényl)-4,4'-diamine) (en gris) dopé par du F6TCNNQ (2,2'-(perfluoronaphthalene-2,6-diylidene)dimalononitrile) (en bleu). Image adaptée de [3]. (Milieu) : Interface PCBM ([6,6]-phényl- C_{61} -butyrate de méthyle)/P3HT (poly(3-hexylthiophène)) désordonnés, utile pour des cellules photovoltaïques organiques. Image adaptée de [4]. (Droite) : Représentation schématique d'un défaut dans un réseau hexagonal de nitrure de bore. Image adaptée de [5].

partitionné en un sous-système « central » ou « actif », et son environnement. Les propriétés électroniques du sous-système d'intérêt sont calculées précisément au niveau quantique tandis que le milieu environnant est traité de façon plus simple. L'environnement ne nous intéresse qu'à la mesure de ses effets sur le sous-système « actif ». L'importance d'une telle approche a été reconnue par le prix Nobel de chimie 2013, remis à Martin Karplus, Michael Levitt et Arieh Warshel pour « la mise au point de modèles multi-échelles de systèmes chimiques complexes ».

Jusqu'à présent, l'approche *ab initio GW* a essentiellement été combinée avec une description semi-empirique continue (« polarizable continuum model ») [6–8] ou discrète (QM/MM) de l'environnement [9–13]. Ce travail doctoral vise à aller au-delà de ces modèles classiques paramétrés pour l'environnement, en proposant une approche simplifiée mais tout de même *ab initio* du milieu polarisable.

Le chapitre 1 illustre de façon qualitative les effets d'écrantage, particulièrement utiles pour comprendre et décrire les expériences de photoémission. Ce chapitre est également dédié à la présentation des méthodes *ab initio* utilisées tout au long de ce manuscrit pour quantifier ces phénomènes. Ainsi, la théorie de la fonctionnelle de la densité (DFT) et sa reformulation par Kohn et Sham sont introduites. Elles servent de point de départ à la théorie de perturbations à N -corps utilisée durant cette thèse, à savoir l'approximation *GW*. Différents aspects de ce formalisme, au cœur de cette thèse, sont également présentés. Une attention particulière est portée à son implémentation dans le code *GW* en bases gaussiennes **BEDEFT**, développé en interne dans notre groupe. Ce chapitre, à la portée très générale, vise à faciliter la compréhension des développements réalisés dans les chapitres suivants.

Le chapitre 2 décrit notre nouvelle approche permettant de réaliser des calculs *GW* sur un sous-système « environné » dans un environnement contenant des centaines de milliers d'atomes. Ce dernier est traité au niveau totalement *ab initio* de l'approximation de la phase aléatoire (RPA). Notre implémentation repose sur l'approximation fragment, consistant à négliger le recouvrement orbitalaire entre différents sous-systèmes, amenant à une susceptibilité

non-interagissante χ_0 diagonale par blocs. La taille des blocs associés est réduite de façon drastique à l'aide d'un algorithme de compression sous contraintes, permettant de conserver les tenseurs de polarisabilité de bas ordres essentiels pour les effets d'écrantage. En alliant une telle méthode à des lois asymptotiques, nous montrons comment calculer à faible coût l'énergie de polarisation d'un C_{60} dans un nombre fini de couches, en surface ou en volume d'un cristal infini.

Le chapitre 3 mesure la validité d'un traitement adiabatique des effets de polarisation de l'environnement, par une comparaison à une description totalement dynamique de la réponse diélectrique de ce dernier. Utilisant une fois de plus la méthode fragment, nous introduisons l'approche QM_{GW}/QM_{COHSEX} , permettant d'allier dans le même calcul une description dynamique de la partie « active » à celle statique $COHSEX$ pour le milieu polarisable. Cette méthode, ainsi que l'approche $\Delta COHSEX$, sont comparées à une description totalement dynamique du système total. Via l'étude d'une surface de C_{60} ou d'une molécule d'eau dans un nanotube de carbone métallique, il apparaît que la méthode QM_{GW}/QM_{COHSEX} reproduit plus fidèlement les résultats dynamiques, avec des erreurs de l'ordre de quelques pour cent sur les énergies de polarisation.

Finalement, le chapitre 4 illustre l'application de la méthode fragment à l'étude des niveaux d'énergie de défauts ponctuels dans du nitrure de bore hexagonal. Il s'agit ici d'atteindre la limite diluée, à savoir celle d'un défaut unique dans un environnement infini. Un tel objectif est accompli en utilisant l'approximation fragment entre les couches, mais également à l'intérieur de ces dernières. Ceci nous permet d'étudier des systèmes de taille suffisamment grande pour entrer dans un régime asymptotique. Il devient alors possible de calculer l'énergie de polarisation d'un défaut dans un système avec un nombre fini (n) de couches, en surface ou en volume d'un cristal de h -BN. Nos résultats mettent en avant le caractère universel en $(1/n)$ d'une telle énergie, indépendamment de la nature exacte du défaut.

Introduction (English version)

The study of the electronic properties of materials is a central issue when attempting to correlate the relations between structure and properties. The reason why some specific combinations of atoms, with a given arrangement, will stand as good conductors or insulators, light absorbers or emitters, or may be of interest in applications related to photovoltaic, photosynthesis, catalysis, etc., can be hopefully found in a better understanding of their electronic properties. Emerging machine learning techniques may be regarded as an attempt to make a direct relation between structure and properties, without involving necessarily intermediate and complex quantum mechanical theories if the “learning set” originates from experiments. It remains that the significant advances of *ab initio* simulations, in the last decades, preserve the hope that the exploration of novel materials by *ab initio* computational techniques may prove useful in providing a better understanding of complex phenomena, from solid state physics to wet chemistry or biology.

The many-body perturbation *GW* theory, which stands as the central formalism in the present doctoral manuscript, illustrates this evolution. Originally developed and tested by Lars Hedin in the 60s [1] for the homogeneous interacting electron gas, early *ab initio* implementations emerged in the mid-80s for the study of the band structures of elemental semiconductors. Today, complex systems, such as disordered interfaces, point defects, interfaces (see FIGURE 2), one- or two-dimensional crystals, defects, etc., containing up to a few hundred atoms, can be routinely studied. More recently, isolated gas phase molecular organic systems are being treated by an increasingly large community, crossing the line between physics and quantum chemistry. In that respect, the success of the *GW* formalism has been coined “a miracle” [2] in this limit of few electrons. Indeed, in the limit of reduced screening, the *GW* approach is expected to reduce to the *GV* formalism, namely Hartree-Fock. Overall, the *GW* approximation stands as a relatively low-level (computationally efficient) approach that is very robust, in the sense that it provides satisfactory results for insulating to metallic, finite size to infinite systems. Such a statement clearly excludes “strongly correlated” systems.

The present doctoral studies attempt to push the limits of the *GW* formalism in its ability to tackle complex systems. By complex systems, we do not mean systems where electronic correlations become stronger: we somehow use the *GW* formalism as it stands without attempting to include higher order diagrams. What we mean are systems for which the complexity lies in the size and in disorder. Unfortunately, many systems of interest can hardly be reduced to periodic boundary conditions, invalidating the historical planewave-basis Bloch-theorem approach developed by solid-state physicists. Still, the concept of medium to long-range screening, inherent to the *GW* formalism, is expected to be extremely relevant for disordered organic systems, molecules in solution, DNA in its wet environment, etc. For such problems, the quantum chemistry community has developed “embedded” techniques, partitioning the collection of atoms in an “active” or “central” subsystem, treated at the best quantum mechanical level, and an environment, that is only of interest for its action on the central subsystem. As such, the environment is usually described at a lower level

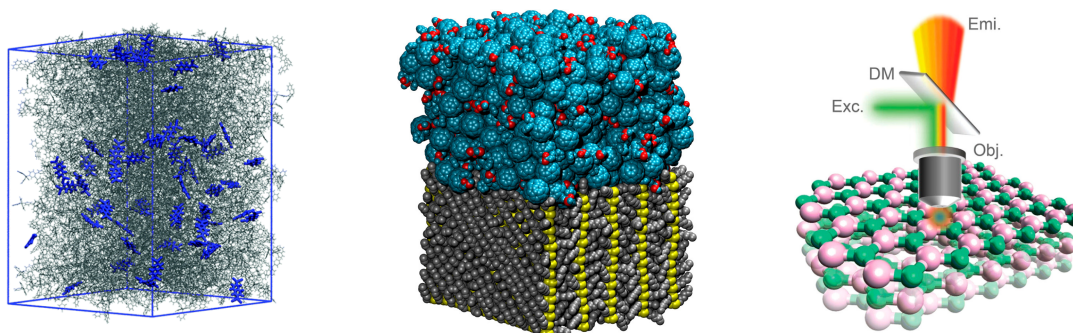


Figure 2: (Left): realistic amorphous morphology of NPB (N,N' -di(1-naphthyl)- N,N' -diphenyl-(1,1'-biphenyl)-4,4'-diamine) (gray wireframe representation) doped with F6TCNNQ (2,2'-(perfluoronaphthalene-2,6-diylidene)dimalononitrile) (blue sticks). Adapted from [3]. (Center): PCBM ([6,6]-phenyl- C_{60} -butyric acid methyl ester)/P3HT (poly(3-hexylthiophene-2,5-diyl)) disordered interface, particularly useful for organic photovoltaic cells. Adapted from [4]. (Right): Schematic representation of a point defect in hexagonal boron nitride. Adapted from [5].

of theory. The importance of such a strategy was recognized by the 2013 chemistry Nobel Prize awarded to Martin Karplus, Michael Levitt and Arieh Warshel for “the development of multiscale models for complex chemical systems”.

Currently, the *ab initio* *GW* approach has been merged with semi-empirical continuous (Polarizable Continuum Model (PCM)) [6–8] or discrete (Quantum Mechanics (QM)/Molecular Mechanics (MM)) description of the environment [9–13]. This doctoral thesis is dedicated to the development of approaches going beyond such parameterized classical models, with a simplified but fully *ab initio* description of the polarizable medium.

The chapter 1 illustrates qualitatively the screening effects, particularly useful to describe and to understand the photoemission experiments. This chapter also presents the *ab initio* methods used throughout this manuscript to quantify such phenomena. Density-Functional Theory (DFT), and its reformulation by Kohn and Sham are introduced. They serve as a starting point for the *GW* many-body perturbation theory. Different aspects of this latter, at the center of this manuscript, are also presented, with a particular emphasis on its implementation in the Gaussian basis *GW* code **BEDEFT** developed in our group. This chapter, of a general scope, aims at making easier the understanding of the following developments.

The chapter 2 describes our new approach to perform *GW* calculations on subsystems “embedded” in an environment made of hundreds of thousands of atoms. The polarizable medium is treated at the fully *ab initio* Random-Phase Approximation (RPA) level. Our implementation is based on the fragment approach, consisting into neglecting the wavefunction overlaps between different subsystems. This leads to a block-diagonal non-interacting electron susceptibility χ_0 . The size of the different blocks is further drastically reduced thanks to a compression under constraints algorithm conserving the low-order polarizability tensors, particularly relevant for the screening effects. The combination of these methods with asymptotic laws enables us to compute affordably the polarization energy of one C_{60} in a finite number of layers, at the surface or in a bulk infinite crystal.

The chapter 3 assesses the validity of an adiabatic treatment of the polarization effects created by the environment, thanks to a comparison to a fully dynamical description of the dielectric response of this latter. Using again the fragment approximation, we introduce the $\text{QM}_{\text{GW}}/\text{QM}_{\text{COHSEX}}$ approach which enables us to combine, in the same calculation, a dynamical description of the “active” part to a static COHSEX one for the polarizable medium. This method, as well as the ΔCOHSEX one, are compared to a fully dynamical description of the total system. The study of a surface of C_{60} , and another one of a water molecule inside a metallic carbon nanotube, point out that the $\text{QM}_{\text{GW}}/\text{QM}_{\text{COHSEX}}$ method is more accurate. It leads to errors on the polarization energies, with respect to a fully dynamical approach, of the order of a few percent.

Finally, the chapter 4 illustrates the application of the fragment method to the study of energy levels of point defects in hexagonal boron nitride. The goal is to reach the dilute limit, representing one unique point defect in an infinite size environment. Such an objective is achieved via the fragmentation between layers, but also inside each of them. This allows us to study systems large enough to enter the asymptotic regime. The polarization energy of a point defect can thus be computed within a slab with a finite number of layers, but also on a surface or within a bulk material. Our results demonstrate that the evolution of the defect energy levels as a function of layer number (n) varies as $(1/n)$ in a universal fashion, namely independently of the type of defect.

Theoretical background and methodology

Contents

Résumé	22
Summary	23
1.1 Theoretical spectroscopy	24
1.1.1 Photoemission spectroscopy	24
1.1.2 From gas phase to crystal phase	25
1.1.3 Simple models of polarization	27
1.1.3.1 Charge in front of a metallic surface and image charges	27
1.1.3.2 Charge in a dielectric cavity	29
1.2 The many-body problem	30
1.2.1 The Born-Oppenheimer approximation	30
1.3 <i>Ab initio</i> approaches	31
1.3.1 Density-Functional Theory (DFT)	31
1.3.1.1 The Hohenberg and Kohn theorems	31
1.3.1.2 The Kohn-Sham formulation	33
1.3.1.3 Exchange-correlation functionals	35
1.3.1.4 Discussion on the meaning of the Kohn-Sham single-particle energies	36
1.3.1.5 DFT in practice	38
1.3.2 The <i>GW</i> formalism	41
1.3.2.1 Green's function	41
1.3.2.2 Lehmann representation and spectral function	42
1.3.2.3 Dyson equation on G	44
1.3.2.4 The self-energy in linear response	46
1.3.2.5 Hedin's equations	48
1.3.2.6 The <i>GW</i> approximation	50
1.3.2.7 The COHSEX decomposition	52
1.3.2.8 The static COHSEX approximation	53
1.3.2.9 <i>GW</i> in practice	54
1.3.2.10 Implementation in BEDEFT	56
1.4 Objectives	62

Résumé

Ce chapitre a pour but de présenter qualitativement les phénomènes physiques majeurs que nous souhaitons étudier dans cette thèse, ainsi que les méthodes générales employées pour y parvenir.

La partie 1.1 permet de définir les grandeurs centrales que nous chercherons à calculer au cours des chapitres suivants. Il s'agit des énergies d'ajout et de retrait d'électron, pouvant être mesurées par des expériences de spectroscopie de photoémission. L'évolution de ces quantités, de la phase gaz à la phase condensée, est qualitativement expliquée et illustrée à l'aide de modèles simples de charges images.

L'approximation de Born-Oppenheimer, présentée dans la section 1.2, permet de simplifier les approches plus quantitatives du problème à N -corps. La section suivante met en avant les deux grandes méthodes *ab initio* utilisées tout au long de cette thèse pour arriver au calcul des niveaux d'énergies électroniques.

La théorie de la fonctionnelle de la densité (DFT) est ainsi présentée dans la section 1.3.1. Les deux théorèmes majeurs de Hohenberg et Kohn sont démontrés, ainsi que la reformulation de Kohn et Sham, qui consiste à retranscrire le problème exact à N -corps par un problème d'électrons non-interagissants. Différents aspects de cette reformulation sont ainsi discutés tels que les fonctionnelles d'échange-corrélation, ou encore le sens des valeurs propres Kohn-Sham, notamment via le théorème de Janak. Enfin, des aspects pratiques sur les calculs DFT réalisés durant cette thèse, sur des systèmes moléculaires de taille finie en bases gaussiennes, sont également présentés.

La partie 1.3.2 permet la présentation du formalisme au cœur de ce travail doctoral. Il s'agit d'une théorie des perturbations à N -corps, à savoir l'approximation GW . Sa grandeur principale, la fonction de Green ordonnée en temps à un corps G , est définie à la fois en temps et en représentation spectrale. L'équation de Dyson sur G , ainsi que l'équation de quasi-particule, sont dérivées à l'aide de l'équation du mouvement de la fonction de Green. D'autres relations sont obtenues via la réponse linéaire du système soumis à une perturbation extérieure. L'ensemble permet d'arriver aux équations de Hedin, et à leurs approximations dans le cadre GW . Différentes formulations de la *self-energy* Σ sont présentées, notamment la version COHSEX et son approximation statique, jouant un rôle essentiel dans les chapitres suivants. Enfin, ce chapitre souligne des aspects pratiques des calculs GW que nous avons menés, comme la présentation des approches $G_0W_0/evGW$, ou celle des caractéristiques propres au code GW développé et utilisé pendant ces trois dernières années.

Ce chapitre se conclut sur les objectifs généraux de ces études, à savoir la description de systèmes complexes de grandes tailles à un niveau totalement *ab initio*, allant au-delà des modèles semi-empiriques utilisés jusqu'à maintenant pour décrire un environnement polarisable.

Summary

This chapter aims at giving a qualitative description of the main physical phenomena studied during this thesis, as well as an overview of the main methods and formalisms used throughout this work.

Section 1.1 illustrates the main physical observables studied during this thesis. They correspond to the electron addition and removal energies, measured in practice through experiments of photoemission spectroscopy. The evolution of such quantities, from the gas phase to the condensed phase, is qualitatively explained and illustrated through simple image charges models.

Section 1.2 leads to a more quantitative description of the N -body problem, with its restriction to the Born-Oppenheimer approximation. The following section aims at presenting the two *ab initio* methods used during this thesis.

Density-Functional Theory (DFT) is briefly described in section 1.3.1. The two theorems of Hohenberg and Kohn are demonstrated, as well as the reformulation by Kohn and Sham. This latter maps the exact N -body problem on a fictitious one, made of non-interacting electrons. Some aspects of such a reformulation are discussed, such as the exchange-correlation functionals as well as the meaning of the Kohn-Sham eigenvalues through the Janak's theorem. Finally, some practical aspects of DFT, associated with calculations done during this thesis on finite size systems and with Gaussian basis sets, are also presented.

Section 1.3.2 presents the main many-body perturbation theory used throughout this thesis, namely the GW formalism. The one-body time ordered Green's function G is introduced, both in time and spectral representation. Its Dyson equation, as well as the quasiparticle equation, are derived thanks to the equation of motion of G . Other relations are also computed, thanks to linear response theory. All of these quantities result in the set of Hedin's equations, and their GW approximations. Various formulations of the self-energy Σ are presented, like the COHSEX decomposition and its static approximation, which plays a major role in the following chapters. Finally, this section illustrates some practical aspects of the GW calculations done during this thesis, including the $G_0W_0/evGW$ approaches, or some specific features of the GW code which I developed rather extensively during the last three years.

In conclusion of this chapter, the main objectives of this doctoral study are presented. My thesis is devoted to set up new fully *ab initio* methods to describe large and complex systems, going beyond the semi-empirical parameterized models used until now to describe large scale polarizable environments.

1.1 Theoretical spectroscopy

1.1.1 Photoemission spectroscopy

Electronic energy levels represent one of the main properties of a quantum system. When interactions between electrons are turned on (*e.g.* via the Coulomb potential), eigenstates of the N -body Hamiltonian become many-body states, which can be different from single Slater determinants. While electronic energy levels are no longer single particle energies, it is still possible to define addition and removal energies. These latter are experimentally measured by Photoemission Spectroscopy (**PES**) and Inverse Photoemission Spectroscopy (**IPES**), as represented in **FIGURE 1.1**.

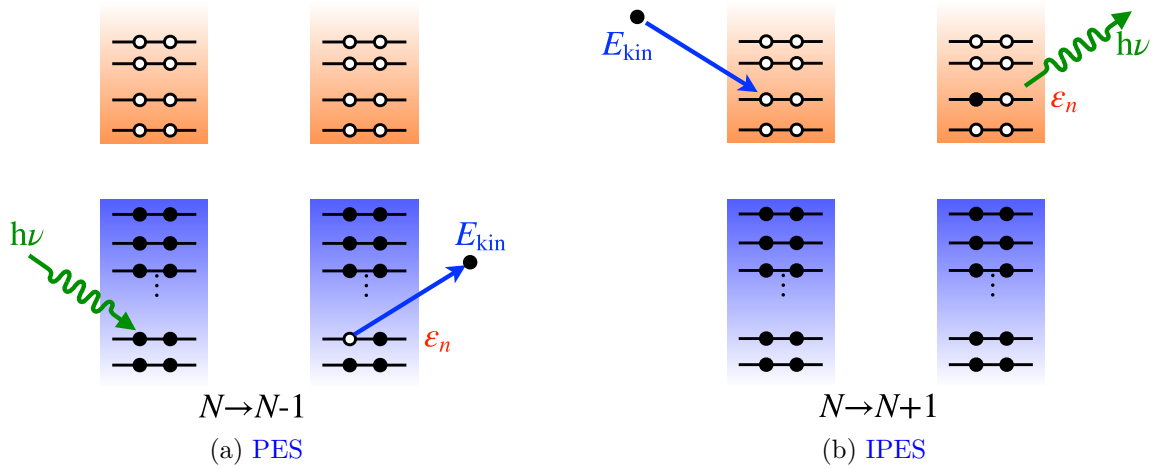


Figure 1.1: Schematic representation of the process of Photoemission (a) and Inverse Photoemission (b). $h\nu$ corresponds to the energy of the incoming/emitted photon and E_{kin} to the kinetic energy of the removed/added electron. N refers to the initial number of electrons and ε_n to the removal/addition energy of an electron. Courtesy of Gian-Marco Rignanesse.

In a **PES** experiment, electrons are ejected from the system of interest due to irradiation with light, ranging from ultraviolet light (Ultraviolet Photoelectron Spectroscopy) to X-rays (X-ray Photoelectron Spectroscopy) according to the type of probed properties. In such an experiment, a photon of energy $h\nu$ impinges on the system, initially in its N -electron ground state of total energy E_0^N . An electron is sent to the vacuum, with a kinetic energy E_{kin} , while the sample remains in the i^{th} excited $(N-1)$ -electron state, of total energy E_i^{N-1} , as represented in **FIGURE 1.1a**. The conservation of energy yields

$$h\nu + E_0^N = E_{\text{kin}} + E_i^{N-1}, \quad (1.1)$$

leading to the definition of the i^{th} electron removal energy

$$\varepsilon_i = E_0^N - E_i^{N-1} < \mu, \quad (1.2)$$

with μ the chemical potential. The particular case $i = 0$ leads to the definition of the Ionization Potential (**IP**), such that $\text{IP} = -\varepsilon_0 = E_0^{N-1} - E_0^N$. The **IP** corresponds to the

minimal energy to remove an electron of the ground state of the N -electron system, and is always positive [14].

The IPES corresponds to the reverse process, to probe unoccupied states. As described by FIGURE 1.1b, an incident electron with kinetic energy E_{kin} is scattered in the sample, originally in its N -electron ground state of total energy E_0^N . A photon of energy $h\nu$ is emitted by the $(N+1)$ -electron system, which ends up in the a^{th} excited $(N+1)$ -electron state, of total energy E_a^{N+1} . The conservation of energy reads

$$E_{\text{kin}} + E_0^N = h\nu + E_a^{N+1}, \quad (1.3)$$

leading to the a^{th} electron addition energy

$$\varepsilon_a = E_a^{N+1} - E_0^N \geq \mu. \quad (1.4)$$

The specific case $a = 0$ leads to the definition of the Electron Affinity (EA), such that $\text{EA} = -\varepsilon_0 = E_0^N - E_0^{N+1}$. The EA corresponds to the opposite of the minimal energy to add an electron to the ground state of the N -electron system. It is negative when the added electron is unbound, while it is positive if the electron is bound.

In this context, the fundamental gap E_{gap} of the system, the one experimentally measured in a photoemission experiment, is defined as

$$E_{\text{gap}} = \text{IP} - \text{EA}. \quad (1.5)$$

This defines one of the main quantity I will try to compute for different systems throughout this thesis.

Finally, an important point to keep in mind for comparison between experimental and theoretical results is that these experimental techniques sample essentially electrons close to the surface of the studied system, because the escape depth of the electrons is small [15].

Through this short study of PES/IPES, we can see that the measurement of the band structure of solids, or the electronic structure of molecules, requires adding explicit charges to the system. This leads to interactions of this added charge with the other N electrons. To better understand these different effects, we can (qualitatively) study the evolution of the IP and of the EA when a molecule goes from the gas phase to a crystal phase.

1.1.2 From gas phase to crystal phase

Qualitatively, when a molecule is embedded in a dense phase (*e.g.* in a solvent, on a surface, at an organic interface...), three main effects alter its electronic structure with respect to the gas phase:

- a) an electrostatic effect, or in other words, a crystal field effect. Atoms or molecules of the environment generate an electrostatic potential thanks to their permanent multipoles (dipole, quadrupole, ...). Such a crystal field may alter the electronic energy levels of the molecule of interest. It is important to note that such an effect is a property of the ground state, and not a response of the environment to an excitation of the studied system;

- b) a dynamical screening effect of the added charge in a photoemission experiment. Contrary to the effect a), the environment reacts to a charged excitation of the subsystem of interest. This “polarization” effect will be the central phenomenon I will try to describe in this present thesis;
- c) a dispersion effect, or in other words, an effect of the delocalization of the wavefunctions. It leads to the creation of energy bands in solids, or the broadening of the energy levels in a disordered system.

These different effects are schematically represented in FIGURE 1.2. A more quantitative study, through the example of a surface of pentacene and perfluoropentacene, can be found in Ref.[11].

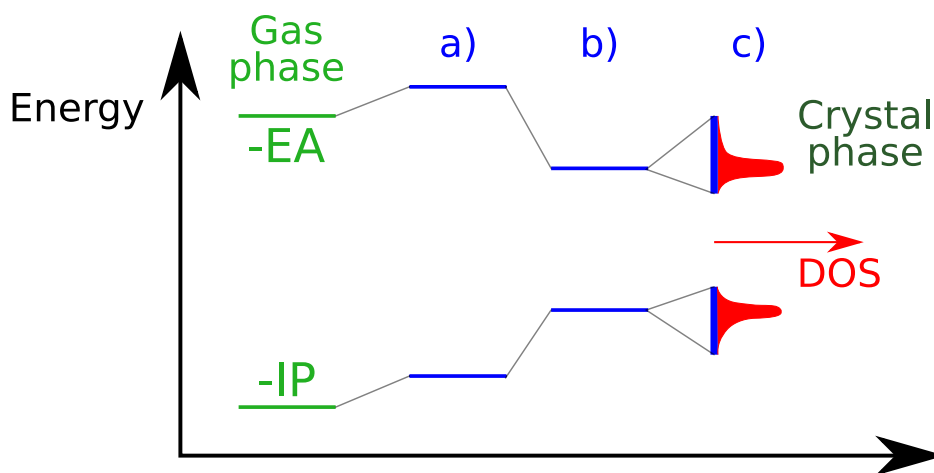


Figure 1.2: Evolution of the ionization potential IP and of the electronic affinity EA of a molecule going from gas phase to crystal phase. Using the notations introduced before: a) electrostatic effects, b) dynamical polarization effects of the environment and c) dispersion effects. The red axis represents the Density Of States (DOS), with respect to the energy (vertical axis). For each effect, the correction to EA can be different from the one of the IP .

The polarization effects b) correspond to the interaction of the added charge with the induced dipoles generated in the environment. The added charge creates a long-range electric field¹ \mathbf{E} . If the environment is polarizable, it responds in the linear regime via the creation on each molecule of an induced dipole $\mathbf{p} = \alpha(\mathbf{E} + \mathbf{E}_{\text{ind}})$ (in red in FIGURE 1.3a), where \mathbf{E}_{ind} is the induced field generated by the response of other molecules, and α the molecular dipolar polarizability tensor. These dipoles create a reaction field Φ^{reac} stabilizing the added charge to the system via the polarization energy, as summarized in FIGURE 1.3b. Another possibility to describe the effects of the environment is to use the dielectric function ϵ , which in general is a tensor. In any case, both α and ϵ are in general dynamical (or frequency-dependent), depending on the energy of the perturbing excitation, as represented in FIGURE 1.3c through the example of silicon.

¹In this thesis, the vectors or matrices are written in bold.

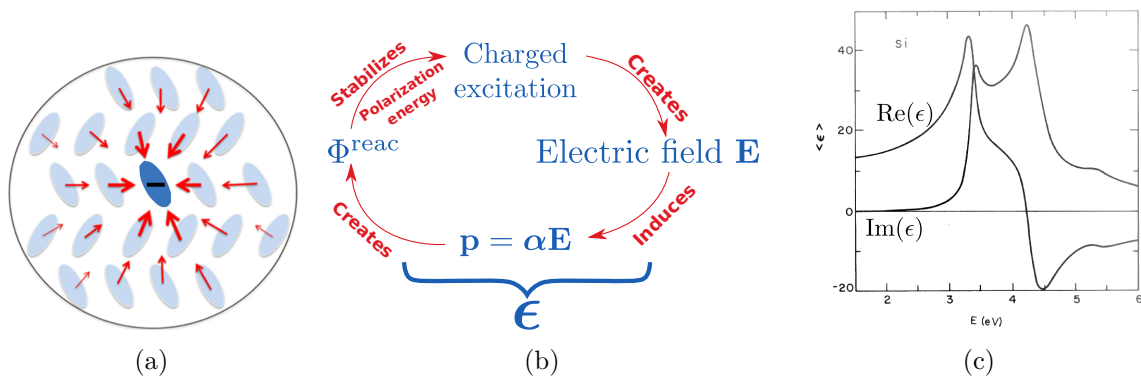


Figure 1.3: (a) Schematic representation of induced dipoles (in red) created by an added negative charge in the dark-blue molecule. Adapted from Ref.[10]. (b) Loop representing the different processes leading to the stabilization of an added charge by a polarizable environment. (c) Real and imaginary part of the isotropic macroscopic dielectric function of silicon in solid phase, with respect to the excitation energy E . Adapted from Ref.[16].

To better understand these polarization effects, we may analyze simple classical models of “image charges” to highlight the main physical phenomena.

1.1.3 Simple models of polarization

1.1.3.1 Charge in front of a metallic surface and image charges

We want to compute the polarization energy P for a charge q in the vacuum in front of a semi-infinite metallic surface of uniform potential $\Phi = 0$, as represented in FIGURE 1.4a. This P corresponds to the work exerted on the charge q , to bring it adiabatically from infinity² to the distance d from the surface. To do so, we adopt a classical electrostatic approach to capture the effects created by the metallic surface and to estimate an order of magnitude of P . Such a model corresponds roughly to a charged molecule in front of a metallic electrode.

Such a polarization energy can be computed via the image charges method, as represented in FIGURE 1.4b. The electrostatic problem is formally equivalent to the one of two charges q and $-q$ in the vacuum, separated by a distance $2d$. As required, the resulting electrostatic potential is equal to zero in the plane (Oyz). The reaction potential created by the image charge is

$$\Phi^{\text{reac}}(\mathbf{r}) = \frac{-q}{4\pi\epsilon_0\|\mathbf{r} + d\mathbf{u}_x\|}, \quad (1.6)$$

with ϵ_0 the vacuum permittivity and \mathbf{u}_x a unitary vector along (Ox). This leads to an electrostatic potential energy between the two charges

$$V^{\text{pot}} = -\frac{q^2}{8\pi\epsilon_0 d}. \quad (1.7)$$

²In this context, it would represent a molecule in gas phase.

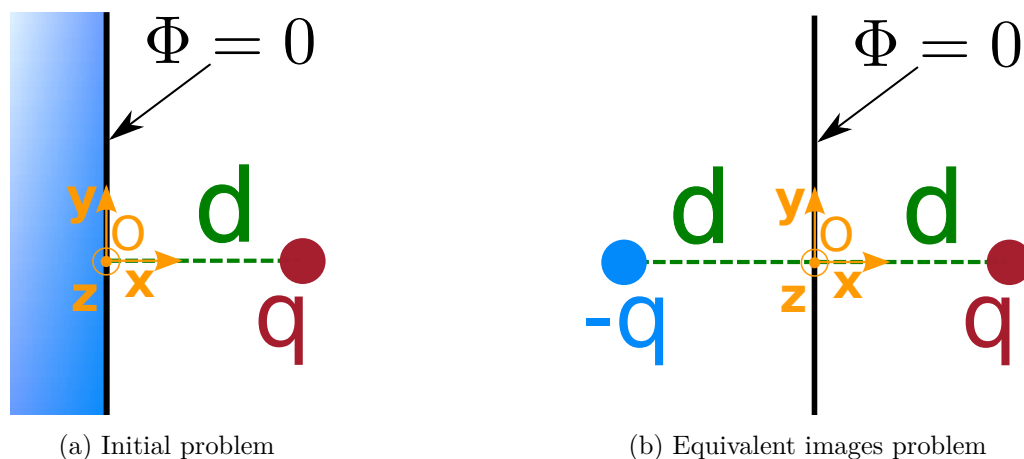


Figure 1.4: (a) “Real” problem of a charge q at distance d (along (Ox) axis) of a semi-infinite metallic surface (in blue) with a uniform electrostatic potential $\Phi = 0$. Metal-vacuum interface is located in the (Oyz) plane. (b) Equivalent images problem, with the interface represented by the black line. A charge $-q$ is located at $-d\mathbf{u}_x$, with \mathbf{u}_x a unitary vector along (Ox) .

To compute the polarization energy, we assume the adiabatic addition of an infinitesimal charge $q d\lambda$ to the already present charge λq , in the configuration of the FIGURE 1.4b (λ going from 0 to 1). The interaction energy of the infinitesimal charge with the image charge $-\lambda q$ is equal to

$$dV^{\text{pot}} = d\lambda q \times \frac{-\lambda q}{8\pi\epsilon_0 d}, \quad (1.8)$$

leading to P such that

$$P = \int dV^{\text{pot}} = - \int_0^1 \frac{q^2}{8\pi\epsilon_0 d} \lambda d\lambda \quad (1.9)$$

$$\boxed{P = -\frac{q^2}{16\pi\epsilon_0 d}}. \quad (1.10)$$

P is negative, independently of the sign of q . Qualitatively, everything happens as if a charge reorganization, with an opposite sign compared to the new real charge q , occurred in the metallic surface. The former stabilizes the latter. Typically, for an organic molecule in front of a metallic electrode, $d \simeq 3.3 \text{ \AA}$, leading to $P \simeq -1.1 \text{ eV}$.

For a molecule in a photoemission experiment, such a model leads to a stabilization of an added electron to the system by an energy P . For an added hole, this leads to add $-P$ to the corresponding energy, as shown below. To understand the effects of the electrode on the gap of the molecule, it should be noticed that adding a hole to the system means to remove an electron. Using the same reasoning and notations as in part 1.1.1, the hole addition energy is thus $-\varepsilon_i = E_i^{N-1} - E_0^N$. Therefore, the presence of the interface means adding P to this energy $-\varepsilon_i$, or equivalently adding $-P$ to ε_i , that is stabilizing the hole by $-P$. It leads to a closing of the gap of $2|P|$ between the gas phase and the presence of a metallic electrode.

The order of magnitude found here with a very simple model is in agreement with more accurate results of the closing of the gap of benzene on top of a graphite surface [17]. Typical

gaps of organic molecules being between 4 eV and 10 eV [18, 19], a polarization energy of this order of magnitude corresponds to significant effects.

1.1.3.2 Charge in a dielectric cavity

Another simple model consists in computing the polarization energy P of a charge q at the center of an empty sphere of radius R . This latter is embedded in a linear homogeneous isotropic dielectric medium of permittivity $\epsilon = \epsilon_0 \epsilon_r$, as depicted in FIGURE 1.5. Such a simple model is closely related to the approaches of PCM [20] used to describe a molecule in a solvent, where this latter is described as a continuous medium. For the sake of simplicity, we consider only the static case.

By spherical symmetry, the created electrostatic field \mathbf{E} is purely radial. The Gauss theorem leads to the following formula for the radial part E_r of the field:

$$\begin{cases} E_r(r) = \frac{1}{4\pi\epsilon_0} \frac{q}{r^2} & \text{for } r < R, \\ E_r(r) = \frac{1}{4\pi\epsilon} \frac{q}{r^2} & \text{for } r > R. \end{cases} \quad (1.11)$$

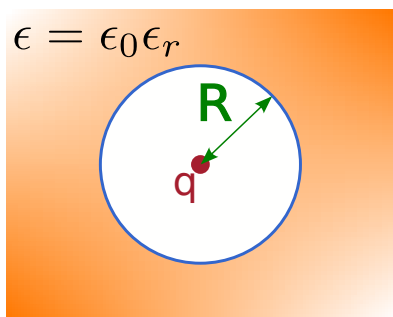


Figure 1.5: Charge q at the center of an empty sphere of radius R . The cavity is inside a linear homogeneous isotropic dielectric medium of permittivity $\epsilon = \epsilon_0 \epsilon_r$.

A surface density of bound charges σ_b appears at the interface vacuum-dielectric medium (in blue in FIGURE 1.5). Using the interface conditions for the radial part of the field leads to

$$\sigma_b = \epsilon_0 E_r(R^+) - \epsilon_0 E_r(R^-) \quad (1.12)$$

$$\sigma_b = \frac{q}{4\pi R^2} \left(\frac{1}{\epsilon_r} - 1 \right). \quad (1.13)$$

Computing the electrostatic potential inside the cavity is formally equivalent to compute the one created by a point charge q at the center, and by the surface charge σ_b on the surface of the cavity. Thus, the total surface charge $4\pi R^2 \sigma_b = q \left(\frac{1}{\epsilon_r} - 1 \right)$ leads to a reaction field on the point charge

$$\Phi^{\text{reac}} = \frac{1}{4\pi\epsilon_0 R} q \left(\frac{1}{\epsilon_r} - 1 \right). \quad (1.14)$$

This corresponds to the potential generated by the induced dipoles inside the dielectric medium, in response to the field generated by q . Similar calculations as the ones of the end of part 1.1.3.1 lead to a polarization energy P equal to

$$P = -\frac{q^2}{8\pi\epsilon_0 R} \left(1 - \frac{1}{\epsilon_r} \right). \quad (1.15)$$

For typical organic systems, $R \simeq 4.5 \text{ \AA}$ [21], $\epsilon_r \simeq 3$ [22, 23] and $P \simeq -1.1 \text{ eV}$. This leads to a closing of the gap of $2|P| \simeq 2.2 \text{ eV}$, namely a significant effect with respect to the absolute values of fundamental gaps.

In the subsequent sections, the objective is to describe the different formalisms used during this thesis to quantitatively compute the effects presented above.

1.2 The many-body problem

Atoms, molecules, and solids are all made of charged atomic nuclei and their corresponding electrons. To describe a quantum system, section 1.1 points out the necessity to compute the excited and ground state total energies E , which are solutions of the non-relativistic and stationary Schrödinger equation

$$H_{\text{tot}}\Psi(\{\mathbf{r}_i\}, \{\mathbf{R}_I\}) = E\Psi(\{\mathbf{r}_i\}, \{\mathbf{R}_I\}). \quad (1.16)$$

$\Psi(\{\mathbf{r}_i\}, \{\mathbf{R}_I\})$ corresponds to the many-body wavefunction of the system depending on $\{\mathbf{R}_I\}$, the set of spatial coordinates of the K ion cores of charge $\{Z_I\}$ and mass $\{M_I\}$, and of $\{\mathbf{r}_i\}$, the set of spatial coordinates of the N electrons. For the sake of simplicity, we do not consider spin variables unless explicitly mentioned. From now on, and throughout the whole manuscript, Hartree atomic units are used, *i.e.* the absolute value of the charge of an electron e , the rest mass of an electron m_e , the reduced Planck constant \hbar and the Coulomb constant $\frac{1}{4\pi\epsilon_0}$ are set to unity. In this context, the Hamiltonian \hat{H}_{tot} in position representation is given by

$$\begin{aligned} H_{\text{tot}} = & -\frac{1}{2} \sum_{i=1}^N \nabla_i^2 - \frac{1}{2} \sum_{I=1}^K \frac{\nabla_I^2}{M_I} + \sum_{i=1}^N \sum_{i<j}^N \frac{1}{|\mathbf{r}_i - \mathbf{r}_j|} \\ & + \sum_{I=1}^K \sum_{I<J}^K \frac{Z_I Z_J}{|\mathbf{R}_I - \mathbf{R}_J|} - \sum_{i=1}^N \sum_{I=1}^K \frac{Z_I}{|\mathbf{r}_i - \mathbf{R}_I|.} \end{aligned} \quad (1.17)$$

The first two terms correspond to the kinetic energy, while the other ones represent respectively the electron-electron, the nuclei-nuclei and the electron-nuclei Coulomb interactions. Thus, Eq.(1.16) is a problem of diagonalization, resulting in eigenwavefunctions in general impossible to split into an electronic and a nuclear factorized parts.

1.2.1 The Born-Oppenheimer approximation

The masses of the nuclei being significantly larger than the mass of the electron ($M_I \gg 1$), it seems wise to decouple the fast dynamics of the electrons and the slow ones of the nuclei. Using an expansion of the Hamiltonian in terms of $(m_e/M)^{1/4}$, with M the average of the nuclei mass, Born and Oppenheimer showed the possibility to decouple the Schrödinger equation in an electronic part and in an ionic part [24]. In this so-called Born-Oppenheimer approximation, the nuclei can be considered as fixed for the dynamics of the electrons, and their positions appear as classical parameters for the (approximated) electronic Hamiltonian

$$H_e = -\frac{1}{2} \sum_{i=1}^N \nabla_i^2 + \sum_{i=1}^N \sum_{i<j}^N \frac{1}{|\mathbf{r}_i - \mathbf{r}_j|} - \sum_{i=1}^N \sum_{I=1}^K \frac{Z_I}{|\mathbf{r}_i - \mathbf{R}_I|.} \quad (1.18)$$

Even though this approximation simplifies the Schrödinger equation, this latter still represents a problem of N interacting electrons (via the Coulomb term) impossible to solve exactly. Real macroscopic systems with a number of electrons of the order of magnitude of the Avogadro number $\sim 10^{23}$ seem totally out of reach with such a direct resolution of the Schrödinger equation. Therefore, additional approximations are required to decrease the complexity of the problem to tackle.

1.3 *Ab initio* approaches

As seen before, the exact resolution of the Schrödinger equation (1.18) is nearly impossible in practice. Yet, quantities of interest can be computed via *ab initio* methods. These approaches, based on the first principles of quantum mechanics, are thus not characterized by the absence of any approximations, but rather by the absence of any adjustable physical parameters [25]. They can be used to characterize the electronic properties of a system before experimental data. Two main classes of methods should be distinguished: the mean-field approaches, like the Hartree-Fock approach and Density-Functional Theory, and the many-body methods, in perturbation theory or not. Such a N -body perturbation theory, namely the GW formalism, is at the heart of this thesis.

From now on, it should be noticed that the room temperature is associated to a thermal energy of ~ 26 meV which is much smaller than typical energy gaps or band dispersions of the considered systems. In the following sections, we will thus describe ground and excited states in their 0 K limit.

1.3.1 Density-Functional Theory (DFT)

DFT is an exact mean-field formalism to compute ground-state total energies and charge densities. Instead of the total knowledge of the N -body wavefunction, DFT only requires the electronic density $n(\mathbf{r})$, a much simpler three-dimensional function, to compute the total energy of the system and other associated quantities. However, the exact functional giving the energy with respect to $n(\mathbf{r})$ is not known, and in practice approximations are used, as explained below.

1.3.1.1 The Hohenberg and Kohn theorems

Given the (normalized) N -body wavefunction Ψ of an electronic system, its electronic density $n(\mathbf{r}_1)$ is defined by the following integral over $(N - 1)$ spatial coordinates:

$$n(\mathbf{r}_1) = N \int \prod_{i=2}^N d\mathbf{r}_i |\Psi(\{\mathbf{r}_i\})|^2, \quad (1.19)$$

leading to the sum rule $\int d\mathbf{r}_1 n(\mathbf{r}_1) = N$. In 1964, Hohenberg and Kohn showed in their seminal paper [26] that the ground state energy of a many-body system can be written as a functional of the density n . The resulting DFT is based on two main theorems, which can be formulated as follows [27]:

Theorem 1: For any system of interacting particles submitted to an external potential $V_{\text{ext}}(\mathbf{r})$, this potential is determined uniquely, modulo an additive constant, by the exact ground state particle density $n_0(\mathbf{r})$.

Proof (*Reductio ad absurdum*): Let us assume there are two external potentials, $V_{\text{ext}}^{(1)}$ and $V_{\text{ext}}^{(2)}$, differing by more than an additive constant, but resulting in the same ground state density $n_0(\mathbf{r})$. They are associated with two different Hamiltonians, $\hat{H}^{(1)}$ and $\hat{H}^{(2)}$,

having two different ground state eigenwavefunctions, $\Psi^{(1)}$ and $\Psi^{(2)}$, of energy $E_0^{(1)}$ and $E_0^{(2)}$. Assuming that both $\hat{H}^{(1)}$ and $\hat{H}^{(2)}$ have a non-degenerate ground state³, and using the Dirac notations, the definition of the ground state leads to

$$E_0^{(1)} = \langle \Psi^{(1)} | \hat{H}^{(1)} | \Psi^{(1)} \rangle < \langle \Psi^{(2)} | \hat{H}^{(1)} | \Psi^{(2)} \rangle = \langle \Psi^{(2)} | \hat{H}^{(2)} | \Psi^{(2)} \rangle + \int d\mathbf{r} n_0(\mathbf{r}) \left(V_{\text{ext}}^{(1)}(\mathbf{r}) - V_{\text{ext}}^{(2)}(\mathbf{r}) \right) \quad (1.20a)$$

$$E_0^{(2)} = \langle \Psi^{(2)} | \hat{H}^{(2)} | \Psi^{(2)} \rangle < \langle \Psi^{(1)} | \hat{H}^{(2)} | \Psi^{(1)} \rangle = \langle \Psi^{(1)} | \hat{H}^{(1)} | \Psi^{(1)} \rangle + \int d\mathbf{r} n_0(\mathbf{r}) \left(V_{\text{ext}}^{(2)}(\mathbf{r}) - V_{\text{ext}}^{(1)}(\mathbf{r}) \right). \quad (1.20b)$$

Adding the two inequalities (1.20a)-(1.20b) leads to $E_0^{(1)} + E_0^{(2)} < E_0^{(1)} + E_0^{(2)}$, which is impossible and therefore proving the theorem.

Theorem 2: An universal functional for the energy $E[n]$, in terms of the density $n(\mathbf{r})$, can be defined, valid for any external potential $V_{\text{ext}}(\mathbf{r})$. For any particular $V_{\text{ext}}(\mathbf{r})$ and number of electrons N , the exact ground state energy of the system is reached at the global minimum value of this functional. This functional reaches its minimum for $n(\mathbf{r}) = n_0(\mathbf{r})$, namely for the exact ground state density.

Proof: Following Hohenberg and Kohn, we restrict ourselves to densities $n(\mathbf{r})$ being acceptable (N -integrable, etc.) ground states densities of the Hamiltonian with some external potential $V_{\text{ext}}(\mathbf{r})$. This latter contains typically the electron-nuclei Coulomb interaction. On such a space, following the theorem 1, the external potential is fully determined by the density. Consequently, this latter determines the Hamiltonian, because the kinetic and the electron-electron part are universal operators, and therefore also its ground state wavefunction Ψ . Still assuming a non-degenerate ground state, this latter is a unique functional of the density $\Psi[n]$ [25]. Thus, it is possible to define on this space a universal functional for the energy $E[n]$ such that

$$E[n] = \langle \Psi[n] | \hat{H} | \Psi[n] \rangle = F_{\text{HK}}[n] + \int d\mathbf{r} V_{\text{ext}}(\mathbf{r})n(\mathbf{r}). \quad (1.21)$$

$F_{\text{HK}}[n] = T[n] + E_{\text{int}}[n]$ is the universal⁴ Hohenberg and Kohn functional, which contains the kinetic energy

$$T[n] = \langle \Psi[n] | \sum_{i=1}^N \frac{\hat{\mathbf{p}}_i^2}{2} | \Psi[n] \rangle, \quad (1.22)$$

and the electron-electron interaction energy

$$E_{\text{int}}[n] = \langle \Psi[n] | \sum_{i=1}^N \sum_{i < j}^N \frac{1}{|\hat{\mathbf{r}}_i - \hat{\mathbf{r}}_j|} | \Psi[n] \rangle. \quad (1.23)$$

Now, let us consider a system made of N electrons, described by the ground state density $n_0(\mathbf{r})$ associated to the external potential $V_{\text{ext}}^{(0)}(\mathbf{r})$. Its ground state energy E_0 is given by

$$E_0 = E[n_0] = \langle \Psi[n_0] | \hat{H}^{(0)} | \Psi[n_0] \rangle = F_{\text{HK}}[n_0] + \int d\mathbf{r} V_{\text{ext}}^{(0)}(\mathbf{r})n_0(\mathbf{r}). \quad (1.24)$$

³Results can be generalized to degenerate ground states [28, 29].

⁴Namely the same for all electron systems.

Let $n_1(\mathbf{r})$ be the density associated to the wavefunction $\Psi^{(1)}$, and let E_1 be its corresponding energy such that

$$E_1 = \langle \Psi^{(1)} | \hat{H}^{(0)} | \Psi^{(1)} \rangle = F_{\text{HK}}[n_1] + \int d\mathbf{r} V_{\text{ext}}^{(0)}(\mathbf{r})n_1(\mathbf{r}). \quad (1.25)$$

The ground state being non-degenerate, we have $E_0 < E_1$, proving the end of the theorem.

1.3.1.2 The Kohn-Sham formulation

So far, the Hohenberg and Kohn theorems have recast the determination of the total energy of an interacting system to a minimization problem of the energy functional $E[n]$ with respect to the density n , under the constraint $\int d\mathbf{r} n(\mathbf{r}) = N$. However, the universal functional $F_{\text{HK}}[n]$, defined in Eq.(1.21), is still unknown. This led Kohn and Sham to introduce, in 1965, their famous approach [30]. Namely, they mapped the true interacting system into an effective non-interacting one submitted to an effective local potential $V_{\text{eff}}(\mathbf{r})$. This auxiliary system, called Kohn-Sham (KS) system, presents the same ground state density n_{0s} and ground state energy as the interacting one. It can be described in terms of N single-particle KS orbitals ϕ_i such that

$$n_{0s}(\mathbf{r}) = \sum_{i=1}^N |\phi_i(\mathbf{r})|^2 \quad (1.26a)$$

$$= n_0(\mathbf{r}) \quad (\text{the true interacting ground state density}). \quad (1.26b)$$

The kinetic energy T_s of this KS system is given by

$$T_s[n_{0s}] = -\frac{1}{2} \sum_{i=1}^N \int d\mathbf{r} \phi_i^*(\mathbf{r}) \nabla^2 \phi_i(\mathbf{r}). \quad (1.27)$$

Even if this formula shows an explicit dependency on the orbitals, T_s is a density functional thanks to the Hohenberg and Kohn theorems for non-interacting particles [25]. In this context, the functional $E[n]$ for the energy of the interacting system can be rewritten

$$E[n] = T_s[n] + E_{\text{H}}[n] + E_{\text{ext}}[n] + E_{\text{XC}}[n], \quad (1.28)$$

with $E_{\text{H}}[n]$ the Hartree term, namely the classical interaction between the N electrons:

$$E_{\text{H}}[n] = \frac{1}{2} \int d\mathbf{r} d\mathbf{r}' \frac{n(\mathbf{r})n(\mathbf{r}')}{|\mathbf{r} - \mathbf{r}'|}, \quad (1.29)$$

and E_{ext} the coupling energy with the external potential, typically containing the electron-nuclei Coulomb interaction:

$$E_{\text{ext}}[n] = \int d\mathbf{r} V_{\text{ext}}(\mathbf{r})n(\mathbf{r}). \quad (1.30)$$

$E_{\text{XC}}[n]$ is the universal exchange-correlation energy functional, defined by (1.28), or equivalently by

$$E_{\text{XC}}[n] = F_{\text{HK}}[n] - T_s[n] - E_{\text{H}}[n] \quad (1.31a)$$

$$= (T[n] - T_s[n]) + (E_{\text{int}}[n] - E_{\text{H}}[n]). \quad (1.31b)$$

This functional represents the difference between the kinetic energy plus the electron-electron interaction energy of the real interacting system, and those of the effective non-interacting system, with the Coulomb energy reduced to the Hartree term. Yet, its exact formula is still unknown, and approximations are required. Since it is a difference, it is likely however to be a much smaller unknown than the original $F_{\text{HK}}[n]$ quantity.

Then the minimization of $E[n]$ of Eq.(1.28) can be performed with respect to the density n . Equivalently, assuming a one-to-one correspondence between the non-interacting ground state density and its corresponding single-particle wavefunctions [25], this minimization can be performed with respect to these latter. The constraints of orthonormality of such a basis set can be enforced through Lagrange multipliers Λ_{ij} . This results in the minimization of the following Lagrangian

$$\mathcal{L}[n(\{\phi_i(\mathbf{r})\})](\Lambda) = E[n(\{\phi_i(\mathbf{r})\})] + \sum_{i \leq j} \Lambda_{ij} (\delta_{i,j} - \langle \phi_i | \phi_j \rangle), \quad (1.32)$$

with $\delta_{i,j}$ the Kronecker delta. This leads to

$$\frac{\delta \mathcal{L}}{\delta \phi_i^*(\mathbf{r})} = \frac{\delta T_s}{\delta \phi_i^*(\mathbf{r})} + \left(\frac{\delta E_{\text{ext}}[n]}{\delta n(\mathbf{r})} + \frac{\delta E_{\text{H}}[n]}{\delta n(\mathbf{r})} + \frac{\delta E_{\text{XC}}[n]}{\delta n(\mathbf{r})} \right) \frac{\partial n}{\partial \phi_i^*(\mathbf{r})} - \sum_{i \leq j} \Lambda_{ij} \phi_j(\mathbf{r}) = 0 \quad (1.33)$$

An unitary rotation of the **KS** orbitals basis set, diagonalizing the Lagrange multipliers matrix Λ of eigenvalues $\{\varepsilon_i\}$, leads to the **KS** equations

$$\left[-\frac{\nabla^2}{2} + V_{\text{eff}}[n_{0s}](\mathbf{r}) \right] \phi_i(\mathbf{r}) = \varepsilon_i \phi_i(\mathbf{r}). \quad (1.34)$$

$V_{\text{eff}}[n](\mathbf{r})$ is a density functional effective potential, such that

$$V_{\text{eff}}[n](\mathbf{r}) = V_{\text{ext}}(\mathbf{r}) + V_{\text{H}}[n](\mathbf{r}) + V_{\text{XC}}[n](\mathbf{r}), \quad (1.35)$$

with $V_{\text{H}}[n](\mathbf{r})$ the Hartree potential

$$V_{\text{H}}[n](\mathbf{r}) = \int d\mathbf{r}' \frac{n(\mathbf{r}')}{|\mathbf{r} - \mathbf{r}'|}, \quad (1.36)$$

and $V_{\text{XC}}[n](\mathbf{r})$ the exchange-correlation potential

$$V_{\text{XC}}[n](\mathbf{r}) = \frac{\delta E_{\text{XC}}[n]}{\delta n(\mathbf{r})}. \quad (1.37)$$

KS-DFT gives access to the total energy of the ground state, and its corresponding density, through coupled non-linear equations of type (1.34). $V_{\text{eff}}[n](\mathbf{r})$ depends on the density, which depends on the solution wavefunctions $\phi_i(\mathbf{r})$ via Eq.(1.26a). Such **KS** equations require a Self-Consistent Field (**SCF**) procedure to be solved. In practice, $V_{\text{eff}}[n](\mathbf{r})$ is first computed via a trial density $n^{(0)}$, providing a first set of eigenvalues and eigenfunctions $\{\varepsilon_i^{(1)}, \phi_i^{(1)}(\mathbf{r})\}$. An improved density $n^{(1)}$ is computed on top of these wavefunctions, and an iterative procedure is set up until convergence of the density. Now, the problem is to find a suitable formula for $E_{\text{XC}}[n]$.

1.3.1.3 Exchange-correlation functionals

An exact formula for the exchange-correlation energy functional is still unknown. Thus, one of the main problems in **KS-DFT** is to find an accurate approximation for it. In practice, even if **KS-DFT** is an exact formalism, $E_{\text{XC}}[n]$ being computed through approximations, real calculations are no longer based on exact formulas. Some of the most widely used approximations are the following ones:

Local Density Approximation (LDA): The first successful approximation was proposed by Hohenberg and Kohn in 1964 [26], namely the Local Density Approximation (**LDA**):

$$E_{\text{XC}}^{\text{LDA}}[n] \simeq \int d\mathbf{r} n(\mathbf{r}) \varepsilon_{\text{XC}}^{\text{LDA}}(n(\mathbf{r})). \quad (1.38)$$

For an electron at \mathbf{r} , its exchange-correlation energy per electron $\varepsilon_{\text{XC}}^{\text{LDA}}(n(\mathbf{r}))$ is supposed to depend only on the density $n(\mathbf{r})$ at this position. $\varepsilon_{\text{XC}}^{\text{LDA}}(n(\mathbf{r}))$ is no longer a functional of n , but a “simple” function of $n(\mathbf{r})$. Ceperley and Alder put this idea in practice in 1980 [31] by performing Quantum Monte Carlo (**QMC**) total energy calculations on interacting Homogeneous Electron Gas (**HEG**), at different constant densities n^{HEG} . Using previous work of Dirac on the exchange energy [32], it is then possible to extract from these computed total energies the correlation-only energy per electron $\varepsilon_{\text{C}}^{\text{HEG}}(n)$. Such **QMC** data have been fitted by different functional forms [33–35], leading to **LDA** functionals.

Even though strictly valid only for a homogeneous electron gas, such functionals have led to quite accurate calculations of lattice parameters of solids [36] (with a tendency to overbind, namely to predict too small lattice parameters). They have also shown their ability to well compute ground-state densities [37], even in inhomogeneous systems.

Generalized Gradient Approximation (GGA): A possibility to improve results of **LDA** is to include information on the possible inhomogeneities of the density, via its gradient, in the exchange-correlation energy. This defines the semi-local Generalized Gradient Approximation (**GGA**), such that

$$E_{\text{XC}}^{\text{GGA}}[n] = \int d\mathbf{r} n(\mathbf{r}) \varepsilon_{\text{XC}}^{\text{GGA}}(n(\mathbf{r}), \nabla n(\mathbf{r})). \quad (1.39)$$

Typical **GGA** functionals are the BLYP (Becke-Lee-Yang-Parr) [38, 39], the PW91 (Perdew-Wang 1991) [40, 41], or the PBE (Perdew-Becke-Ernzherof) [42] functionals. For example, the PBE functional improves the accuracy of the predicted lattice parameters of metals, as compared to **LDA** (with a tendency to underbind, namely with too large lattice parameters) [36], but does not give better results for non metallic-systems.

Hybrid functionals: In general, **LDA** and **GGA** functionals cannot really reproduce the long-range behavior of the potential felt by an electron [43]. They also suffer from the problem of self-interaction. $V_{\text{XC}}[n]$ both acts on occupied orbitals, and is built on them, through the density. This is equivalent to have an electron in interaction with itself, which can be dramatic for localized orbitals. To solve these problems, hybrid-functionals have been designed. They are usually based on a mixture of **LDA** or **GGA** functional and of exact

exchange energy E_X^{HF} defined in the Hartree-Fock (HF) theory, computed in the current context with the KS wavefunctions via

$$E_X^{\text{HF}} = -\frac{1}{2} \sum_{ij}^{\text{occ}} \iint \mathrm{d}\mathbf{r} \mathrm{d}\mathbf{r}' \frac{\phi_i^*(\mathbf{r})\phi_j(\mathbf{r})\phi_j^*(\mathbf{r}')\phi_i(\mathbf{r}')}{|\mathbf{r} - \mathbf{r}'|} \delta_{\sigma_i, \sigma_j}. \quad (1.40)$$

Here the spin variable σ_i have been reintroduced for clarity, and the sums run over occupied states. Using such functionals and denoting N the number of electrons of the system, a calculation goes from a $\mathcal{O}(N^3)$ scaling with pure density functionals to a $\mathcal{O}(N^4)$ scaling [25]. Typical hybrid functionals are the B3LYP (Becke 3 parameters) [44] or the PBEh (PBE-hybrid) functional. This latter, massively used in this thesis, is built on the PBE functional via

$$E_{\text{XC}}^{\text{PBEh}}[n](\alpha) = E_{\text{XC}}^{\text{PBE}}[n] + \alpha \left(E_X^{\text{HF}}[n(\{\phi_i\})] - E_X^{\text{PBE}}[n] \right), \quad (1.41)$$

with $E_X^{\text{PBE}}[n]$ the exchange part of the PBE functional, and $\alpha \in [0; 1]$. The specific value of $\alpha = 0.25$ corresponds to the PBE0 functional [45, 46].

Finally, the search for exchange-correlation functionals leading to universal (or at least working for a large number of materials) and accurate description of observables based on total energy (lattice parameters, binding energy, electronic density...), is still one of the main challenge in DFT. Two main strategies are setting up. The first one consists in building functionals enforcing exact constraints, like the exchange-correlation hole sum rule, asymptotic behavior [43]... The second one is based on fits of functionals on experimental data, with the help recently of machine learning. A discussion on the development of exchange-correlation functionals over the last decades can be found in Ref.[47].

1.3.1.4 Discussion on the meaning of the Kohn-Sham single-particle energies

As seen in part 1.3.1.2, KS-DFT also provides us with single-particle eigenvalues. Even if it seems attractive to consider such energies as electronic energy levels, no obvious link between both quantities can be established. As seen in part 1.1.1, page 24, the electronic energy levels of an interacting system are defined as total-energy differences between a charged and the neutral system. At the opposite, the KS-DFT eigenvalues $\{\varepsilon_i\}$ are only introduced as Lagrange multipliers, to enforce orthonormality of the wavefunctions $\{\phi_i(\mathbf{r})\}$. To emphasize the differences between the two types of energies, one should consider the sum of KS-DFT eigenvalues

$$\sum_{i=1}^N \varepsilon_i = \sum_{i=1}^N \int \mathrm{d}\mathbf{r} \phi_i^*(\mathbf{r}) \left(-\frac{\nabla^2}{2} + V_{\text{eff}}[n](\mathbf{r}) \right) \phi_i(\mathbf{r}) \quad (1.42)$$

$$= T_s[n] + \int \mathrm{d}\mathbf{r} (V_{\text{ext}}(\mathbf{r}) + V_{\text{H}}[n](\mathbf{r}) + V_{\text{XC}}[n](\mathbf{r}))n(\mathbf{r}). \quad (1.43)$$

This can be compared to the true ground-state energy $E[n]$ of the N -electron system, such that

$$E[n] = T_s[n] + E_{\text{H}}[n] + E_{\text{ext}}[n] + E_{\text{XC}}[n], \quad (1.44)$$

which can be rewritten

$$E[n] = \sum_{i=1}^N \varepsilon_i - E_{\text{H}}[n] + E_{\text{XC}}[n] - \int d\mathbf{r} V_{\text{XC}}[n](\mathbf{r})n(\mathbf{r}). \quad (1.45)$$

This equation highlights the difficulties to assimilate the **KS-DFT** eigenvalues to total-energy differences. In particular, the **KS-DFT** gap $E_{\text{gap}}^{\text{KS}} = \varepsilon_{N+1} - \varepsilon_N$ struggles into reproducing fundamental gaps in agreement with experimental values [48], because this latter is defined as $E_{\text{gap}} = (E_0^{N+1} - E_0^N) - (E_0^N - E_0^{N-1})$, with E_0^M the ground state total energy of the M -electron system.

However, it is possible to give a meaning to **KS-DFT** eigenvalues, via the Janak's theorem [49]. In his paper in 1978, Janak introduced a generalization of **KS-DFT** with fractional occupation numbers $\{f_i\}$. Each eigenstate of Eq.(1.34), described by $\{\varepsilon_i, \phi_i(\mathbf{r})\}$, is associated to an occupation factor such that $f_i \in [0; 1]$. Such an approach allows the total number of electron N to be real, and not only integer. The total energy turns to be now a functional of the one-body wavefunctions, but also a function of the occupations numbers $E[n(\{\phi_i(\mathbf{r})\})](\{f_i\})$. The ground state energy is computed via its minimization with respect to the two types of arguments. In this approach, the Janak formula leads to ε_i equal to

$$\varepsilon_i = \frac{\partial E}{\partial f_i}. \quad (1.46)$$

The **KS-DFT** eigenvalues, computed up to now, correspond to the specific configuration $f_i \in \{0; 1\}$ for empty or occupied levels. Equation (1.46) shows that they are associated to variation of the total energy with respect to an infinitesimal change of the charge of the system. On the other side, electronic energy levels, measured in (inverse) photoemission experiments, correspond to changes of the total energy when an entire electron is added or removed to the system.

It has also been shown that the exact ground state total energy of N electrons E_0^N , with the exact exchange-correlation functional and $N \in \mathbb{R}_+$ (so not only integer), is a piecewise linear function with respect to N [50]. More explicitly, for $N = N_0 + \omega$, with $N_0 \in \mathbb{N}$ and $\omega \in [0; 1]$, E_0^N is given by

$$E_0^N = (1 - \omega)E_0^{N_0} + \omega E_0^{N_0+1}. \quad (1.47)$$

In particular, such a formula can be used to compute the highest occupied **KS** eigenvalues ε_N of a system made of N electrons, with N an integer number, leading to [51]

$$\varepsilon_N = E_0^N - E_0^{N-1}. \quad (1.48)$$

This equation shows that the highest occupied **KS** eigenvalue is exactly the inverse of the Ionization Potential (**IP**). The same result can be obtained alternatively by looking at the exponential decay of the charge density in the case of finite size systems [52]. This is known as the **IP**-theorem [53], which gives a physical meaning (only) to the highest occupied **KS** eigenvalue. However, there is no such well-defined meaning for the other eigenvalues, and this relation only holds in “exact” **DFT**, namely assuming that one knows the exact exchange-correlation potential.

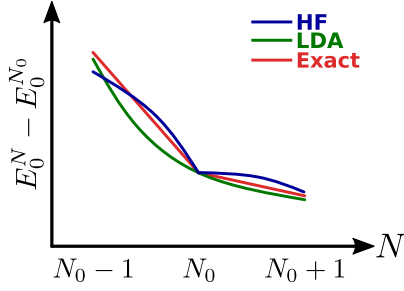


Figure 1.6: Typical shape of the variation of the ground state total energy E_0^N , with respect to the number of electron N , around its value for $N = N_0$. With exact exchange-correlation functional, this function is piecewise linear, while it becomes convex with the LDA and concave in the HF approximation. Inspired from [54, 55].

In practice, the exchange-correlation functional is approximated, leading to a total energy E_0^N which is no longer piecewise linear with respect to N . As represented in FIGURE 1.6, it has been shown that the HF approximation leads to a concave energy curve, while a (semi)-local approximation such that the LDA leads to a mostly convex curve [54, 56]. Such opposite curvatures can be seen as yet another reason for the development of hybrid functionals, where the mixing of the different approximations may restore the piecewise linearity of the energy curve E_0^N with respect to N . Such a rational offers a theoretical ground to develop tuned functionals, as an alternative to functionals fitted onto experimental data.

Even if the KS-DFT eigenstates are not formally designed to reproduce excited properties of a system, as the ones measured in (inverse) photoemission spectroscopy, they can be used as valuable and affordable starting point of many-body perturbation theories such as the GW formalism. This latter, the central theory of this thesis, is detailed in section 1.3.2. Before describing this formalism, we finish this part, about (general) DFT, with some details about real implementations of KS-DFT, as the one used during this thesis.

1.3.1.5 DFT in practice

In practice, the diverse equations of KS-DFT need to be expressed in finite size basis sets, to be solved numerically on computers via algebraic equations. This leads to operators represented as finite size matrices or wavefunctions as vectors. For example, a given wavefunction $\phi_i(\mathbf{r})$ is represented in the basis set of functions $\{\alpha_\mu(\mathbf{r})\}$, of dimension M , by

$$\phi_i(\mathbf{r}) = \sum_{\mu=1}^M c_{i,\mu} \alpha_\mu(\mathbf{r}). \quad (1.49)$$

In this context, the Eq.(1.34) becomes

$$\left[-\frac{\nabla^2}{2} + V_{\text{eff}}[n_{0s}](\mathbf{r}) \right] \sum_{\mu=1}^M c_{i,\mu} \alpha_\mu(\mathbf{r}) = \varepsilon_i \sum_{\mu=1}^M c_{i,\mu} \alpha_\mu(\mathbf{r}). \quad (1.50)$$

Multiplying on the left by a given function $\alpha_\nu^*(\mathbf{r})$, and integrating over $\mathbf{r} \in \mathbb{R}^3$, this equation leads to the following generalized eigenvalue problem

$$\mathbf{Hc}_i = \varepsilon_i \mathbf{Sc}_i, \quad (1.51)$$

with \mathbf{H} and \mathbf{S} two $M \times M$ matrices such that

$$[\mathbf{H}]_{\nu\mu} = \int d\mathbf{r} \alpha_{\nu}^*(\mathbf{r}) \left[-\frac{\nabla^2}{2} + V_{\text{eff}}[n_{0s}](\mathbf{r}) \right] \alpha_{\mu}(\mathbf{r}) \quad (1.52)$$

$$[\mathbf{S}]_{\nu\mu} = \int d\mathbf{r} \alpha_{\nu}^*(\mathbf{r}) \alpha_{\mu}(\mathbf{r}). \quad (1.53)$$

\mathbf{c}_i is the column vector of coefficients, of dimension M , such that $[\mathbf{c}_i]_{\mu} = c_{i,\mu}$. One of the objective of real calculations of **KS-DFT** is to compute these sets of coefficients $\{c_{i,\mu}\}$. It should be noticed that the introduction of a finite dimension basis set leads to approximations of the exact solutions, which could be computed in the Complete Basis Set (**CBS**) limit. Therefore, one should use a basis set close enough of the **CBS** to reach a good accuracy for the final results, but also small enough in terms of dimension to do calculations in a reasonable time.

The choice of the basis sets depends on the type of studied systems. For example, a plane-wave basis is often well-adapted to describe an infinite periodic crystal. Concerning this thesis, we restrict ourselves only to finite size system, where atom-centered basis functions leads to a good compromise between accuracy and dimension of the basis set. Each atom I is associated to a basis set \mathcal{B}_I of functions centered on its nucleus, and the total basis set \mathcal{B} is the direct sum of all these bases, namely $\mathcal{B} = \bigoplus_I \mathcal{B}_I$. More particularly, we use Gaussian Type Orbital (**GTO**) basis functions, with the Gaussian-basis **DFT** code ORCA [57, 58]. A primitive **GTO**, centered on nuclei at \mathbf{R}_I , is defined by

$$\alpha_{l,m,\zeta,I}(\mathbf{r}) = R_{l,\zeta}(|\mathbf{r} - \mathbf{R}_I|) Y_{l,m} \left(\frac{\mathbf{r} - \mathbf{R}_I}{|\mathbf{r} - \mathbf{R}_I|} \right), \quad (1.54)$$

with

$$R_{l,\zeta}(|\mathbf{r} - \mathbf{R}_I|) = \aleph_{l,\zeta} |\mathbf{r} - \mathbf{R}_I|^l \exp(-\zeta |\mathbf{r} - \mathbf{R}_I|^2). \quad (1.55)$$

$Y_{l,m}$ is a spherical harmonic of degree, or angular momentum, l and order, or magnetic quantum number, m . $\aleph_{l,\zeta}$ is a normalization factor and ζ is a real positive number which controls the extent of the radial part. An important property of these **GTOs** is given by the Gaussian product theorem. Namely, the product of two Gaussian functions $G_1(\mathbf{r}) = \exp(-\zeta_1 |\mathbf{r} - \mathbf{R}_1|^2)$ and $G_2(\mathbf{r}) = \exp(-\zeta_2 |\mathbf{r} - \mathbf{R}_2|^2)$ is still a Gaussian function $G_3 = C_3 \exp(-\zeta_3 |\mathbf{r} - \mathbf{R}_3|^2)$, such that

$$\zeta_3 = \zeta_1 + \zeta_2, \quad \mathbf{R}_3 = \frac{\zeta_1 \mathbf{R}_1 + \zeta_2 \mathbf{R}_2}{\zeta_1 + \zeta_2} \quad \text{and} \quad C_3 = \exp\left(-\frac{\zeta_1 \zeta_2 |\mathbf{R}_1 - \mathbf{R}_2|^2}{\zeta_1 + \zeta_2}\right).$$

This leads to analytic expressions [59, 60] for example for integrals of products of **GTOs** (like the one of Eq.(1.53)), or using also Boys functions, Coulomb integrals of the type⁵

$$(\alpha_{\lambda_1} \alpha_{\lambda_2} | \alpha_{\lambda_3} \alpha_{\lambda_4}) = \int d\mathbf{r} d\mathbf{r}' \frac{\alpha_{\lambda_1}^*(\mathbf{r}) \alpha_{\lambda_2}^*(\mathbf{r}) \alpha_{\lambda_3}(\mathbf{r}') \alpha_{\lambda_4}(\mathbf{r}')}{|\mathbf{r} - \mathbf{r}'|}. \quad (1.56)$$

To improve the description of wavefunctions, for example near the nuclei, basis sets of **GTOs** are often built on Contracted Gaussian Functions (**CGFs**), allowing to improve the description

⁵For the sake of compactness, we denote by λ all the coefficients (l, m, ζ, I) .

of Slater-like atomic orbitals without increasing the size of the basis set. The angular part of a CGF $\alpha_{l,m,I}^{\text{CGF}}$ is the same as the one of a primitive GTO, as defined in Eq.(1.54). Yet, its radial part R_l^{CGF} becomes a fixed linear combination of radial parts of primitive GTOs, namely

$$R_l^{\text{CGF}}(|\mathbf{r} - \mathbf{R}_I|) = \sum_{p=1}^P a_p R_{l,\zeta_p}(|\mathbf{r} - \mathbf{R}_I|). \quad (1.57)$$

An additional possibility to enhance the quality of such basis sets is to use split-valence basis sets. These latter are built on the fact that valence electrons are more involved in chemical processes than the core electrons. Therefore, the atomic split-valence basis set \mathcal{B}_I , associated to atom I , is made of one CGF per core atomic orbital, and several CGFs per valence atomic orbital. Accordingly to the number of CGF per valence atomic orbital, such bases are called split-valence double-zeta, triple-zeta, quadruple-zeta, and so on, basis sets. However, only increasing the number of CGF per atom does not automatically lead to a better quality basis. CGFs with different properties should be included. The first possibility is to add polarization functions, namely CGFs with higher angular momentum l . Atoms could benefit from higher flexibility to form chemical bonds in all directions. Another possibility is to add diffuse functions, namely CGFs with small $\{\zeta_p\}$, to improve the description of wavefunctions far from the nucleus. Many basis sets have been developed, and they can be found for example in the Basis Set Exchange website [61]. Concerning this thesis, the main type of basis sets used for calculations are the following ones:

Pople basis sets [62, 63]: The group of John Pople developed split-valence basis sets labeled by “ $P_0 - \left(\prod_{i=1}^d P_i\right)G$ ”. P_0 is the number of primitive GTO per CGF of each core atomic orbital. Namely, for each core atomic orbital, $P = P_0$ in Eq.(1.57). “ d ” is the number of CGF per valence atomic orbital. Each i^{th} valence CGF is a sum of P_i GTO. The addition of an asterisk “*” after the “G” (respectively of a plus sign “+” just before the “G”) means that polarization functions (respectively diffuse functions) are added on all atoms, except the hydrogen and helium ones. A double symbol means that all atoms benefit from these additional functions. For example, in this thesis, we use the triple-zeta 6-311G* basis set. Each core atomic orbital is a CGF which is the sum of 6 primitive GTOs. Each valence atomic orbital is associated to three CGFs. The first one is a sum of 3 primitive GTOs, while the two other ones are simple primitive GTOs. All atoms, different from the hydrogen and helium ones, benefit also from polarization functions.

Karlsruhe basis sets [64]: The Karlsruhe basis sets correspond to split-valence basis sets, with label of the type “def2- d VP” such that $d \in \{S, TZ, QZ\}$ corresponds respectively to a {double-, triple-, quadruple-}zeta basis set. “P” stands for polarization functions, and a second added “P” means that two sets of such functions are used. A “D” at the end of the label means that diffuse functions are added. For example, the def2-TZVPD correspond to a triple-zeta split-valence basis sets, with polarization and diffuse functions.

1.3.2 The *GW* formalism

As explained in section 1.1, we would like to characterize the studied systems by their removal and addition energies. The calculation of such quantities needs to take into account the interaction of the added charge with its environment, thus requiring to go beyond the mean-field picture depicted by DFT in section 1.3.1. To describe the response of the system to such perturbations, we turn to the Many-Body Perturbation Theory (MBPT) via the *GW* approximation. This latter is at the heart of my thesis.

1.3.2.1 Green's function

The central object of the *GW* approximation is the time ordered single-particle Green's function G defined as

$$G(1, 2) = -i \langle N | \hat{T} [\hat{\psi}(1) \hat{\psi}^\dagger(2)] | N \rangle. \quad (1.58)$$

i is the imaginary unit such that $i^2 = -1$, $(l) \in \{1, 2\}$ corresponds to an abbreviated notation for the position, time and spin variables $(t_l, \mathbf{r}_l, \sigma_l)$ and $|N\rangle$ is the normalized ground state of the N -body system. \hat{T} is the Wick time-ordering operator, which orders its arguments from right to left in ascending time order, and adds a factor $(-1)^P$, with P the number of interchanges of fermionic operators from the original given order [65]. The $\hat{\psi}(l)$ and $\hat{\psi}^\dagger(l)$ operators are the annihilation and creation field operators, within the Heisenberg representation, at position \mathbf{r}_l and time t_l , with spin σ_l .

To better understand this definition, let assume that $t_1 > t_2$, leading to $\hat{T} = \hat{I}$ in Eq.(1.58), with \hat{I} the identity operator. $\hat{\psi}^\dagger(2)$ creates an electron, on top of the ground state, at time t_2 and position \mathbf{r}_2 , with spin σ_2 . This state is then propagated from time t_2 to t_1 . At this time t_1 , one electron with spin σ_1 is annihilated at position \mathbf{r}_1 by $\hat{\psi}(1)$. G can be seen as a propagator of the added electron. For $t_1 < t_2$, the same interpretation can be done, but for an added hole to the system.

This Green's function G is particularly useful to compute the ground-state expectation value of single-particle operator \hat{O} [66, 67]. In second quantization, such an operator depending only on one time index t is given by \hat{O} , such that

$$\hat{O}(t) = \int d(1, 2) \delta(t - t_2) \delta(t_2 - t_1) \hat{\psi}^\dagger(1) O(1, 2) \hat{\psi}(2), \quad (1.59)$$

where $\int d(l)$ is a shorthand notation for integration (or sum) over the three variables inside (l) , and $\delta(t_i - t_j)$ the Dirac distribution. This leads to

$$\langle N | \hat{O}(t) | N \rangle = - \int d(1, 2) \delta(t - t_2) \delta(t_2^+ - t_1) O(1, 2) \langle N | \hat{T} [\hat{\psi}(2) \hat{\psi}^\dagger(1)] | N \rangle, \quad (1.60)$$

with $t_2^+ = t_2 + \eta$. η is an infinitesimal positive real number added to t_2 to introduce the time-ordering operator \hat{T} , required in the definition of G . Such a formula can be rewritten

$$\langle N | \hat{O}(t) | N \rangle = -i \int d(1, 2) \delta(t - t_2) \delta(t_2^+ - t_1) O(1, 2) G(2, 1), \quad (1.61)$$

underlying the usefulness of the Green's function.

Furthermore, the total energy E_N^0 of the system can also be computed using only the single-particle Green's function via the Galitskii-Migdal formula [68]:

$$E_N^0 = -\frac{i}{2} \sum_{\sigma_1, \sigma_2} \delta_{\sigma_1, \sigma_2} \int d\mathbf{r}_1 \lim_{\mathbf{r}_2 \rightarrow \mathbf{r}_1} \lim_{t_2 \rightarrow t_1^+} \left[i \frac{\partial}{\partial t_1} + H_0(\mathbf{r}_1) \right] G(1, 2), \quad (1.62)$$

where $\delta_{\sigma_1, \sigma_2}$ is the Kronecker delta, and $H_0(\mathbf{r}_1) = -\nabla_{\mathbf{r}_1}^2/2 + V_{\text{ext}}(\mathbf{r}_1)$ with $V_{\text{ext}}(\mathbf{r}_1)$ the external potential (with *e.g.* the ionic potential). It is also possible to go further and to extract the desired addition and removal energies from this Green's function, as explained below.

1.3.2.2 Lehmann representation and spectral function

The link between addition and removal energies, and the Green's function, can be shown thanks to the Lehmann (or spectral) representation. To compute it, we restrict ourselves to time-independant Hamiltonian \hat{H} , leading to a Green's function depending only on time difference $\tau = t_1 - t_2$, namely $G(1, 2) = G(\mathbf{x}_1, \mathbf{x}_2; \tau)$. Here, \mathbf{x}_l corresponds to the space-spin coordinates, namely $\mathbf{x}_l = (\mathbf{r}_l, \sigma_l)$. Introducing the Heaviside distribution Θ such that

$$\Theta(x) = \begin{cases} 0 & \text{if } x < 0 \\ 1/2 & \text{if } x = 0 \\ 1 & \text{if } x > 0, \end{cases} \quad (1.63)$$

and using the closure relations in the Fock space $\{|M, n\rangle\}$, where $|M, n\rangle$ is the n^{th} excited state with M electrons, Eq.(1.58) can be rewritten

$$\begin{aligned} iG(\mathbf{x}_1, \mathbf{x}_2; \tau) = & \Theta(\tau) \sum_a \langle N | \hat{\psi}(1) | N+1, a \rangle \langle N+1, a | \hat{\psi}^\dagger(2) | N \rangle \\ & - \Theta(-\tau) \sum_i \langle N | \hat{\psi}^\dagger(2) | N-1, i \rangle \langle N-1, i | \hat{\psi}(1) | N \rangle. \end{aligned} \quad (1.64)$$

Using the Schrödinger representation, such that *e.g.* $\hat{\psi}(l) = \exp(i\hat{H}t_l) \hat{\psi}(\mathbf{x}_l) \exp(-i\hat{H}t_l)$, Eq.(1.64) becomes

$$\begin{aligned} iG(\mathbf{x}_1, \mathbf{x}_2; \tau) = & \Theta(\tau) \sum_a \langle N | \hat{\psi}(\mathbf{x}_1) | N+1, a \rangle \langle N+1, a | \hat{\psi}^\dagger(\mathbf{x}_2) | N \rangle e^{i(E_0^N - E_a^{N+1})\tau} \\ & - \Theta(-\tau) \sum_i \langle N | \hat{\psi}^\dagger(\mathbf{x}_2) | N-1, i \rangle \langle N-1, i | \hat{\psi}(\mathbf{x}_1) | N \rangle e^{-i(E_0^N - E_i^{N-1})\tau}. \end{aligned} \quad (1.65)$$

with E_n^M the total energy of the n^{th} excited states with M electrons. We recognize exactly the addition and removal energies defined in section 1.1.1 and measured in practice in Photoemission Spectroscopy (PES) and Inverse Photoemission Spectroscopy (IPES) experiments, namely

$$\varepsilon_i = E_0^N - E_i^{N-1} \quad \text{for } \varepsilon_i < \mu \quad (1.66a)$$

$$\varepsilon_a = E_a^{N+1} - E_0^N \quad \text{for } \varepsilon_a \geq \mu, \quad (1.66b)$$

with μ the chemical potential. We define the Lehmann amplitudes $\{f_n(\mathbf{x})\}$ such that

$$f_i(\mathbf{x}) = \langle N-1, i | \hat{\psi}(\mathbf{x}) | N \rangle \quad (1.67a)$$

$$f_a(\mathbf{x}) = \langle N | \hat{\psi}(\mathbf{x}) | N+1, a \rangle. \quad (1.67b)$$

Using the following convention for the Fourier transform of a function $f(\tau)$

$$f(\omega) = \int_{-\infty}^{+\infty} d\tau f(\tau) e^{i\omega\tau} \quad \text{and} \quad f(\tau) = \frac{1}{2\pi} \int_{-\infty}^{+\infty} d\omega f(\omega) e^{-i\omega\tau}, \quad (1.68)$$

and the following representation of the Heaviside distribution [69]

$$\Theta(\pm\tau) = \mp \frac{1}{2i\pi} \int_{-\infty}^{+\infty} d\omega \frac{e^{-i\omega\tau}}{\omega \pm i\eta}, \quad (1.69)$$

with η an infinitesimal positive shift, the Fourier transform of G , with respect to τ , is given by

$$G(\mathbf{x}_1, \mathbf{x}_2; \omega) = \sum_i \frac{f_i(\mathbf{x}_1) f_i^*(\mathbf{x}_2)}{\omega - \varepsilon_i - i\eta} + \sum_a \frac{f_a(\mathbf{x}_1) f_a^*(\mathbf{x}_2)}{\omega - \varepsilon_a + i\eta}. \quad (1.70)$$

Such a formula highlights that the addition and removal energies are given by the poles of the Lehmann representation of G .

Starting from Eq.(1.70), it is possible to introduce the spectral function [70]:

$$A(\mathbf{x}_1, \mathbf{x}_2; \omega) = \sum_i f_i(\mathbf{x}_1) f_i^*(\mathbf{x}_2) \delta(\omega - \varepsilon_i) + \sum_a f_a(\mathbf{x}_1) f_a^*(\mathbf{x}_2) \delta(\omega - \varepsilon_a), \quad (1.71)$$

such that

$$G(\mathbf{x}_1, \mathbf{x}_2; \omega) = \int d\omega' \frac{A(\mathbf{x}_1, \mathbf{x}_2; \omega')}{\omega - \omega' + i\eta \operatorname{sgn}(\omega' - \mu)}, \quad (1.72)$$

with $\operatorname{sgn}(x)$ the sign function, namely $\operatorname{sgn}(x) = 2\Theta(x) - 1$. This spectral function obeys the following sum-rule

$$\int d\omega A(\mathbf{x}_1, \mathbf{x}_2; \omega) = \delta(\mathbf{x}_1 - \mathbf{x}_2), \quad (1.73)$$

with $\delta(\mathbf{x}_1 - \mathbf{x}_2) = \delta(\mathbf{r}_1 - \mathbf{r}_2) \delta_{\sigma_1, \sigma_2}$, because

$$\begin{aligned} \sum_i f_i(\mathbf{x}_1) f_i^*(\mathbf{x}_2) + \sum_a f_a(\mathbf{x}_1) f_a^*(\mathbf{x}_2) &= \sum_i \langle N | \hat{\psi}^\dagger(\mathbf{x}_2) | N-1, i \rangle \langle N-1, i | \hat{\psi}(\mathbf{x}_1) | N \rangle \\ &\quad + \sum_a \langle N | \hat{\psi}(\mathbf{x}_1) | N+1, a \rangle \langle N+1, a | \hat{\psi}^\dagger(\mathbf{x}_2) | N \rangle \\ &= \delta(\mathbf{x}_1 - \mathbf{x}_2), \end{aligned} \quad (1.74)$$

thanks to the anticommutation relation

$$\{\hat{\psi}(\mathbf{x}_1), \hat{\psi}^\dagger(\mathbf{x}_2)\} = \hat{\psi}(\mathbf{x}_1) \hat{\psi}^\dagger(\mathbf{x}_2) + \hat{\psi}^\dagger(\mathbf{x}_2) \hat{\psi}(\mathbf{x}_1) = \delta(\mathbf{x}_1 - \mathbf{x}_2), \quad (1.75)$$

and the closure relation in the Fock space. Such a spectral function gives also access to the ground state density $n(\mathbf{x})$ for the system of N electrons via

$$\begin{aligned} \int_{-\infty}^{\mu} d\omega A(\mathbf{x}, \mathbf{x}; \omega) &= \langle N | \hat{\psi}^\dagger(\mathbf{x}) \hat{\psi}(\mathbf{x}) | N \rangle \\ &= n(\mathbf{x}). \end{aligned} \quad (1.76)$$

Finally, using the following relation between distributions [71]

$$\frac{1}{\omega - \omega_0 \pm i\eta} = \text{pv}\left(\frac{1}{\omega - \omega_0}\right) \mp i\pi\delta(\omega - \omega_0), \quad (1.77)$$

with $\text{pv}\left(\frac{1}{\omega - \omega_0}\right)$ the Cauchy principal value, the diagonal part of the spectral function can be rewritten

$$A(\mathbf{x}, \mathbf{x}; \omega) = \frac{1}{\pi} \text{sgn}(\mu - \omega) \text{Im} [G(\mathbf{x}, \mathbf{x}; \omega)]. \quad (1.78)$$

This diagonal part is thus real (and positive thanks to Eq.(1.71)), and will be particularly useful to compute in practice and to give a physical meaning to the Quasiparticle (QP) energies, as detailed below, in section 1.3.2.10.

1.3.2.3 Dyson equation on G

The definition of G based on the knowledge of the many-body wavefunctions for the N , $(N-1)$ and $(N+1)$ electron systems is not useful in practice to calculate the Green's function. We can however compute its Equation of Motion (EOM). Rewriting the electronic Hamiltonian of equation 1.18 in second quantization⁶ as

$$\hat{H} = \int d\mathbf{x} \hat{\psi}^\dagger(\mathbf{x}) H_0(\mathbf{r}) \hat{\psi}(\mathbf{x}) + \frac{1}{2} \iint d\mathbf{x} d\mathbf{x}' \frac{\hat{\psi}^\dagger(\mathbf{x}) \hat{\psi}^\dagger(\mathbf{x}') \hat{\psi}(\mathbf{x}') \hat{\psi}(\mathbf{x})}{|\mathbf{r} - \mathbf{r}'|}, \quad (1.79)$$

with $H_0(\mathbf{r}) = -\nabla_{\mathbf{r}}^2/2 + V_{\text{ext}}(\mathbf{r})$, such that $V_{\text{ext}}(\mathbf{r})$ is the external potential (with *e.g.* the ionic potential), the EOM of the annihilation field operator obeys the following formula [66]

$$\begin{aligned} i \frac{\partial \hat{\psi}(1)}{\partial t_1} &= [\hat{\psi}(1), \hat{H}] \\ &= e^{i\hat{H}t_1} [\hat{\psi}(\mathbf{x}_1), \hat{H}] e^{-i\hat{H}t_1}, \end{aligned} \quad (1.80)$$

with $[\hat{A}, \hat{B}] = \hat{A}\hat{B} - \hat{B}\hat{A}$ the commutator. Using the following formulas [66]

$$[\hat{A}, \hat{B}\hat{C}] = \{\hat{A}, \hat{B}\}\hat{C} - \hat{B}\{\hat{A}, \hat{C}\} \quad (1.81a)$$

$$\{\hat{A}, \hat{B}\hat{C}\} = \{\hat{A}, \hat{B}\}\hat{C} - \hat{B}[\hat{A}, \hat{C}] \quad (1.81b)$$

with $\{\hat{A}, \hat{B}\} = \hat{A}\hat{B} + \hat{B}\hat{A}$ the anticommutator, and the anticommutation relations (1.75), this leads to

$$i \frac{\partial \hat{\psi}(1)}{\partial t_1} = \left(H_0(1) + \int d(3) \hat{\psi}^\dagger(3) V(1, 3) \hat{\psi}(3) \right) \hat{\psi}(1), \quad (1.82)$$

where we have introduced $H_0(1) = H_0(\mathbf{r}_1)$ and the Coulomb potential $V(1, 3) = \delta(t_1 - t_3) V(\mathbf{x}_1, \mathbf{x}_3) = \delta(t_1 - t_3) / |\mathbf{r}_1 - \mathbf{r}_3|$.

Introducing the two-particle Green's function G_2 such that

$$i^2 G_2(1, 3; 2, 3') = \langle N | \hat{T} [\hat{\psi}(1) \hat{\psi}(3) \hat{\psi}^\dagger(3') \hat{\psi}^\dagger(2)] | N \rangle, \quad (1.83)$$

⁶Here, we take into account the spin part, even if during all this thesis we restrict ourselves to spin-paired system.

the EOM of the Green's function is given by [66, 69]

$$\left[i \frac{\partial}{\partial t_1} - H_0(1) \right] G(1, 2) + i \int d(3) V(1, 3) G_2(1, 3^+; 2, 3^{++}) = \delta(1, 2), \quad (1.84)$$

where we add infinitesimal positive shifts η to $t_3^+ = t_3 + \eta$ and $t_3^{++} = t_3^+ + \eta$ to keep the proper ordering of field operators, and where we introduce $\delta(1, 2) = \delta(t_1 - t_2) \delta(\mathbf{x}_1 - \mathbf{x}_2)$. This equation (1.84) highlights that the EOM of the single-particle Green's function requires the knowledge of the two-particle Green's function. In fact, it can be shown that the EOM for the n -particle Green's function requires the knowledge of the $(n + 1)$ -particle Green's function [66]. This is the Green's function hierarchy.

To formally close the equation (1.84) and to avoid dealing with a recurrence relation, we introduce the non-local and time-dependent Hartree-exchange-correlation self-energy $\bar{\Sigma}(1, 3)$ such that [14, 69]

$$\int d(3) \bar{\Sigma}(1, 3) G(3, 2) = -i \int d(3) V(1, 3) G_2(1, 3^+; 2, 3^{++}). \quad (1.85)$$

Equivalently, using the definition of the inverse F^{-1} of the functional F such that [72]

$$\int d(3) F(1, 3) F^{-1}(3, 2) = \int d(3) F^{-1}(1, 3) F(3, 2) = \delta(1, 2), \quad (1.86)$$

the equation (1.85) can be rewritten

$$\bar{\Sigma}(1, 4) = -i \int d(2, 3) V(1, 3) G_2(1, 3^+; 2, 3^{++}) G^{-1}(2, 4). \quad (1.87)$$

We can separate out the Hartree potential defined by⁷

$$V_H(\mathbf{r}) = \int d\mathbf{r}' \frac{n(\mathbf{r}')}{|\mathbf{r} - \mathbf{r}'|} \quad (1.89a)$$

$$= -i \int d(3) V(1, 3) G(3, 3^+), \quad (1.89b)$$

leading to the definition of the self-energy $\Sigma(1, 3) = \bar{\Sigma}(1, 3) - \delta(1, 3) V_H(1)$, with $V_H(1) = V_H(\mathbf{r}_1)$, such that

$$\left[i \frac{\partial}{\partial t_1} - H_0(1) - V_H(1) \right] G(1, 2) - \int d(3) \Sigma(1, 3) G(3, 2) = \delta(1, 2). \quad (1.90)$$

If G_0 corresponds to the Hartree Green's function, solution of

$$\left[i \frac{\partial}{\partial t_1} - H_0(1) - V_H(1) \right] G_0(1, 2) = \delta(1, 2), \quad (1.91)$$

⁷The total electronic density $n(\mathbf{r}) = \sum_{\sigma} n(\mathbf{x})$ can be related to the single-particle Green's function via Eq.(1.61), with the time-independent density operator such that $\hat{O}(\mathbf{x}) = \sum_{i=1}^N \delta(\mathbf{x} - \hat{\mathbf{x}}_i)$. This leads to [66]

$$n(\mathbf{x}) = -iG(\mathbf{x}, t; \mathbf{x}, t^+). \quad (1.88)$$

the equation (1.90) can be rewritten as the following Dyson equation [14, 69]

$$G(1, 2) = G_0(1, 2) + \int d(3, 4) G_0(1, 3) \Sigma(3, 4) G(4, 2), \quad (1.92)$$

or equivalently, after the factorization of G and multiplication on the left by G_0^{-1}

$$G^{-1}(1, 2) = G_0^{-1}(1, 2) - \Sigma(1, 2). \quad (1.93)$$

To better understand the role of the self-energy Σ , let us recall that $G(1, 2)$ and $G_0(1, 2)$ depends only on the time difference $\tau = t_1 - t_2$. Therefore, $\Sigma(1, 2)$ depends also only on τ . The Fourier transform into frequency space of Eq.(1.90), with respect to τ , is given by

$$[\omega - H_0(\mathbf{r}_1) - V_H(\mathbf{r}_1)]G(\mathbf{x}_1, \mathbf{x}_2; \omega) - \int d\mathbf{x}_3 \Sigma(\mathbf{x}_1, \mathbf{x}_3; \omega)G(\mathbf{x}_3, \mathbf{x}_2; \omega) = \delta(\mathbf{x}_1 - \mathbf{x}_2). \quad (1.94)$$

We can introduce the Lehmann representation of G in Eq.(1.94). If we consider that the pole ε_n is discrete and nondegenerate, multiplying such an equation by $(\omega - \varepsilon_n)/f_n^*(\mathbf{x}_2)$, and taking the limit $\omega \rightarrow \varepsilon_n$, leads to [67, 69]

$$[H_0(\mathbf{r}_1) + V_H(\mathbf{r}_1)]f_n(\mathbf{x}_1) + \int d\mathbf{x}_3 \Sigma(\mathbf{x}_1, \mathbf{x}_3; \varepsilon_n)f_n(\mathbf{x}_3) = \varepsilon_n f_n(\mathbf{x}_1). \quad (1.95)$$

This equation (1.95), referred to as the Quasiparticle (QP) equation, gives access to the Lehmann amplitudes and their corresponding addition/removal energies. Such an equation shows similarities with the Kohn-Sham equations (1.34), but the exchange-correlation potential is replaced by the self-energy Σ , which acts as a non-local and dynamical potential, depending on the value ε_n we want to compute.

At this step, it should be noticed that such an equation reformulates the exact N -body problem as a one-body QP equation, with a self-energy. To qualitatively understand this, one should keep in mind that an additional electron or hole in the system creates around itself a polarization cloud. Namely, because of Coulomb and Pauli repulsions, a variation of charge appears to screen the added charge. In this context, a QP corresponds to an additional charge and the perturbation of its environment around itself [14]. QPs are thus globally neutral and hardly interact with each other, making it possible to describe them by a one-body equation [73]. The interaction of the added charge with its polarization cloud becomes internal to the QP and is encoded in the self-energy [14, 73].

Up to now, Σ and G are still exact. However, solving exactly equations (1.92) or (1.95) is extremely difficult, and in practice approximations are needed. The goals of the following parts is to explain one of them, namely the GW approximation.

1.3.2.4 The self-energy in linear response

One of the key idea to get rid of the two-particle Green's function G_2 in the formula of the self-energy $\bar{\Sigma}$ in Eq.(1.87)⁸, is to compute the linear response of G with respect to a time-dependent perturbation of the Hamiltonian (1.79), described by

$$\hat{H}_{\text{pert}}(t_1) = \int d\mathbf{x}_1 \hat{\psi}^\dagger(\mathbf{x}_1) U(1) \hat{\psi}(\mathbf{x}_1), \quad (1.96)$$

⁸And therefore Σ .

with $U(1)$ a time-dependent local and external potential. At the end of the derivation, this potential will be set equal to zero. Under such a perturbation, the EOM of G becomes [69]

$$\left[i \frac{\partial}{\partial t_1} - H_0(1) - U(1) \right] G(1, 2) + i \int d(3) V(1, 3) G_2(1, 3^+; 2, 3^{++}) = \delta(1, 2). \quad (1.97)$$

This leads to the following Dyson equation

$$G^{-1}(1, 2) = \tilde{G}_0^{-1}(1, 2) - U(1)\delta(1, 2) - \bar{\Sigma}(1, 2), \quad (1.98)$$

where \tilde{G}_0 corresponds to the non-interacting Green's function of the following Hamiltonian⁹

$$\left[i \frac{\partial}{\partial t_1} - H_0(1) \right] \tilde{G}_0(1, 2) = \delta(1, 2). \quad (1.99)$$

Thanks to the Schwinger functional derivative technique [74], it can be shown, for example using the representation of the single-particle Green's function in interaction picture [66, 67, 72], that

$$\frac{\delta G(1, 2)}{\delta U(3)} = G(1, 2)G(3, 3^+) - G_2(1, 3; 2, 3^+). \quad (1.100)$$

Using this formula in Eq.(1.87) leads to¹⁰

$$\bar{\Sigma}(1, 4) = -\delta(1, 4) i \int d(3) V(1, 3)G(3, 3^+) + i \int d(2, 3) V(1^+, 3) \frac{\delta G(1, 2)}{\delta U(3)} G^{-1}(2, 4). \quad (1.101)$$

The first term is exactly the Hartree potential $\delta(1, 4)V_H(1)$, leading to the following formula for the self-energy Σ :

$$\Sigma(1, 2) = i \int d(3, 4) V(1^+, 3) \frac{\delta G(1, 4)}{\delta U(3)} G^{-1}(4, 2). \quad (1.102)$$

Using the following equation [72]

$$\frac{\delta F(1, 2)}{\delta B(3)} = - \int d(4, 5) F(1, 4) \frac{\delta F^{-1}(4, 5)}{\delta B(3)} F(5, 2), \quad (1.103)$$

and the definition (1.86), the equation (1.102) can be rewritten

$$\Sigma(1, 2) = -i \int d(3, 4) V(1^+, 3)G(1, 4) \frac{\delta G^{-1}(4, 2)}{\delta U(3)}. \quad (1.104)$$

Such an expression is not appropriate to take the limit $U \rightarrow 0$ because it requires the explicit dependency of G with respect to U . Therefore, the next step is to reformulate this equation in a suitable way to perform such a limit.

⁹Contrary to Eq.(1.91), this Hamiltonian has no Hartree term.

¹⁰Normally, to go from Eq.(1.87) to Eq.(1.101) we should use the formula (1.100) with (3) replaced by (3⁺). However, the term $G(3, 3^+)$ depends only on the difference of the time arguments and $t_3^+ - t_3^{++} = t_3 - t_3^+$. Concerning the second term, we do a substitution $t_3^+ = t_3 + \eta = t_3'$ and we use the fact that $V(1, 3)$ also depends only on the time difference $t_1 - t_3$.

1.3.2.5 Hedin's equations

In 1965, Lars Hedin computed a set of integro-differential equations [1], leading to an exact formula for the self-energy Σ . While an expansion of Σ with respect to the bare Coulomb potential V was known to show difficulties, he decided to expand the self-energy with respect to the dynamical screened Coulomb potential W . Qualitatively, such an interaction $W(1, 2)$ corresponds to the potential at (1), created by both a source charge at (2) and the polarizable environment, as described in parts 1.1.2 and 1.1.3, pages 25 to 29. The screened Coulomb potential W is normally smaller than the bare one V , because the interaction is reduced by the screening of the other electrons of the environment.

To arrive at Hedin's equations, we start from the results of part 1.3.2.4, namely the linear response of the system with respect to a perturbation $U(1)$. Using Eqs.(1.89), let $\varphi(1)$ be the total potential such that

$$\varphi(1) = U(1) + V_H(1). \quad (1.105)$$

We can define the time-ordered inverse dielectric function ϵ^{-1} such that

$$\epsilon^{-1}(1, 2) = \frac{\delta\varphi(1)}{\delta U(2)} \quad (1.106a)$$

$$= \delta(1, 2) + \int d(3) V(1, 3)\chi(3, 2). \quad (1.106b)$$

χ is the reducible polarizability such that

$$\chi(1, 2) = -i \frac{\delta G(1, 1^+)}{\delta U(2)} \quad (1.107a)$$

$$= \frac{\delta n(1)}{\delta U(2)}, \quad (1.107b)$$

where we have used the Eq.(1.88), with $n(1) = n(\mathbf{x}_1)$ the electronic density. This corresponds to the variation of the electronic density with respect to a variation of the external perturbation. Such a quantity is related to the irreducible polarizability $\tilde{\chi}$, namely the same variation of $n(1)$, but with respect to the total potential $\varphi(2)$

$$\tilde{\chi}(1, 2) = -i \frac{\delta G(1, 1^+)}{\delta \varphi(2)}, \quad (1.108)$$

via the following Dyson-like equation

$$\chi(1, 2) = \tilde{\chi}(1, 2) + \int d(34) \tilde{\chi}(1, 3)V(3, 4)\chi(4, 2). \quad (1.109)$$

Such an equation can be demonstrated using Eq.(1.106) and the following chain rule [25]

$$\frac{\delta F[B[C]](1)}{\delta C(2)} = \int d(3) \frac{\delta F[B](1)}{\delta B(3)} \frac{\delta B[C](3)}{\delta C(2)}. \quad (1.110)$$

In this context, the dynamical screened Coulomb potential W , is defined by

$$W(1, 2) = \int d(3) \epsilon^{-1}(1, 3)V(3, 2) \quad (1.111)$$

or equivalently, using the previous equations on the polarizabilities,

$$W(1, 2) = V(1, 2) + \int d(3, 4) V(1, 3)\chi(3, 4)V(4, 2) \quad (1.112a)$$

$$= V(1, 2) + \int d(3, 4) V(1, 3)\tilde{\chi}(3, 4)W(4, 2) \quad (1.112b)$$

To obtain a set of equations, one should introduce the vertex function Γ such that

$$\Gamma(1, 2, 3) = -\frac{\delta G^{-1}(1, 2)}{\delta \varphi(3)}. \quad (1.113)$$

Using the chain rule of Eq.(1.110) in Eq.(1.104), and the previous definitions, leads to the following formula of the self-energy

$$\Sigma(1, 2) = i \int d(3, 4) G(1, 4)W(3, 1^+)\Gamma(4, 2, 3). \quad (1.114)$$

As depicted by this equation, a more tractable and more amenable to approximations formula for Γ is required. The equation (1.98), which can be rewritten $G^{-1}(1, 2) = \tilde{G}_0^{-1}(1, 2) - \varphi(1)\delta(1, 2) - \Sigma(1, 2)$, leads to

$$\Gamma(1, 2, 3) = \delta(1, 2)\delta(1, 3) + \frac{\delta \Sigma(1, 2)}{\delta \varphi(3)} \quad (1.115a)$$

$$= \delta(1, 2)\delta(1, 3) + \int d(4, 5) \frac{\delta \Sigma(1, 2)}{\delta G(4, 5)} \frac{\delta G(4, 5)}{\delta \varphi(3)} \quad (1.115b)$$

$$= \delta(1, 2)\delta(1, 3) + \int d(4, 5, 6, 7) \frac{\delta \Sigma(1, 2)}{\delta G(4, 5)} G(4, 6)G(7, 5)\Gamma(6, 7, 3), \quad (1.115c)$$

where we have used the chain rule (1.110) and Eq.(1.103).

At this step, the Eq.(1.108) can be reformulated, using the definition of Γ of Eq.(1.113) and the formula (1.103), leading to

$$\tilde{\chi}(1, 2) = -i \int d(3, 4)G(1, 3)\Gamma(3, 4, 2)G(4, 1^+). \quad (1.116)$$

Now, taking the limit of $U \rightarrow 0$ gives the exact closed set of Hedin's equations [1]

$$G(1, 2) = G_0(1, 2) + \int d(3, 4) G_0(1, 3)\Sigma(3, 4)G(4, 2) \quad (1.117a)$$

$$\Gamma(1, 2, 3) = \delta(1, 2)\delta(1, 3) + \int d(4, 5, 6, 7) \frac{\delta \Sigma(1, 2)}{\delta G(4, 5)} G(4, 6)G(7, 5)\Gamma(6, 7, 3) \quad (1.117b)$$

$$\tilde{\chi}(1, 2) = -i \int d(3, 4)G(1, 3)\Gamma(3, 4, 2)G(4, 1^+) \quad (1.117c)$$

$$W(1, 2) = V(1, 2) + \int d(3, 4) V(1, 3)\tilde{\chi}(3, 4)W(4, 2) \quad (1.117d)$$

$$\Sigma(1, 2) = i \int d(3, 4) G(1, 4)W(3, 1^+)\Gamma(4, 2, 3). \quad (1.117e)$$

These equations represent an iterative solution of the many-body problem. Starting from an initial guess for Σ and G , Γ , $\tilde{\chi}$ and then W can be computed. Then, the computation of all five quantities can be done up to self-consistency, as represented in FIGURE 1.7. However, in practice these equations are extremely complex to solve, and approximations are required.

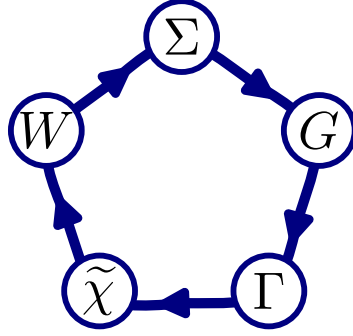


Figure 1.7: Hedin's pentagram, which is a symbolic representation of the Hedin's equations. Each quantity, in each vertex, is iteratively computed until self-consistency via its corresponding equation (1.117), represented by one edge.

1.3.2.6 The GW approximation

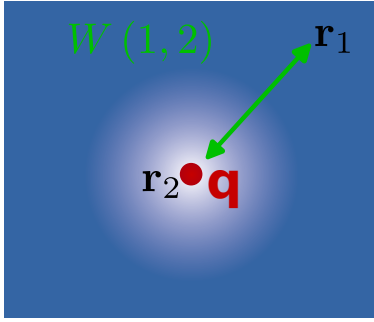


Figure 1.8: Schematic representation of a charge variation around an added charge q in (2) (in red). The electron gas of the environment is represented in blue, and the charge variation by a gradation of blue. $W(1, 2)$ is the dynamical screened Coulomb potential in (1) created by such a charge.

One of the central quantities of the Hedin's equation is the screened Coulomb potential W . It is possible to better understand its physical meaning via classical arguments, through its formula (1.112a). For the sake of simplicity, we limit ourselves to the static limit and neglect the spin. Let us assume we add a point test charge q in \mathbf{r}_2 . Such a charge generates a potential $q/|\mathbf{r} - \mathbf{r}_2|$ in all the space, creating a charge variation δn^{ind} around itself, represented by a gradation of blue in FIGURE 1.8, and given by

$$\delta n^{\text{ind}}(\mathbf{r}', \mathbf{r}_2) = \int d\mathbf{r} \chi(\mathbf{r}', \mathbf{r}) \frac{q}{|\mathbf{r} - \mathbf{r}_2|} \quad (1.118)$$

If $q > 0$, electrons accumulate around q , while a charge $q < 0$ creates a depletion of electrons around itself: it is namely the screening effects. The total field, at \mathbf{r}_1 , generated by the charge q and δn^{ind} is

$$\frac{q}{|\mathbf{r}_1 - \mathbf{r}_2|} + \int d\mathbf{r}' d\mathbf{r} \frac{1}{|\mathbf{r}_1 - \mathbf{r}'|} \chi(\mathbf{r}', \mathbf{r}) \frac{q}{|\mathbf{r} - \mathbf{r}_2|} \quad (1.119)$$

We recover the formula of W (1.112a) in the static limit. In general, W depends on time difference (or frequency via its Fourier transform), allowing the relaxation and screening of the QPs [14]. In polarizable materials, where screening effects are notable, W is significantly reduced as compared to the bare Coulomb potential V . This has led Hedin to propose to keep only the first-order of Σ of Eq.(1.117e) with respect to W [1], or equivalently to approximate $\Gamma = \delta(1, 2)\delta(1, 3)$ in Eq.(1.117b). In this approximation, called the GW approximation, the Hedin's equations become¹¹

¹¹In the GW approximation, $\tilde{\chi}$ is replaced by the notation χ_0 .

$$\begin{aligned}
G(1,2) &= G_0(1,2) + \int d(3,4) G_0(1,3)\Sigma(3,4)G(4,2) & (1.120a) \\
\Gamma(1,2,3) &= \delta(1,2)\delta(1,3) & (1.120b) \\
\chi_0(1,2) &= -iG(1,2)G(2,1^+) & (1.120c) \\
W(1,2) &= V(1,2) + \int d(3,4) V(1,3)\chi_0(3,4)W(4,2) & (1.120d) \\
\Sigma(1,2) &= iG(1,2)W(2,1^+). & (1.120e)
\end{aligned}$$

The Eq.(1.120e) gives its name to the approximation. This set of equation can also be represented by Feynman diagrams, as illustrated in FIGURE 1.9.

$$\begin{aligned}
\text{---} \overline{\overline{G}} \text{---} &= \text{---} \overline{\overline{G_0}} \text{---} + \text{---} \overline{\overline{\text{---} \text{---} \text{---}}} \text{---} & (a) \\
\text{---} \overline{\overline{\Gamma}} \text{---} &= \bullet & (b) \\
\text{---} \overline{\overline{\chi_0}} \text{---} &= \text{---} \overline{\overline{\text{---} \text{---} \text{---}}} \text{---} & (c) \\
\text{---} \overline{\overline{W}} \text{---} &= \text{---} \overline{\overline{V}} \text{---} + \text{---} \overline{\overline{\text{---} \text{---} \text{---}}} \text{---} & (d) \\
\text{---} \overline{\overline{\Sigma}} \text{---} &= \text{---} \overline{\overline{\text{---} \text{---} \text{---}}} \text{---} & (e)
\end{aligned}$$

Figure 1.9: Diagrammatic representation of the Hedin's equations, via Feynman diagrams. Adapted from [14].

Using the convention of Eq.(1.68), such a formula can be Fourier transformed in time with respect to $\tau = t_1 - t_2$, leading to

$$\Sigma(\mathbf{x}_1, \mathbf{x}_2; \varepsilon) = \frac{i}{2\pi} \int_{-\infty}^{+\infty} d\omega e^{i\omega\eta_1} G(\mathbf{x}_1, \mathbf{x}_2; \omega + \varepsilon) W(\mathbf{x}_1, \mathbf{x}_2; \omega), \quad (1.121)$$

with η_1 a positive infinitesimal shift. To better understand the meaning of this self-energy, this latter can be split into two parts, namely its energy-independent exchange part $\Sigma^X(\mathbf{x}_1, \mathbf{x}_2)$, and its energy-dependent correlation part $\Sigma^C(\mathbf{x}_1, \mathbf{x}_2; \varepsilon)$, such that $\Sigma(\mathbf{x}_1, \mathbf{x}_2; \varepsilon) = \Sigma^X(\mathbf{x}_1, \mathbf{x}_2) + \Sigma^C(\mathbf{x}_1, \mathbf{x}_2; \varepsilon)$. Its correlation part is defined by

$$\Sigma^C(\mathbf{x}_1, \mathbf{x}_2; \varepsilon) = \frac{i}{2\pi} \int_{-\infty}^{+\infty} d\omega e^{i\omega\eta_1} G(\mathbf{x}_1, \mathbf{x}_2; \omega + \varepsilon) [W(\mathbf{x}_1, \mathbf{x}_2; \omega) - V(\mathbf{x}_1, \mathbf{x}_2)], \quad (1.122)$$

and its exchange part by

$$\Sigma^X(\mathbf{x}_1, \mathbf{x}_2) = \frac{i}{2\pi} \int_{-\infty}^{+\infty} d\omega e^{i\omega\eta_1} G(\mathbf{x}_1, \mathbf{x}_2; \omega + \varepsilon) V(\mathbf{x}_1, \mathbf{x}_2) \quad (1.123a)$$

$$= - \sum_i f_i(\mathbf{x}_1) f_i^*(\mathbf{x}_2) V(\mathbf{x}_1, \mathbf{x}_2). \quad (1.123b)$$

The last formula (1.123b) [67, 75] can be computed using the Eq.(1.70) page 43 and the residue theorem [71] over the closed curve \mathcal{C}^+ of the FIGURE 1.10, in the limit of the radius $R \rightarrow \infty$. The sum runs only over states such that $\varepsilon_i < \mu$. This decomposition can be compared to another one, namely the Coulomb-Hole plus Screened-Exchange (COHSEX) decomposition presented in part 1.3.2.7.

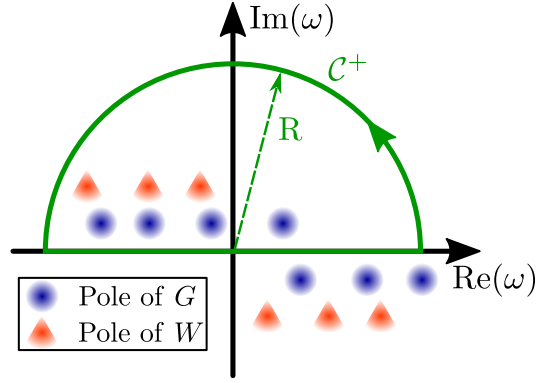


Figure 1.10: Schematic representation of the poles of G and W in the complex plane. \mathcal{C}^+ is a complex semicircle contour, of radius R , enclosing all the poles located in the upper-plane, and no pole of the lower-plane.

Finally, it should be noticed that the GW method is now accessible in many *ab initio* codes and has been widely successful in predicting electron addition and removal energies [14].

1.3.2.7 The COHSEX decomposition

The Coulomb-Hole plus Screened-Exchange (COHSEX) decomposition is another way to split the GW self-energy, namely in its Screened-Exchange (SEX) Σ^{SEX} and its Coulomb-Hole (COH) Σ^{COH} parts, such that $\Sigma = \Sigma^{\text{SEX}} + \Sigma^{\text{COH}}$. Its static version, presented below, is an important approximation playing a central role in my thesis.

In the absence of magnetic fields¹², which is the case during all this thesis, the screened Coulomb potential W can be written in its spectral representation such that [48, 70, 78]

$$W(\mathbf{x}_1, \mathbf{x}_2; \omega) = V(\mathbf{x}_1, \mathbf{x}_2) + \sum_{\lambda > 0} w_\lambda(\mathbf{x}_1)w_\lambda(\mathbf{x}_2) \left[\frac{1}{\omega - \Omega_\lambda + i\eta_2} - \frac{1}{\omega + \Omega_\lambda - i\eta_2} \right], \quad (1.124)$$

where η_2 is a strictly positive infinitesimal shift. Denoting $|N, \lambda\rangle$ the λ^{th} excited states with N electrons, of total energy E_λ^N , the fluctuation potential¹³ w_λ , and its corresponding charge neutral excitation Ω_λ , are defined by

$$w_\lambda(\mathbf{x}) = \int d\mathbf{x}' \frac{\langle N, \lambda | \psi^\dagger(\mathbf{x}') \psi(\mathbf{x}') | N, 0 \rangle}{|\mathbf{r} - \mathbf{r}'|} \quad (1.125a)$$

$$\Omega_\lambda = E_\lambda^N - E_0^N. \quad (1.125b)$$

¹²See [76, 77] for a more general situation.

¹³If there is no magnetic fields, the eigenstates $|N, \lambda\rangle$ can be chosen real, as well as w_λ [48].

The positions of the poles of G and W are schematically represented in FIGURE 1.10.

Using the Eq.(1.70) page 43 and Eq.(1.124), we can apply the residue theorem [71] over the closed curve \mathcal{C}^+ of the FIGURE 1.10 to compute the Eq.(1.121). Taking the limit $R \rightarrow \infty$, the poles of $G(\mathbf{r}_1, \mathbf{r}_2; \varepsilon)$ in the upper complex plane lead to the SEX term

$$\Sigma^{\text{SEX}}(\mathbf{x}_1, \mathbf{x}_2; \varepsilon) = - \sum_i f_i(\mathbf{x}_1) f_i^*(\mathbf{x}_2) W(\mathbf{x}_1, \mathbf{x}_2; \varepsilon_i - \varepsilon), \quad (1.126)$$

where the sum runs only over states such that $\varepsilon_i < \mu$. This Σ^{SEX} looks like a dynamically screened exchange, where the bare Coulomb potential V is replaced by W in the exact exchange of Eq.(1.123b).

Using the same method, the poles of W in the upper complex plane lead to the COH term, such that

$$\Sigma^{\text{COH}}(\mathbf{x}_1, \mathbf{x}_2; \varepsilon) = \sum_n f_n(\mathbf{x}_1) f_n^*(\mathbf{x}_2) \sum_{\lambda > 0} \frac{w_\lambda(\mathbf{x}_1) w_\lambda(\mathbf{x}_2)}{\varepsilon - \varepsilon_n - \Omega_\lambda + i\eta \times \text{sgn}(\varepsilon_n - \mu)} \quad (1.127)$$

where the sum on n runs over all the states.

At this step, the COHSEX decomposition is still exact, but it can be seen as the starting point of an additional approximation, namely the static COHSEX approximation.

1.3.2.8 The static COHSEX approximation

In the static COHSEX approximation [1, 37, 67, 79, 80], we consider the limit $\varepsilon - \varepsilon_n = 0$ in all the term of the equations (1.126) and (1.127), leading to

$$\Sigma_{\text{static}}^{\text{SEX}}(\mathbf{x}_1, \mathbf{x}_2) = - \sum_i f_i(\mathbf{x}_1) f_i^*(\mathbf{x}_2) W(\mathbf{x}_1, \mathbf{x}_2; \omega = 0) \quad (1.128a)$$

$$\Sigma_{\text{static}}^{\text{COH}}(\mathbf{x}_1, \mathbf{x}_2) = \frac{1}{2} \delta(\mathbf{x}_1 - \mathbf{x}_2) [W - V](\mathbf{x}_1, \mathbf{x}_2; \omega = 0). \quad (1.128b)$$

To arrive at the equation (1.128b), the η term is removed because there is no longer singularity, and the closure relation (1.74) is used. Such a static COHSEX approximation, often called abusively simply the COHSEX approximation, can also be computed via arguments on the time structure of G and W [1, 67]. One should note that taking directly the limit $W(\mathbf{x}_1, \mathbf{x}_2; \omega = 0)$ in Eq.(1.121) would lead only to the static SEX term (1.128a), missing the static COH term (1.128b). The physical meaning of this latter term, both static and local in space-spin, can be understood via classical arguments. It is related to the energy required to adiabatically add a point charge to the system.

Similarly to simple models presented in section 1.1.3 page 27, let us assume we add an infinitesimal point charge¹⁴ $\pm \delta(\mathbf{r} - \mathbf{r}_0) d\lambda$ to the already present charge $\pm \delta(\mathbf{r} - \mathbf{r}_0) \lambda$ (for λ going from 0 to 1). This added charge induces a charge variation in the environment, given by Eq.(1.118), leading to an interaction energy, created by the polarization cloud, equal to

$$dE_{\text{ind}} = \int d\mathbf{r}_1 d\mathbf{r}_2 d\mathbf{r}_3 d\mathbf{r}_4 \frac{(\pm \lambda \delta(\mathbf{r}_4 - \mathbf{r}_0))}{|\mathbf{r}_4 - \mathbf{r}_3|} \chi(\mathbf{r}_3, \mathbf{r}_2) \frac{(\pm d\lambda \delta(\mathbf{r}_1 - \mathbf{r}_0))}{|\mathbf{r}_2 - \mathbf{r}_1|} \quad (1.129a)$$

$$= \lambda d\lambda [W - V](\mathbf{r}_0, \mathbf{r}_0; \omega = 0). \quad (1.129b)$$

¹⁴For the sake of simplicity, we omit the spin variable.

The total energy required to add this point charge is given by

$$E_{\text{ind}} = \int dE_{\text{ind}} = \int_0^1 d\lambda \lambda [W - V](\mathbf{r}_0, \mathbf{r}_0; \omega = 0) \quad (1.130a)$$

$$= \frac{1}{2} [W - V](\mathbf{r}_0, \mathbf{r}_0; \omega = 0), \quad (1.130b)$$

which is directly related to the formula of the static COH self-energy (1.128b).

Even if the static COHSEX approximation gives a good qualitative description of the physical effects, it shows difficulties to give accurate results [48]. For example, it is known to lead to fundamental gaps which are too large [79, 81]. However, this approximation requiring W at only one frequency ($\omega = 0$) is computationally interesting, making the calculations faster, as explained in section 1.3.2.10. One of the main goal of this thesis is to quantitatively probe the accuracy of such an approach, in the context of calculating the screening contribution from a large environment.

To conclude this part, about the general GW approximation, we give some details about real implementations of such a formalism, as the one used during this thesis.

1.3.2.9 GW in practice

In practice, one of the most widely used approaches is the non-self-consistent G_0W_0 one. Starting from a mean-field Green's function $G = G_0$, such an approach corresponds to the first iteration of the Hedin's equations (1.120). In general, G_0 corresponds the Green's function of a Hartree-Fock or Kohn-Sham (KS)-DFT mean-field Hamiltonian, closer to the interacting one G than the Hartree Green's function [14]. Using similar arguments than the ones used to go from $\bar{\Sigma}$ to Σ in Eq.(1.90), the equation (1.120a) becomes [82]

$$G(1, 2) = G_0(1, 2) + \int d(3, 4) G_0(1, 3) [\Sigma(3, 4) - V_{\text{XC}}(3, 4)] G(4, 2), \quad (1.131)$$

with $V_{\text{XC}}(3, 4) = V_{\text{XC}}(\mathbf{x}_3) \delta(3, 4)$ the exchange-correlation potential¹⁵.

In practice, during all this thesis, we restrict ourselves to spin-paired (or unpolarized) systems. Therefore, from now on and for the sake of simplicity, we drop the spin variable σ and take into account spin-degeneracy when required.

In this context, the Green's function G_0 is given by

$$G_0(\mathbf{r}_1, \mathbf{r}_2; \omega) = \sum_n \frac{\phi_n^0(\mathbf{r}_1) \phi_n^{0*}(\mathbf{r}_2)}{\omega - \varepsilon_n^0 + i\eta \times \text{sgn}(\varepsilon_n^0 - \mu)}, \quad (1.132)$$

with $\{\varepsilon_n^0, \phi_n^0(\mathbf{r})\}$ the eigenvalues and the eigenfunctions of the (spin-paired) mean-field Hamiltonian. The sum runs over all the states. The RPA irreducible polarizability χ_0 [83], or here independent-electron susceptibility, is computed via the product of G_0 via Eq.(1.120c). It is given by the Adler-Wiser expression [84, 85]

$$\chi_0(\mathbf{r}_1, \mathbf{r}_2; \omega) = \sum_{m,n} (f_m - f_n) \frac{\phi_m^{0*}(\mathbf{r}_1) \phi_n^0(\mathbf{r}_1) \phi_m^0(\mathbf{r}_2) \phi_n^{0*}(\mathbf{r}_2)}{\omega - (\varepsilon_n^0 - \varepsilon_m^0) + i\eta \times \text{sgn}(\varepsilon_n^0 - \varepsilon_m^0)}, \quad (1.133)$$

¹⁵It can be non-local in space, for example if hybrid functionals are used.

with $\{f_n\}$ the level occupation numbers, such that $f_n \in \{0, 2\}$ to take into account the spin-degeneracy¹⁶. Each sum runs over all the states. The corresponding screened Coulomb potential, denoted W_0 , is then computed via Eq.(1.120d). This leads to $\Sigma(1, 2) = iG_0(1, 2)W_0(2, 1^+)$, giving the name to this approach. Finally, the Lehmann amplitudes $\{f_n(\mathbf{r})\}$ are approximated by the mean-field eigenstates $\{\phi_n^0(\mathbf{r})\}$. Projecting onto $\langle \phi_n^0 |$, the QP equation (1.95) becomes

$$\varepsilon_n = \varepsilon_n^0 + \langle \phi_n^0 | \Sigma(\varepsilon_n) - V_{\text{XC}} | \phi_n^0 \rangle. \quad (1.134)$$

The self-energy depending on the QP energy ε_n we want to compute, this equation requires a self-consistent solution. Such an approach, based only on one iteration of the Hedin's equation, can present a significant dependence on the initial guess, namely on the mean-field values $\{\varepsilon_n^0, \phi_n^0(\mathbf{r})\}$ [14]. This is illustrated in FIGURE 1.11, where the fundamental gap in gas phase of the fullerene C₆₀, one of the central molecule of my thesis, is computed for different methods. Starting from a KS-DFT mean-field calculation, with a hybrid functional PBEh(α) (see section 1.3.1.3 page 35), the gap is computed with respect to the fraction of exact exchange α . Calculations are done with the Gaussian basis def2-TZVP, and its corresponding Resolution of the Identity (RI) basis def2-TZVP-RI (see section 1.3.2.10 for more information about technical details). The KS-DFT gap, represented by blue dots, shows a linear trend, going from 1.7 eV to 7.0 eV, highlighting the difficulties of this method to predict a value close to the experimental reference of 4.9 eV [86] (dashed line). In the same time, the G_0W_0 approach (orange dots) leads to results in better agreement with the experimental value. The error is at most 0.7 eV, with 1.1 eV between its two extreme predicted values.

To reduce the dependency of the results on the initial guess, one possibility is to reach self-consistency in the GW Hedin's equation [87–94]. This also cures further problems associated with multiple QP solutions [95, 96]. However, a fully self-consistent procedure is computationally expensive. One approximate solution consists into performing self-consistency only on the QP energies $\{\varepsilon_n\}$, leading to the $evGW$ approach [18, 92, 97–99] which is an eigenvalue-self-consistent scheme. In this $evGW$ approach, after the first G_0W_0 iteration, the new QP energies $\{\varepsilon_n\}$ are kept to replace the initial energies $\{\varepsilon_n^0\}$ in the definition of G_0 (1.132). The eigenfunctions $\{\phi_n^0(\mathbf{r})\}$ are kept the same. Thanks to this new G_0 , a new loop of Hedin's equation is completed, leading to new QP energies. The process is iterated until convergence of these energies. This approach has led to improvements in the predicted fundamental gap for molecular systems [18, 100]. In FIGURE 1.11, the amplitudes of variation of the gap of a C₆₀ at the $evGW$ level with 6 iterations, represented by green dots, decreases to 0.4 eV, with a maximal error of 0.5 eV.

As stated before, this graph also shows the tendency of the static COHSEX approach (red dots) to overestimates the fundamental gap, with a minimal error of 0.5 eV.

After this presentation of the different GW approaches, I would like to give some details about the implementation of the code I have used and whose I developed some parts during my thesis.

¹⁶It should be noticed that we restrict ourselves only to spin-independent Hamiltonian, like Eq.(1.79). This leads to $G(1, 2) = \delta_{\sigma_1, \sigma_2} G(\mathbf{r}_1, t_1, \mathbf{r}_2, t_2)$ [72]. Therefore, χ_0 is also diagonal with respect to the spin. In this context, Eq.(1.133) appears as a shortcut notation for $\chi_0(\mathbf{r}_1, \mathbf{r}_2; \omega) = \sum_{\sigma} \chi_0(\mathbf{r}_1, \sigma, \mathbf{r}_2, \sigma; \omega)$, leading in particular to $f_n \in \{0, 2\}$ for spin-paired system. Such a shortcut, which embeds the spin summation, is particularly useful in Eq.(1.120d). This enables us to directly replace $\int d(3, 4)$ by $\int d\mathbf{r}_3 dt_3 d\mathbf{r}_4 dt_4$ [83].

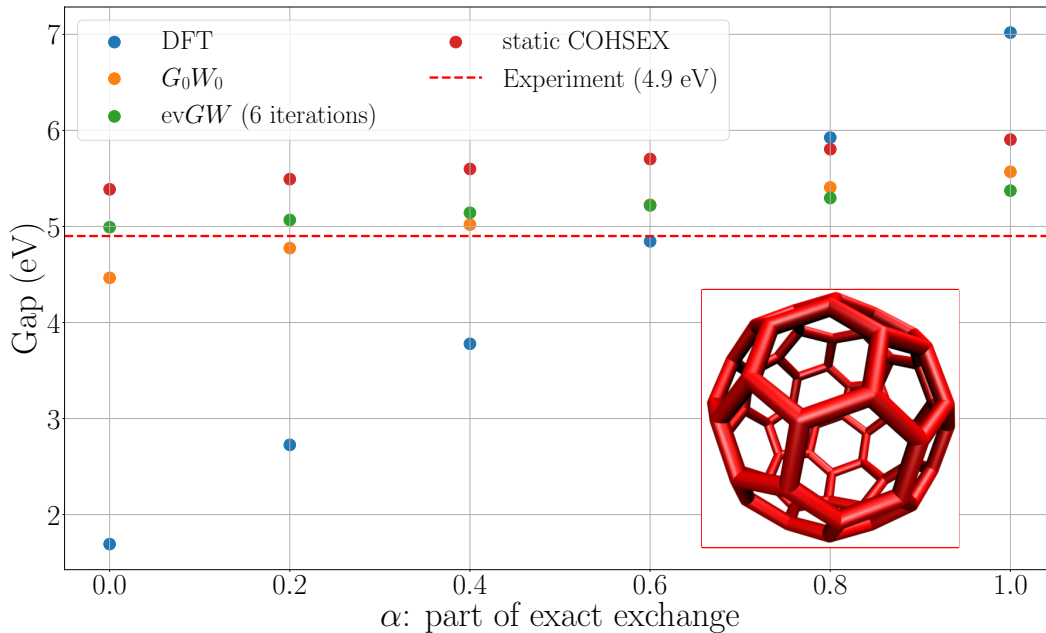


Figure 1.11: Fundamental gap (eV) of a C_{60} in gas phase, with respect to the part of exact exchange used in the exchange-correlation functional $PBEh(\alpha)$. **KS-DFT** calculations are done with the def2-TZVP basis, while **GW** calculations are done using our Gaussian basis **GW** code **BEDEFT** with the **RI** basis def2-TZVP-RI (see section 1.3.2.10 for more technical details). Experimental value comes from [86]. Inset: symbolic representation of a C_{60} .

1.3.2.10 Implementation in **beDeft**



Figure 1.12: Logo of **BEDEFT**, our Gaussian-basis **GW/BSE** code developed in our group.

All the **GW** calculations and developments presented in this thesis have been done in the massively-parallel Gaussian-basis **GW/Bethe–Salpeter Equation (BSE)** code **Beyond Density-Functional Theory (BEDEFT)** [78, 101], a rewriting and extension of the **FIESTA** code [7, 10, 18, 102, 103]. This code, whose logo is depicted in **FIGURE 1.12**, has been developed in our group for calculations on non-periodic finite size systems. An insight into a typical input file, with the main methods developed during this thesis, is given in **appendix C** page 167.

Resolution of the Identity (RI): Our code adopts a **RI** formalism [104–106] where the orbitals products $\{\phi_n^0 \phi_m^0\}$, appearing for example in the definition of χ_0 Eq.(1.133), are expressed over a Gaussian auxiliary basis set $\{P\}$:

$$\phi_n^0(\mathbf{r}) \phi_m^0(\mathbf{r}) \stackrel{\text{RI}}{\simeq} \sum_P \mathcal{F}_P(\phi_n^0 \phi_m^0) P(\mathbf{r}). \quad (1.135)$$

Diverse choices are possible for the coefficients $\{\mathcal{F}_P\}$ [106], and during this thesis, unless explicitly mentioned, I use the so-called Coulomb-fitting approach (RI-V) [107] such that

$$\mathcal{F}_P(\phi_n^0 \phi_m^0) = \sum_Q [\mathbf{V}^{-1}]_{PQ} (Q \parallel \phi_n^0 \phi_m^0). \quad (1.136)$$

\mathbf{V}^{-1} is the inverse of the auxiliary basis Coulomb matrix of coefficients $[\mathbf{V}]_{PQ} = (P \parallel Q)$, with $(\cdot \parallel \cdot)$ the Coulomb integral. As we restrict ourselves only to finite-size systems, without magnetic field, the Gaussian auxiliary functions $\{P\}$ can be taken to be real, as well as the Molecular Orbitals (MOs) $\{\phi_n^0\}$. This auxiliary basis set globally follows the same rules as the ones developed for the basis sets used at the KS-DFT level in section 1.3.1.5 page 38. However, we consider only auxiliary basis sets developed in terms of cubic harmonics (and not solid harmonics). Using the Cartesian coordinates such that $\mathbf{r} = (x, y, z)$, primitive auxiliary Gaussian Type Orbitals (GTOs) are given by

$$P_{n_x, n_y, n_z, \zeta, I}(\mathbf{r}) = \aleph_{n_x, n_y, n_z, \zeta} (x - X_I)^{n_x} (y - Y_I)^{n_y} (z - Z_I)^{n_z} \exp(-\zeta |\mathbf{r} - \mathbf{R}_I|^2). \quad (1.137)$$

\mathbf{R}_I corresponds to the position of the I^{th} atom. (n_x, n_y, n_z) are natural numbers, $\aleph_{n_x, n_y, n_z, \zeta}$ a normalization factor and ζ is a real positive number controlling the width of the Gaussian part. Such auxiliary basis sets have been optimized for each standard Gaussian KS basis set, as for example the “def2-TZVP-RI” [108–110] associated to the corresponding “def2-TZVP” Karlsruhe basis sets, or are more universal as the Coulomb fitting auxiliary basis developed by Weigend [111]. They can also be found in the Basis Set Exchange website [61].

While the dimension of the product space spanned by the KS orbitals products $\{\phi_n^0 \phi_m^0\}$ grows formally as $\mathcal{O}(N^2)$, with respect to the number of electrons N , the locality of GTOs leads in practice to a linear growth $\mathcal{O}(N)$ in terms of system size. The auxiliary basis set exploits this fact by further reducing the prefactor associated to this linear growth. As an example, the prefactor associated to the number of non-zero KS basis product elements with respect to the KS basis size would be 200–300, while the auxiliary basis is only 3–4 times the size of this latter. With such a RI, the most expensive steps of a GW calculation becomes the computation of χ_0 of Eq.(1.133) which scales as $\mathcal{O}(N^4)$ [14].

Then, one important step is the computation of the frequency integral (1.122).

Frequency integral: To compute such an integral, BEDEFT relies on a Contour Deformation (CD) plus an Analytic Continuation (AC) approaches [78, 112, 113]. The CD method transforms the integral along the real axis as a contour integral along the closed curve \mathcal{C} of FIGURE 1.13, in the limit $R \rightarrow \infty$. Defining $W_{\text{scr}} = (W - V)$ the screening potential, Eq.(1.122) becomes¹⁷

$$\begin{aligned} \Sigma^{\text{C}}(\mathbf{r}_1, \mathbf{r}_2; \varepsilon) = & -\frac{1}{2\pi} \int_{-\infty}^{+\infty} d\omega G(\mathbf{r}_1, \mathbf{r}_2; \varepsilon + i\omega) W_{\text{scr}}(\mathbf{r}_1, \mathbf{r}_2; i\omega) \\ & - \sum_i^{\text{occ}} \phi_i^0(\mathbf{r}_1) \phi_i^0(\mathbf{r}_2) W_{\text{scr}}(\mathbf{r}_1, \mathbf{r}_2; \varepsilon_i - \varepsilon) \Theta(\varepsilon_i - \varepsilon) \\ & + \sum_a^{\text{unocc}} \phi_a^0(\mathbf{r}_1) \phi_a^0(\mathbf{r}_2) W_{\text{scr}}(\mathbf{r}_1, \mathbf{r}_2; \varepsilon_a - \varepsilon) \Theta(\varepsilon - \varepsilon_a), \end{aligned} \quad (1.138)$$

¹⁷Lehmann amplitudes are replaced by mean-field eigenfunctions to mimic real calculations.

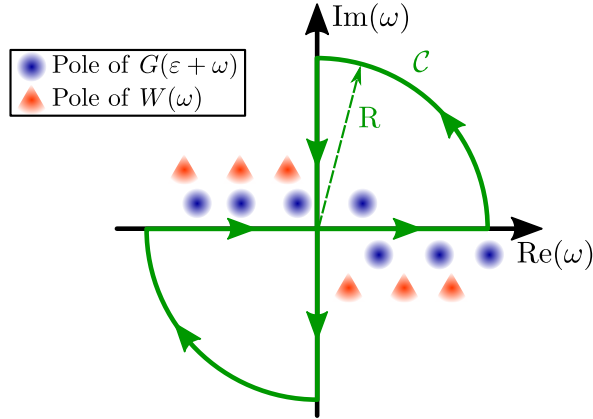


Figure 1.13: Schematic representation of the poles of G and W in the complex plane. \mathcal{C} is the complex contour, potentially enclosing poles of $G(\omega + \varepsilon)$ in the first or third quadrant (such that $\text{Re}(\omega) \cdot \text{Im}(\omega) > 0$), used for the CD approach.

with Θ the Heaviside distribution, and i/a denoting the occupied/unoccupied states, respectively. Thanks to the absence of imaginary poles of W_{scr} (see Eq.(1.124)), the numerical integration over the imaginary axis can be performed with a few quadrature points. In practice, only $n_\omega = 12$ imaginary frequencies $\{i\omega\}$ are used to compute such an integral. The residues¹⁸ $W_{\text{scr}}(\mathbf{r}_1, \mathbf{r}_2; \varepsilon_n - \varepsilon)$ appearing in Eq.(1.138) are computed through an AC of W_{scr} to the real axis. During all this thesis, unless explicitly mentioned, the AC is required only for states with energy close to the gap and is performed directly from the n_ω imaginary frequencies. Such an AC leads to no-extra cost. If required, additional complex frequencies, parallel to the real axis with an imaginary part, can be added to improve the accuracy of the AC [78]. This can be used for example for core states.

At this step, it should be noticed that each imaginary frequency $i\omega$ of the quadrature requires the calculation of the corresponding $W_{\text{scr}}(i\omega)$, and therefore of $\chi_0(i\omega)$. The computation of this latter is the only step scaling as $\mathcal{O}(N^4)$. On the other hand, in the static COHSEX approximation, only the static limit $W_{\text{scr}}(\omega = 0)$, and therefore $\chi_0(\omega = 0)$, is required. Therefore, for systems large enough, BEDEFT leads to static COHSEX calculations which are around n_ω times cheaper than the corresponding G_0W_0 calculations. In practice, this represents an order of magnitude of difference.

An additional possibility to speed-up calculations is to reduce the scaling of the computation of χ_0 via a space-time approach.

Cubic-scaling GW: BEDEFT offers the possibility to run GW calculations with a cubic-scaling thanks to a space-time approach [101, 114]. The scaling reduction of the computation of χ_0 comes from its calculation on a Real Space (RS) grid $\{\mathbf{r}_k\}$, at imaginary times $\{i\tau\}$. To better understand this method, it should be noticed that the Eq.(1.133) of the non-interacting

¹⁸ W is an even function with respect to ω , as shown by Eq.(1.124).

electron susceptibility can be rewritten thanks to the RI

$$\chi_0(\mathbf{r}_1, \mathbf{r}_2; \omega) \stackrel{\text{RI}}{\simeq} \sum_{P,Q} [\mathbf{X}_0(\omega)]_{PQ} P(\mathbf{r}_1) Q(\mathbf{r}_2), \quad (1.139)$$

with coefficients such that

$$[\mathbf{X}_0(\omega)]_{PQ} = \sum_{m,n} (f_m - f_n) \frac{\mathcal{F}_P(\phi_m^0 \phi_n^0) \mathcal{F}_Q(\phi_m^0 \phi_n^0)}{\omega - (\varepsilon_n^0 - \varepsilon_m^0) + i\eta \times \text{sgn}(\varepsilon_n^0 - \varepsilon_m^0)}. \quad (1.140)$$

The first step is to disentangle the occupied and unoccupied MOs in the weight factors $\{\mathcal{F}_P(\phi_m^0 \phi_n^0)\}$. This is done via a separable RI on an optimized RS grid $\{\mathbf{r}_k\}$ such that

$$\mathcal{F}_P(\phi_m^0 \phi_n^0) = \sum_k [\mathbf{M}]_{Pk} \phi_m^0(\mathbf{r}_k) \phi_n^0(\mathbf{r}_k), \quad (1.141)$$

where the matrix \mathbf{M} , of coefficients $\{[\mathbf{M}]_{Pk}\}$, is computed via a least-square problem, with $\mathcal{O}(N^3)$ operations [114]. This leads to

$$[\mathbf{X}_0(\omega)]_{PQ} = \sum_{k,k'} [\mathbf{M}]_{Pk} \chi_0(\mathbf{r}_k, \mathbf{r}_{k'}; \omega) [\mathbf{M}]_{Qk'}. \quad (1.142)$$

As explained before, in practice χ_0 needs to be evaluated only on the imaginary axis. Thus, using the Laplace transform [115, 116]

$$\frac{1}{i\omega - (\varepsilon_a^0 - \varepsilon_i^0)} - \frac{1}{i\omega + (\varepsilon_a^0 - \varepsilon_i^0)} = -2 \int_0^{+\infty} d\tau \cos(\omega\tau) e^{-(\varepsilon_a^0 - \varepsilon_i^0)\tau} \quad (1.143)$$

where a/i index unoccupied/occupied states, respectively, this leads to the computation of χ_0 in imaginary time, such that

$$\chi_0(\mathbf{r}_k, \mathbf{r}_{k'}; i\tau) = 2G^<(\mathbf{r}_k, \mathbf{r}_{k'}; i\tau) G^>(\mathbf{r}_{k'}, \mathbf{r}_k; -i\tau). \quad (1.144)$$

These propagators $G^<$ and $G^>$ are given by [114]

$$G^<(\mathbf{r}_k, \mathbf{r}_{k'}; i\tau) = i \sum_i^{\text{occ}} \phi_i^0(\mathbf{r}_k) \phi_i^0(\mathbf{r}_{k'}) e^{(\varepsilon_i^0 - \mu)\tau} \quad (1.145a)$$

$$G^>(\mathbf{r}_{k'}, \mathbf{r}_k; -i\tau) = -i \sum_a^{\text{unocc}} \phi_a^0(\mathbf{r}_{k'}) \phi_a^0(\mathbf{r}_k) e^{-(\varepsilon_a^0 - \mu)\tau} \quad (1.145b)$$

with $\tau > 0$ and μ the chemical potential¹⁹. Occupied and unoccupied MOs are thus totally disentangled. The RS grid scaling as $\mathcal{O}(N)$, the required $G^<(i\tau)$ and $G^>(-i\tau)$ can be computed with $\mathcal{O}(N^3)$ operations, as well as $\chi_0(i\tau)$ of Eq.(1.144). Finally, the representation of χ_0 in the auxiliary basis set, given by Eq.(1.142), can also be computed with $\mathcal{O}(N^3)$ operations thanks to matrix products and integral quadrature.

Such an approach leads to an accuracy at the meV level for QP energies, with respect to a more traditional Coulomb-fitting RI-V approach [101].

Eventually, once all the different operators are calculated, one of the last step consists into solving the QP equation (1.134).

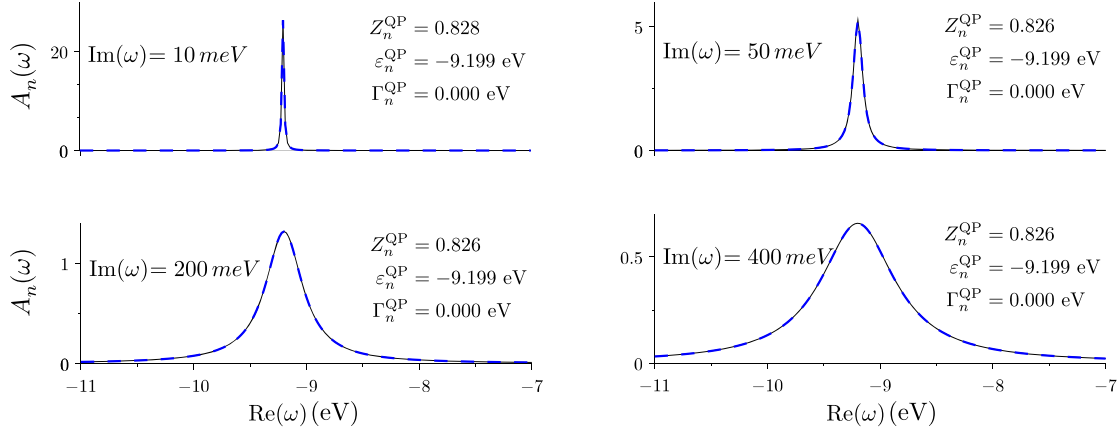


Figure 1.14: Spectral function $A_n(\omega)$ of the TCNQ molecule, for $n = \text{HOMO}$ and a G_0W_0 calculation on top of a **KS** calculation with a PBE0 functional. $A_n(\omega)$ is computed along axes parallel to the real axis, such that $\text{Im}(\omega) \in \{10, 50, 200, 400\}$ meV. The blue dashed line corresponds to the fit given by the Eq.(1.149). The **QP** energy $\varepsilon_n^{\text{QP}}$, the renormalization factor Z_n^{QP} and the lifetime Γ_n^{QP} appear as independent of the choice of the line parallel to the real axis, aiming at fitting the calculated spectral function. Graphs adapted from [78].

Solving of the Quasiparticle (QP) equation: To solve such a **QP** equation, in practice **BEDEFT** uses the diagonal part, in the **KS** basis set, of the spectral function A of Eq.(1.78) page 44. More particularly, the diagonal parts of A and $\Sigma - V_{\text{XC}}$ are defined such that

$$A_n(\omega) = \langle \phi_n^0 | A(\omega) | \phi_n^0 \rangle \quad (1.146a)$$

$$\Sigma_n(\omega) - V_{\text{XC},n} = \langle \phi_n^0 | \Sigma(\omega) - V_{\text{XC}} | \phi_n^0 \rangle. \quad (1.146b)$$

Neglecting the non-diagonal part of $\Sigma - V_{\text{XC}}$, the Eq.(1.146a) is given by

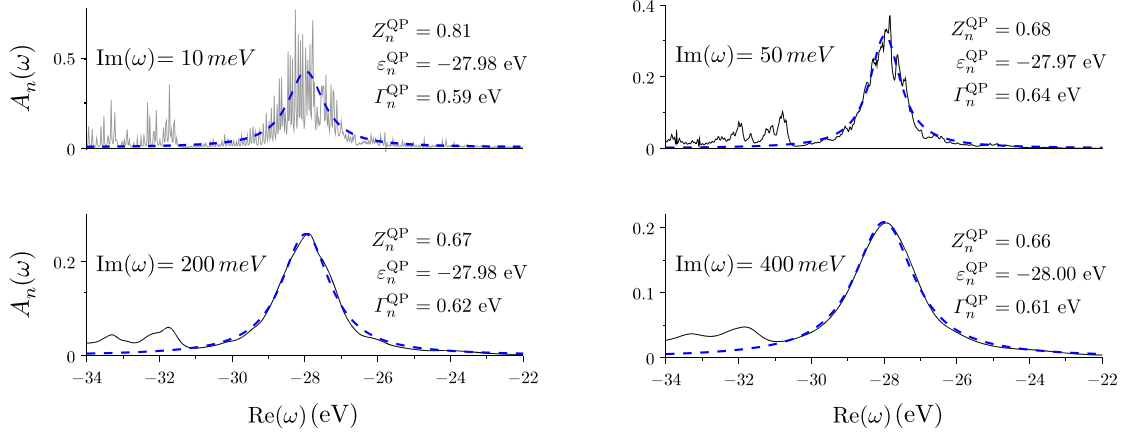
$$A_n(\omega) = \frac{1}{\pi} \left| \text{Im} \left[\frac{1}{\omega - \varepsilon_n^0 - (\Sigma_n(\omega) - V_{\text{XC},n})} \right] \right|. \quad (1.147)$$

Using the equation (1.134), and having in mind that $\Sigma_n(\omega)$ is in general complex, $A_n(\omega)$ is fitted by the following Lorentzian function [78]

$$A_n^{\text{fit}}(\omega) = \frac{1}{\pi} \left| \text{Im} \left[\frac{Z_n^{\text{QP}}}{\omega - (\varepsilon_n^{\text{QP}} + i\Gamma_n^{\text{QP}})} \right] \right| \quad \text{with} \quad (Z_n^{\text{QP}}, \varepsilon_n^{\text{QP}}, \Gamma_n^{\text{QP}}) \in \mathbb{R}^3. \quad (1.148)$$

Z_n^{QP} is the renormalization factor, $\varepsilon_n^{\text{QP}}$ the **QP** energy and Γ_n^{QP} its inverse lifetime. As seen in the definition of the spectral function (1.71) page 43, $A_n(\omega)$ is a sum of Dirac distributions. The induced broadening of A_n^{fit} , characterized by Γ_n^{QP} , can be seen as the merging of many peaks close enough in energy and centered around $\varepsilon_n^{\text{QP}}$ [14]. This latter is associated to the energy of the corresponding **QP**. The mean-field eigenstate $|\phi_n^0\rangle$ being normalized, the

¹⁹Taking the reference of the energies $\{\varepsilon_n^0\}$ at the chemical potential, or Fermi level, μ ensures convergence of Eq.(1.145) without any modification of Eq.(1.143).

Figure 1.15: Same as in FIGURE 1.14, but for $n = \text{HOMO} - 35$.

frequency integral of the exact $A_n(\omega)$ should be equal to 1 thanks to Eq.(1.73). Z_n^{QP} being equal to the integral under the Lorentzian **QP** peak, it quantifies the validity of the **QP** approximation to capture all the spectral weight. The part of $A_n(\omega)$ not described by such a **QP** peak is called the incoherent or satellite structure and can be associated to collective excitations of the system [48, 82]. At this step, it should be noticed that, contrary to the poles of the Green's function located on the real axis, the computed **QP** poles $\varepsilon_n^{\text{QP}} + i\Gamma_n^{\text{QP}}$ are complex and are no longer difference of exact eigenvalues of the $N(\pm 1)$ -body Hamiltonian [14].

In practice, $A_n^{\text{fit}}(\omega)$ is fitted along a ω axis parallel to the real axis, with a constant imaginary part $\text{Im}(\omega)$, leading to [78]

$$A_n^{\text{fit}}(\omega) = \frac{Z_n^{\text{QP}}}{\pi} \frac{|\text{Im}(\omega) - \Gamma_n^{\text{QP}}|}{\left(\text{Re}(\omega) - \varepsilon_n^{\text{QP}}\right)^2 + \left(\text{Im}(\omega) - \Gamma_n^{\text{QP}}\right)^2}. \quad (1.149)$$

The impact of the choice of $\text{Im}(\omega)$ is shown in the FIGURE 1.14, through the example of the Highest Occupied Molecular Orbital (**HOMO**) state of the TCNQ molecule.

For such a state, the **QP** peak is well-defined, with a pole separated from the others. This leads to Z_n^{QP} , $\varepsilon_n^{\text{QP}}$ and Γ_n^{QP} totally independent of the choice of $\text{Im}(\omega)$. The inverse lifetime Γ_n^{QP} vanishes, corresponding to the predicted behavior for states near the gap [78].

This influence of $\text{Im}(\omega)$ is also studied in the FIGURE 1.15, through the example of a deeper state, namely the (**HOMO** - 35)th state of the same TCNQ molecule. A small value of $\text{Im}(\omega) = 10 \text{ meV}$ leads to a huge number of peaks, each one associated with a small value of Z_n^{QP} . Increasing the value of $\text{Im}(\omega)$ leads to a better defined **QP** peak. When such a value is not too small, the 3 fitted coefficients are quite independent of this chosen imaginary part. In practice, a value of $\text{Im}(\omega) = 100 \text{ meV}$ is retained.

1.4 Objectives

Finally, I would like to conclude this chapter by providing the main objectives of this thesis. As highlighted before, the *GW* formalism is growing in popularity for the accurate description of the electronic properties of condensed matter systems in solid-state physics and more recently chemistry. Unfortunately, its application to complex systems of interest in nanosciences, chemistry, or even biology, is hampered by the large associated computing time cost, in particular in the case of disordered systems, or systems immersed in an opened environment (a solvent, a molecular medium, an electrode, etc.). Therefore, in many situations, the studied systems need to be divided into two parts, namely a subsystem of interest and its environment. In general, this latter is not described at the same quantum level as the former.

Similarly to the ideas developed in section 1.1.3.2 page 29, the Polarizable Continuum Model (PCM) [117, 118] corresponds to a quantum system embedded in a cavity described by a linear homogeneous isotropic macroscopic dielectric constant. A better model of screening inhomogeneities at short range can also be reached thanks to discrete polarizable models [119–125]. In these approaches, denoted Quantum Mechanics (QM)/Molecular Mechanics (MM), or QM/MM_{pol} to highlight the polarizable character of the environment, each atom of this latter is described by semi-empirical effective polarizable centers, such that the correct molecular polarizability tensor or the macroscopic dielectric tensor of the environment in the low frequency limit is well reproduced. The merging of the *GW* formalism with the PCM [6, 8] and discrete polarizable models [9–13] has been already tackled in our group before the beginning of this thesis.

The goal of my thesis is to go further and to focus on the development of multiscale techniques. The main objective is to merge high-level many-body treatments of the subsystem of interest, namely using the *GW* formalism, with a simplified but fully *ab initio* description of the electrostatic and dielectric environment beyond semi-empirical parameterized models.

Embedded *GW* formalism in a fully *ab initio* QM/QM' approach

Contents

Résumé	64
Summary	65
2.1 Introduction	66
2.2 Analytical developments	67
2.2.1 Fragment approach	67
2.2.2 Constrained compression of $\mathbf{X}_g^{(I)}(\omega)$	69
2.2.3 Minimization problem for $\tilde{\mathbf{X}}_g^{(I)}(\omega)$	71
2.2.4 Minimal effective polarization basis set $\{\gamma\}$	74
2.3 Application to organic molecules	75
2.3.1 Technical details	75
2.3.2 Validity of the fragment approach	77
2.3.3 Validation of the compression method for \mathbf{X}_g	78
2.3.4 Large scale environments: the C_{60} crystal and surface structures	84
2.3.5 Computational details: CPU and memory requirements	90
2.4 Conclusion	90

This chapter is largely inspired from our work published in The Journal of Chemical Physics [126].

Résumé

Ce chapitre présente une approche pour effectuer des calculs *GW* pour un sous-système quantique inclus dans un environnement polarisable discret de très grande taille, contenant des centaines de milliers d'atomes. Ce dernier est traité au niveau totalement *ab initio* de l'approximation de la phase aléatoire.

La partie 2.2 détaille les développements analytiques réalisés pour atteindre cet objectif. Ce chapitre repose sur la méthode fragment, consistant à négliger le recouvrement orbitalaire entre fonctions d'onde de différents sous-systèmes. Après une présentation de cette approche, amenant à une susceptibilité électronique non-interagissante χ_0 diagonale par blocs, nous décrivons notre méthode de compression de la taille des sous-matrices associées aux fragments de l'environnement. Cette réduction se traduit par un problème de régression de la susceptibilité électronique interagissante, en phase gaz, des différents sous-systèmes. Nous proposons une solution obtenue par minimisation sous contraintes dans laquelle les tenseurs de polarisabilité de bas ordres sont exactement conservés pour chaque fragment. Nous détaillons également notre méthode pour calculer une base de « polarisation » minimale, dans laquelle sont exprimées les différentes matrices d'intérêt. L'ensemble de ces étapes permet de réduire de façon drastique le coût de l'inversion de l'équation de Dyson associée au potentiel de Coulomb écranté W , tout en préservant la description à courte comme à longue portée des effets d'écrantage.

La partie 2.3 est dédiée à l'application de cette approche à des systèmes moléculaires organiques, dans une approche Δ COHSEX. La méthode fragment est d'abord testée via l'étude de systèmes à faible nombre de C_{60} , pour lesquels l'approximation fragment peut être abandonnée. La partie compression des matrices associées à l'environnement est validée par l'étude d'amas sphériques de fullerènes, ainsi que d'une molécule de pentacène. Ceci nous permet alors d'étudier des systèmes de grande taille, comprenant jusqu'à 202 020 atomes de carbone, en moins de 10 000 heures CPU, à un niveau de base def2-TZVP. Ces résultats, sur des systèmes de taille finie, sont alors couplés à des lois asymptotiques. Nous pouvons ainsi calculer l'énergie de polarisation associée à un C_{60} dans un cristal infini à trois dimensions, dans une surface, dans une sous-surface ainsi que dans un bloc à deux dimensions avec un nombre variable de couches.

Summary

In this chapter, we present a many-body *GW* formalism for quantum subsystems embedded in discrete polarizable environments containing up to several hundred thousand atoms. These latter are described at a fully *ab initio* random-phase approximation level.

Section 2.2 details the analytical developments done during this thesis to reach such an objective. These developments are based on a fragment approximation, consisting in neglecting the wavefunction overlap between different subsystems. After a presentation of this approach, which results into a block-diagonal independent-electron susceptibility χ_0 , we describe our compression method for the susceptibility blocks associated to fragments of the environment. Such a reduction in size is made possible thanks to a fit procedure of the interacting-electron susceptibilities, in the gas phase, of the different subsystems. Our scheme preserves exactly the low order polarizability tensors through a constrained minimization scheme, insuring the proper long-range reaction field. Our method leads to express the susceptibility associated with each fragment into a very compact minimal “polarization” basis set. This approach dramatically reduces the cost associated with inverting the Dyson equation for the screened Coulomb potential W , while preserving the description of short to long-range screening effects.

In section 2.3, such a method is applied to organic molecular systems, in a Δ COHSEX approach. The fragment approximation is tested on systems made of a few numbers of C_{60} , for which calculations without the fragment approach can be afforded. The compression scheme, for fragments in the environment, is validated through the study of spherical clusters of fullerenes, as well as a pentacene molecule. Then, we can run calculations on large scale systems, containing up to 202 020 carbon atoms, within less than 10 000 CPU hours, at the def2-TZVP level. These results, on finite size systems, are then coupled to asymptotic laws. They give access to the polarization energy associated to a C_{60} in a bulk, surface and subsurface crystals, as well as in a slab structure with varying number of layers.

2.1 Introduction

As presented in chapter 1, the *GW* formalism is particularly suited to capture the polarization effects created by an environment. Such phenomena can have a large impact on electronic energy levels, and can lead to renormalizations of some electronvolts. However, the environment can be large and complex, and can hardly be described by such an *ab initio* formalism because of large computation time and memory footprint requirements. Even if recent studies showed that *GW* calculations with cubic or even lower scaling could be achieved, [101, 127–137], such a formalism has still difficulties to capture all the dielectric, or screening, effects associated with systems containing thousands of atoms. Polarization energies converging slowly with the size of the studied system, brute force approaches are impossible for large systems. As described in section 1.4 page 62, this has led to Quantum Mechanics (QM)/Molecular Mechanics (MM) techniques. The part of interest is described at the *GW* level, while the environment can be described by a Polarizable Continuum Model (PCM) or discrete polarizable models. Yet, these approaches are based on empirical values for the macroscopic dielectric constant of the environment, or its molecular polarizability tensors.

The main objective of this chapter is to go further, and to develop a fully *ab initio* method to run embedded *GW* calculations on hundreds of thousands of atoms in the environment. Following the idea of the QM/MM approaches, we want to split our system into two parts, namely the subsystem of interest and its environment. The central subsystem is treated at the *GW* level, and the environment relies on a simpler representation, based on the fully *ab initio* Random-Phase Approximation (RPA). Such an approach is entitled QM/QM'. This chapter is devoted to the presentation of its analytical formulation, and its corresponding application to crystal of fullerenes.

More particularly, we want to calculate the Quasiparticle (QP) energies for a “central” molecule (a fullerene) surrounded by hundreds of other molecules. Calculations will be performed here at the non-self-consistent static Coulomb-Hole plus Screened-Exchange (COHSEX) level. We first adopt the fragment approximation that neglects the overlap of wavefunctions between molecules, labeled fragments. In such an approximation, the (non-self-consistent) Green’s function of the central molecule is the same as that of the isolated (gas phase) Kohn-Sham one. Further, the non-interacting susceptibility of the full system χ_0 is block-diagonal, and can be calculated with a $\mathcal{O}(N)$ scaling, with respect to total number of electrons N . However, the inversion of the Dyson equation, required to get the restriction of the screened Coulomb potential W to the central molecule of interest, remains prohibitive. This problem is bypassed by expressing the susceptibility associated with each molecule (fragment) of the environment into a very compact “polarization” basis that preserves very faithfully the restriction of W onto the central molecule of interest. The polarization energies are then calculated at the Δ COHSEX level, namely, as the variation of the static COHSEX energy levels from the gas phase to the dense environment. The impact on the polarization energies of neglecting the dynamical nature of the self-energy will be explored in the chapter 3.

2.2 Analytical developments

2.2.1 Fragment approach

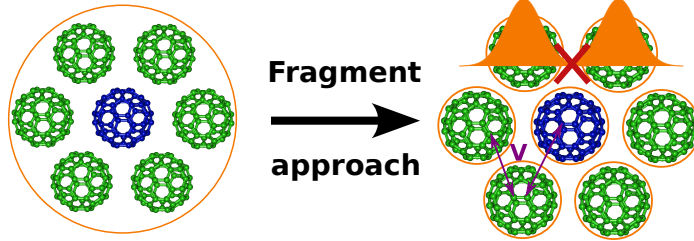


Figure 2.1: Schematic representation of the fragment approximation, where each C_{60} is considered as one fragment. Instead of considering these 7 C_{60} as one entire system, the overlap between wavefunctions of different molecules is neglected, but each fragment is still interacting with the others via the bare Coulomb potential V entering the Dyson equation for W .

As presented in section 1.3.2.10 page 56, the most expensive step of a GW calculation, for a system large enough, is the calculation of the independent-electron susceptibility χ_0 . To reduce its $\mathcal{O}(N^4)$ scaling with respect to the number of electrons N , we resort to a fragment approximation. As depicted in FIGURE 2.1, such a method consists into neglecting the wavefunction overlaps between weakly interacting subsystems. These fragment or subsystem approaches have been recently implemented at the GW and Bethe–Salpeter Equation (BSE) levels for systems based on weakly interacting subunits like molecular systems [138–143], interfaces [17, 144–146] or two-dimensional (2D) materials [147, 148].

To better understand the advantages of such an approximation, let us recall that our GW code Beyond Density-Functional Theory (BEDeFT) is based on a Resolution of the Identity (RI) formalism as presented in section 1.3.2.10. χ_0 is given by

$$\chi_0(\mathbf{r}_1, \mathbf{r}_2; \omega) \stackrel{\text{RI}}{\simeq} \sum_{P,Q} [\mathbf{X}_0(\omega)]_{PQ} P(\mathbf{r}_1) Q(\mathbf{r}_2), \quad (2.1)$$

with coefficients such that

$$[\mathbf{X}_0(\omega)]_{PQ} = \sum_{m,n} (f_m - f_n) \frac{\mathcal{F}_P(\phi_m^0 \phi_n^0) \mathcal{F}_Q(\phi_m^0 \phi_n^0)}{\omega - (\varepsilon_n^0 - \varepsilon_m^0) + i\eta \times \text{sgn}(\varepsilon_n^0 - \varepsilon_m^0)}. \quad (2.2)$$

$\mathbf{X}_0(\omega)$ is a matrix and corresponds to the representation of χ_0 in the auxiliary basis set $\{P\}$. In particular, the equation (1.136) page 57 shows that the fitting coefficients $\mathcal{F}_P(\phi_m^0 \phi_n^0)$ are null when the two Kohn-Sham (KS) Molecular Orbitals (MOs) ϕ_m^0 and ϕ_n^0 do not overlap. By hypothesis, this is the case for two MOs of two different fragments. Moreover, each product $(\phi_m^0 \phi_n^0)$ is fitted only on the auxiliary basis of its corresponding fragment. The full auxiliary basis set of the total system being the direct sum of basis sets of its subsystems, the joint contribution of two different fragments to Eq.(2.2) is equal to zero. In other words, the matrix $\mathbf{X}_0(\omega)$ is block diagonal. Its (I)th block, denoted $\mathbf{X}_0^{(I)}(\omega)$, corresponds to the gas phase,

i.e. isolated, non-interacting susceptibility of the (I)th fragment. The total non-interacting Green's function G_0 is also the sum of the gas phase non-interacting Green's functions $G_0^{(I)}$.

To understand the impact of this approach, we define $\mathbf{X}(\omega)$ the representation of the full system interacting susceptibility χ in the total auxiliary basis set, and \mathbf{V} the matrix of Coulomb interactions in the same basis set. Its coefficients are given by $[\mathbf{V}]_{PQ} = (P||Q)$, with $(\cdot||\cdot)$ a Coulomb integral. In such a basis, the (Fourier transform of the) Dyson equation (1.109) page 48 can be rewritten

$$\mathbf{X}(\omega) = \mathbf{X}_0(\omega) + \mathbf{X}_0(\omega)\mathbf{V}\mathbf{X}(\omega). \quad (2.3)$$

Labeling $\mathbf{V}^{(IJ)}$ the matrix equal to Coulomb interactions between the auxiliary basis sets of fragment (I) and (J), and zero otherwise, this equation is equivalent to

$$\mathbf{X}(\omega)^{-1} = \mathbf{X}_0(\omega)^{-1} - \sum_{I,J} \mathbf{V}^{(IJ)}. \quad (2.4)$$

Let $\mathbf{X}_g(\omega)$ be the block-diagonal matrix such that its (I)th block is equal to $\mathbf{X}_g^{(I)}(\omega)$, namely the gas phase (isolated) **interacting** susceptibility of the (I)th fragment. Such a block is given by

$$\mathbf{X}_g^{(I)}(\omega)^{-1} = \mathbf{X}_0^{(I)}(\omega)^{-1} - \mathbf{V}^{(I)}, \quad (2.5)$$

with $\mathbf{V}^{(I)}$ the matrix of the Coulomb interactions in the auxiliary basis set of the (I)th fragment. Thus, the equation (2.4) can be rewritten

$$\mathbf{X}(\omega)^{-1} = \mathbf{X}_g(\omega)^{-1} - \sum_{I \neq J} \mathbf{V}^{(IJ)}, \quad (2.6)$$

where only the off-diagonal Coulomb blocks $\mathbf{V}^{(IJ)}$, with $I \neq J$, appear explicitly. The Coulomb interactions inside each fragment are already taken into account, in the diagonal blocks of the gas phase interacting susceptibility $\mathbf{X}_g(\omega)$.

In such a fragment approximation, calculating all the diagonal blocks $\mathbf{X}_0^{(I)}(\omega)$, or equivalently all the $\mathbf{X}_g^{(I)}(\omega)$ blocks, scales as $\mathcal{O}(N)$. In other words, such a step scales linearly with respect to the total number of fragments. This represents an important saving with respect to the initial $\mathcal{O}(N^4)$ scaling. The bottleneck becomes now the inversion of the Dyson equation (2.6) with its $\mathcal{O}(N^3)$ scaling. Indeed, such an equation can be rewritten

$$\mathbf{X}(\omega) = \mathbf{X}_g(\omega) + \mathbf{X}_g(\omega)\mathbf{V}^{\text{off}}\mathbf{X}(\omega), \quad (2.7)$$

with \mathbf{V}^{off} a dense matrix whose diagonal blocks are null, such that

$$\mathbf{V}^{\text{off}} = \sum_{I \neq J} \mathbf{V}^{(IJ)}. \quad (2.8)$$

Due to the off-diagonal blocks $\mathbf{V}^{(I \neq J)}$, the full interacting susceptibility $\mathbf{X}(\omega)$, as well as the corresponding screened Coulomb potential matrix $\mathbf{W}(\omega) = \mathbf{V} + \mathbf{V}\mathbf{X}(\omega)\mathbf{V}$, are not block-diagonal. Therefore, their calculations, for large systems, require large memory footprints and computation times. As such, the largest fragment-based *GW* calculations done until

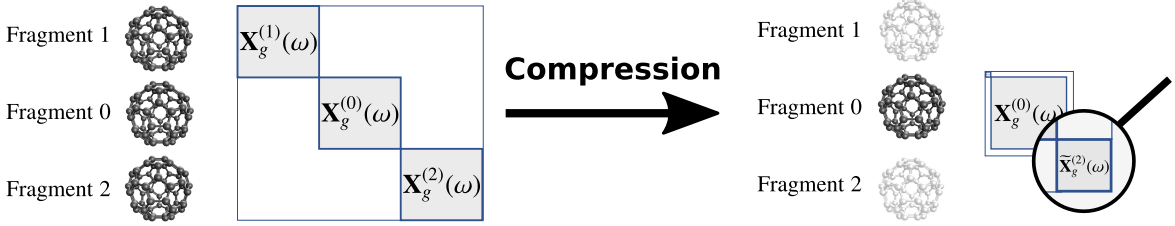


Figure 2.2: (Left): Symbolic representation of the fragment approach, through the total gas phase block-diagonal interacting susceptibility $\mathbf{X}_g(\omega)$. (Right): Representation of the same matrix, but after compression of the diagonal blocks associated with fragments in the environment, namely the shaded C_{60} . The block associated to the fragment of interest ($I = 0$) is not compressed, and keeps the same size as before.

now, to the best of our knowledge, was done on 595 benzene molecules (3570 non-hydrogen atoms) in the case of molecular systems [140].

To tackle such a problem, and to be able to study bigger systems, we have developed an algorithm to optimally reduce the size of each diagonal block $\mathbf{X}_g^{(I)}(\omega)$, and therefore the final size of the matrices to invert.

2.2.2 Constrained compression of $\mathbf{X}_g^{(I)}(\omega)$

To give some orders of magnitude of the current problem, it should be noticed that the def2-TZVP-RI auxiliary basis set, associated to the triple-zeta def2-TZVP basis set, is composed of 95 orbitals for atoms like B, C, N or O. Such a dimension leads for environment of the order of 10^5 atoms, which is the targeted size during this thesis, to matrices \mathbf{X} or \mathbf{W} of the order of 10^7 in size. Using double precision, such matrices would need of the order of a petabyte of memory to be stored, which is currently nearly inaccessible. Thus, we have developed new methods to reduce the size of the matrices of interest.

More particularly, for the fragment of interest whose we want to compute its GW QP energies, we keep its full auxiliary basis set. However, for the other fragments of the environment, we would like to reproduce as best as possible their meaningful physical effects. Namely, we want to conserve their contribution to the screening potential $W_{\text{scr}} = V\chi V$ corresponding to the induced dipoles, quadrupoles, etc., in response to a charged excitation of the system of interest. **In other words, what we want to calculate is the restriction of \mathbf{W} to the central fragment of interest, not the full details of this matrix onto the fragments in the environment.** This may be done without the full details of the susceptibility of these latter, in their auxiliary basis sets $\{P\}$. Therefore, we search for a compact representation of their gas phase interacting susceptibility $\chi_g^{(I)}(\omega)$, leading to a total gas phase interacting susceptibility $\mathbf{X}_g(\omega)$ as represented in FIGURE 2.2. In other words, for each fragment (I) of the environment, we look for a lower-rank approximation $\tilde{\chi}_g^{(I)}(\omega)$ to

$\chi_g^{(I)}(\omega)$, namely a model susceptibility, such that

$$\chi_g^{(I)}(\mathbf{r}_1, \mathbf{r}_2; \omega) \stackrel{\text{RI}}{\simeq} \sum_{P,Q} [\mathbf{X}_g^{(I)}(\omega)]_{PQ} P(\mathbf{r}_1)Q(\mathbf{r}_2) \quad (2.9)$$

$$\stackrel{\text{MODEL}}{\simeq} \tilde{\chi}_g^{(I)}(\mathbf{r}_1, \mathbf{r}_2; \omega) = \sum_{\gamma, \gamma'} [\tilde{\mathbf{X}}_g^{(I)}(\omega)]_{\gamma\gamma'} \gamma(\mathbf{r}_1)\gamma'(\mathbf{r}_2). \quad (2.10)$$

Following previous models of induced charges and dipoles of QM/MM techniques [149], the small polarization basis set $\{\gamma\}$ could be a minimal Gaussian (sp^3) four-orbitals basis per atom. However, we have decided to set up a more automated way to compute such a basis, as explained in section 2.2.4 page 74.

Once the polarization basis $\{\gamma\}$ is given, we compute the coefficients of the model susceptibility $\tilde{\mathbf{X}}_g^{(I)}(\omega)$ via a minimization problem. Denoting $\tilde{\mathbf{X}}_m^{(I)}(\omega)$ the matrix of minimization variables for a given isolated fragment (I), the error on its gas phase interacting susceptibility is given by

$$\Delta\chi_g^{(I)}(\mathbf{r}_1, \mathbf{r}_2; \omega) = \sum_{\gamma, \gamma'} [\tilde{\mathbf{X}}_m^{(I)}(\omega)]_{\gamma\gamma'} \gamma(\mathbf{r}_1)\gamma'(\mathbf{r}_2) - \sum_{P,Q} [\mathbf{X}_g^{(I)}(\omega)]_{PQ} P(\mathbf{r}_1)Q(\mathbf{r}_2), \quad (2.11)$$

which is associated to the following error on the screening potential

$$\Delta W_{\text{scr}}^{(I)}(\mathbf{r}_1, \mathbf{r}_2; \omega) = \int d\mathbf{r}_3 d\mathbf{r}_4 V(\mathbf{r}_1, \mathbf{r}_3) \Delta\chi_g^{(I)}(\mathbf{r}_3, \mathbf{r}_4; \omega) V(\mathbf{r}_4, \mathbf{r}_2). \quad (2.12)$$

The required matrix $\tilde{\mathbf{X}}_g^{(I)}(\omega)$ minimizes such an error through a basis set of test functions $\{t\}$, via the following equation

$$\tilde{\mathbf{X}}_g^{(I)}(\omega) = \underset{\left\{ [\tilde{\mathbf{X}}_m^{(I)}(\omega)]_{\gamma\gamma'} \right\}}{\text{argmin}} \sum_{t, t'} \left| \langle t | \Delta W_{\text{scr}}^{(I)}(\omega) | t' \rangle \right|^2. \quad (2.13)$$

Since this error on the screening potential is measured on a basis set of test functions, we can design this latter to specifically probe some characteristics of $W_{\text{scr}}^{(I)}(\omega)$ we would like to preserve.

Our first attempt was to take, for each fragment (I), its test basis set $\{t\}$ equal to its auxiliary basis set $\{P\}$. However, this choice leads to rather poor results, as detailed in section 2.3 page 75. Indeed, such a model susceptibility $\tilde{\mathbf{X}}_g^{(I)}(\omega)$ is not designed to perform a *GW* calculation directly on the fragment (I) itself. As shown by Eq.(2.6) or Eq.(2.7), such a block aims at computing the total interacting susceptibility $\mathbf{X}(\omega)$ which couples all fragments, to perform, in the end, a *GW* calculation only on the fragment of interest ($I = 0$). As such, the fit of $\tilde{\mathbf{X}}_g^{(I)}(\omega)$ should reproduce, as best as possible, the effects of the fragment (I) on the other ones. This should be done for its nearest neighbors up to those at long-range, for which interactions are dominated by low order momenta of its polarizability tensor.

To set up a simple method, we have decided to keep the test basis set $\{t\}$ localized on atoms of the fragment (I) for which we compute its model susceptibility. This enables a compression of its susceptibility $\mathbf{X}_g^{(I)}(\omega)$ independent of the reduction for the other fragments.

The test basis set $\{t\}$ is designed to probe the effects of the reference susceptibility at short to middle range. To achieve this goal, we develop test sets uniformly sampling the Coulomb interaction. Starting from a set of functions $\{t_0\}$, we orthonormalize it with respect to the Coulomb norm, leading to the test basis $\{t_1\}$. Namely, writing \mathbf{V}_0 the Coulomb matrix such that its coefficients are equal to $(t_0||t'_0)$, the i^{th} vector's coordinates of $\{t_1\}$, in the basis set $\{t_0\}$, is given by the i^{th} column of $\mathbf{V}_0^{-1/2}$. This basis set is such that $(t_1||t'_1) = \delta_{t_1,t'_1}$, with δ_{t_1,t'_1} the Kronecker delta. Two of such sets are created:

- (i) one spanning the auxiliary basis set, namely such that $\{t_0\} = \{P\}$;
- (ii) another one $\{t_1^d\}$, based on a set of diffuse orbitals $\{t_0^d\}$. They aim at probing the effects of the screening potential $W_{\text{scr}}^{(\text{I})}(\omega)$ in the vicinity of the fragment (I), where other fragments of the environment¹ should be located. The basis set $\{t_0^d\}$ consists of atom-centered (s,p,d,f,g) diffuse Gaussian orbitals with, for sake of simplicity, the same $e^{-\zeta r^2}$ radial part.

The final test basis set $\{t\}$ is the direct sum of $\{t_1\}$ and $\{t_1^d\}$. The first set is down-weighted with respect to the second one, by a factor 1/50, to strengthen the influence of the diffuse functions during the compression fitting process.

Moreover, to preserve the long-range interactions created by a given fragment (I), we enforce low order Cartesian momenta of the interacting susceptibility via exact constraints of the type

$$\langle x^m y^n z^p | \Delta \chi_g^{(\text{I})}(\omega) | x'^m y'^n z'^p \rangle = \int d\mathbf{r} d\mathbf{r}' x^m y^n z^p \Delta \chi_g^{(\text{I})}(\mathbf{r}, \mathbf{r}'; \omega) x'^m y'^n z'^p = 0. \quad (2.14)$$

We denote l_{max} the maximal order $m+n+p$ and $m'+n'+p'$ enforced for a specific fragment. For example, the choice $l_{\text{max}} = 1$ leads to the preservation of the fragment neutral monopole, as well its dipolar polarizability tensor. Along with the adding of diffuse functions in the test basis set, such a constraint should ensure an accurate reproduction of the screening potential $W_{\text{scr}}^{(\text{I})}(\omega)$ in the vicinity of the considered fragment, as well as at long-range.

At this step, I had to derive equations to solve the minimization problem Eq.(2.13).

2.2.3 Minimization problem for $\widetilde{\mathbf{X}}_g^{(\text{I})}(\omega)$

This subsection is devoted to the computation of the model susceptibility $\widetilde{\mathbf{X}}_g^{(\text{I})}(\omega)$ solution of the equation (2.13), under constraints of type (2.14). From now on and for compactness, I drop the exponent (I) because I focus only on one fragment, and the frequency index ω . Results can be computed separately for each required frequency.

Let \mathbf{B} be the Coulomb matrix between the auxiliary basis and the test basis, such that its coefficients are $(P||t)$, where $(\cdot||\cdot)$ indicates a Coulomb integral. Let $\mathbf{\Gamma}$ be the Coulomb matrix between the polarization basis and the test basis, with coefficients $(\gamma||t)$, and \mathbf{E} (respectively \mathbf{R}) the overlap matrix between the auxiliary basis set (respectively the polarization basis

¹I recall that the compression for the fragment (I) is done independently of any other fragment (J). Everything happens as if these latter did not exist.

set) and the constraint basis, with coefficients $\langle P|x^m y^n z^p\rangle$ (respectively $\langle \gamma|x^m y^n z^p\rangle$). The equation (2.13) can be reformulated as

$$\tilde{\mathbf{X}}_g = \underset{\tilde{\mathbf{X}}_m}{\operatorname{argmin}} \left\| \mathbf{B}^\dagger \mathbf{X}_g \mathbf{B} - \mathbf{\Gamma}^\dagger \tilde{\mathbf{X}}_m \mathbf{\Gamma} \right\|^2, \quad (2.15)$$

with $\|\cdot\|$ the Frobenius norm, such that $\|\mathbf{A}\|^2 = \operatorname{Tr}(\mathbf{A}^\dagger \mathbf{A})$, with $\operatorname{Tr}(\mathbf{A})$ denoting the trace of the matrix \mathbf{A} . Such a minimization is performed under the constraints of Eq.(2.14), which can be rewritten

$$\mathbf{R}^\dagger \tilde{\mathbf{X}}_m \mathbf{R} = \mathbf{E}^\dagger \mathbf{X}_g \mathbf{E}. \quad (2.16)$$

Such a $N_\gamma \times N_\gamma$ matrix² $\tilde{\mathbf{X}}_g$ is computed via feasible solutions, namely matrices satisfying all constraints enforced by the equation (2.16). Then, among all such feasible solutions, we compute the optimal one, which minimizes Eq.(2.15).

To go further, one should introduce the Singular Value Decomposition (SVD) of matrices [150]. Namely, for a given matrix \mathbf{M} of size $m \times n$, and of rank r , its SVD is a factorization of the type

$$\mathbf{M} = \mathbf{U}_M \mathbf{\Sigma}_M \mathbf{V}_M^\dagger, \quad (2.17)$$

where \mathbf{U}_M and \mathbf{V}_M are $m \times m$ and $n \times n$, respectively, complex³ unitary matrices. $\mathbf{\Sigma}_M$ is a $m \times n$ rectangular diagonal matrix with real and positive values on its diagonal. Such diagonal elements $\sigma_i^M = [\mathbf{\Sigma}_M]_{ii}$ are called the singular values, and the number of strictly positive value is equal to the rank r of \mathbf{M} . They are ordered such that $\sigma_1^M \geq \sigma_2^M \geq \dots \geq \sigma_r^M > 0$. The compact SVD is a variant, where only the r first columns of \mathbf{U}_M and \mathbf{V}_M are kept. $\mathbf{\Sigma}_M$ becomes a $r \times r$ invertible square matrix, containing only the strictly non-negative singular values. Such a SVD also leads to the definition of the pseudo inverse \mathbf{M}^\oplus of the matrix \mathbf{M} , such that

$$\mathbf{M}^\oplus = \mathbf{V}_M \mathbf{\Sigma}_M^\oplus \mathbf{U}_M^\dagger, \quad (2.18)$$

where $\mathbf{\Sigma}_M^\oplus$ is a diagonal $n \times m$ real rectangular matrix such that

$$[\mathbf{\Sigma}_M^\oplus]_{ii} = \begin{cases} \frac{1}{\sigma_i^M} & \text{if } \sigma_i^M > 0 \\ 0 & \text{if } \sigma_i^M = 0. \end{cases} \quad (2.19)$$

Concerning the initial problem of constrained minimization, one can define, for the sake of compactness, the two following matrices $\mathbf{O} = \mathbf{E}^\dagger \mathbf{X}_g \mathbf{E}$ and $\mathbf{Z} = \mathbf{B}^\dagger \mathbf{X}_g \mathbf{B}$. Assuming that the rank of \mathbf{R} is equal to the number of constraints N_{cstr} ⁴, the compact SVD of $\mathbf{R} = \mathbf{U}_R \mathbf{\Sigma}_R \mathbf{V}_R^\dagger$ is such that \mathbf{V}_R^\dagger and $\mathbf{\Sigma}_R$ are invertible. The equation (2.16) becomes equivalent to

$$\mathbf{U}_R^\dagger \tilde{\mathbf{X}}_m \mathbf{U}_R = \mathbf{\Sigma}_R^{-1} \mathbf{V}_R^\dagger \mathbf{O} \mathbf{V}_R \mathbf{\Sigma}_R^{-1}. \quad (2.20)$$

²In equations (2.15) and (2.16), matrices \mathbf{B} , $\mathbf{\Gamma}$, \mathbf{R} and \mathbf{E} are real because in finite size system, without magnetic field, MOs can be taken to be real. So the computation of $\tilde{\mathbf{X}}_g$ can be reduced to two identical and independent problems of minimization under constraints, namely on one side its real part, and on the other side its imaginary part. In the following paragraphs of this chapter, for the sake of simplicity and compactness, \mathbf{X} matrices (with different subscripts and superscripts) are an abbreviation for their real or imaginary parts.

³Unless explicitly mentioned, we restrict ourselves only to real matrices \mathbf{M} , and therefore also to real orthogonal matrices \mathbf{U}_M and \mathbf{V}_M .

⁴In practice, $N_{\text{cstr}} \leq 10$ while $N_\gamma \geq 60$ and the basis sets are such that this hypothesis is valid.

Inverting the rectangular matrix \mathbf{U}_R requires considering the nullspace of \mathbf{U}_R^\dagger , of which we write an orthonormal basis as the columns of the $N_\gamma \times (N_\gamma - N_{\text{cstr}})$ matrix \mathbf{K} such that $\mathbf{U}_R^\dagger \mathbf{K} = \mathbf{0}$. Under these considerations, $\tilde{\mathbf{X}}_m$ has the form

$$\tilde{\mathbf{X}}_m = \mathbf{U}_R \Sigma_R^{-1} \mathbf{V}_R^\dagger \mathbf{O} \mathbf{V}_R \Sigma_R^{-1} \mathbf{U}_R^\dagger + \mathbf{K} \mathbf{M}_1 + \mathbf{M}_2 \mathbf{K}^\dagger, \quad (2.21)$$

where \mathbf{M}_1 and \mathbf{M}_2 are unknown matrices. So far, there are some redundancies in the \mathbf{M}_1 and \mathbf{M}_2 terms which can be lifted by projection on \mathbf{U}_R and \mathbf{K} orthogonal supplementary subspaces. At the end, defining $\mathbf{C} = \Sigma_R^{-1} \mathbf{V}_R^\dagger \mathbf{O} \mathbf{V}_R \Sigma_R^{-1}$, and using the fact that both \mathbf{O} and \mathbf{Z} are symmetric, Eq.(2.21) becomes

$$\tilde{\mathbf{X}}_m = \mathbf{U}_R \mathbf{C} \mathbf{U}_R^\dagger + \mathbf{K} \mathbf{A}_1 \mathbf{K}^\dagger + \mathbf{U}_R \mathbf{A}_2 \mathbf{K}^\dagger + \mathbf{K} \mathbf{A}_2^\dagger \mathbf{U}_R^\dagger, \quad (2.22)$$

where \mathbf{A}_1 and \mathbf{A}_2 are computed via the equation (2.15). Assuming a symmetric $\tilde{\mathbf{X}}_m$ leads to $\mathbf{A}_1^\dagger = \mathbf{A}_1$.

Such a minimization problem (2.15) can be solved thanks to methods of matrix calculus, and more particularly the derivative of the trace function with respect to a matrix. For a given scalar function f such that

$$\begin{aligned} f : \mathbb{R}^{m \times n} &\longrightarrow \mathbb{C} \\ \mathbf{X} &\longmapsto f(\mathbf{X}), \end{aligned} \quad (2.23)$$

namely a complex-valued function taking as argument a real matrix, its derivative with respect to \mathbf{X} is a $m \times n$ complex matrix such that its coefficients (i, j) is given by [151]

$$\left[\frac{\partial f}{\partial \mathbf{X}} \right]_{ij} = \frac{\partial f}{\partial ([\mathbf{X}]_{ij})}. \quad (2.24)$$

Defining $\mathbf{H}(\mathbf{A}_1, \mathbf{A}_2) = (\mathbf{Z} - \Gamma^\dagger \tilde{\mathbf{X}}_m \Gamma)^\dagger (\mathbf{Z} - \Gamma^\dagger \tilde{\mathbf{X}}_m \Gamma)$, where $\tilde{\mathbf{X}}_m$ is given by Eq.(2.22), and extending the definition (2.24) to a scalar function of two matrices, the equation (2.15) leads to derivative conditions

$$\frac{\partial \text{Tr}(\mathbf{H}(\mathbf{A}_1, \mathbf{A}_2))}{\partial \mathbf{A}_1} = \mathbf{0} \quad (2.25a)$$

$$\frac{\partial \text{Tr}(\mathbf{H}(\mathbf{A}_1, \mathbf{A}_2))}{\partial \mathbf{A}_2} = \mathbf{0} \quad (2.25b)$$

I derive in appendix A.1 page 157 the solutions to this problem, leading to an optimal solution $\tilde{\mathbf{X}}_g$. Defining the matrices \mathbf{P} such that $\mathbf{P} = (\mathbf{K}^\dagger \Gamma)^\oplus \mathbf{K}^\dagger$, and \mathbf{L} such that $\mathbf{L} = \mathbf{R}^\oplus [\mathbf{I}_{N_\gamma} - \Gamma \mathbf{P}]$, where \mathbf{I}_{N_γ} is the identity matrix of size N_γ , such an optimal solution is given by

$$\tilde{\mathbf{X}}_g = \mathbf{L}^\dagger \mathbf{O} \mathbf{L} + \mathbf{P}^\dagger \mathbf{Z} \Gamma^\oplus + (\Gamma^\oplus)^\dagger \mathbf{Z} \mathbf{P} - \mathbf{P}^\dagger \mathbf{Z} \mathbf{P}. \quad (2.26)$$

The particular situation where no constraints are enforced is equivalent to the case where $\mathbf{R} = \mathbf{0}$, $\mathbf{L} = \mathbf{0}$, $\mathbf{K} = \mathbf{I}_{N_\gamma}$ and $\mathbf{P} = \Gamma^\oplus$. The formula (2.26) simplifies thus into

$$\tilde{\mathbf{X}}_g = (\Gamma^\oplus)^\dagger \mathbf{Z} \Gamma^\oplus. \quad (2.27)$$

After having derived the formula (2.26), I have also implemented this constrained minimization procedure into our code `BEDEFT`. I had to understand the structure of this massively-parallel code, which follows the object-oriented paradigm, and then to develop new attributes and methods. I developed new routines, from methods for the user-interface to choose different parameters, to implementation of the formula (2.26) via linear algebra methods essentially based on the Scalable Linear Algebra PACKage (`ScaLAPACK`) library [152], by way of methods dedicated to the creation and storage of the different involved basis sets, matrices. . .

So far, the choice of the polarization basis set $\{\gamma\}$ has been left arbitrary. Contrary to the induced charge-and-dipole models used in semi-empirical QM/MM techniques, we follow here a more automated route, as detailed in the following subsection.

2.2.4 Minimal effective polarization basis set $\{\gamma\}$

We have decided to compute the polarization basis set by a generalized minimization process, that is we include $\{\gamma\}$ in the minimization problem via

$$\{\gamma\} = \operatorname{argmin}_{\{\gamma_m\}} \left(\min_{\left\{ \left[\tilde{\mathbf{x}}_m^{(I)}(\omega) \right]_{\gamma_m \gamma'_m} \right\}} \sum_{t,t'} \left| \langle t | \Delta W_{\text{scr}}^{(I)}(\omega) | t' \rangle \right|^2 \right). \quad (2.28)$$

In practice, the γ functions are expressed in the auxiliary basis set $\{P\}$ associated with fragment (I), namely

$$\gamma(\mathbf{r}) = \sum_P C_{\gamma P} P(\mathbf{r}). \quad (2.29)$$

The $\{C_{\gamma P}\}$ coefficients are now the minimization variables. In practice, the only input choice is now the number N_γ of $\gamma(\mathbf{r})$ polarization vectors. It should be noticed that formally, setting N_γ to the dimension of the original auxiliary basis set leads to a model susceptibility $\tilde{\mathbf{X}}_g(\omega)$ strictly equal to the reference $\mathbf{X}_g(\omega)$. Such an equality holds independently of the choice of the test basis or the constraints. This somewhat complex minimization problem is tackled by iterating over two distinct steps:

- (i) inner optimization of the $\tilde{\mathbf{X}}_g^{(I)}(\omega)$ matrix elements at fixed $\{\gamma\}$ via Eq.(2.13), which is solved exactly through linear algebra;
- (ii) outer optimization of the $\{C_{\gamma P}\}$ coefficients at fixed $\tilde{\mathbf{X}}_g^{(I)}(\omega)$ matrix elements which is done using gradient descent techniques.

More details about this last step are given in appendix A.2 page 159.

In the simplest case where test functions $\{t\}$ only span the auxiliary basis set $\{P\}$, and in the absence of constraint, the Eckart–Young–Mirsky theorem states that the N_γ optimal $\{\gamma\}$ polarization vectors are similar to those defined in references [153, 154], namely the leading eigenvectors of the so-called symmetrized susceptibility. The present minimization formulation allows further flexibility with the introduction of test functions and constraints,

allowing on-the-fly design of model dielectric functions for specific purposes, emphasizing short-to-long-range or on-site accuracy.

To conclude this section about the fragment approach and its diverse developments, it should be noticed that the operations described above (calculations of the reference $\mathbf{X}_g^{(I)}(\omega)$ and the compressed $\tilde{\mathbf{X}}_g^{(I)}(\omega)$ matrices, SVD decomposition of related matrices, etc.) are performed on isolated fragments. This leads to a computational cost that is linear in the number of distinct fragments. In turn, the number of operations related to inverting the Dyson equation (2.7) for the total interacting susceptibility $\mathbf{X}(\omega)$, involving interactions between all fragments, keeps the same cubic scaling $\mathcal{O}(N^3)$ but its associated prefactor is dramatically reduced. As shown in section 2.3, the optimal polarization basis can be made typically 10^2 times smaller than the original auxiliary basis set while preserving the polarization energy in the meV range. This leads to a reduction of the order of 10^6 of the cost associated with obtaining an accurate screened Coulomb potential \mathbf{W} on the central fragment ($I = 0$).

2.3 Application to organic molecules

To validate and to use the different methods presented in section 2.2, I have studied structures of C_{60} , as well as a pentacene molecule.

2.3.1 Technical details

As detailed in section 1.3.2.9 page 54, a Kohn-Sham (KS)-Density-Functional Theory (DFT) calculation is required as a starting point for a GW one. Here, input KS eigenstates are generated at the def2-TZVP PBE0 [45, 46] level with the ORCA package [57, 58]. We adopt the corresponding def2-TZVP-RI auxiliary basis sets associated with the Coulomb-fitting Resolution of the Identity (RI-V) approach [104, 106]. The molecular geometries for the C_{60} and the pentacene are obtained at the def2-TZVP PBE0 level. The Face-Centered Cubic (FCC) C_{60} dense phase is constructed taking experimental lattice parameters [155] ($a_0 = 14.17 \text{ \AA}$), neglecting orientational disorder. The considered C_{60} surface is the (111) one.

In this chapter, all polarization energies P_n are computed at the static COHSEX level, as presented in section 1.3.2.8 page 53. Following previous studies [10, 11, 138–141], such a polarization energy P_n , for a given energy level n , is taken to be the difference between the static COHSEX energy level in the presence of a polarizable environment and its analog in the gas phase, namely:

$$P_n = \varepsilon_n^{GW_e} - \varepsilon_n^{GW_g} \simeq \underbrace{\varepsilon_n^{\text{COHSEX}_e} - \varepsilon_n^{\text{COHSEX}_g}}_{=P_n^{\Delta\text{COHSEX}}}, \quad (2.30)$$

where the index (e) and (g) in $GW_{e/g}$ and $\text{COHSEX}_{e/g}$ stand for embedded (e) and gas (g) phases, respectively. Since only the static susceptibility needs to be calculated, it is one order of magnitude cheaper than a fully dynamical GW approach. Indeed, this latter requires the calculation of $n_\omega \simeq 12$ independent-electron $\chi_0(i\omega)$ susceptibilities along the imaginary axis in our Analytic Continuation (AC) scheme, as explained in section 1.3.2.10. The accuracy of using such a static limit for the polarization energies induced by a neighboring dielectric

medium was first analyzed in the case of molecules close to a metallic substrate [17]. Such an approximation, that considers only the low-frequency limit of the environment electronic dielectric response, is consistent with standard PCM implementations. In these latter, the macroscopic dielectric constant originating from electronic degrees of freedom is taken to be the optical one in the low frequency limit (square of the refractive index). Similarly, in standard QM/MM implementations, the semi-empirical atomic polarizabilities are designed to reproduce the fragment electronic polarizability in the static limit [149]. Extension to dynamical reaction fields will be discussed in chapter 3 page 93.

From the knowledge of such a polarization energy P_n , calculated at the static Δ COHSEX level, the absolute Quasiparticle (QP) energy can be obtained as

$$\varepsilon_n^{GW_e} \simeq \varepsilon_n^{GW_g} + P_n^{\Delta\text{COHSEX}}. \quad (2.31)$$

In the fragment approximation, and in the absence of wavefunction hybridization, such a value yields the energy of the corresponding band center. The band dispersion, represented by the continuous Density Of States (DOS) in FIGURE 2.3, originates from wavefunction hybridization between fragments, and therefore cannot be accounted for. In particular, one

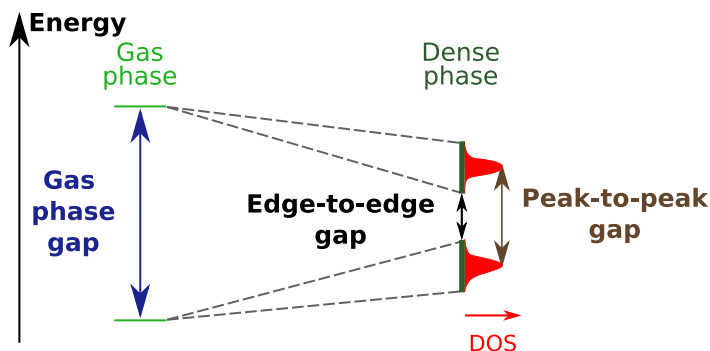


Figure 2.3: Schematic representation of the closing of the fundamental gap, from gas phase to dense phase. The Density Of States (DOS), in red, represents the broadening of the discrete energy levels and the creation of bands. In dense phase, two types of gaps can be defined. The edge-to-edge gap (in black) is computed between the bottom of the Lowest Unoccupied Molecular Orbital (LUMO) band and the top of the Highest Occupied Molecular Orbital (HOMO) band, while the peak-to-peak gap (in brown) is computed between the two maxima of the DOS of these two bands.

can recover the experimental peak-to-peak gap in the dense phase, namely the difference of energy between the HOMO and LUMO band centers, as represented in FIGURE 2.3. In the following, when needed, the gas phase $\varepsilon_n^{GW_g}$ QP energies will be calculated at the partially self-consistent evGW level (see section 1.3.2.9), which we label evGW@PBE0 to highlight the choice of the DFT exchange-correlation functional. Such an approach has been shown [92, 98] to be more accurate than non-self-consistent calculations, unless an optimally tuned functional is used for the starting KS-DFT calculation [98, 156].

Finally, it should be noticed that in the fragment approximation, the total non-interacting Green's function G_0 is the sum, over all the fragments (I), of the gas phase non-interacting

Green’s functions $G_0^{(I)}$. Thus, each fragment (I) possesses its own QP states associated to localized wavefunctions $\{\phi_n^{(I)}(\mathbf{r})\}$, although the renormalization of the corresponding QP energies take into account effects of the environment, namely of the other fragments. In other words, while the interacting susceptibility matrix $\mathbf{X}(\omega = 0)$ of Eq.(2.7) is defined and computed for the full system, only the diagonal blocks of the static screened Coulomb potential matrix $\mathbf{W}(\omega = 0) = \mathbf{V} + \mathbf{V}\mathbf{X}(\omega = 0)\mathbf{V}$, entering Eq.(1.128) page 53, are required to correct the different fragments. Labeling $\mathbf{W}^{(I)}$ the diagonal block corresponding to the restriction of \mathbf{W} to the (I)th fragment, I have implemented a routine to compute only these small blocks for the explicitly corrected fragments, instead of the bigger full matrix. This enables us to save both on memory footprint and Central Processing Unit (CPU) time aspects because, in the following, we only perform an explicit *GW* correction for the fragment of interest ($I = 0$).

2.3.2 Validity of the fragment approach

We start by assessing the quality of the fragment approximation, without using the compression method. Namely, we measure the impact of neglecting the overlap of MOs for a small number of fullerenes. To do so, we compare calculations performed using the fragment approximation to reference calculations where all fullerenes in the environment are treated as a single subsystem, allowing wavefunction delocalization over all molecules in the environment. We focus on the closing of the peak-to-peak gap of a “central” C_{60} (in red, FIGURE 2.4) induced by the screening originating from the environment (blue molecules, FIGURE 2.4). In gas phase,

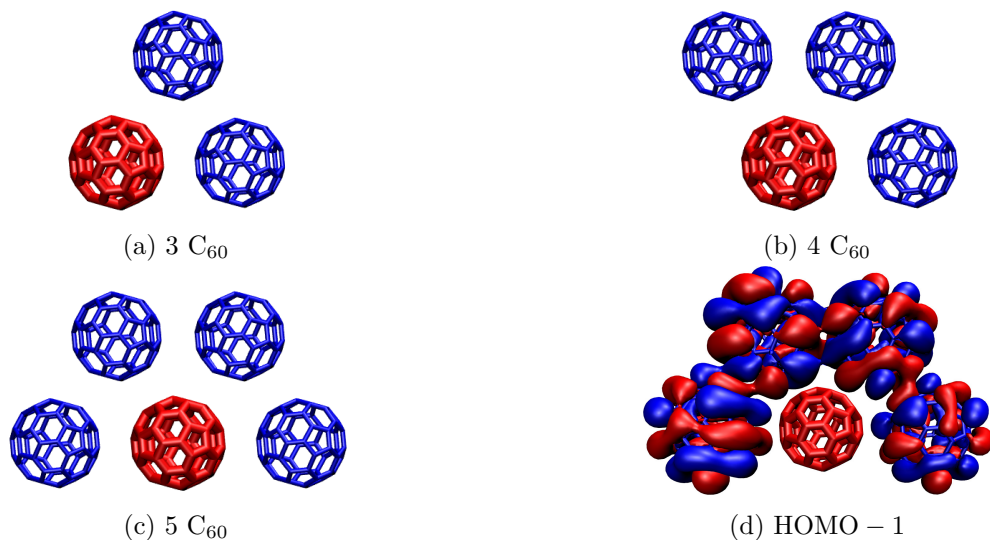


Figure 2.4: Representations of the systems with (a) 3 C_{60} , (b) 4 C_{60} and (c) 5 C_{60} used to test the fragment approach. In red, the fullerene for which we calculate the difference $P_{\text{Gap}}^{\Delta\text{COHSEX}}$ between the systems represented here and the gas phase. In (d) we represent the delocalized (HOMO-1) molecular orbital associated with the 4 C_{60} in the environment of system (c) beyond the fragment approximation.

the HOMO of such a molecule is fivefold degenerate, and its LUMO threefold degenerate. Thus, in all systems, we compute the peak-to-peak gap of the central C₆₀ as the difference between the average of its three LUMOs, and its five HOMOs. In the following, unless explicitly mentioned, the term “gap” is an abbreviation for the peak-to-peak gap. Its closing is computed via

$$P_{\text{Gap}}(n) = \text{Gap}(n \text{ C}_{60}) - \text{Gap}(1 \text{ C}_{60}), \quad (2.32)$$

where $\text{Gap}(n \text{ C}_{60})$ corresponds to the gap of the central C₆₀ surrounded by $(n - 1)$ other fullerenes.

Due to the cost of calculating the non-interacting susceptibility beyond the fragment approximation, the number of fullerenes in the environment is limited to four. To compare data on the same footing, we leave the central (red) fullerene as an isolated fragment to prevent delocalization of the associated HOMOs and LUMOs. What we want to explore is thus the impact of fragmenting the environment.

The results are provided in Table 2.1. The impact of the fragment approximation, namely not allowing the delocalization of the molecular orbitals over all fullerenes in the environment, ranges from 0.5 meV to 2.2 meV, remaining below the percent error. Even though limited to rather small systems, such an exploration provides a better understanding of the quality of the fragment approximation. One should note that the $P_{\text{Gap}}^{\Delta\text{COHSEX}}$ associated with the 5 C₆₀ system (-0.45 eV) represents already $\sim 32\%$ of the infinite surface limit ($P_{\text{Gap}}^{\Delta\text{COHSEX}} = -1.4$ eV; see FIGURE 2.11 page 86 with the blue symbols).

Table 2.1: Variation $P_{\text{Gap}}^{\Delta\text{COHSEX}}$, from the gas phase to the 3, 4, and 5 C₆₀ systems, for the central C₆₀ (in red in FIGURE 2.4) allowing wavefunction delocalization over all C₆₀ in the environment. The error induced by fragmenting the environment is provided in absolute value and in percentage.

System	$P_{\text{Gap}}^{\Delta\text{COHSEX}}$ (meV)	Error (meV)	Relative error (%)
3 C ₆₀	-245	0.5	0.2
4 C ₆₀	-348	1.0	0.3
5 C ₆₀	-447	1.5	0.3

The effects of the fragmentation being quantitatively measured, we can now test the compression method of \mathbf{X}_g .

2.3.3 Validation of the compression method for \mathbf{X}_g

We start by looking at the evolution of the static dipolar polarizability tensor for a given fullerene, in the gas phase, obtained with the model susceptibility matrix as a function of N_γ (the number of polarization vectors we keep). Namely, I have computed

$$[\boldsymbol{\alpha}]_{ij} = - \int d\mathbf{r} d\mathbf{r}' r_i \left(\sum_{\gamma, \gamma'}^{N_\gamma} \gamma(\mathbf{r}) [\tilde{\mathbf{X}}_g(\omega = 0)]_{\gamma\gamma'} \gamma'(\mathbf{r}') \right) r'_j, \quad (2.33)$$

for $r_i \in \{x, y, z\}$. This tensor is a key quantity for the long-range screening effects originating from a given fragment, and represents thus a direct measure of the accuracy of the fitted

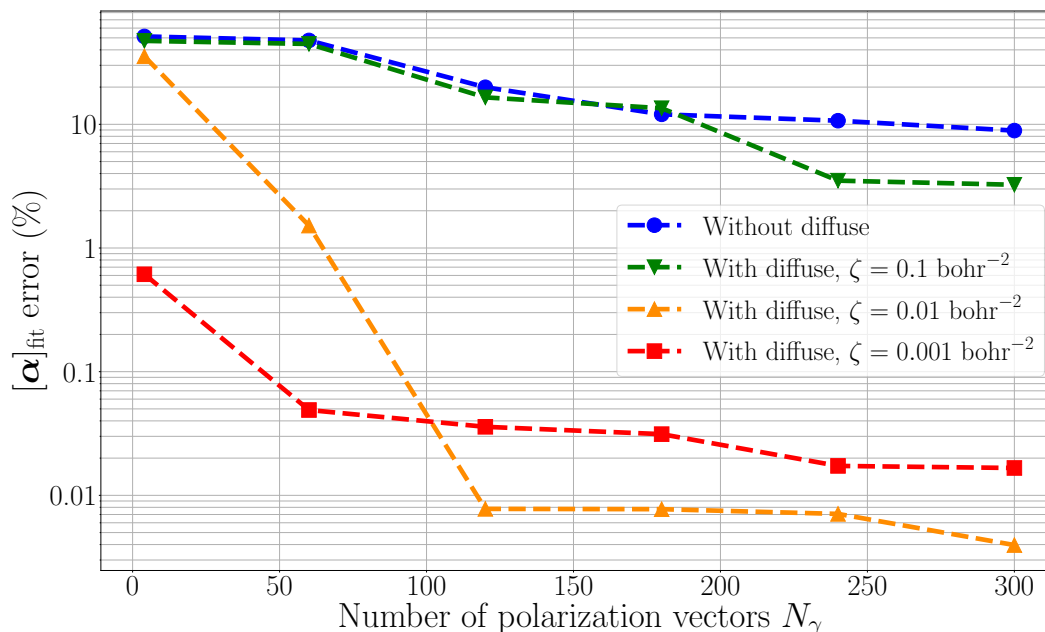


Figure 2.5: Evolution of the relative error $\|[\alpha]_{\text{fit}} - [\alpha]_{\text{ref}}\| / \|[\alpha]_{\text{ref}}\|$ (in percentage) for a fullerene RPA dipolar polarizability tensor $[\alpha]$ (see Eq.(2.33)) as a function of the number N_γ of polarization vectors (maximum number 5700). $\|\cdot\|$ corresponds to the Frobenius norm. $[\alpha]_{\text{ref}}$ is computed with the susceptibility described in the full auxiliary basis (with 5700 vectors), while $[\alpha]_{\text{fit}}$ is calculated using only N_γ polarization vectors. Results for different choices of test functions are plotted.

susceptibility. First, we explore the strategy where the test functions $\{t\}$ are taken to span the auxiliary basis set $\{P\}$ located on the fragment (a fullerene) for which we build the model susceptibility. Relative errors on the (Frobenius) norm of the dipolar polarizability tensor, with respect to a reference calculation using the full auxiliary basis set (5700 vectors), are represented in FIGURE 2.5 (blue dots). As expected, this error decreases as the number of polarization vectors increases. For $N_\gamma = 240$, the relative error is of the order of 10%, that is still rather large. This number $N_\gamma = 240$ corresponds to a typical minimal sp^3 basis per atom of the kind used in semi-empirical induced charges-and-dipoles polarizable models.

I now perform the same exercise but adding to the test functions $\{t\}$ a set of atom-centered diffuse Gaussian orbitals, as explained in section 2.2.2 page 71. Such diffuse functions are typically one set of (s,p,d,f,g) orbitals per atom with, for sake of simplicity, the same $e^{-\zeta r^2}$ radial part. Results for different values of ζ are reported on FIGURE 2.5. A value of $\zeta = 0.1 \text{ bohr}^{-2}$ (green down triangles), comparable to $\zeta = 0.2 \text{ bohr}^{-2}$ for the most diffuse carbon atomic orbital in the def2-TZVP-RI basis set, does not improve the quality of the fit. Increasing the diffuse character of these functions, with $\zeta = 0.01 \text{ bohr}^{-2}$ (orange up triangles) improves significantly the quality of the results. For $N_\gamma = 120$, namely, $\simeq 2\%$ of the dimension of the original auxiliary basis set $\{P\}$, the relative error is below 0.01%. Increasing too much the extent of the diffuse orbitals, with *e.g.*, $\zeta = 0.001 \text{ bohr}^{-2}$ (red squares) degrades the quality of the results. Even if relative errors are smaller with such a small ζ value in the

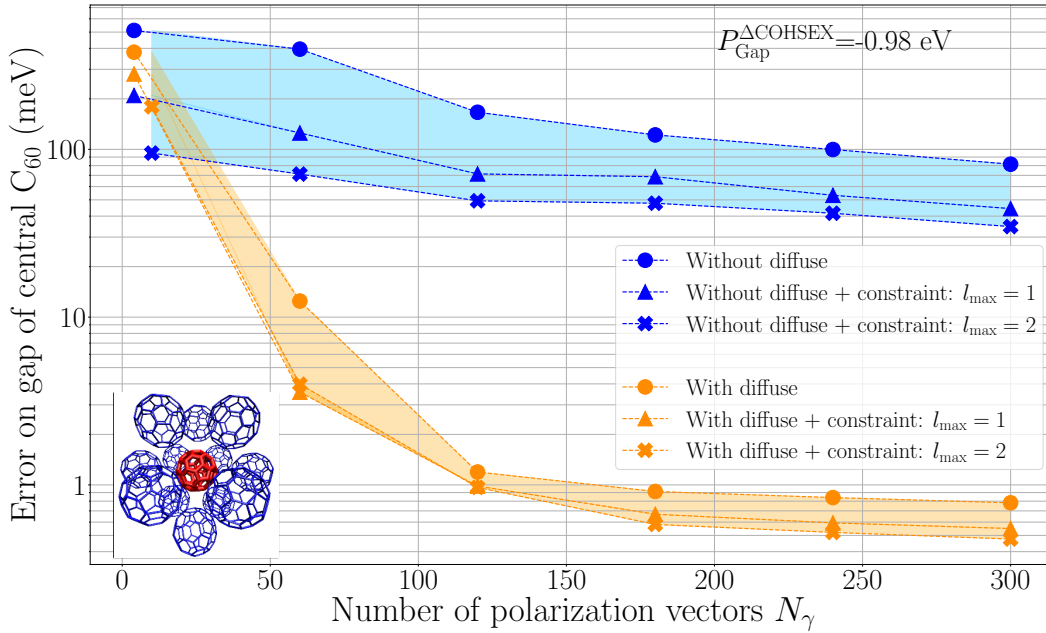


Figure 2.6: Error on the central C_{60} (red, inset) gap as a function of the number N_γ of polarization vectors per C_{60} in the first-neighbors shell (blue, Inset). Energies on the ordinates are in meV and log-scale. Results for test functions with and without diffuse orbitals, with and without constraints (see section 2.2.2 page 69), are shown. Diffuse functions use $\zeta = 0.01 \text{ bohr}^{-2}$. The reference $P_{\text{Gap}}^{\Delta\text{COHSEX}} = -0.98 \text{ eV}$ corresponds to the gap reduction from the gas phase to the 13- C_{60} cluster when all fragments are described by their full basis ($N_\gamma = 5700$).

limit of a very small number of polarization vectors ($N_\gamma = 4$ or 60), $\zeta = 0.001 \text{ bohr}^{-2}$ leads to greater errors than $\zeta = 0.01 \text{ bohr}^{-2}$ for larger values of N_γ .

The quality of the polarizability tensor obtained with the low-rank susceptibility insures that long-range interactions will be accurately reproduced. We now focus on nearest-neighbor interactions. We study in particular the peak-to-peak energy gap associated with a fullerene (in red in the inset of FIGURE 2.6) surrounded by its first shell of 12 nearest-neighbors (in blue).

In a standard fragment calculation at the full def2-TZVP/def2-TZVP-RI level, the central C_{60} peak-to-peak gap closes by $\sim 0.98 \text{ eV}$ due to the enhanced screening induced by the first shell of neighbors. This represents about 60% of the total polarization energy (see the orange dots in the FIGURE 2.11 page 86) as compared to a fullerene in a fullerite, namely an infinite fullerene crystal.

We now study the effect of reducing the size N_γ of the polarization basis on the 12 surrounding C_{60} . As previously, I start by using test functions taken only in the span of the auxiliary basis $\{P\}$ of the fragment (a fullerene) whose model susceptibility is fitted. The results are provided on FIGURE 2.6 (blue dots). As expected, the error on the central C_{60} peak-to-peak gap, as compared to the reference calculation, decreases with the number of polarization vectors. For $N_\gamma = 240$, the error is of the order of 100 meV, allowing to have

a qualitative result but representing still an error of the order of 10% with respect to the targeted polarization energy. As discussed above, this error converges to zero with N_γ equal to the size of the original atom-centered Gaussian auxiliary basis set (5700 vectors), but the convergence is too slow.

Similarly to the previous study of the polarizability, I now add diffuse functions in the test basis, with $\zeta = 0.01 \text{ bohr}^{-2}$. The related evolution of the error on the polarization energy for the gap is represented in FIGURE 2.6 (orange dots). Clearly, the addition of diffuse functions, allowing to test the quality of the model $\mathbf{V}\tilde{\mathbf{X}}_g^{(I)}\mathbf{V}$ screening potential in the vicinity of the molecule (I), dramatically accelerates the convergence of the polarization energy with respect to the size of the model susceptibility matrix. For $N_\gamma = 180$, namely $\simeq 3\%$ of the original susceptibility matrix size (5700) for one C_{60} , the error is now of the order of 1 meV, reaching quantitative accuracy.

I further add the constraints Eq.(2.14), with and without diffuse functions, to enforce the exact dipolar polarizability tensor with $l_{\text{max}} = 1$ (up triangles in FIGURE 2.6), or up to second order moments with $l_{\text{max}} = 2$ (crosses in FIGURE 2.6). In all cases, the constraints improve the accuracy, in particular in the small N_γ limit, even though their impact is not as important as adding diffuse test functions. Such a behavior can be understood by looking, *e.g.*, at FIGURE 2.5 for $\zeta = 0.01 \text{ bohr}^{-2}$ and $N_\gamma = 120$. The dipolar polarizability is already quite well reproduced so that the constraint leads to a small improvement. FIGURE 2.6 reveals that the constraint $l_{\text{max}} = 2$ improves very slightly the error on the gap, in comparison to the constraint $l_{\text{max}} = 1$. When diffuse functions are added to the test basis, the differences between $l_{\text{max}} = 1$ (orange up triangles) and $l_{\text{max}} = 2$ (orange crosses) are less than 0.1 meV for $N_\gamma \geq 120$. Since imposing the constraint comes at no cost, we keep $l_{\text{max}} = 1$ in the forthcoming calculations.

I also provide in FIGURE 2.7 the same study but for the HOMO and LUMO energies⁵. To allow a log-scale representation, only the absolute value of the errors are plotted. Negative errors are indicated by markers surrounded by black bold edges. Very similar results are obtained as compared to the gap study. Taking $N_\gamma = 180$ polarization vectors, the value at which the error on the gap becomes lower than 1 meV, we find that the errors on the absolute HOMO and LUMO energies are only slightly larger, at the 3-4 meV scale. As such, not only energy differences, but also absolute energy levels, are described quite accurately with very few optimal polarization vectors to describe the environment susceptibility.

Very similar results as the ones presented in FIGURE 2.6 can also be obtained by considering KS basis sets, and associated auxiliary basis sets, containing diffuse orbitals. As a matter of fact, it is well documented that the description of response properties, such as the polarizability, converges faster when diffuse channels are included for the description of MOs and associated density [157, 158]. For sake of consistence with our def2-TZVP/def2-TZVP-RI calculations, we adopt the def2-TZVPD/def2-TZVPD-RI basis sets [158] that add diffuse channels for better response properties. The resulting data are presented in FIGURE 2.8. Due to the addition of diffuse orbitals in the KS basis, the closing of the gap increases by about 2%, from

⁵Following the same arguments as in section 2.3.2 page 77, the embedded HOMO (respectively LUMO) energy is computed as the average over the five highest occupied (respectively three lowest unoccupied) energy levels.

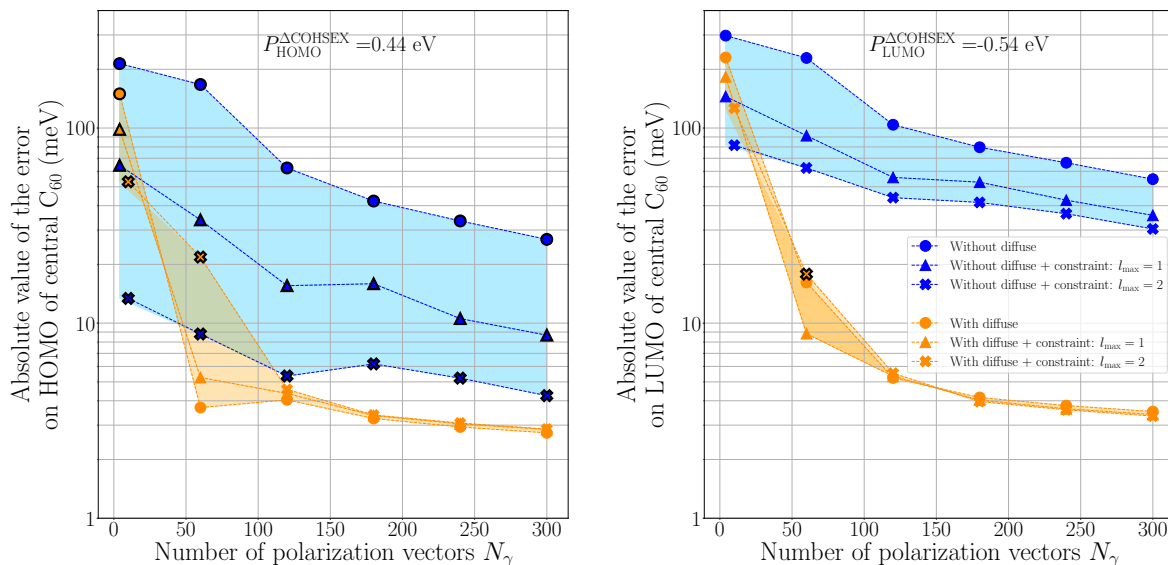


Figure 2.7: Same as FIGURE 2.6 but for the $P_{\text{HOMO}}^{\Delta\text{COHSEX}}$ and $P_{\text{LUMO}}^{\Delta\text{COHSEX}}$ energies, where the $P^{\Delta\text{COHSEX}}$ means the evolution between the gas phase and the first-shell-of-neighbors environment (see Inset in FIGURE 2.6). Data with black bold edges indicate negative values.

$P_{\text{Gap}}^{\Delta\text{COHSEX}} = -0.98 \text{ eV}$ to $P_{\text{Gap}}^{\Delta\text{COHSEX}} = -1.00 \text{ eV}$, indicating a slightly enhanced screening, consistent with an enhanced molecular polarizability. In the presence of diffuse orbitals ($\zeta = 0.01 \text{ bohr}^{-2}$) in the test set, together with imposing the $l_{\text{max}} = 1, 2$ constraints, the error reaches the meV error for $N_\gamma \geq 120$. The evolution of the error with the number N_γ of polarization vectors is very similar to what we obtained in FIGURE 2.6, demonstrating that our scheme (diffuse test functions and constraints) is universal, that is rather independent of the chosen input KS basis set.

The test provided above for the polarization energy originating from the first-nearest-neighbors is the most stringent test. For fragments located farther away, the dipolar component of the screening potential, that we strictly impose, becomes more and more dominant. This is illustrated in FIGURE 2.9 where we study the peak-to-peak gap of a C_{60} surrounded now by its two nearest-neighbor shells (see the inset of FIGURE 2.9). The size of this cluster amounts to 55 fullerenes. When all fullerenes are described at their full def2-TZVP/def2-TZVP-RI level (in the fragment approximation), the gap of the central fullerene closes by 1.25 eV from the gas phase to the 55- C_{60} cluster geometry. In this graph, I represent the effect of reducing the size N_γ of the polarization basis used to describe the susceptibility of the 42 surrounding C_{60} in the second shell, keeping the full auxiliary basis to describe the central fullerene and its first-nearest-neighbor shell. As such, we mainly focus on the error induced by the fitting process on fragments located at middle to long-range of the central subsystem of interest.

Consistently with the results obtained for the first shell of neighbors (FIGURE 2.6), my calculations confirm that the addition of diffuse orbitals in the test set dramatically helps in reducing the error below the meV with a small number of N_γ polarization vectors (compare orange and blue data in FIGURE 2.9). Further, as compared to the first-nearest neighbors

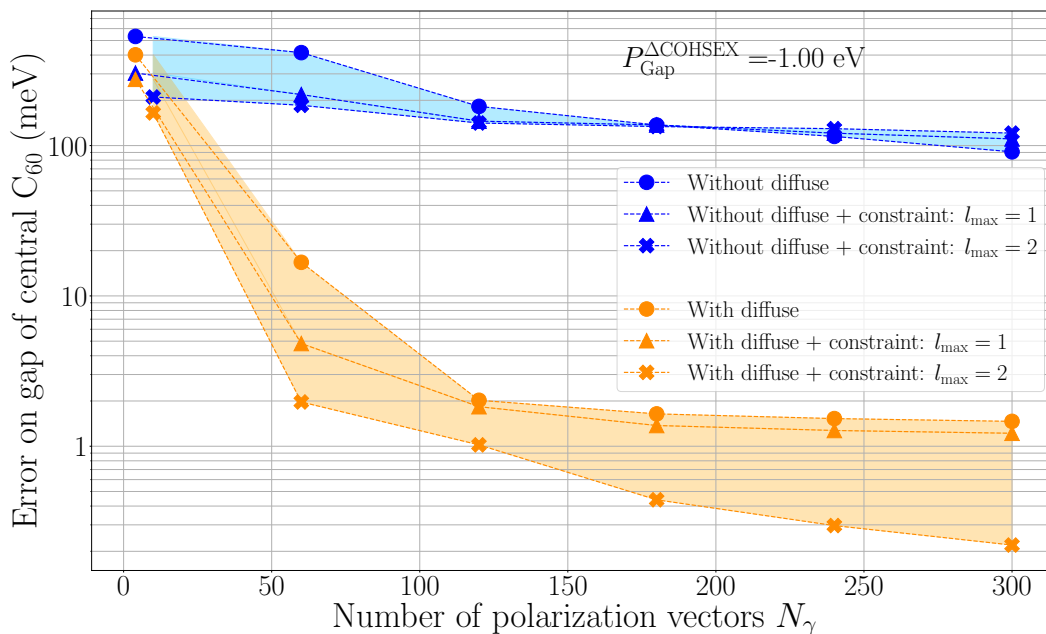


Figure 2.8: Same results as in FIGURE 2.6, but the def2-TZVP/def2-TZVP-RI basis sets are replaced by the def2-TZVPD/def2-TZVPD-RI basis sets. The reference $P_{\text{Gap}}^{\Delta\text{COHSEX}} = -1.00$ eV corresponds to the gap reduction from the gas phase to the 13-C₆₀ cluster when all fragments are described by their full def2-TZVPD-RI auxiliary basis set ($N_\gamma = 6900$).

case, a smaller number N_γ of polarization vectors is needed to go below the meV error when the constraint on the dipolar polarizability ($l_{\text{max}} = 1$) is imposed. This is the signature that in the long-range, the dipolar response dominates the screening potential, or reaction field. The combination of diffuse test orbitals with $\zeta = 0.01$ bohr⁻² with the constraint $l_{\text{max}} = 1$ leads to an error of the order of 0.1 meV for $N_\gamma = 60$, namely one polarization vector per atom. This is a dramatic reduction of the size of the polarization basis needed to describe the susceptibility blocks entering the Dyson equation (2.7) page 68.

As a final validation, I plot in FIGURE 2.10 the static screening potential, or reaction field, $W_{\text{scr}}(\mathbf{r}, \mathbf{r}_0; \omega = 0) = [v\chi v](\mathbf{r}, \mathbf{r}_0; \omega = 0)$ associated with an elementary positive source point-charge located in \mathbf{r}_0 , in the vicinity of a single pentacene molecule. Namely, for a test charge located in \mathbf{r}_0 , I plot $W_{\text{scr}}(\mathbf{r}, \mathbf{r}_0; \omega = 0)$ as a function of \mathbf{r} in the pentacene plane. In the case of a single fragment molecule, the reaction field reduces to $v\chi^{(I)}v$, with (I) the index of that molecule. The reference screening potential is provided in FIGURE 2.10(a) while the error associated with the model susceptibility, for a fixed $N_\gamma = 70$ number of retained polarization vectors among the 2314 vectors of the original def2-TZVP-RI basis, is represented in the other subfigures. FIGURE 2.10(b) shows the case where the test basis set does not contain diffuse functions. In FIGURE 2.10(c) I add diffuse functions ($\zeta = 0.01$ bohr⁻²), while FIGURE 2.10(d) illustrates the fit of χ with the same diffuse functions and the constraint $l_{\text{max}} = 1$. Clearly, the error associated with the screening potential around a given pentacene molecule (in meV units) is dramatically reduced upon adding diffuse test functions and the constraint on the dipolar polarizability tensor. The fullerene molecule is purposely replaced by a pentacene to

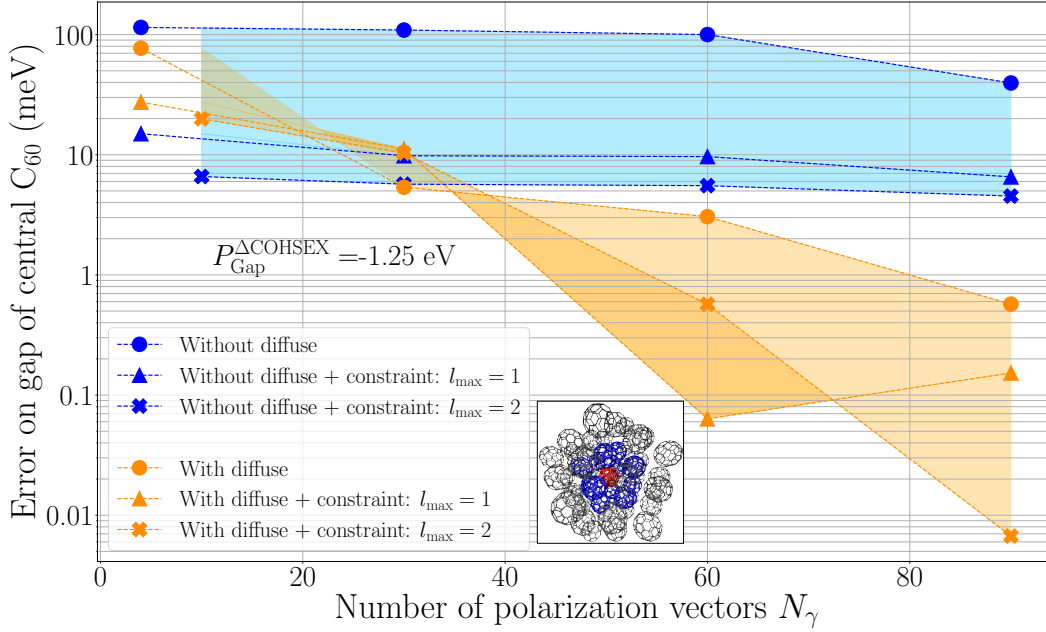


Figure 2.9: Error on the gap for a fullerene surrounded by its two first-shells of neighbors. The susceptibility of the central (in red, inset) and 12 first-nearest-neighbors (in blue, inset) C_{60} are described by the full auxiliary basis (5700 orbitals), while the susceptibility for each of the 42 C_{60} in the second shell of neighbors (in gray, inset) is described by N_γ polarization vectors. Energies on the ordinates are in meV and log-scale. Results for test functions with and without diffuse orbitals, with and without constraints (see section 2.2.2 page 69), are shown. Diffuse functions use $\zeta = 0.01 \text{ bohr}^{-2}$. The value $P_{\text{Gap}}^{\Delta\text{COHSEX}} = -1.25 \text{ eV}$ corresponds to the reference gap reduction for the central C_{60} from the gas phase to this 55- C_{60} cluster configuration when all fragments are described with their full basis sets.

indicate that the accuracy of the present scheme is hardly system dependent.

After having tested and validated different parameters for the compression of the susceptibility, we can now use this method to study large scale environment, which represents the main objective of this thesis.

2.3.4 Large scale environments: the C_{60} crystal and surface structures

Beyond the small cluster models, we now study the evolution of the gap of a fullerene from the gas phase to a C_{60} FCC crystal environment. We thus want to calculate the closing of the gap by screening effects in the limit of an infinite environment. Such a quantity, labeled $P_{\text{Gap}}^{\Delta\text{COHSEX}}$ and defined via Eq.(2.32) page 78, is also coined the polarization energy. We will consider the cases of a C_{60} in a bulk (fullerite) and further of a C_{60} at the (111) surface and sub-surface. Experimental photoemission experiments are very much surface sensitive, with a limited penetration depth of the input photons or electrons, so that comparison with the surface location is more appropriate. The bulk limit is obtained by immersing a C_{60} molecule in a sphere of fullerenes with increasing radius. The surface and subsurface limits are

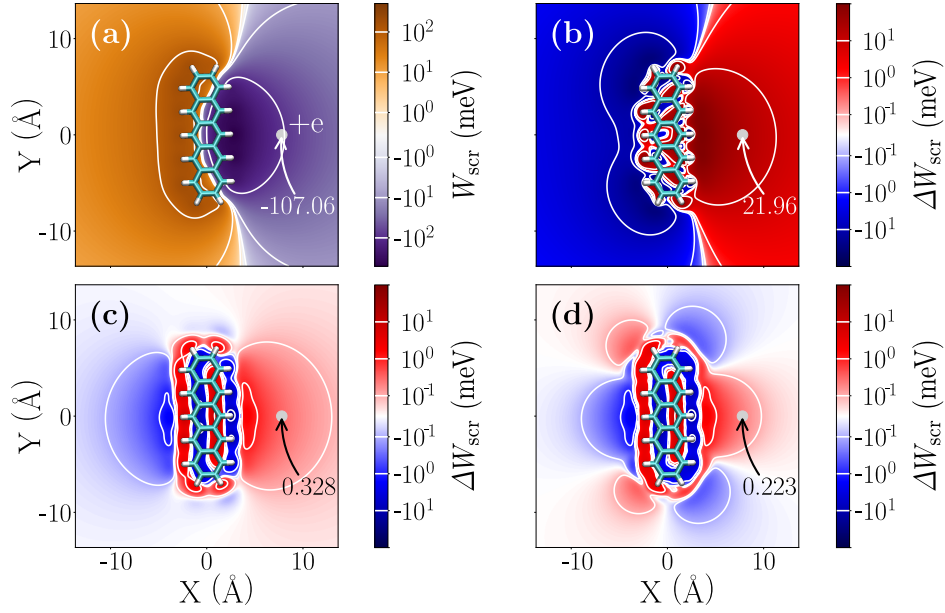


Figure 2.10: In plane $W_{\text{scr}}(\mathbf{r}, \mathbf{r}_0; \omega = 0) = [v\chi v](\mathbf{r}, \mathbf{r}_0; \omega = 0)$ static screening potential generated by a pentacene molecule in response to a positive unit source charge (gray dot indicated by $+e$) in \mathbf{r}_0 . In (a), the full screening potential. In (b), (c) and (d) the error $\Delta W_{\text{scr}}(\mathbf{r}, \mathbf{r}_0; \omega = 0)$ (see Eq.(2.12) page 70) with respect to the full screening potential upon substituting the full χ by its low-rank approximation (with 70 polarization vectors). In (b), low-rank χ model obtained without diffuse functions in the test basis set $\{t\}$; in (c) adding diffuse orbitals to the test basis set $\{t\}$; and in (d) adding further the constraint on the dipolar molecular polarizability $l_{\text{max}} = 1$. Coordinates are in angstroms, and units of the screening potential are in meV and in log-scale. Equipotentials at $(\pm 1, \pm 10, \pm 100)$ meV in figure (a), and at $(\pm 0.1, \pm 1, \pm 10)$ meV in figures (b), (c) and (d) are represented by white lines. The value of the reference and of the error associated with the screening potential at the position of the source is indicated.

obtained by using half-a-sphere of polarizable fullerenes in the environment. In the absence of wavefunction delocalization (or band dispersion) in the fragment approach, we still focus on the peak-to-peak gap, namely the gap between the center of the HOMO and LUMO bands as defined in FIGURE 2.3 page 76. We emphasize that the absence of permanent ground-state dipole, quadrupole, etc., in fullerene molecules, precludes the influence of any electrostatic crystal field in the ground state.

In the present case of fullerene crystals, the reference $\mathbf{X}_g^{(I)}$ susceptibility can be constructed for a single fullerene and the resulting fitted and compressed $\tilde{\mathbf{X}}_g^{(I)}$ matrix can be “copied” to form the model susceptibility block associated with each fullerene in the environment. Even though rotational disorder was not explored in this study, rotating the $\tilde{\mathbf{X}}_g^{(I)}$ matrix, to follow the rotation of a given fullerene, can be implemented. Beyond rotations, the effect on the polarization energy of changes in the susceptibility matrix associated with slight atomic distortions around some average equilibrium geometry, is expected to be small but may be

explored in future studies.

I have run the calculations with the parameters described above, namely keeping the full auxiliary def2-TZVP-RI basis set to describe the susceptibility of the C_{60} of interest for which I perform these embedded *GW* calculations. The same full auxiliary basis set is also used for its first-nearest neighbors. For the rest of the environment, namely the second-nearest neighbors and those located farther away, I keep $N_\gamma = 60$ optimized polarization vectors for each fullerene. Diffuse test functions with $\zeta = 0.01 \text{ bohr}^{-2}$ are adopted with the $l_{\max} = 1$ constraint. We focus on the gap closing ($P_{\text{Gap}}^{\Delta\text{COHSEX}}$) from the gas to the dense phase. Such a polarization energy, originating from the screening by the environment, is described at the ΔCOHSEX level as emphasized in section 2.3.1.

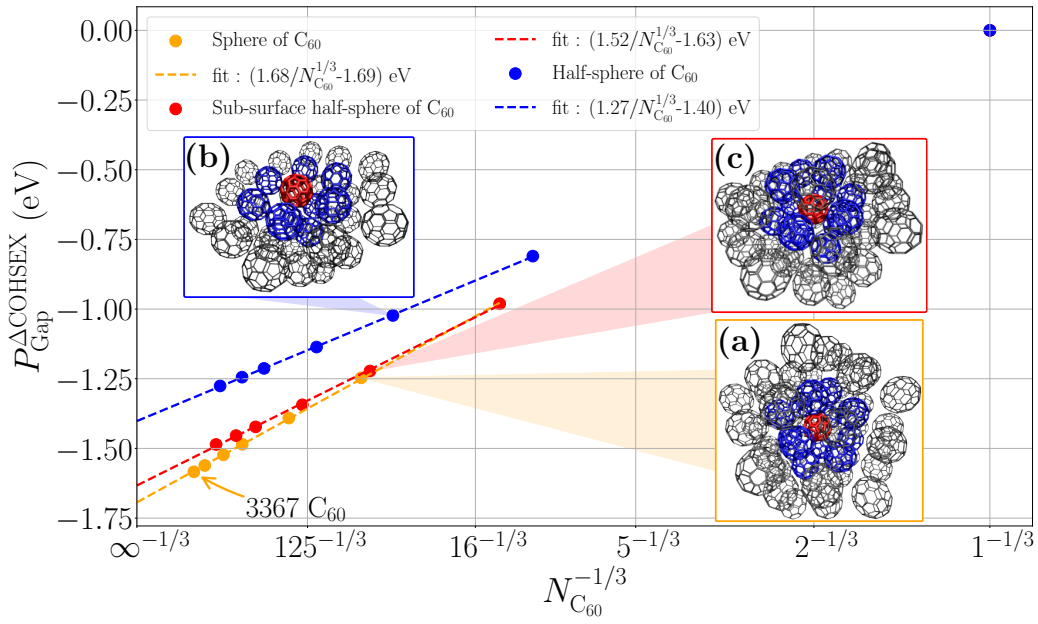


Figure 2.11: Evolution of the gap closing $P_{\text{Gap}}^{\Delta\text{COHSEX}}$, at the static ΔCOHSEX level, between a gas phase fullerene and $N_{C_{60}}$ systems, as a function of $1/N_{C_{60}}^{1/3}$. The orange/blue/red dots show calculations for one C_{60} embedded at the center of a sphere (in red in inset (a)), at the surface of a half-sphere (inset (b)), and at the subsurface of a half-sphere (inset (c)), respectively. Dashed lines represent $[a/N_{C_{60}}^{1/3} + b]$ fits.

I plot in FIGURE 2.11 the evolution of the polarization energy, or $P_{\text{Gap}}^{\Delta\text{COHSEX}}$, associated with the peak-to-peak gap for a bulk C_{60} (orange dots), a surface C_{60} (blue dots) and a C_{60} at subsurface (red dots), as a function of $1/N_{C_{60}}^{1/3}$, where $N_{C_{60}}$ represents the number of fullerenes retained in the sphere or half-sphere we use for the environment. Analytic derivations show indeed that such a polarization energy converges slowly, with an affine behavior with respect to $1/N_{C_{60}}^{1/3}$ in the asymptotic regime [123].

To demonstrate such a behavior, and to generalize it to systems at different dimensions, one could use a simple model. Similarly to a photoemission experiment, let us imagine that a localized charge, represented by a black dot in FIGURE 2.12, is added to the system. At long-

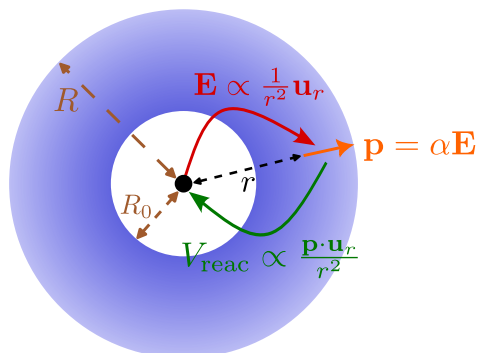


Figure 2.12: Schematic representation of an isotropic system of radial size R , such that a charge (black dot) is added at its center. Such a charge creates at long distance r (in the blue area, farther away than a given distance R_0) an electric field $\mathbf{E} \propto \frac{1}{r^2} \mathbf{u}_r$ (in red). The polarizable environment reacts by an induced dipole $\mathbf{p} = \alpha \mathbf{E}$ (orange vector), with α the dipolar polarizability. It stabilizes the added charge thanks to the reaction field $V_{\text{reac}}(r) \propto \frac{\mathbf{p} \cdot \mathbf{u}_r}{r^2}$ (in green).

range, such a perturbation can be approximated as a point charge. It generates a Coulomb potential $V \propto \frac{1}{r}$, with r the distance to the charge and \propto indicating the proportionality. In other words, it produces an electric field $\mathbf{E} \propto \frac{\mathbf{u}_r}{r^2}$, with \mathbf{u}_r the radial unit vector in spherical coordinates. The components of the polarizable environment react to this perturbation in the linear response domain by an induced dipole $\mathbf{p} = \alpha \mathbf{E}$, with α their dipolar polarizability. Such a dipole mainly controls the long-range behavior of the reaction field, created by the environment to stabilize the added charge and given by $V_{\text{reac}}(r) \propto \frac{\mathbf{p} \cdot \mathbf{u}_r}{r^2} \propto \frac{1}{r^4}$. This model is schematically represented in FIGURE 2.12. For an isotropic system at D dimensions, of radial size R and centered around the added charge, the polarization energy P of this latter is given by

$$P = a_0 + a_1 \int_{R_0}^R dr r^{D-1} V_{\text{reac}}(r). \quad (2.34)$$

R_0 corresponds to the radial size at which the reaction field enters the asymptotic regime (in blue in FIGURE 2.12), and (a_0, a_1) are some characteristic constants of the studied system. Using $V_{\text{reac}}(r) \propto \frac{1}{r^4}$, such an equation becomes

$$P = a + \frac{b}{R^{4-D}}, \quad (2.35)$$

with (a, b) two characteristic constants of the system.

For the (hemi-)spheres of C_{60} , $D = 3$ and $N_{C_{60}} \propto R^3$, or equivalently $R \propto N_{C_{60}}^{1/3}$ in the asymptotic regime. This leads to the aforementioned affine relation of the polarization energy with respect to $1/N_{C_{60}}^{1/3}$. This asymptotic behavior is confirmed numerically in FIGURE 2.11 by the straight dashed-line fits, one for each type of system, going through the calculated energies in the large $N_{C_{60}}$ limit.

In the asymptotic infinite bulk size limit, the gap of the central C_{60} is closing by 1.69 eV (orange dashed line) with respect to the gas phase. This can be compared to the polarization

energy of the biggest studied system. Calculations are performed for spheres containing up to 3367 C_{60} , representing 202 020 carbon atoms. The gap of such a system closes by 1.58 eV, which represents a difference of 0.11 eV with respect to the extrapolated infinite size value. This highlights the difficulty to capture the polarization energy with an accuracy within the 0.1 eV threshold when limited size environments are considered.

In order to compare to the $G_0W_0@LDA$ 3.0 eV peak-to-peak gap in a fully periodic bulk calculation performed by Shirley and Louie in their pioneering study [159], I compute the def2-TZVP $G_0W_0@LDA$ gap for an isolated fullerene. Subtracting the 1.69 eV polarization energy in the bulk limit to our gas phase 4.46 eV $G_0W_0@LDA$ HOMO-LUMO gap, we end up with a 2.8 eV peak-to-peak gap, in fair agreement with the periodic $G_0W_0@LDA$ value.

I also compute the asymptotic infinite limit for the gap of one C_{60} located at the (111) surface (see Inset FIGURE 2.11(b)). The blue dashed line gives an asymptotic closing of the gap amounting to 1.40 eV, which is in good agreement with the experimental values of 1.1 eV [160], 1.2 eV [161, 162] or 1.4 eV [163, 164]. Such values were obtained by taking the provided experimental peak-to-peak gaps subtracted to the experimental 4.9 eV gap value for a fullerene in gas phase [86]. Alternatively, I have also computed the def2-TZVP evGW@PBE0 gap value for one C_{60} in the gas phase. In the partially self-consistent evGW approach, the HOMO and LUMO energy levels are converged at the 0.1 meV level at the seventh cycle. Taking the computed 5.1 eV gas phase gap value, and adding the calculated polarization energy at the surface, one obtains a surface peak-to-peak gap of 3.7 eV, within the 3.5 eV to 3.8 eV experimental range. The presence of a metallic substrate when performing photoemission experiments, potentially enhancing the screening in the limit of few C_{60} layers, and alternatively the limited screening from the fullerene crystal in the few layer limits, may explain variations between experimental values. On the theoretical side, the influence of the fragment approximation, together with treating screening effects in the static COHSEX limit, remains to be studied.

In addition, the polarization energy is calculated for one C_{60} at the subsurface (see Inset FIGURE 2.11(c)), namely for one C_{60} in the middle of the layer just below the one at the top. The red dashed fit provides an asymptotic infinite size polarization energy of 1.63 eV. This value, closer to the bulk limit (difference of 0.06 eV) than the surface limit (difference of 0.23 eV), tends to show a rapid convergence of the polarization energy with respect to the depth of the considered fullerene. Namely, a fullerene in the subsurface presents properties already close to those in the bulk case.

We finally conclude this study by making a connection to periodic slab calculations, namely the traditional approach for the study of surfaces with periodic boundary conditions. In such periodic simulations, the unit cell is made of some layers of the material (the slab part), as well as a large vacuum area above the atoms. The height of this part should be large enough to restrict as best as possible interactions between the top of the slab and the bottom of its periodic image (which should not exist for a perfect slab at two dimensions). Along that line, I converge the polarization energy through the addition of C_{60} infinite sublayers, rather than by increasing the radius R of a half-sphere of polarizable molecules. Such a representation can be obtained by creating stacks of disks with increasing lateral radius R_{2D} , as represented in the Inset FIGURE 2.13(a). For a given number n of layers, the polarization energy is computed for different radius R_{2D} , and then is extrapolated to the limit $R_{2D} \rightarrow \infty$

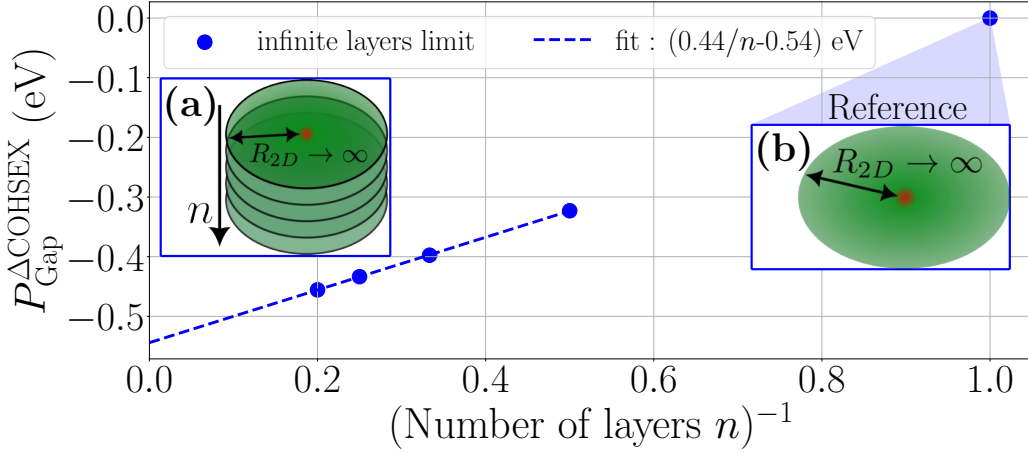


Figure 2.13: Gap evolution for one C_{60} at the surface (in red, inset (a)), as a function of the inverse of the number n of C_{60} layers. Here, the reference is the gap of a fullerene in an infinite C_{60} monolayer (see inset (b)). For each value of n , the infinite size layer(s) limit is obtained by extrapolating disk(s) to their infinite R_{2D} radius. The dashed line represents the $[a/n + b]$ fit.

thanks to the formula (2.35) for $D = 2$. Namely, such an energy follows asymptotically an affine relation with respect to $1/R_{2D}^2$ or to $1/N_{C_{60}}$, using the fact in such cylindrical stacks $N_{C_{60}} \propto R_{2D}^2$.

To go further and to reach the infinite limit $n \rightarrow \infty$ of infinite radial size layers (*i.e.* a true surface), such that $R_{2D} \rightarrow \infty$, one needs an asymptotic relation between the polarization energy and the number of layers n . To do so, one should restart from Eq.(2.34) for $D = 3$, and use cylindrical coordinates with ρ the radial in-plane distance, and z the axial coordinate (or height). Using $V_{\text{reac}}(r) \propto \frac{1}{(\rho^2 + z^2)^2}$ for a slab of finite height h and infinite radial size (as represented in the inset FIGURE 2.13(a)), and denoting h_0 the height at which the reaction field enters the asymptotic regime, the equation (2.34) becomes

$$P = a_0 + a_1 \int_{h_0}^h dz \int_0^{+\infty} d\rho \frac{\rho}{(\rho^2 + z^2)^2} \quad (2.36a)$$

$$P = a_0 + b_1 \int_{h_0}^h dz \frac{1}{z^2} \quad (2.36b)$$

$$P = a + \frac{b}{h} \quad (2.36c)$$

The height of the slab h being proportional to the number of layers n , the polarization energy follows asymptotically an affine relation with respect to $1/n$.

To confirm such a relation, I have computed, in FIGURE 2.13, $P_{\text{Gap}}^{\Delta\text{COHSEX}}$ with respect to $1/n$. Here, this polarization energy $P_{\text{Gap}}^{\Delta\text{COHSEX}}$ corresponds to the difference between the gap of one C_{60} , at the top of a slab of n layers in the limit $R_{2D} \rightarrow \infty$, and the same gap in the limit of an infinite radial size monolayer, as represented in FIGURE 2.13(b). The asymptotic affine behavior is numerically confirmed in FIGURE 2.13 by the straight dashed-line fit, leading

to an extrapolated value $P_{\text{Gap}}^{\Delta\text{COHSEX}} = 0.54\text{ eV}$. It should be emphasized that for ($n = 5$), only 85% of this polarization energy is captured, highlighting the difficulty to converge such long-range effects.

Summing the 0.85 eV polarization energy of one C_{60} embedded in an infinite size monolayer, and the asymptotic polarization energy of 0.54 eV coming from an infinite number of layers with respect to a single monolayer, we find a total polarization energy of 1.39 eV. This value is nearly identical to the 1.40 eV value obtained with the “half-sphere” surface approach, showing a good agreement between the two methods.

Finally, I would like to conclude this section with some details about computational resources required to run such calculations, to show that such results are affordable.

2.3.5 Computational details: CPU and memory requirements

The calculation for the biggest studied system made of 3367 C_{60} , amounting to 202 020 atoms as discussed in section 2.3.4, required around 8000 total CPU hours⁶ distributed on 720 cores. Alternatively, this represents a typical wall-time (time to completion of the run) of approximately 11 hours. Such a calculation was performed using the Irene SKL partition (Intel Skylake 8168 processors, with a base frequency of 2.70 GHz) of the IRENE supercomputer from GENCI-TGCC. Only 2.5 terabytes of memory were used to study this system, making it possible to run such calculations on smaller-size computer clusters. Such a small memory footprint was made possible thanks to the small dimension (60) of the polarization basis for each fragment in the environment. Let us stress out here that describing each fullerene by its full def2-TZVP-RI basis, of dimension 5700, would lead to a memory footprint of 2.6 petabytes for each related matrices, with similar requirements for the total Coulomb potential \mathbf{V} or the total susceptibility matrix \mathbf{X} . It would have been impossible to store any of these large matrices on the 310 terabytes available on the supercomputer used for this study. The present numbers are certainly indicative and may change depending on the chosen parameters, but they illustrate how efficient QM/QM' (*GW/RPA*) calculations can be when using compressed susceptibility blocks for the environment.

2.4 Conclusion

In this chapter, I have presented fully *ab initio* QM/QM' embedded *GW* calculations with a polarizable environment containing up to 200 000 atoms, with total typical CPU timings below 10 000 hours at the def2-TZVP level. Such calculations are made possible by adopting a fragment, or sub-system, approximation. Further, the susceptibility matrices associated with the fragments in the environment are reduced on-the-fly to a very low-rank representation, with block dimensions equivalent to the number of atoms in the fragment. This approach yields representations even more compact than standard semi-empirical approaches based on polarizable atoms described by onsite (sp^3) local charges and induced dipoles, namely 1 degree of freedom per site as compared to the 4 degrees of polarizable atoms. Such a

⁶This corresponds to the result of the multiplication between the elapsed real time needed to run the calculation, and the number of cores required for the simulation.

reduction allows inverting the Dyson equation for the screened Coulomb potential \mathbf{W} with very limited CPU and memory requirements.

The present scheme is certainly far from being optimal. The choice of the same localization parameter (ζ) for all (s,p,d,f,g) diffuse channels in the ensemble of test functions could, *e.g.*, lead to forthcoming improvements. Our main point was however to show that very simple choices could already dramatically help in constructing model susceptibility operators both extremely compact and accurate in reproducing medium-to-long-range screening potentials.

Finally, the GW formalism allows us to define a dynamical dielectric response, going beyond the standard low-frequency limit in the optical range of common PCM or QM/MM approaches. The importance of such dynamical corrections needs to be assessed, calculating the polarization energies within the full dynamical GW formalism rather than its static COHSEX limit. This is the main objective of the following chapter 3.

Static versus dynamically embedded *GW* formalism

Contents

Résumé	94
Summary	95
3.1 Introduction	96
3.2 The different types of embedding	97
3.2.1 The fully dynamical approach	97
3.2.2 The Δ COHSEX approach	98
3.2.3 The QM_{GW}/QM_{COHSEX} approach	99
3.2.3.1 Embedding generalities	99
3.2.3.2 Static COHSEX from a simple pole model	100
3.2.3.3 Folding of the static COHSEX environment	102
3.3 Application to dense phase of C_{60}	104
3.3.1 Technical details	104
3.3.2 Polarization basis set for dynamical susceptibilities	105
3.3.3 Discussion on P_n^{COH} and P_n^{SEX}	106
3.3.4 C_{60} infinite surface at the G_0W_0 level	107
3.3.5 Assessment of the adiabatic approximation for the environment	109
3.3.6 The $QM_{GW}/QM_{GW}/QM_{COHSEX}$ approach	114
3.4 A water molecule inside a metallic nanotube	115
3.5 Conclusion	116

This chapter is largely inspired from our work published in the Journal of Chemical Physics [165].

Résumé

Les modèles polarisables discrets ou continus, pour l'étude de propriétés électroniques de sous-systèmes environnés, reposent essentiellement sur une description statique des propriétés diélectriques de l'environnement. Une telle approximation repose sur l'hypothèse d'électrons du milieu environnant réagissant instantanément à une excitation dans la partie d'intérêt. L'environnement polarisable est donc traité dans une limite adiabatique. S'appuyant sur les méthodes développées dans le chapitre 2, permettant une description totalement *ab initio* de l'environnement dans le cadre du formalisme GW , ce chapitre a pour but de mesurer la validité de cette hypothèse adiabatique, grâce à une comparaison à une description totalement dynamique de la réponse diélectrique de l'environnement.

La partie 3.2 présente les différents niveaux de description du milieu polarisable utilisés dans ce chapitre, permettant de calculer des énergies de polarisation du sous-système d'intérêt. L'approche de type QM_{GW}/QM_{GW} , utilisant la réponse dynamique de l'environnement, sert de référence. Elle s'appuie sur la méthode fragment, ainsi que la méthode de compression de la susceptibilité, présentées précédemment. Elle est comparée à l'approche $\Delta COHSEX$, nécessitant uniquement la limite statique de la réponse diélectrique des sous-systèmes environné et environnant. Nous introduisons également une approche QM_{GW}/QM_{COHSEX} , permettant d'allier dans le même calcul une description dynamique GW pour la partie d'intérêt, à une description statique $COHSEX$ pour l'environnement.

Ces différentes méthodes sont comparées dans la partie suivante 3.3 via l'étude d'un fullerène à la surface d'un cristal de C_{60} . Afin de faciliter nos calculs, et notamment la méthode de compression de la susceptibilité, nous montrons la possibilité de se restreindre à une base de polarisation calculée dans le cas statique. Dans le cadre de l'approche QM_{GW}/QM_{COHSEX} , l'importance d'un traitement statique $COHSEX$ de l'environnement est ensuite illustrée sur une demi-sphère de 302 C_{60} . Après avoir effectué les calculs dynamiques QM_{GW}/QM_{GW} de référence, permettant de calculer l'énergie de polarisation du gap dans la limite d'une surface infinie, nous mesurons la précision de ces deux approches statiques. Ce système de fullerènes, dans lequel la dynamique du sous-système d'intérêt est identique à celle du milieu polarisable, est *a priori* défavorable à un traitement adiabatique de ce dernier. Alors que l'approche $\Delta COHSEX$ introduit une erreur de 17.5% sur l'énergie de polarisation du gap dans la limite d'une surface infinie, la méthode QM_{GW}/QM_{COHSEX} n'induit que 2.9% d'erreur. Afin de vérifier la robustesse de ces résultats, nous étudions également le cas d'une molécule de C_{60} entourée d'autres fullerènes, dont le gap Kohn-Sham DFT est modifié « à la main ». Cette étude illustre que l'approximation adiabatique pour l'environnement est d'autant meilleure que le gap de ce dernier est grand par rapport à celui de la partie d'intérêt. Enfin, nous montrons également que l'approche QM_{GW}/QM_{COHSEX} peut être améliorée, en décrivant au niveau GW dynamique les premiers voisins de la molécule étudiée, menant à une approche de type $QM_{GW}/QM_{GW}/QM_{COHSEX}$.

Finalement, nous étudions dans la partie 3.4 le cas d'une molécule d'eau dans un nanotube de carbone métallique. Alors que l'approximation adiabatique devrait être appliquée à la molécule d'eau à grand gap, et non pas à l'environnement (le nanotube), l'approche QM_{GW}/QM_{COHSEX} induit une erreur sur l'énergie de polarisation du gap ne dépassant pas les 7%.

Summary

Continuum or discrete polarizable models for the study of electronic properties in embedded subsystems rely mostly on the restriction of the surrounding electronic dielectric response to its low frequency limit. Such a description hinges on the assumption that the electrons in the surrounding medium react instantaneously to any excitation in the central subsystem, treating thus the environment in the adiabatic limit. Exploiting the embedded *GW* formalism methods developed in the chapter 2, with an environment described at the fully *ab initio* level, this chapter assesses the merits of the adiabatic limit with respect to an environment where the full dynamics of the dielectric response is considered.

Section 3.2 presents the different types of embedding used throughout this chapter, enabling us to compute polarization energies for the subsystem of interest. The calculations within the $\text{QM}_{GW}/\text{QM}_{GW}$ approach, based on the fully dynamical response of the environment, serve as reference. They are performed within the fragment approximation, in combination with the compression method for the susceptibility, as presented in the previous chapter. These results are compared to the ΔCOHSEX approach, requiring only the static limit of the dielectric response of the embedding and embedded subsystems. We also introduce a $\text{QM}_{GW}/\text{QM}_{\text{COHSEX}}$ approach, allowing us to merge in a single calculation a fully dynamical *GW* description for the part of interest, with a static COHSEX approximation for the environment.

These different methods are compared in the following section 3.3 via the study of a fullerene at the surface of a C_{60} crystal. To make easier our calculations, in particular for the compression method of the susceptibility, we show that we can restrict ourselves to a static polarization basis set. Within the $\text{QM}_{GW}/\text{QM}_{\text{COHSEX}}$ framework, we highlight the necessity to treat the effects of the environment at the static COHSEX level through the example of a hemisphere of 302 C_{60} . After having computed reference gap polarization energies via the fully dynamical $\text{QM}_{GW}/\text{QM}_{GW}$ approach, enabling us to extrapolate such a quantity to the infinite size surface limit, we assess the accuracy of the two static methods. Such a fullerene system, where the dynamics of the embedded and embedding subsystems are similar, is *a priori* not suited to an adiabatic treatment of the environment. While the ΔCOHSEX approach leads to an error on the gap polarization energy of 17.5% in the infinite size surface limit, the $\text{QM}_{GW}/\text{QM}_{\text{COHSEX}}$ method induces only a relative error of 2.9%. To test the robustness of these results, we also study a C_{60} molecule at the surface of a fullerene hemisphere, where the Kohn-Sham *DFT* gap of these latter is modified “by hand”. The results show that the adiabatic approximation becomes formally better validated, with a reduced error, when the gap of the environment increases with respect to the one of the part of interest. Eventually, we illustrate that the $\text{QM}_{GW}/\text{QM}_{\text{COHSEX}}$ method can be improved if the first-nearest-neighbors of the studied molecule are also described at the fully dynamical *GW* level. This leads to a $\text{QM}_{GW}/\text{QM}_{GW}/\text{QM}_{\text{COHSEX}}$ approach.

Finally, section 3.4 is dedicated to the study of a water molecule inside a carbon metallic nanotube. Even though the adiabatic approximation should be applied to the large gap water molecule, and not to the nanotube of the environment, the $\text{QM}_{GW}/\text{QM}_{\text{COHSEX}}$ approach induces an error on the gap polarization energy below 7%.

3.1 Introduction

The description of the electronic properties of a quantum subsystem embedded in a large and complex electrostatic and dielectric environment stands as a severe challenge to quantum mechanical modeling. Thus, I have presented in chapter 2 a fully *ab initio* Quantum Mechanics (QM)/QM' *GW* formalism, allowing us to consider very large scale atomistic environments, with a dielectric response described at the Random-Phase Approximation (RPA) level. Following previous merging of this Many-Body Perturbation Theory (MBPT) formalism with Polarizable Continuum Model (PCM) [6, 7] or semi-empirical QM/Molecular Mechanics (MM) discrete polarizable approaches for the environment [6, 9–13, 166], this latter was treated at the static level [123, 124, 167], through the Δ COHSEX approach.

In such an approximation, we have seen that we only retain the environment electronic susceptibility $\chi(\omega)$ in its low frequency limit ($\omega \rightarrow 0$). This hinges on the assumption that the electrons in the environment respond instantaneously¹ to an electronic excitation in the central subsystem. This is an adiabatic approximation for the environment. Using the spectral representation of $\chi(\omega)$ [70], or the equivalent one of the screened Coulomb potential $W(\omega)$ which presents the same poles, given by Eq.(1.124) page 52, such a hypothesis is expected to be valid if the gap of the environment is much larger than that of the central subsystem. Qualitatively, the dynamical response of the environment should be approximately the same as the static limit one, for all the energies of interest which should be much smaller than the values of the poles of the environment. In other situations, where such a decoupling is not verified, in particular when the environment is characterized by a gap smaller than that of the embedded subsystem, such an approximation needs to be validated. A critical assessment was recently proposed on the basis of model solutes and solvents [168]. In addition, a pioneering dynamical implementation of the PCM combined with the *GW* formalism was proposed, but without comparisons to results obtained in the static PCM limit [8].

The main objective of this chapter is to assess the adiabatic limit for the embedding system. To do so, we can take advantage of the *ab initio* treatment of the RPA dielectric response of this environment developed in the chapter 2. This allows us to explore straightforwardly the impact of switching the full dynamics of its susceptibility. In this chapter, we consider situations where the adiabatic approximation for the environment is expected to fail. Following the previous results, we study the polarization energies of a fullerene molecule at the surface of a fullerene crystal, a situation where there is no energy decoupling between the embedded and embedding subsystems electronic response. We also explore the case of a water molecule inside a metallic carbon nanotube, where the adiabatic approximation should be used for the large gap water molecule, not for the environment (the metallic nanotube). In these diverse systems, we compare the accuracy of various implementations of the adiabatic approach for the surrounding polarizable medium, within the *GW* framework. We show in particular that such an approximation, when properly implemented, does not induce errors larger than 10% for the gap polarization energy. Such results can be obtained via a $\text{QM}_{\text{GW}}/\text{QM}_{\text{COHSEX}}$ approach, where the subsystem of interest is treated at the fully dynamical *GW* level, while the environment is treated within an analog of the Coulomb-Hole

¹The inverse Fourier transform, in time difference τ , of the approximated $\chi(\omega) = \chi(\omega = 0)$ for all ω , is proportional to the Dirac distribution $\delta(\tau)$.

plus Screened-Exchange (COHSEX) approximation.

3.2 The different types of embedding

In this section, I present the three types of embedding used throughout this chapter, for a system of interest into a polarizable environment. They enable us to test the adiabatic approximation for the environment. As detailed in chapter 2, in all situations our embedding strategy relies on the fragment, or subsystem, approximation. Such an approach assumes a weak overlap between the wavefunctions of the various fragments, resulting in a block-diagonal independent-electron susceptibility χ_0 . The main objective of these embedding methods is to compute the energy level shifts

$$P_n = \varepsilon_n^{\text{embedded}} - \varepsilon_n^{\text{gas}}, \quad (3.1)$$

with ε_n the n^{th} energy level, from the isolated (gas) phase to the embedded phase. Such shifts are labeled polarization energies and can be as large as several electronvolts.

Strategies to go beyond the fragment approximation have been developed at the ground-state Density-Functional Theory (DFT) [169] and many-body [140, 170] levels, attempting in particular to correct the non-interacting susceptibility by the effect of the residual interaction between subsystems. Such developments stand aside from the present chapter, devoted to the validity of the adiabatic approximation for the environment electronic response.

3.2.1 The fully dynamical approach

Working with a fully *ab initio* description of the environment, we can avoid any adiabatic approximation for the environment, and thus we can have access to reference calculations. The extension to dynamical screening is formally straightforward. Following the Contour Deformation (CD) plus Analytic Continuation (AC) scheme of our *GW* code Beyond Density-Functional Theory (BEDEFT), as detailed in section 1.3.2.10 page 56, we need to calculate the total interacting-electron susceptibility $\chi(\omega)$ for each of the n_ω required imaginary frequencies. In practice, we retain $n_\omega = 12$ frequencies. To reduce the computational cost of these calculations, we can also use the compression method for the gas phase susceptibility of the fragments in the environment, as detailed in chapter 2. This method can be easily adapted to the fully dynamical situation.

Namely, in the fragment approximation, I recall that the Dyson equation for $\chi(\omega)$, and its corresponding matrix representation $\mathbf{X}(\omega)$ in the auxiliary basis set $\{P\}$ associated to the Resolution of the Identity (RI) formalism, is given by

$$\mathbf{X}(\omega) = \mathbf{X}_g(\omega) + \mathbf{X}_g(\omega)\mathbf{V}^{\text{off}}\mathbf{X}(\omega). \quad (3.2)$$

The dense matrix \mathbf{V}^{off} , such that its diagonal blocks are null, is equal to

$$\mathbf{V}^{\text{off}} = \sum_{I \neq J} \mathbf{V}^{(IJ)}, \quad (3.3)$$

with $\mathbf{V}^{(IJ)}$ the matrix of Coulomb interactions between the auxiliary basis sets of fragments (I) and (J), and zero otherwise. $\mathbf{X}_g(\omega)$ is a block-diagonal matrix, such that its (I)th block

corresponds to $\mathbf{X}_g^{(I)}(\omega)$, the gas phase **interacting** susceptibility of the (I)th fragment. Each of these isolated fragment susceptibility blocks is constructed following Eq.(2.5) page 68. The computational cost of building all these blocks $\mathbf{X}_g^{(I)}(\omega)$ grows linearly with the number N_f of fragments. In the following sections, I study the case of a C₆₀ bulk or surface crystal. All the fullerenes being related by translations, all the $\mathbf{X}_g^{(I)}(\omega)$ blocks can be obtained at no cost from a single fullerene gas phase susceptibility. In the limit of a very large number of fragments, the remaining cost lies essentially in inverting the Dyson equation (3.2). Such a cost can be dramatically reduced thanks to our compression method. This latter aims at computing a low-rank approximation $\tilde{\mathbf{X}}_g^{(I)}(\omega)$ of these blocks, such that

$$\chi_g^{(I)}(\mathbf{r}_1, \mathbf{r}_2; \omega) \stackrel{\text{RI}}{\simeq} \sum_{P, Q} \left[\mathbf{X}_g^{(I)}(\omega) \right]_{PQ} P(\mathbf{r}_1) Q(\mathbf{r}_2) \quad (3.4)$$

$$\stackrel{\text{MODEL}}{\simeq} \sum_{\gamma, \gamma'} \left[\tilde{\mathbf{X}}_g^{(I)}(\omega) \right]_{\gamma\gamma'} \gamma(\mathbf{r}_1) \gamma'(\mathbf{r}_2). \quad (3.5)$$

In our specific method, we have decided to express the elements of the optimal polarization basis set $\{\gamma\}$, of dimension N_γ , as a linear combination of the auxiliary basis functions $\{P\}$. N_γ should be as small as possible to study large scale systems, while preserving a good accuracy on the polarization energies for the central fragment of interest.

In practice, the matrices $\tilde{\mathbf{X}}_g^{(I)}(\omega)$ and their corresponding polarization basis set $\{\gamma\}$ should be recomputed for each of the n_ω imaginary frequencies of the CD-AC scheme, via our minimization method under constraints explained in section 2.2, pages 67 to 75. However, for the sake of simplicity, we adopt the static optimal polarization basis vectors $\{\gamma(\omega = 0)\}$ for the n_ω frequencies, and we only reoptimize the coefficients of the matrix $\tilde{\mathbf{X}}_g^{(I)}(\omega)$ for each frequency. The accuracy of this approximation is assessed in section 3.3.2 page 105. A similar choice was made in pioneering studies involving generalized plasmon-pole models [171] or effective representation of dielectric matrices [153, 154, 172]. The dynamical susceptibility was expressed in a static basis of polarization vectors, based on the leading eigenvectors of a symmetrized representation $\mathbf{V}^{1/2} \mathbf{X}(\omega = 0) \mathbf{V}^{1/2}$ of the static susceptibility.

In the following sections, it should be noticed that the susceptibilities of the central fragment and its first shell of neighbors are always described within the full auxiliary basis set $\{P\}$. Fitting by optimal polarization basis sets is thus used only for second-nearest-neighbor fragments and beyond.

3.2.2 The Δ COHSEX approach

At the opposite, in several studies merging the *GW* formalism with semi-empirical polarizable environments [6, 10, 11, 17, 144], or in the chapter 2 where the polarizable medium was treated at a fully *ab initio* level, the polarization energy P_n was efficiently calculated via an adiabatic approximation for the environment. More exactly, P_n was computed as an energy difference between two static COHSEX calculations performed with and without the environment, namely

$$P_n^{\Delta\text{COHSEX}} = \varepsilon_n^{\text{COHSEX, embedded}} - \varepsilon_n^{\text{COHSEX, gas}}, \quad (3.6)$$

with ε_n the n^{th} energy level. The absolute Quasiparticle (QP) energies for the embedded system can be obtained by adding these polarization energies to the corresponding gas phase *GW* QP energies, computed for example at the *evGW* level. In that respect, such an approach is essentially perturbative. This simple and efficient scheme is labeled Δ COHSEX below.

As shown in Eq.(1.128) page 53, the static COHSEX approximation to the *GW* self-energy only requires the low-frequency limit of the screened Coulomb potential $W(\omega \rightarrow 0)$, or equivalently of the interacting electron susceptibility $\chi(\omega \rightarrow 0)$. As such, it offers an obvious route for treating the environment within the adiabatic limit. Furthermore, both the embedded and embedding subsystems are treated on the same footing. It remains, however, that the static COHSEX approximation is known to dramatically overestimate gaps, which are the difference between the Ionization Potential (IP) and the Electron Affinity (EA), as defined in section 1.1.1 page 24. The static COHSEX approach tends to overestimate the IP and to underestimate the EA. Taken as an energy difference between the gas and embedded environments, it was found that reasonable polarization energies could be obtained. This stems presumably from a cancellation of errors between the gas and embedded static COHSEX calculations. While computationally very efficient, the following sections nevertheless show that this approach can yield sizable errors as compared to a fully dynamical treatment of both the embedded and embedding subsystems. This is presumably due to an incomplete cancellation of errors, together with the error inherent to the adiabatic approximation for the environment.

Following the previous studies in chapter 2, such an approach can be easily coupled to the compression method for the susceptibility of the fragments in the environment.

3.2.3 The $\text{QM}_{\text{GW}}/\text{QM}_{\text{COHSEX}}$ approach

Finally, the third embedding strategy we would like to develop consist into a merging of the two previous approaches. More explicitly, we want to treat the fragment of interest at the fully dynamical level, while the environment is described, in the **same** calculation, at the static COHSEX level. Such a method is entitled the $\text{QM}_{\text{GW}}/\text{QM}_{\text{COHSEX}}$ approach. The goal is to take advantage of the accuracy of the dynamical *GW* formalism for the part of interest, and to benefit from the efficiency of the static COHSEX for the large scale environment.

To achieve such an objective, we first work on a reformulation of the screened Coulomb potential $W(\omega)$, more amenable to approximations for the environment.

3.2.3.1 Embedding generalities

We divide the total system into the central subsystem of interest (labeled by (A)) and the environment (labeled by (B)) and, following the fragment approximation, we assume non-overlapping wavefunctions between the two subsystems (A) and (B). This results in an additive total non-interacting electron $\chi_0(\omega)$ operator, in the sense that

$$\chi_0(\mathbf{r}_1, \mathbf{r}_2; \omega) = \chi_0^{(A)}(\mathbf{r}_1, \mathbf{r}_2; \omega) + \chi_0^{(B)}(\mathbf{r}_1, \mathbf{r}_2; \omega), \quad (3.7)$$

where $\chi_0^{(S)}(\mathbf{r}_1, \mathbf{r}_2; \omega)$ corresponds to the isolated (gas phase) non-interacting susceptibility of the subsystem S . This is just an equivalent reformulation of the block-diagonal character of

the matrix representation $\mathbf{X}_0(\omega)$ of $\chi_0(\omega)$, but in real space. Dropping the space variable for the sake of compactness, the Dyson equation (1.120d) page 51 for the screened Coulomb potential W becomes equivalent to

$$W(\omega)^{-1} = V^{-1} - \chi_0^{(A)}(\omega) - \chi_0^{(B)}(\omega) \quad (3.8a)$$

$$= \tilde{V}(\omega)^{-1} - \chi_0^{(A)}(\omega). \quad (3.8b)$$

The potential \tilde{V} is defined by the following Dyson equation

$$\tilde{V}(\omega) = V + V \cdot \chi_0^{(B)}(\omega) \cdot \tilde{V}(\omega), \quad (3.9)$$

where the operation \cdot indicates the matrix product for two spatial-dependent functions, namely such that

$$[D \cdot B](\mathbf{r}_1, \mathbf{r}_2) = \int d\mathbf{r}_3 D(\mathbf{r}_1, \mathbf{r}_3) B(\mathbf{r}_3, \mathbf{r}_2). \quad (3.10)$$

The equation (3.9) can be rewritten

$$\tilde{V}(\omega) = V + V_{\text{reac}}(\omega) \quad (3.11)$$

$$V_{\text{reac}}(\omega) = V \cdot \chi_g^{(B)}(\omega) \cdot V, \quad (3.12)$$

where $\chi_g^{(B)}(\omega)$ is the interacting susceptibility of the environment (B) *in the absence of the other subsystem*, namely in gas phase. The potential $V_{\text{reac}}(\omega)$ is the so-called reaction field. Qualitatively, a charge density change upon excitation, for example in the subsystem (A), generates through the V Coulomb interaction a charge density change in the environment (B), proportional to $\chi_g^{(B)}(\omega) \cdot V$. In return, this latter exerts a reaction field on (A) via V . Finally, the equation (3.8b) can be rewritten

$$W(\omega) = \tilde{V}(\omega) + \tilde{V}(\omega) \cdot \tilde{\chi}^{(A)}(\omega) \cdot \tilde{V}(\omega) \quad (3.13)$$

$$\tilde{\chi}^{(A)}(\omega) = \chi_0^{(A)}(\omega) + \chi_0^{(A)}(\omega) \cdot \tilde{V}(\omega) \cdot \tilde{\chi}^{(A)}(\omega). \quad (3.14)$$

$\tilde{\chi}^{(A)}(\omega)$ appears as an interacting susceptibility of the central subsystem of interest (A) when its Coulomb interactions are renormalized by the reaction field created by the environment (B).

The next step, to develop a **QM_{GW}/QM_{COHSEX}** approach, is to find a way to directly incorporate the static **COHSEX** approximation for the subsystem (B) inside the expression of $\chi_g^{(B)}(\omega)$.

3.2.3.2 Static **COHSEX** from a simple pole model

In this part, we focus on a system considered as a whole, namely without any subdivision. We recover here the static **COHSEX** approximation within a very simple pole model for the susceptibility, as an alternative to original approaches relying on the time-domain analysis of the response operators [1, 37, 67]. Namely, taking as initial information only the low-frequency limit of the screened Coulomb potential $W(\omega \rightarrow 0)$, or equivalently of the susceptibility $\chi(\omega \rightarrow 0)$, we assume a simple pole model $\chi_\lambda(\omega)$. This latter is defined by

$$\chi_\lambda(\mathbf{r}, \mathbf{r}'; \omega) = \chi(\mathbf{r}, \mathbf{r}'; \omega = 0) \times \frac{\lambda}{2} \left[\frac{1}{\omega + \lambda - i\eta} - \frac{1}{\omega - \lambda + i\eta} \right], \quad (3.15)$$

with λ an unique pole energy for simplicity, and η a strictly positive infinitesimal shift. Such an expression has the correct low and high frequency limits and time-ordering structure in the energy plane. The full static **COHSEX** expression of the self-energy Σ can be simply recovered by taking the pole energy λ to infinity **after** performing the energy integration, as illustrated below.

We separate the *GW* self-energy $\Sigma = \Sigma^X + \Sigma^C$ into its bare-exchange part Σ^X and its correlation part Σ^C , with

$$\Sigma^X(\mathbf{r}, \mathbf{r}') = \frac{i}{2\pi} \int_{-\infty}^{+\infty} d\omega e^{i\eta\omega} G(\mathbf{r}, \mathbf{r}'; \varepsilon + \omega) V(\mathbf{r}, \mathbf{r}') \quad (3.16a)$$

$$= - \sum_i^{\text{occ}} \phi_i(\mathbf{r}) \phi_i^*(\mathbf{r}') V(\mathbf{r}, \mathbf{r}'), \quad (3.16b)$$

where the sum runs over the occupied states, associated to the Molecular Orbitals (**MOs**) $\{\phi_i\}$. Following the Eq.(1.122) page 51, and using the fact that $W(\omega) = V + V \cdot \chi(\omega) \cdot V$, the correlation-only self-energy, built on the model susceptibility, reads

$$\Sigma_\lambda^C(\mathbf{r}, \mathbf{r}'; \varepsilon) = \frac{i}{2\pi} \int_{-\infty}^{+\infty} d\omega e^{i\eta\omega} G(\mathbf{r}, \mathbf{r}'; \varepsilon + \omega) \times [V \cdot \chi_\lambda(\omega) \cdot V](\mathbf{r}, \mathbf{r}'), \quad (3.17)$$

where we use the convention of Eq.(3.10). Using Eq.(3.15) and the two following integral identities

$$\int_{-\infty}^{+\infty} d\omega \frac{1}{\omega + \varepsilon - (\varepsilon_i + i\eta)} \left(\frac{1}{\omega + \lambda - i\eta} - \frac{1}{\omega - \lambda + i\eta} \right) = \frac{2i\pi}{\lambda + \varepsilon - \varepsilon_i} \quad (3.18a)$$

$$\int_{-\infty}^{+\infty} d\omega \frac{1}{\omega + \varepsilon - (\varepsilon_a - i\eta)} \left(\frac{1}{\omega + \lambda - i\eta} - \frac{1}{\omega - \lambda + i\eta} \right) = -\frac{2i\pi}{\lambda + \varepsilon_a - \varepsilon}, \quad (3.18b)$$

which can be shown thanks to the residue theorem [71], the correlation part becomes

$$\Sigma_\lambda^C(\mathbf{r}, \mathbf{r}'; \varepsilon) = -[V \cdot \chi(\omega = 0) \cdot V](\mathbf{r}, \mathbf{r}') \times \frac{\lambda}{2} \left(\sum_i \frac{\phi_i(\mathbf{r}) \phi_i^*(\mathbf{r}')}{\lambda + \varepsilon - \varepsilon_i} - \sum_a \frac{\phi_a(\mathbf{r}) \phi_a^*(\mathbf{r}')}{\lambda + \varepsilon_a - \varepsilon} \right), \quad (3.19)$$

with (i) indexing the occupied states, and (a) the empty ones. The limit $\lambda \rightarrow \infty$ results in the frequency-independent correlation part Σ_∞^C such that

$$\Sigma_\infty^C(\mathbf{r}, \mathbf{r}') = \frac{1}{2} [W(\mathbf{r}, \mathbf{r}'; \omega = 0) - V(\mathbf{r}, \mathbf{r}')] \times \left[\sum_a \phi_a(\mathbf{r}) \phi_a^*(\mathbf{r}') - \sum_i \phi_i(\mathbf{r}) \phi_i^*(\mathbf{r}') \right]. \quad (3.20)$$

Using the fact that

$$\sum_a \phi_a(\mathbf{r}) \phi_a^*(\mathbf{r}') - \sum_i \phi_i(\mathbf{r}) \phi_i^*(\mathbf{r}') = \sum_n \phi_n(\mathbf{r}) \phi_n^*(\mathbf{r}') - 2 \sum_i \phi_i(\mathbf{r}) \phi_i^*(\mathbf{r}'), \quad (3.21)$$

where (n) index all the states, and the closure relation

$$\sum_n \phi_n(\mathbf{r}) \phi_n^*(\mathbf{r}') = \delta(\mathbf{r} - \mathbf{r}'), \quad (3.22)$$

we recover the static **COHSEX** approximation

$$\Sigma(\mathbf{r}, \mathbf{r}') = \Sigma^X(\mathbf{r}, \mathbf{r}') + \Sigma_\infty^C(\mathbf{r}, \mathbf{r}') \quad (3.23a)$$

$$= \Sigma_{\text{static}}^{\text{SEX}}(\mathbf{r}, \mathbf{r}') + \Sigma_{\text{static}}^{\text{COH}}(\mathbf{r}, \mathbf{r}'), \quad (3.23b)$$

as defined in Eq.(1.128) page 53. The same strategy will be used here below for the susceptibility $\chi_g^{(B)}(\omega)$, in order to properly merge a polarizable environment, restricted to its static **COHSEX** approximation, with a fully dynamical GW formalism for the central subsystem.

3.2.3.3 Folding of the static **COHSEX** environment

To avoid relying on the cancellation of errors at the static Δ **COHSEX** level, we now merge the fully dynamical GW formalism with a polarizable environment described at the static **COHSEX** level, via a simple pole model $\chi_{g,\lambda}^{(B)}(\omega)$ as described in section 3.2.3.2. More exactly, we start from the equations (3.12) and (3.14) for the folding of the screening effects of the environment, and the definition (1.122) page 51 of the correlation self-energy Σ^C . The exchange part of the self-energy of the subsystem (A) is unchanged by the environment in a fragment approximation, and is given by $\Sigma_{(A)}^X$ such that

$$\Sigma_{(A)}^X(\mathbf{r}, \mathbf{r}') = \frac{i}{2\pi} \int_{-\infty}^{+\infty} d\omega e^{i\eta\omega} G^{(A)}(\mathbf{r}, \mathbf{r}'; \varepsilon + \omega) V(\mathbf{r}, \mathbf{r}') \quad (3.24a)$$

$$= - \sum_{i \in (A)}^{\text{occ}} \phi_i(\mathbf{r}) \phi_i^*(\mathbf{r}') V(\mathbf{r}, \mathbf{r}'). \quad (3.24b)$$

$G^{(A)}$ corresponds to the Green's function of the subsystem (A), and the sum runs only over the occupied states of (A). The restriction of the correlation part of the self-energy, denoted $\Sigma_{(A)}^C$, becomes

$$\begin{aligned} \Sigma_{(A)}^C(\mathbf{r}, \mathbf{r}'; \varepsilon) &= \lim_{\lambda \rightarrow \infty} \frac{i}{2\pi} \int_{-\infty}^{+\infty} d\omega e^{i\eta\omega} G^{(A)}(\mathbf{r}, \mathbf{r}'; \varepsilon + \omega) \\ &\quad \times \left[V_{\text{reac}}(\mathbf{r}, \mathbf{r}'; \omega, \lambda) + \left(\tilde{V} \cdot \tilde{\chi}^{(A)} \cdot \tilde{V} \right)(\mathbf{r}, \mathbf{r}'; \omega, \lambda) \right]. \end{aligned} \quad (3.25)$$

The simple pole λ is added as an argument to all the quantities which depend explicitly on its value. The limit $\lambda \rightarrow \infty$ is taken after the frequency integration, as emphasized in section 3.2.3.2.

Concerning the second term of the screening potential in Eq.(3.25), namely the $[\tilde{V} \cdot \tilde{\chi}^{(A)} \cdot \tilde{V}](\omega, \lambda)$ contribution, we show in appendix B page 163 that it is possible to interchange the limit on λ , and the frequency integral. The corresponding term becomes

$$\lim_{\lambda \rightarrow \infty} \frac{i}{2\pi} \int_{-\infty}^{+\infty} d\omega e^{i\eta\omega} G^{(A)}(\mathbf{r}, \mathbf{r}'; \varepsilon + \omega) \left(\tilde{V}(\omega, \lambda) \cdot \tilde{\chi}^{(A)}(\omega, \lambda) \cdot \tilde{V}(\omega, \lambda) \right)(\mathbf{r}, \mathbf{r}') \quad (3.26a)$$

$$= \frac{i}{2\pi} \int_{-\infty}^{+\infty} d\omega e^{i\eta\omega} G^{(A)}(\mathbf{r}, \mathbf{r}'; \varepsilon + \omega) \left(\tilde{V}(0) \cdot \tilde{\chi}_{\text{stat-env}}^{(A)}(\omega) \cdot \tilde{V}(0) \right)(\mathbf{r}, \mathbf{r}'). \quad (3.26b)$$

Using the equations (3.11) and (3.12), $\tilde{V}(0)$ is built on the static limit of the reaction field such that, for all ω :

$$\lim_{\lambda \rightarrow \infty} \tilde{V}(\omega, \lambda) = \lim_{\lambda \rightarrow \infty} \left(V + V \cdot \chi_{g,\lambda}^{(B)}(\omega) \cdot V \right) \quad (3.27a)$$

$$= V + V \cdot \chi_g^{(B)}(0) \cdot V \quad (3.27b)$$

$$\stackrel{\text{DEF}}{=} \tilde{V}(0), \quad (3.27c)$$

where we have used the limit $\lambda \rightarrow \infty$ in the definition (3.15). $\chi_g^{(B)}(0)$ corresponds to the correct (without model) static susceptibility of the environment (B). For the susceptibility entering the Eq.(3.26b), $\tilde{\chi}_{\text{stat-env}}^{(A)}(\omega)$ corresponds to the interacting susceptibility of the subsystem (A), when its Coulomb interactions are renormalized by the static reaction field created by the environment (B). More exactly, using the limit when λ tends to infinity in the formula (3.14) leads to the following definition:

$$\lim_{\lambda \rightarrow \infty} \left[\tilde{\chi}^{(A)}(\omega, \lambda) \right]^{-1} = \lim_{\lambda \rightarrow \infty} \left(\left[\chi_0^{(A)}(\omega) \right]^{-1} - \tilde{V}(\omega, \lambda) \right) \quad (3.28a)$$

$$= \left[\chi_0^{(A)}(\omega) \right]^{-1} - \tilde{V}(0) \quad (3.28b)$$

$$\stackrel{\text{DEF}}{=} \left[\tilde{\chi}_{\text{stat-env}}^{(A)}(\omega) \right]^{-1}. \quad (3.28c)$$

To sum up, the $[\tilde{V} \cdot \tilde{\chi}^{(A)} \cdot \tilde{V}](\omega, \lambda)$ contribution in Eq.(3.25) is treated by considering directly the static response $\chi_g^{(B)}(\omega = 0)$ of the environment (B) in the renormalization of the Coulomb interactions of the central part (A). At the opposite, the contribution of the term $V_{\text{reac}}(\mathbf{r}, \mathbf{r}'; \omega, \lambda)$ is reminiscent of the static COHSEX approximation, and care must be taken to properly include the analog of the Coulomb-Hole (COH) term.

Following the treatment exposed in section 3.2.3.2, the pole energy λ is taken to infinity **after** performing the integration. Overall, the V_{reac} contribution to the integral (3.25), in the proper adiabatic limit $\lambda \rightarrow \infty$, can be reformulated as the sum of two self-energy terms such that

$$\lim_{\lambda \rightarrow \infty} \frac{i}{2\pi} \int_{-\infty}^{+\infty} d\omega e^{i\eta\omega} G^{(A)}(\mathbf{r}, \mathbf{r}'; \varepsilon + \omega) V_{\text{reac}}(\mathbf{r}, \mathbf{r}'; \omega, \lambda) = \Sigma_{V_{\text{reac}}}^{\text{SEX}}(\mathbf{r}, \mathbf{r}') + \Sigma_{V_{\text{reac}}}^{\text{COH}}(\mathbf{r}, \mathbf{r}'). \quad (3.29)$$

They are defined by

$$\Sigma_{V_{\text{reac}}}^{\text{SEX}}(\mathbf{r}, \mathbf{r}') = - \sum_{i \in (A)}^{\text{occ}} \phi_i(\mathbf{r}) \phi_i^*(\mathbf{r}') V_{\text{reac}}(\mathbf{r}, \mathbf{r}'; \omega = 0) \quad (3.30a)$$

$$\Sigma_{V_{\text{reac}}}^{\text{COH}}(\mathbf{r}, \mathbf{r}') = \frac{1}{2} \sum_{n \in (A)} \phi_n(\mathbf{r}) \phi_n^*(\mathbf{r}') V_{\text{reac}}(\mathbf{r}, \mathbf{r}'; \omega = 0), \quad (3.30b)$$

where the sum over (i) runs over occupied states of (A), while the sum over (n) runs over all its states. The formulas (3.30) provide the P_n^{COH} and P_n^{SEX} direct contributions of the static reaction field $V_{\text{reac}}(0)$ to the polarization energies

$$P_n^{\text{COH/SEX}} = \langle \phi_n | \Sigma_{V_{\text{reac}}}^{\text{COH/SEX}} | \phi_n \rangle. \quad (3.31)$$

Similarly to the standard [COHSEX](#) approximation, switching straightforwardly ω to zero for the reaction field in Eq.(3.29), or equivalently interchanging the limit on λ and the frequency integral on ω , would lead to neglecting P^{COH} . Only the Screened-Exchange ([SEX](#)) term P^{SEX} would survive. As discussed in section 3.3.3 page 106, it would lead to non-negligible errors.

Finally, it should be noticed that both in Eq.(3.26) and Eq.(3.29), only the static response of the environment (*B*) is required, via its static susceptibility $\chi_g^{(B)}(\omega = 0)$. At the opposite, the part of interest (*A*) is treated at a fully dynamical level. The [QM_{GW}/QM_{COHSEX}](#) approach enable us to directly probe the adiabatic limit for the environment. From the point of view of the efficiency, such an approach is promising because the computation of the large scale $\chi_g^{(B)}$ of the environment is performed only at one frequency $\omega = 0$. For systems large enough, this is one order of magnitude cheaper than a fully dynamical calculation, requiring with our code [BEDEFT](#) $n_\omega = 12$ frequencies. To go further in the reduction of computation times, the compression method detailed in chapter 2 can also be used for the computation of the susceptibility of the (*B*) part.

For this new description of the environment, I have developed new routines in [BEDEFT](#). For example, I have implemented functions for the user-interface to define some parameters. I have also created new methods dedicated to the creation, storage, and usage of the different matrices describing the effects of the environment, to perform the static embedding of this latter on the part of interest.

3.3 Application to dense phase of C_{60}

To compare the different embedding methods presented in section 3.2, and to assess the adiabatic approximation for the environment, I have first studied a dense phase of C_{60} . Following the studies of the chapter 2, we use the fragment approximation and each fullerene is considered as one fragment.

3.3.1 Technical details

The Kohn-Sham ([KS](#))-[DFT](#) calculations required as starting points for the *GW* ones are performed at the def2-TZVP level [64], with a PBE0 exchange-correlation functional [45, 46], via the ORCA package [57, 58]. We adopt the corresponding def2-TZVP-RI [108] auxiliary basis sets associated with the Coulomb-fitting Resolution of the Identity ([RI](#))-V approach [104, 106]. The molecular geometry for the C_{60} is also computed at the def2-TZVP PBE0 level. In our fragment approach, since the C_{60} molecule does not present any ground-state dipole, quadrupole, etc., we do not attempt to include environmental electrostatic effects in the ground state. We focus on the dynamics of screening at the *GW* level. The dynamical *GW* calculations are performed at the non-self-consistent G_0W_0 level, with our *GW* code [BEDEFT](#). They are done using the Contour Deformation ([CD](#)) scheme, based on $n_\omega = 12$ quadrature imaginary frequencies, plus an Analytic Continuation ([AC](#)) of the screened potential $W(\omega)$. More details can be found in section 1.3.2.10 page 56. For the fragments (*I*) of the environment described in an optimal polarization basis set $\{\gamma\}$, their gas phase

interacting electron susceptibility $\mathbf{X}_g^{(I)}(\omega)$ are compressed under the constraint $l_{max} = 1$ (see section 2.2.2 page 69). This leads to the preservation of the exact dipolar polarizability tensor.

The Face-Centered Cubic (FCC) C₆₀ dense phase is constructed taking experimental lattice parameters [155] ($a_0 = 14.17 \text{ \AA}$), neglecting orientational disorder. The considered C₆₀ surface is the (111) one. Photoemission Spectroscopy (PES) is very much surface sensitive due to the large absorption of incoming photons/electrons by the first layer. Fullerene surfaces have been extensively studied experimentally [160–164], providing valuable reference data. The fragment approximation preventing the formation of bands originating from wavefunction overlap, it is the so-called peak-to-peak gap that is studied, as detailed in section 2.3.1 page 75. This corresponds to the energy difference between the centers of the Highest Occupied Molecular Orbital (HOMO) and Lowest Unoccupied Molecular Orbital (LUMO) bands. Unless explicitly mentioned, the term “gap” refers to the peak-to-peak gap in the following sections. It should be noticed that the HOMO of a C₆₀ in gas phase is fivefold degenerate, and its LUMO threefold degenerate. Following the discussion in section 2.3.2 page 77, we always compute the peak-to-peak gap of the central C₆₀ as the difference between the average of its three LUMOs energy levels, and its five HOMOs energy levels.

3.3.2 Polarization basis set for dynamical susceptibilities

As explained in section 3.2.1 page 97, I have first assessed an additional approximation for the polarization basis vectors $\{\gamma\}$ of the fragments (I) in the environment. Namely, we have decided to keep the static optimal polarization basis vector $\{\gamma(\omega = 0)\}$ for all the n_ω frequencies of the AC-CD scheme, instead of refitting this basis set for each frequency. Only the matrix coefficients of the model susceptibility $\tilde{\mathbf{X}}_g^{(I)}(\omega)$ (see Eq.(3.5) page 98) are recomputed at each frequency.

To show the accuracy of this approach, I study the energy levels (HOMO², LUMO² and gap) for a central fullerene surrounded by two shells of neighbors in a bulk configuration (see inset FIGURE 3.1). I plot the error associated with replacing the gas phase interacting susceptibility $\mathbf{X}_g^{(I)}(\omega)$ by the model one, for the fragments (I) strictly beyond the first-shell of neighbors. This error is plotted as a function of the number N_γ of chosen static $\{\gamma(\omega = 0)\}$ vectors per fullerene.

The errors go below the meV for a number of $\{\gamma\}$ functions as small as 60, namely no more than the number of atoms in a fullerene. This can be compared to 5700, the size of the full def2-TZVP-RI auxiliary basis set per fullerene. These results suggest that we can keep the static polarization basis set $\{\gamma(\omega = 0)\}$ for all frequencies. In the following sections, calculations are done within this approximation. We also keep $N_\gamma = 60$ polarization vectors for fullerenes located strictly beyond the first-nearest-neighbors, while these latter and the central C₆₀ are described by their full auxiliary basis set. Due to the exact preservation of the fullerene dipolar polarizability tensor in the constrained fitting process, the induced error by this approach becomes negligible. This allows us to invert the Dyson equation (3.2) at each frequency for an environment involving hundreds of fullerenes, with very limited Central Processing Unit (CPU) and memory requirements.

²As discussed in section 3.3.1, the embedded HOMO (respectively LUMO) energy level is computed as the average over the five highest occupied (respectively three lowest unoccupied) QP energies.

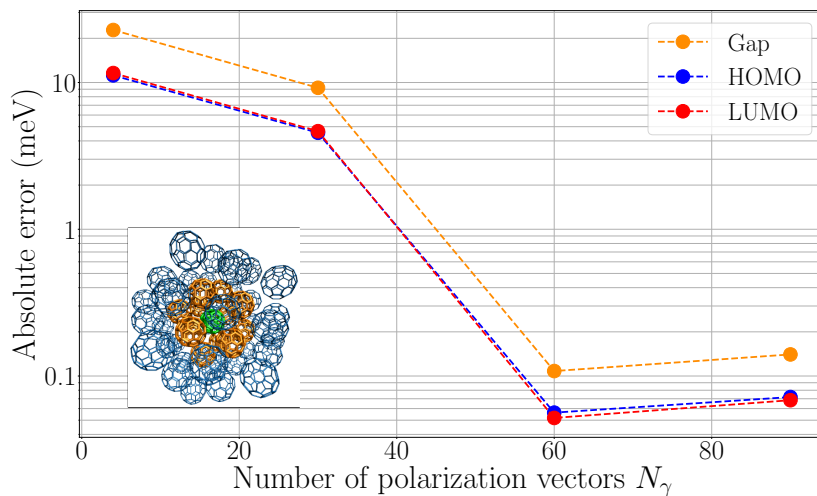


Figure 3.1: Absolute value of the errors on the gap, **HOMO** and **LUMO** energy levels, for a fullerene surrounded by its two first-shell of neighbors in a sphere (bulk) geometry. The susceptibility of the central (in green, inset) and 12 first-nearest-neighbors (in orange, inset) C_{60} are described by the full auxiliary basis (5700 orbitals). The susceptibility of each of the 42 C_{60} in the second-shell of neighbors (in blue, inset) is described by N_γ polarization vectors. Energies on the ordinates are in meV and log-scale. Errors for the **HOMO** are negative. Calculations performed at the fully dynamical G_0W_0 level both for the embedded and embedding subsystems.

3.3.3 Discussion on P_n^{COH} and P_n^{SEX}

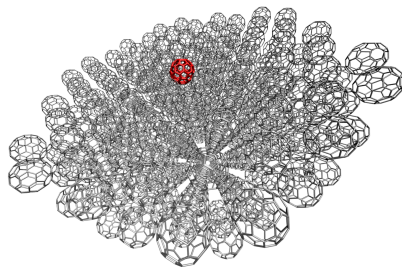


Figure 3.2: Representation of the hemisphere made of 302 C_{60} . The central surface C_{60} of interest (A) is in red, while the fullerenes of the environment (B) are in gray.

Before comparing the different methods for the description of the environment, we would like to discuss on the importance of computing both P_n^{COH} and P_n^{SEX} (see Eq.(3.31) page 103) in the $QM_{GW}/QM_{\text{COHSEX}}$ approach. To do so, we study a fullerene at the surface of a 302 fullerene hemisphere, as represented in FIGURE 3.2. More exactly, we analyze in table 3.1 these two terms, together with the total polarization energy (see Eq.(3.1) page 97) resulting from Eq.(3.25). Using the previous notations, the subsystem of interest (A) corresponds to the central C_{60} , while the 301 other C_{60} compose the environment (B). The shifts in energy are presented for the **HOMO**, **LUMO** energy levels and the gap of the fullerene, from the gas

Table 3.1: Decomposition of the $\text{QM}_{GW}/\text{QM}_{\text{COHSEX}}$ polarization energy (eV) for one fullerene molecule at the surface of a hemisphere of 302 fullerenes. The P_n^{COH} and P_n^{SEX} terms correspond to the two contributions defined in Eq.(3.31).

	P_n^{COH}	P_n^{SEX}	$P_n^{\text{COH+SEX}}$	P_n	$P_n - P_n^{\text{COH+SEX}}$
HOMO	-0.98	1.63	0.65	0.46	-0.19
LUMO	-1.00	0.26	-0.74	-0.54	0.20
Gap	-0.02	-1.37	-1.39	-1.00	0.39

phase to the center of the C₆₀ hemisphere.

We observe that while the reaction field P_n^{SEX} contribution accounts for most of the polarization energy for the peak-to-peak gap, this is not the case for individual energy levels. As a matter of fact, the P_n^{SEX} contribution to unoccupied states is small. Clearly, for the absolute position of individual levels, P_n^{COH} cannot be neglected. In other words, switching directly ω to zero for the reaction field in Eq.(3.29) page 103, resulting in the absence of P_n^{COH} , would lead to inaccurate results. A similar analysis can be found in Ref. [17] in the case of a molecule facing a graphene substrate, as well as in the reference [37]. This latter shows that the use of the full static COHSEX Hamiltonian provides a much better approximation to the GW operator, as compared to the static SEX-only term.

We note further that the $P_n^{\text{COH}} + P_n^{\text{SEX}} = P_n^{\text{COH+SEX}}$ direct contributions from the reaction field differ from the total polarization energies P_n . The differences, reported in the last column, represent the impact of the renormalization of the integrand along the imaginary axis, namely the frequency integral of $G^{(A)}[\tilde{V} \cdot \tilde{\chi}^{(A)} \cdot \tilde{V} - V \cdot \chi_g^{(A)} \cdot V]$. This points to the fact that a perturbative approach, where the gas phase GW energy levels are only corrected by the P_n^{COH} and P_n^{SEX} reaction field direct contributions, may lead to an error as large as about 40% considering *e.g.* the case of the peak-to-peak gap.

3.3.4 C₆₀ infinite surface at the G_0W_0 level

To assess the adiabatic approximation for the embedding subsystem, I have first computed polarization energies at the fully dynamical G_0W_0 level, without any adiabatic (instantaneous response) approximation for the environment. More exactly, in FIGURE 3.3, I plot the polarization energy P_{Gap} associated with the gap of a surface C₆₀ (in green in the inset), as a function of the number $N_{\text{C}_{60}}$ of fullerenes in a surrounding hemisphere. This will serve as a reference for calculations performed at the ΔCOHSEX or $\text{QM}_{GW}/\text{QM}_{\text{COHSEX}}$ levels, namely in an adiabatic limit for the surrounding fullerenes.

Due to screening, the surface fullerene gap is closing with a $(1/R)$ scaling law, with R the radius of the environment hemisphere. Equivalently, the gap closing follows an affine relation with respect to $N_{\text{C}_{60}}^{-1/3}$, where $N_{\text{C}_{60}}$ is the total number of fullerenes, as detailed in section 2.3.4 page 87. The quality of the affine fit indicates that the considered $N_{\text{C}_{60}}$ are large enough to enter the asymptotic $1/R$ scaling law regime. In the infinite limit, our dynamical calculations provide a polarization energy of -1.2 eV for the surface fullerene gap. This can be compared with experimental values of -1.1 eV [160], -1.2 eV [161, 162] or -1.4 eV [163,

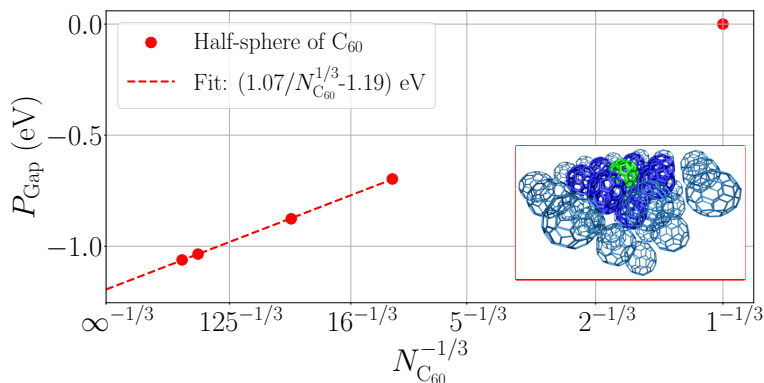


Figure 3.3: Evolution of the gap polarization energy for a C_{60} located at the surface of a FCC crystal hemisphere containing $N_{\text{C}_{60}}$ fullerenes (see inset with the “central” surface fullerene in green). The dashed line is the affine fit as a function of $N_{\text{C}_{60}}^{-1/3}$, which is proportional to $1/R$, with R the hemisphere radius. The red dots point to systems with $N_{\text{C}_{60}}=1, 10, 37, 302$ and 534. Calculations performed at the fully dynamical G_0W_0 level.

164] obtained by subtracting the experimental 4.9 eV gas phase fullerene HOMO-LUMO gap [86] to the experimental surface peak-to-peak gap.

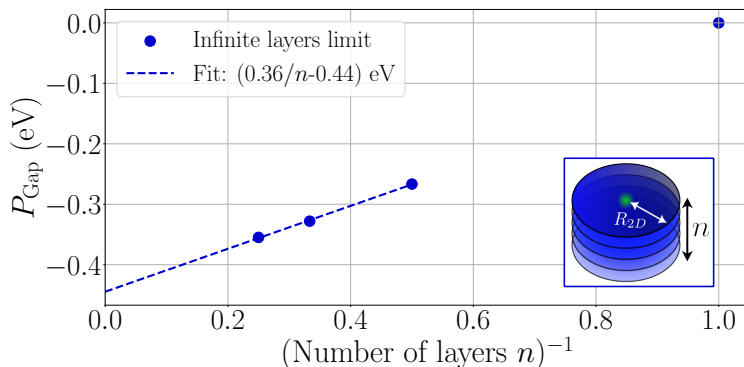


Figure 3.4: Evolution of the gap polarization energy P_{Gap} for a C_{60} located at the surface (in green in the inset) of a FCC fullerene crystal containing (n) layers, in a slab geometry. Taking as reference the gap of a fullerene in an infinite C_{60} monolayer, P_{Gap} is computed with respect to $1/n$. The dashed line represents the $[a/n + b]$ fit. Calculations performed at the fully dynamical G_0W_0 level.

Following exactly the same method as the one used for the FIGURE 2.13 page 89, I plot in FIGURE 3.4 the results to recover the same surface dynamical limit, by growing the crystal layer-by-layer as in a slab calculation. For a given (n) number of layers, the polarization energy is obtained by growing disks of C_{60} with increasing R_{2D} radius (see inset of FIGURE 3.4), extrapolating data with a $1/R_{2D}^2$ scaling law. Taking as a reference the polarization energy for a fullerene in a single fullerene layer ($P_{n=1} = -0.74 \text{ eV}$), the polarization energy follows an affine asymptotic law with respect to $(1/n)$ (see Eq.(2.36) page 89). One finds a

$P_{n=\infty} = -0.74 - 0.44 = -1.18$ eV surface polarization energy, in good agreement with the -1.19 eV of the hemisphere method.

3.3.5 Assessment of the adiabatic approximation for the environment

I now address the central issue of this chapter, namely the impact of assuming that the environment responds instantaneously to an electronic excitation in a surface fullerene. In the case of a fullerene inside a fullerene crystal, the decoupling of excitation energies between the central subsystem and its environment is clearly not satisfied. The resulting errors in the gap polarization energy P_{Gap} for the two static embedding approaches, as compared to fully dynamical calculations, are provided in FIGURE 3.5.

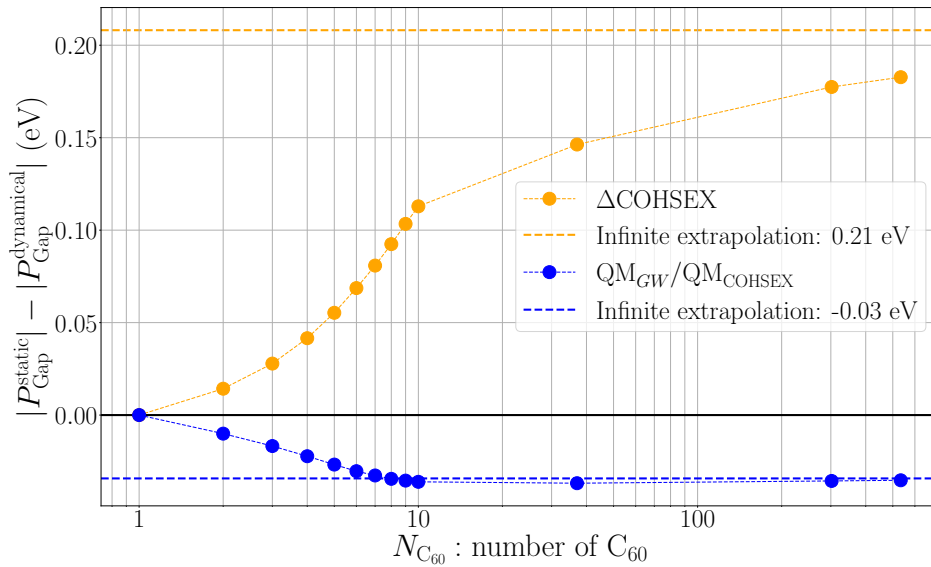


Figure 3.5: Errors, in eV, on the gap polarization energy P_{Gap} when using a static description of the environment within the ΔCOHSEX (orange dots) and $\text{QM}_{\text{GW}}/\text{QM}_{\text{COHSEX}}$ (blue dots) schemes, as compared to a fully dynamical calculation. Errors calculated as a function of the number of fullerenes in the hemisphere. The first and second shells of neighbors correspond to $N_{C_{60}} = 10$ and $N_{C_{60}} = 37$. The abscissa axis is in log-scale. Dashed lines represent the errors in the extrapolated infinite size limit.

Considering first the case of static ΔCOHSEX calculations (orange dots), we observe that the error in the gap polarization energy grows with the number of surrounding fullerenes. As a matter of fact, the error grows rapidly when completing the first shell of neighbors (up to $N_{C_{60}} = 10$), more slowly when completing the second shell of neighbors (up to $N_{C_{60}} = 37$), etc. By using the extrapolation methods detailed in section 3.3.4, we can compute this error for an infinite size surface. Asymptotically, the total error on the gap polarization energy amounts to 0.208 eV, namely, a very sizable 17.5% of error as compared to the fully dynamical calculation. Following the convention of the FIGURE 3.5, a positive error means that the ΔCOHSEX scheme overestimates the closing of the gap by screening.

I now address the case of the $\text{QM}_{\text{GW}}/\text{QM}_{\text{COHSEX}}$ scheme (blue dots), merging a fully

dynamical *GW* calculation for the subsystem of interest (*A*), namely the central surface C_{60} , with the proper static screening limit for the environment (*B*). The error is found to be significantly reduced as compared to the ΔCOHSEX scheme, with an asymptotic error of -0.034 eV . This amounts to a much reduced 2.9% error with respect to the fully dynamical asymptotic $P_{\text{Gap}}^{\text{dynamical}} = -1.19\text{ eV}$. As another important difference with the ΔCOHSEX approach, the error essentially builds within the first-shell of neighbors. This really means that in the $\text{QM}_{\text{GW}}/\text{QM}_{\text{COHSEX}}$ scheme, only the closely lying molecular fragments really need to be treated at the fully dynamical level, to totally reproduce the effect of the environment dynamical response.

I also plot similar results for the polarization energies associated with the individual **HOMO** and **LUMO** energy levels in FIGURE 3.6, showing globally the same behavior as the gap. The $\text{QM}_{\text{GW}}/\text{QM}_{\text{COHSEX}}$ approach induces less error than the ΔCOHSEX scheme, not only for the energy difference of the gap, but also for the absolute energy levels.

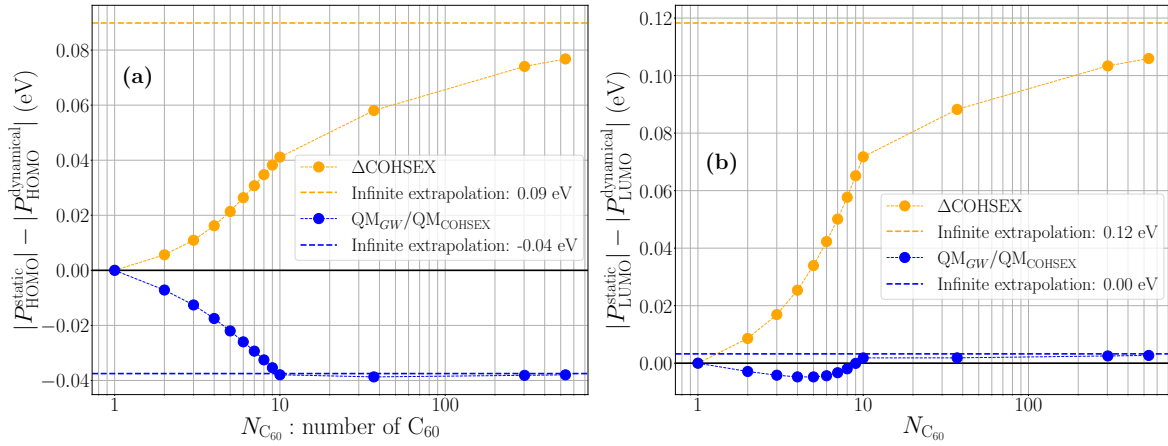


Figure 3.6: Errors on the polarization energy for the (a) **HOMO** and (b) **LUMO** energy levels, when adopting a static description of the environment within the ΔCOHSEX (orange dots) and $\text{QM}_{\text{GW}}/\text{QM}_{\text{COHSEX}}$ (blue dots) schemes, as compared to a fully dynamical calculation. Errors (in eV) are given as a function of the number of fullerenes. The abscissa axis is in log-scale. Dashed lines represent the errors in the extrapolated infinite size limit.

To better analyze the values of the errors, I conduct again in FIGURE 3.7 the same study, but I focus on the relative error, given in percentage. The ΔCOHSEX method leads to increasing relative error with respect to the number of C_{60} , while at the opposite, the $\text{QM}_{\text{GW}}/\text{QM}_{\text{COHSEX}}$ scheme results into decreasing relative error.

The reason why the static approximation for the environment induces larger errors at short-range, namely for polarizable fragments located close to the central subsystem of interest, was hinted at in Ref. [17]. Focusing, *e.g.*, on the ϕ_H **HOMO** eigenstate of the subsystem of interest (*A*), with **QP** energy ε_H , the fully dynamical **SEX**-like contribution³ to

³Such a contribution can be computed by taking into account the fully dynamical susceptibility of the environment (*B*), namely without using a simple pole model to describe this latter. In this case, using the same method as the one to compute the formula (1.126) page 53, the static equation (3.30a) can be adapted to lead to the dynamical ones (3.32).

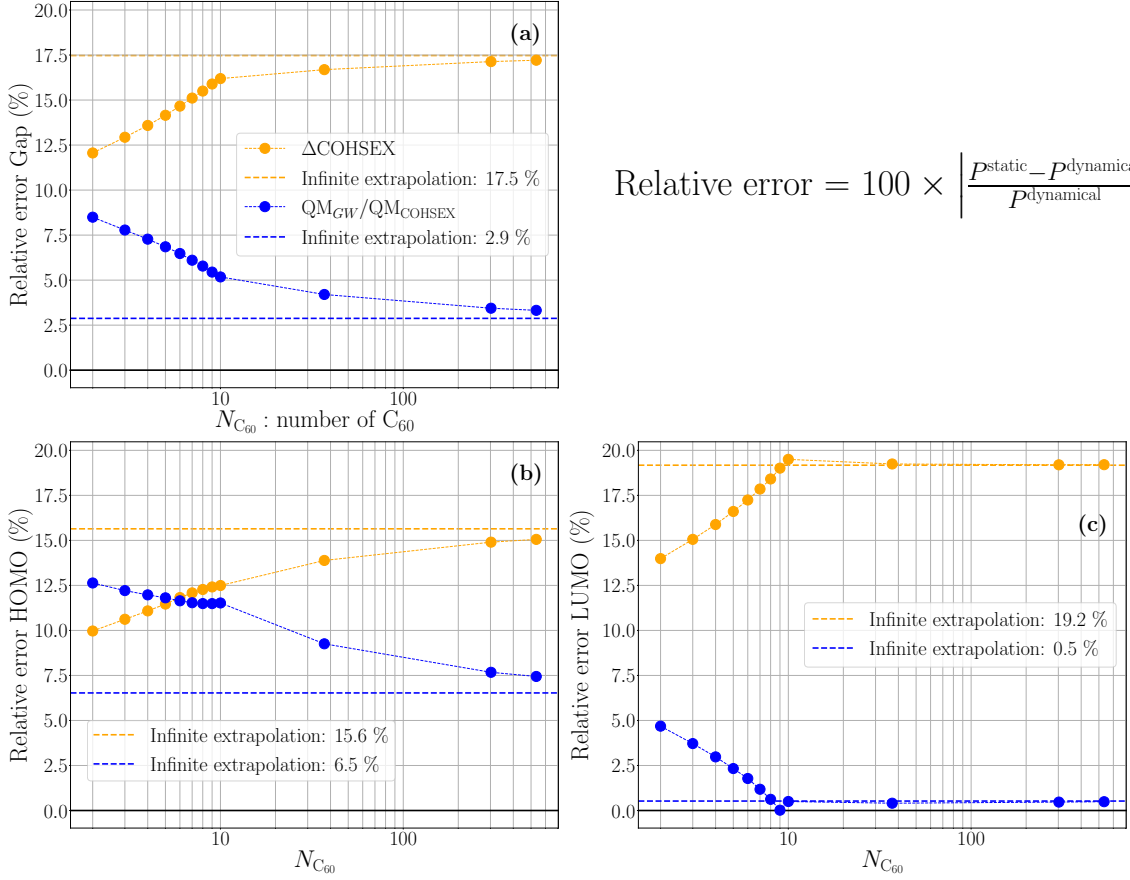


Figure 3.7: Relative errors on the polarization energy for (a) the gap, (b) the HOMO and (c) LUMO energy levels, when using the reaction field static limit within the ΔCOHSEX (orange dots) and $\text{QM}_{\text{GW}}/\text{QM}_{\text{COHSEX}}$ (blue dots) schemes, as compared to a fully dynamical calculation. The error is calculated as a function of the number of fullerenes. Relative errors are in percentage, and the abscissa axis in log-scale. Dashed lines represent the errors in the extrapolated infinite size limit.

the polarization energy reads

$$P_H^{\text{SEX}}(\varepsilon_H) = \langle \phi_H | \Sigma_{\text{V}_{\text{reac}}}^{\text{SEX}}(\varepsilon_H) | \phi_H \rangle \quad (3.32a)$$

$$= - \sum_{i \in (A)}^{\text{occ}} \langle \phi_i \phi_H | V_{\text{reac}}(\varepsilon_H - \varepsilon_i) | \phi_i \phi_H \rangle. \quad (3.32b)$$

In the limit of a smoothly varying reaction field over the extent of the central subsystem, orthogonalization of the MOs reduces the sum to the ($i=\text{HOMO}$) terms, and only the static $V_{\text{reac}}(\varepsilon_H - \varepsilon_H = 0)$ reaction field contribution is required. The same reasoning holds for the P_H^{COH} term. Qualitatively, adding far standing fullerenes amounts to adding components of the reaction field that are more and more smoothly varying on the central subsystem. Thereby, these distant fragments present decreasing contribution to the total error associated with the static limit for the environment. In the same smoothly varying limit, for example for

the polarization energies of an hemisphere of 302 C_{60} in table 3.1 page 107, one observes that the P^{SEX} contribution tends to vanish for the unoccupied states. For the occupied states, the P^{COH} term tends to $(-1/2)$ of the P^{SEX} contribution [17].

In terms of efficiency, it should be noticed that the fragment approximation transfers most of the computer time requirements to the cubic-scaling inversion of the Dyson equation (3.2) for the susceptibility χ . In the fully dynamical scheme, such an inversion must be performed n_ω times, with n_ω the number of frequencies sampling the imaginary axis ($n_\omega=12$ in this chapter). In the $\text{QM}_{GW}/\text{QM}_{\text{COHSEX}}$ scheme, the construction of the environment static susceptibility $\chi^{(B)}(\omega=0)$ requires inverting only once the corresponding Dyson equation. In the limit of systems with large scale environment, the dynamical scheme is thus formally n_ω times more expensive than the $\text{QM}_{GW}/\text{QM}_{\text{COHSEX}}$ one. In practice, the calculation of the (static) bare Coulomb potential entering the Eq.(3.2), with a quadratic-scaling, is also expensive in time. However, such a cost is independent of n_ω , because the corresponding matrix is computed once before being stored for the other frequencies. In the present stage of implementation, this leads for the largest studied system in this chapter, namely an embedded GW calculation over 534 fullerenes, to calculations in 420 CPU hours and 150 CPU hours at the fully dynamical G_0W_0 and $\text{QM}_{GW}/\text{QM}_{\text{COHSEX}}$ levels, respectively. This represents a factor ~ 3 between the two approaches.

To further explore the impact of the adiabatic limit for the polarizable medium, we consider now an environment of fictitious fullerenes where their **KS-DFT HOMO-LUMO** gap has been artificially changed in a scissor fashion. More exactly, for each fragment (I) in the environment, I move rigidly in energy its occupied manifold with respect to its unoccupied one. Such modified **KS** energy levels are used to construct their corresponding gas phase susceptibility diagonal blocks $\mathbf{X}_g^{(I)}(\omega)$, in the fully dynamical, ΔCOHSEX and $\text{QM}_{GW}/\text{QM}_{\text{COHSEX}}$ limits. The PBE0 energy levels for the central (surface) C_{60} are not modified (PBE0 **HOMO-LUMO** gap of 2.99 eV).

I plot in FIGURE 3.8 the associated error on the gap polarization energy, as a function of the modified **KS-DFT** gap. I keep constant here the number of surrounding fullerenes ($N_{C_{60}} = 534$). As expected, the absolute value of the error increases/decreases when the input **HOMO-LUMO** gap of the surrounding fullerenes is decreased/increased with respect to the unmodified central surface fullerene. When the gap of the surrounding fullerenes becomes larger, the adiabatic approximation for the environment becomes formally better validated and the error induced by the static approximation is reduced. Again, both in the small and large environment gap limits, the $\text{QM}_{GW}/\text{QM}_{\text{COHSEX}}$ scheme (blue dots) provides the smallest error, with a 3.9% maximum relative error in the limit of a small environmental gap. In such a limit, the adiabatic approximation for the surrounding medium is expected to fail. I also provide in FIGURE 3.9 the same plot but for the individual **HOMO** and **LUMO** energy levels. The graphs indicate that there is no cancellation of errors between the **HOMO** and **LUMO** data, and globally the absolute value of the errors at the ΔCOHSEX and $\text{QM}_{GW}/\text{QM}_{\text{COHSEX}}$ levels increase when the gap of the surrounding medium C_{60} decreases. This is consistent with the idea that treating the environment in the adiabatic limit is an approximation that becomes questionable if the surrounding medium has a smaller gap than the central subsystem. One notes however that the increase in the error remains limited.

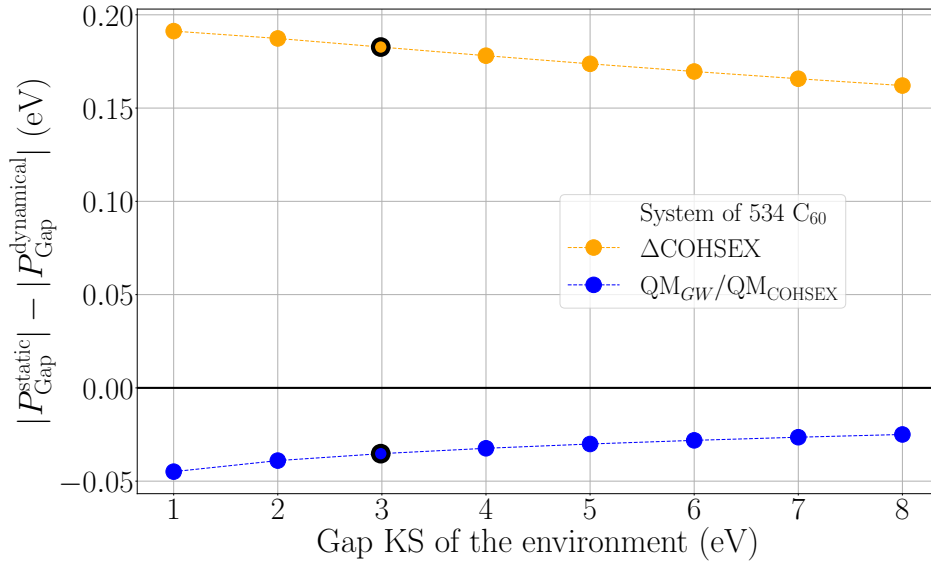


Figure 3.8: Errors, in eV, on the gap polarization energy when using a static limit for the description of the environment, as compared to a fully dynamical calculation. The error is calculated as a function of the fictitious gap of the surrounding fullerenes (see text). The color code is the same as in FIGURE 3.5. Data with black bold edges correspond to the true Kohn-Sham (KS)-DFT PBE0 fullerene gap (2.99 eV).

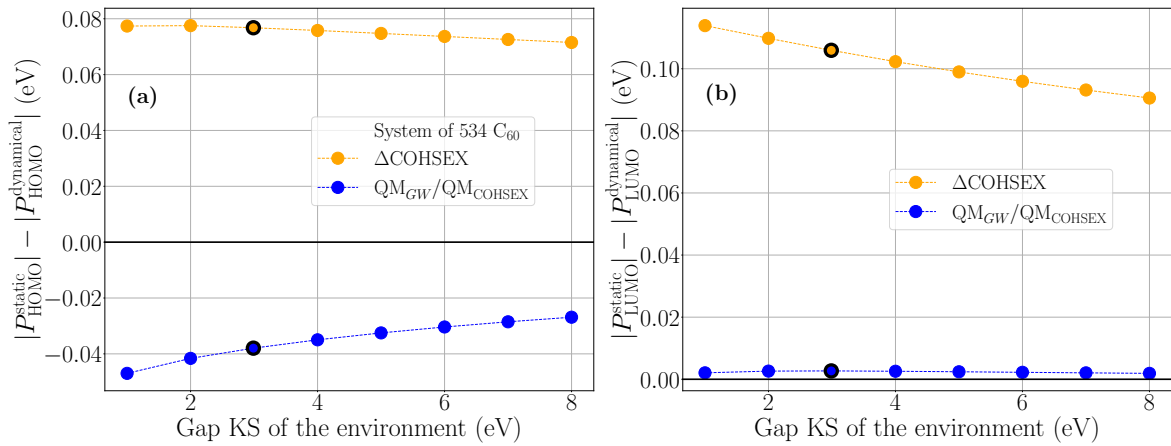


Figure 3.9: Same as FIGURE 3.8, but for the errors on the polarization energy for (a) the HOMO and (b) the LUMO energy levels. Note that we subtract the absolute value of the polarization energies (the polarization energy for the HOMO/LUMO energy level is always positive/negative).

3.3.6 The $QM_{GW}/QM_{GW}/QM_{COHSEX}$ approach

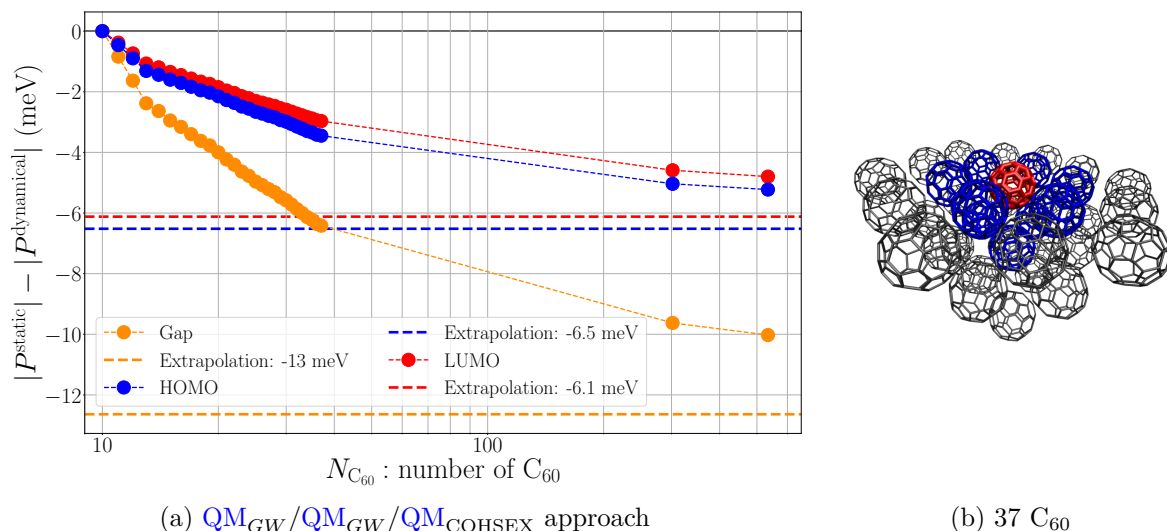


Figure 3.10: (a) Errors, in meV, on the polarization energy of the gap (orange dots), the HOMO (blue dots) and the LUMO (red dots) energy levels of the central surface C_{60} , in a $QM_{GW}/QM_{GW}/QM_{COHSEX}$ approach. Taking as a reference fully dynamical calculations, errors are computed as a function of the number of fullerenes $N_{C_{60}}$ in the hemisphere. Abscissa axis is in log-scale. Dashed lines represent the errors in the extrapolated infinite size limit. The first and second shells of neighbors correspond to $N_{C_{60}} = 10$ and $N_{C_{60}} = 37$. Contrary to previous graphs, the errors are null for $N_{C_{60}} = 10$, because the central C_{60} (in red in (b)) and its 9 first-nearest neighbors (in blue in (b)) are described at the fully dynamical GW level. The fragment farther away (in gray in (b)) are treated at the static $COHSEX$ level. (b) Schematic representation of the hemisphere made of 37 C_{60} .

Finally, to try to improve the accuracy of the QM_{GW}/QM_{COHSEX} approach, I have increased the proportion of the system treated at the fully dynamical GW level. Following the notations of section 3.2.3 page 99, the part of interest (A) is now composed of the fragment of interest, plus some others. In the particular example of the half-sphere of C_{60} , the group (A) is made of the central fullerene (in red in FIGURE 3.10b), of which is computed the polarization energies, plus its 9 first-nearest neighbors (in blue in the same figure). The other C_{60} , in gray, are still treated at the static $COHSEX$ level. To emphasize the particular treatment of the central C_{60} , such a scheme can be regarded as a $QM_{GW}/QM_{GW}/QM_{COHSEX}$ approach.

In the FIGURE 3.10a, I plot the errors induced by this method on the polarization energies of the central C_{60} . Taking as reference the fully dynamical GW calculations, I have computed the error on the gap, the HOMO and the LUMO energy levels. In comparison to the results in the infinite size limit of the FIGURE 3.6, at the QM_{GW}/QM_{COHSEX} level, the error on the LUMO energy level is not improved. At the opposite, we can notice a reduction by a factor 6 of the error on the HOMO energy level, to reach a value of -6.5 meV. The same error for the gap, in comparison to the FIGURE 3.5, is also reduced to a value of -13 meV. This represents

a smaller relative error of 1.1%.

This example shows that treating the first-nearest-neighbors only at the fully dynamical level, while assuming the adiabatic limit for farther lying fragments, allows improving the accuracy of the calculations.

3.4 A water molecule inside a metallic nanotube

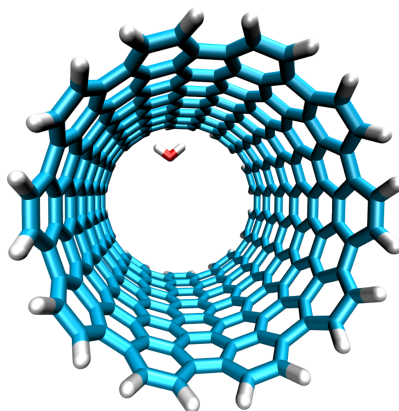


Figure 3.11: Geometry of the $\text{H}_2\text{O}@(\text{10},\text{10})$ nanotube section model system. The nanotube section contains 280 carbon atoms with hydrogen-passivated edges. The water molecule adopts a close to “one-leg” geometry [173] with an OH bond pointing towards a hexagon center.

We conclude this exploration by considering the case of a water molecule inserted inside a long section of a metallic (10, 10) carbon nanotube, as represented in FIGURE 3.11. The behavior of water inside carbon nanotubes has been the subject of many studies, targeting a better understanding of the structure of confined water and the nature of friction at the water/tube interface [174], for applications to energy generation through inverse osmosis and water desalinization [175, 176]. Such studies stand much ahead of the present exploration aiming at better understanding the impact of dynamical versus static screening. The case of a metallic surrounding medium, with a vanishing gap, offers a stringent test for the assumption that the environment responds instantaneously to an electronic excitation in the central subsystem, namely here the water molecule.

For this water-inside-nanotube system, containing 323 atoms, the tube relaxation has been performed with the SIESTA package [177], for the sake of efficiency. This has been done at the double-zeta plus polarization level within the Local Density Approximation (LDA) [33]. Keeping the nanotube positions frozen, the water molecule relaxation has been achieved using the van der Waals Density Functional (vdW-DF) of Dion and coworkers [178, 179]. Concerning our many-body calculations, since we target the response of a metallic tube, we favored input KS eigenstates generated at the LDA level, with the ORCA package, over hybrid functionals. We adopt the double-zeta def2-TZVP basis set, together with the def2-TZVP-RI auxiliary basis set. For the sake of efficiency, the nanotube susceptibility has been

calculated within our recently implemented cubic-scaling Real Space (RS) imaginary-time approach [101, 114], as detailed in section 1.3.2.10 page 56. This induces errors at the meV level for QP energies, as compared to a def2-TZVP/def2-TZVP-RI calculation within our standard Coulomb-fitting RI-V implementation. The fully dynamical G_0W_0 calculation for the water-plus-nanotube system, involving the calculation of the total susceptibility $\chi(\omega)$ for $n_\omega = 12$ imaginary frequencies, required no more than a thousand CPU hours in total at the def2-TZVP/def2-TZVP-RI level [180].

Due to its finite size, the nanotube LDA gap is finite, amounting to 0.3 eV. Even though not strictly metallic, the nanotube gap is significantly smaller than that of the water molecule (6.92 eV, LDA value). The water and nanotube are treated as separate fragments, namely we do not allow hybridization between them and focus on long-range screening. The closing of the water molecule HOMO-LUMO gap, from the gas phase to the nanotube-intercalated geometry, amounts to -2.09 eV, -2.23 eV and -2.41 eV, at the fully dynamical, QM_{GW}/QM_{COHSEX} and $\Delta COHSEX$ schemes, respectively. Again, the QM_{GW}/QM_{COHSEX} scheme yields the smallest error ($\sim 7\%$) as compared to the $\Delta COHSEX$ approach ($\sim 15\%$ error). This is consistent with the data of FIGURE 3.8 in the limit of a small gap environment. The error on the gap polarization energy benefits here, however, from a small compensation of errors, between the polarization energies of the two frontier energy levels. At the $\Delta COHSEX$ and QM_{GW}/QM_{COHSEX} levels, the P_{HOMO} is overestimated by 357 meV and 225 meV respectively, as compared to the fully dynamical calculation, a rather large variation. However, the absolute value of P_{LUMO} is underestimated by 37 meV and 86 meV, respectively.

In conclusion, we observe that even in a situation where the environment adiabatic treatment is expected to fail, a static description of the polarizable medium yields an error on the gap polarization energy smaller than 7% when correctly treated. This tends to indicate that what should matter is the relative position of the neutral excitation spectra, namely the poles of the susceptibility, for the embedded and embedding subsystems. In that respect, comparing just the HOMO-LUMO gaps may not be an accurate criterion.

3.5 Conclusion

Within the framework of an embedded QM/QM' GW framework, I have studied in this chapter the validity of the adiabatic approximation for the environment. Namely, I have assessed the assumption that the electronic degrees of freedom in the environment (treated at the QM' level) respond instantaneously to an excitation in the central subsystem (treated at the QM level). In practice, this amounts to restricting the environment electronic susceptibility to its low frequency $\chi_g^{(B)}(\omega \rightarrow 0)$ limit, where (B) points to the environment. As a first test case, I have in particular explored a fullerene at the surface of a fullerene crystal. This is a paradigmatic organic crystal where there is no decoupling in the excitation energy spectrum between the embedded and embedding subsystems. Furthermore, I have studied the case of a water molecule inside a metallic carbon nanotube section regarded as the environment. In such a situation, the adiabatic limit for the environment is formally not expected to be valid.

Reference calculations are performed at the QM_{GW}/QM_{GW} level, where both embedded and embedding subsystems are treated at the fully dynamical level, within a fragment

approximation. Our findings are that the proper adiabatic limit for the environment consists of a $\text{QM}_{GW}/\text{QM}_{\text{COHSEX}}$ approach. In this scheme, the reaction field from the environment is treated in the same fashion as the static COHSEX approximation to the full GW self-energy. Maximum errors in the gap polarization energy, that is the energy shift of the gap from the isolated (gas) to the embedded phase, are found to remain below 10%. If better accuracy is desired, we found that treating the first-nearest-neighbors only at the fully dynamical level, while assuming the adiabatic limit for farther lying fragments, allows us to reduce the error. Such a scheme may be regarded as a $\text{QM}_{GW}/\text{QM}_{GW}/\text{QM}_{\text{COHSEX}}$ approach.

In contrast, the scheme employed in previous work, namely the ΔCOHSEX approach, is found to induce much larger errors. This method consists of following the shift of the energy levels from a gas phase $\text{QM}_{\text{COHSEX}}$, to an embedded $\text{QM}_{\text{COHSEX}}/\text{QM}_{\text{COHSEX}}$ calculation. This represents an approach where both the embedded and embedding subsystems are treated consistently in the static COHSEX limit. As compared to a fully dynamical GW calculation, the static COHSEX scheme is well-known to lead to inaccurate energy levels of the central (embedded) subsystem. The comparison to the more accurate $\text{QM}_{GW}/\text{QM}_{\text{COHSEX}}$ calculation tends to show that such an inaccuracy does not fully cancel out, between the gas and embedded systems.

In the last two chapters, the fragment approach has been applied to study molecular systems, with well-separated subsystems. In the following chapter 4, I show that such a method can also be relevant to study point defects in an insulator covalent crystal.

Polarization energies of point defects in hexagonal boron nitride via the fragment approach

Contents

Résumé	120
Summary	121
4.1 Introduction	122
4.2 Methodology	123
4.2.1 Fragmentation of hexagonal Boron Nitride (<i>h</i> -BN)	123
4.2.2 Environmental effects: observables of interest	125
4.2.3 Technical details	125
4.2.4 Geometries of the fragments	127
4.3 Fragmentation of the monolayer	129
4.4 Fragmentation of the multilayers	134
4.5 Point defects in the surface and bulk limit	136
4.6 Universality of the polarization energies among the different defects	139
4.7 Defect levels with respect to <i>h</i>-BN valence band edge	141
4.8 Conclusion	145

This chapter is largely inspired from our work published in Physical Review Materials [181].

Résumé

Ce chapitre illustre l'application de la méthode fragment, développée dans les deux chapitres précédents, à l'étude des niveaux d'énergie de défauts ponctuels dans du nitrure de bore hexagonal (*h*-BN). Alors qu'une telle étude est généralement réalisée avec des conditions aux limites périodiques, créant des interactions entre les défauts périodiquement translétés, nous cherchons ici à atteindre la vraie limite diluée. L'application de la méthode fragment à un système covalent semble bien moins naturelle que dans le cas de systèmes moléculaires faiblement liés.

La section 4.2 présente la méthodologie adoptée pour cette étude, basée sur l'utilisation de fragments de forme hexagonale de nitrure de bore, permettant par pavage de reconstruire du *h*-BN monocouche, ou multicouche. La fragmentation est appliquée entre les couches de *h*-BN, mais également à l'intérieur de chacune d'entre elles. Ceci nous permet d'étudier l'évolution des niveaux d'énergie d'un défaut, de la phase gaz (un seul fragment avec défaut) à une phase environnée, où l'opérateur susceptibilité du *h*-BN environnant est reconstruit par morceaux. Les défauts d'intérêt, à savoir le dimère de carbone CC, son variant CC- $\sqrt{7}$, et le défaut avec lacune $C_B V_N$ sont présentés dans la partie 4.2.4.

Dans la section 4.3, nous étudions tout d'abord les niveaux d'énergie des défauts dans la limite diluée de la monocouche. L'utilisation d'une loi asymptotique affine en fonction de $1/N_{\text{at}}$, avec N_{at} le nombre total d'atomes de bore et d'azote de la monocouche considérée, permet de calculer les niveaux d'énergie de défaut dans cette limite diluée. Les résultats obtenus à l'aide d'un seul fragment de taille croissante, avec défaut, ou ceux calculés par la méthode fragment avec des hexagones d'une centaine d'atomes, montrent un accord de l'ordre de la dizaine de meV au niveau $G_0 W_0$ ou statique COHSEX. La possibilité de découper la monocouche covalente en fragments pour le calcul de la susceptibilité est attribué au caractère très courte portée de cette fonction de réponse dans les isolants. La préservation par la fragmentation des effets d'écrantage à moyenne et longue portée est également illustrée par l'étude du ratio entre le potentiel de Coulomb écranté W statique, et celui non renormalisé V .

Comme dans les chapitres précédents, la possibilité de fragmenter le système pour le calcul de la susceptibilité permet d'atteindre des tailles de systèmes remarquables. L'approche fragment permet d'étudier bien plus facilement la limite diluée en surface, ou en volume, des niveaux d'énergies de défauts. Une telle limite est obtenue à l'aide d'une loi asymptotique sur l'énergie de polarisation $P = P_0/n + P_\infty$, où n correspond au nombre de couches du système considéré. L'étude des différents défauts montre dans la section 4.6 que les coefficients P_0 et P_∞ sont relativement universels. Ils dépendent du milieu environnant et de la position du défaut (en surface ou en volume), mais très peu du type de défaut considéré.

Nos calculs prenant en compte tous les électrons pour des systèmes de taille finie, les niveaux d'énergie des défauts sont directement calculés par rapport au niveau du vide. Toutefois, la partie 4.7 est l'occasion de calculer les variations de ces niveaux de quasiparticule par rapport au haut de la bande de valence du *h*-BN. L'étude des états électroniques étendus par l'approche fragment est bien plus délicate.

Summary

This chapter is dedicated to the application of the fragment approach, developed in the two previous chapters, to the study of energy levels of point defects in hexagonal Boron Nitride (*h*-BN). While such a problem is traditionally tackled using periodic boundary conditions, leading to interactions between the periodically translated defects, we would like to reach the true dilute limit. Furthermore, the use of the fragment method for a covalent system seems much less justified as compared to weakly bound organic crystals.

Section 4.2 outlines the methodology adopted in this study, based on the use of hexagonal fragments of boron nitride used to reconstruct very large size *h*-BN mono- or multi-layer systems. The fragmentation process is applied between layers of *h*-BN, but also inside each of them. This allows us to study the evolution of the energy levels of a defect, from the gas phase (only one defected fragment) to the embedded phase, where the embedding *h*-BN susceptibility is reconstructed thanks to the fragment approach. The defects of interest, namely the carbon-dimer CC, its variant $CC-\sqrt{7}$, and the nitrogen-vacancy $C_B V_N$, are presented in section 4.2.4.

In section 4.3, we study the defects in the monolayer dilute limit. Thanks to an asymptotic affine law with respect to $1/N_{\text{at}}$, with N_{at} the total number of boron and nitrogen atoms of the considered monolayer, we can compute the associated energy levels in this true dilute limit. The results computed via the study of one defected fragment of increasing size, and the ones obtained via the fragment method with hexagonal subsystems of a hundred of atoms, show a good agreement of the order of a ten of meV at the G_0W_0 and static COHSEX levels. The possibility to cut the monolayer into small pieces for the calculation of the susceptibility originates in the very-short range nature of this response function in insulators. The preservation of middle- to long-range screening effects upon fragmentation is also illustrated through the study of the ratio between the static screened Coulomb potential W and the bare one V .

As in previous chapters, the use of the fragmentation approach in the construction of the susceptibility allows us to study very large scale systems at the many-body level. This enables us to study very efficiently the dilute limit of defect energy levels in the surface and bulk configurations. The dilute bulk limit is reached thanks to an asymptotic law for the polarization energy $P = P_0/n + P_\infty$, where n corresponds to the number of layers of the considered system. The study of various defects shows in section 4.6 that the P_0 and P_∞ coefficients are almost universal. They depend on the type of polarizable host and the position of the defect (surface or bulk), but hardly on the defect type.

Our all-electron finite-size calculations provide energy levels directly related to the vacuum level. However, we compute in section 4.7 the defects quasiparticle levels with respect to the valence band maximum. The study of delocalized electronic states with the fragment approach is less reliable.

4.1 Introduction

In the previous chapters 2 and 3, the fragment approach has essentially been applied to C_{60} in crystal-like structures, where each molecule is well-separated from the others. In this present chapter, we would like to go further by using this scheme for other types of systems. More particularly, we start from the fact that the one-body Green's functions $G(\mathbf{r}, \mathbf{r}'; \omega)$ presents an exponential decay in Real Space (RS) in the case of insulators [182]. The corresponding susceptibility $\chi_0(\mathbf{r}, \mathbf{r}'; \omega)$ is thus also very short-ranged, following an exponential decay thanks to the Eq.(1.120c) page 51. Such a behavior seems to be compatible with the fragment approximation. In this context, we have decided to study polarization energies of point defects in hexagonal Boron Nitride (*h*-BN), which is a layered covalent insulator system.

This kind of defects in such a polarizable medium has generated much research activity both at the experimental [5, 183–195] and theoretical [196–221] level to better understand their unique photoluminescent properties. The large gap of the host *h*-BN allows a variety of localized occupied and unoccupied defect states controlling the absorption and emission spectrum across the visible range. While the optical properties of defects can be used as a way to unravel their chemical nature, thanks to the comparison between theoretical and experimental optical emission energies and line shapes, much less is experimentally known about their electronic energy levels as measured by photoemission. Still, optical properties are strongly related to an accurate description of defect electronic properties, together with the strength of the excitonic electron-hole screened interaction. Furthermore, the position of the defect energy levels in the host gap, in conjunction with structural reorganization energies, allows us to predict its charge state as a function of the chemical potential [212].

The exploration with *ab initio* simulations of the electronic properties of defects in the true dilute limit, corresponding to one unique point defect in an infinite size environment, remains a difficult task. The most common Periodic Boundary Conditions (PBC) calculations, with defects periodically repeated, require rather large unit cells to minimize spurious defect-defect interactions. This is all the more a difficulty in the case of charged defects for which Coulomb truncation techniques must be used to annihilate long-range Coulomb interactions between periodic images [222]. Furthermore, at the efficient Kohn-Sham (KS) Density-Functional Theory (DFT) level, the position of the electronic energy levels is known to be strongly sensitive to the choice of the exchange-correlation functional, limiting the predictive nature of the related calculations. In the absence of experimental photoemission data characterizing defect levels, this may lead to difficulties on the best strategy to adopt. Recently, a scheme based on enforcing Koopman's like conditions [223] illustrated the importance of changing the amount of exact exchange at the generalized KS-DFT level as a function of the number of *h*-BN layers [207]. At the *GW* level, following pioneering studies for defects in three-dimensional (3D) systems [224–229], calculations for defects in cubic [230] and hexagonal [196–199, 207, 213, 218–221] BN have been conducted in a few groups.

As a caveat of properly accounting for charging effects, *GW* calculations also encounter difficulties associated with spurious long-range Coulomb interactions between images in the case of PBC. As analyzed in the case of defected *h*-BN systems [199], two-dimensional (2D) *GW* calculations converge slowly, both with the amount of vacuum between repeated images and with the in-plane unit-cell size. While Coulomb truncation techniques can be used to avoid

spurious interlayer interactions for the monolayer limit [199, 231, 232], eliminating interactions between periodically repeated defects within a layer, without affecting the in-plane screening by the *h*-BN host, stands as a difficult challenge. In the bulk limit, the necessity to include a sufficient number of pristine layers in the *c*-axis direction further increases computational cost. As a matter of fact, *GW* calculations for defects in *h*-BN were conducted essentially for monolayers [196, 198, 199, 207, 213, 218, 220, 221], with one study of defected three-layer systems [207] and one bulk study with two-layers per unit-cell [219].

In this chapter, we propose an alternative finite-size cluster approach, based on the fragment approximation. This enables us to perform *GW* calculations of defect energy levels in *h*-BN, reaching the monolayer, few-layers, surface, and bulk dilute limit conditions. Defected and pristine flakes with increasing lateral size are stacked, reaching sizes large enough to safely extrapolate to the infinite limit for a given number of layers. We show that convergence with respect to in-plane dimensions can be dramatically facilitated with the fragment approximation. This allows us to reconstruct each layer by patching large *h*-BN fragments, neglecting wavefunctions overlap between fragments on the same or neighboring layers. We can study at the many-body level systems containing several thousand atoms, reaching sizes large enough to reliably extrapolate to the infinite 2D or 3D limits. Defect energy level variations from the monolayer to a *n*-layer system follow a simple $(P_0/n + P_\infty)$ polarization energy behavior. The slope and asymptotic coefficients P_0 and P_∞ characterize mainly the host and the position of the defect (surface or bulk), but hardly the defect type. Our study rationalizes the evolution of defect energy levels as a function of the number of layers. As a result, data obtained for the monolayer, or very-few layer systems, can be easily extrapolated to the surface or bulk limit without the need to perform additional many-body calculations.

4.2 Methodology

This section is dedicated to the general methodology adopted throughout this chapter, to study the energy levels of point defects in *h*-BN within the *GW* formalism. More particularly, we would like to tackle the problem of the true dilute limit of defect, corresponding to one unique point defect in an undefected infinite size environment.

4.2.1 Fragmentation of *h*-BN

The price of calculating the screened Coulomb potential W for large multilayer systems (like the *h*-BN) in the dilute defect limit is prohibitively expensive. To reduce such a cost, we have decided to resort to the fragment approach, as detailed in section 2.2.1 page 67. In such an approximation, one assumes that the system is partitioned into subsystems (labeled also fragments or flakes below) with weakly overlapping wavefunctions. The matrix representation $\mathbf{X}_0(\omega)$ of the non-interacting susceptibility $\chi_0(\omega)$, in the auxiliary basis set associated to the Resolution of the Identity (RI) technique (see section 1.3.2.10 page 56), becomes block diagonal. Its (I)th block, denoted $\mathbf{X}_0^{(I)}(\omega)$, corresponds to the gas phase, *i.e.* isolated, non-interacting susceptibility of the (I)th fragment. This represents a considerable saving since in the fragment limit the cost of calculating the overall χ_0 does not grow quartically with

system size, but only linearly. If the fragments are identical, *e.g.* just translations of the same fragment with identical susceptibility blocks, calculating the overall χ_0 is independent of the system size. As illustrated in the two previous chapters, such a fragment *GW* approach is used in particular in the study of molecular organic crystals, with weak interactions between molecular units [138, 141]. It is also applied to nanotube bundles [233], or layered 2D systems bound by weak van der Waals interactions, defining the field of 2D-genomics [146–148, 234].

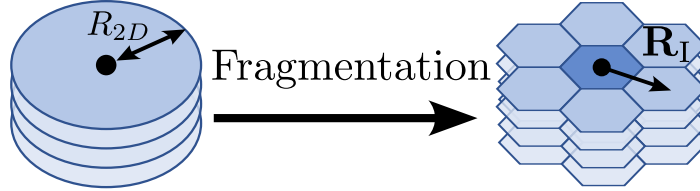


Figure 4.1: Symbolic representation of a finite-size multilayer system. The defect is represented here by the black dot at the center of the surface layer or central fragment in darker blue. On the left, without fragmentation, convergence to the infinite size layer limit can be achieved by increasing the lateral radius R_{2D} with a large computational cost increase. With fragmentation, as represented on the right, the same limit is reached by adding shells of first-, second-, etc. nearest neighbor domains, namely undefected hexagonal fragments translated by a set of $\{\mathbf{R}_I\}$ vectors.

In this chapter, we do not only neglect the wavefunction overlap between neighboring layers, as already done in several studies [146–148, 234], but we further fragment individual monolayers in domains. This is done by “reconstructing” monolayers by patching hexagonal *h*-BN fragments, as symbolically represented in FIGURE 4.1. In real space, the fragment approximation results in a total independent-electron susceptibility $\chi_0(\mathbf{r}, \mathbf{r}'; \omega)$ which is the sum of the gas-phase independent-electron susceptibilities of all fragments. Indexing by (I) the different fragments, with (I = 0) the defected one, the fragmentation of the *h*-BN leads to

$$\chi_0(\mathbf{r}, \mathbf{r}'; \omega) = \chi_0^{(I=0)}(\mathbf{r}, \mathbf{r}'; \omega) + \sum_{I>0} \chi_0^{(I)}(\mathbf{r}, \mathbf{r}'; \omega) \quad (4.1a)$$

$$= \chi_0^{(\text{defect})}(\mathbf{r}, \mathbf{r}'; \omega) + \sum_{I>0} \chi_0^{(\text{pristine})}(\mathbf{r} - \mathbf{R}_I, \mathbf{r}' - \mathbf{R}_I; \omega), \quad (4.1b)$$

where $\chi_0^{(\text{pristine})}$ is the susceptibility of an undefected (pristine) *h*-BN fragment and the $\{\mathbf{R}_I\}$ are the translations needed to reconstruct all layers with fragments of *h*-BN. Such an approach only requires the susceptibility $\chi_0^{(\text{defect})}(\mathbf{r}, \mathbf{r}'; \omega)$ of an isolated defected *h*-BN fragment and the susceptibility $\chi_0^{(\text{pristine})}(\mathbf{r}, \mathbf{r}'; \omega)$ of an undefected *h*-BN fragment. This latter will be “translated” to compute the full system susceptibility $\chi_0(\mathbf{r}, \mathbf{r}'; \omega)$. For the defected layer, the central fragment contains the defect, as represented in FIGURE 4.1, surrounded by shells of first-, second-, etc. nearest-neighbor pristine *h*-BN fragments. In practice, each layer contains up to fourth-neighbor fragments, amounting to 57 flakes containing typically 86 to 138 atoms each. This enables us to reach lateral sizes large enough to allow extrapolation to the infinite layer size limit for a given number of layers, as presented in section 2.3.4 pages 87 to 89. The accuracy of this scheme will be carefully validated below.

4.2.2 Environmental effects: observables of interest

Denoting ε_n the n^{th} energy level, the main objective of this chapter is to compute the energy level shifts

$$\Delta_n = \varepsilon_n^{\text{embedded}} - \varepsilon_n^{\text{gas}}. \quad (4.2)$$

Such a shift is computed from the gas phase, namely an isolated defected fragment, to the embedded phase, where the defected fragment is surrounded by undefected hexagonal *h*-BN flakes. In the following sections, this is computed at the fully dynamical *GW* level $\Delta_n^{\text{GW}} = \varepsilon_n^{\text{GW, embedded}} - \varepsilon_n^{\text{GW, gas}}$, or this is approximated at the static Coulomb-Hole plus Screened-Exchange (**COHSEX**) level (see section 1.3.2.8 page 53). Following the two previous chapters, this leads to the Δ **COHSEX** approach, such that $\Delta_n^{\text{COHSEX}} = \varepsilon_n^{\text{COHSEX, embedded}} - \varepsilon_n^{\text{COHSEX, gas}}$. This static approximation offers the advantage that the screened Coulomb potential W only needs to be calculated at the low-frequency limit ($\omega \rightarrow 0$), greatly reducing computer cost. In the present Analytic Continuation (**AC**) and Contour Deformation (**CD**) implementation of *GW* in our code Beyond Density-Functional Theory (**BEDEFT**) (see section 1.3.2.10 page 56), for which the dynamical susceptibility needs to be calculated at typically $n_\omega = 12$ frequencies along the imaginary axis, the static **COHSEX** approximation is thus an order-of-magnitude cheaper than the fully dynamical *GW* approach. Such an approximation was shown to yield significantly too large gaps [79] but has been central to most previous studies implementing the fragment many-body techniques [17, 141] or the combination of many-body techniques with models of dielectric environment [6, 7]. In such studies, environmental corrections are calculated at the Δ **COHSEX** level. It would have been also possible to compute Δ_n at the $\text{QM}_{\text{GW}}/\text{QM}_{\text{COHSEX}}$, as defined in section 3.2.3 page 99. However, chronologically the results of this chapter 4 were produced at the beginning of my 3-year thesis, while the chapter 3 was developed at the end of these 3 years.

This energy shift Δ_n may be decomposed into two contributions:

- a) the shift of the **KS-DFT** energies $\Delta_n^{\text{KS}} = (\varepsilon_n^{\text{KS, embedded}} - \varepsilon_n^{\text{KS, gas}})$. This quantity accounts for hybridization, confinement, or electrostatic effects in the ground state.
- b) the shift due to screening effects at the fully dynamical *GW* level, or approximated at the Δ **COHSEX** level. This occurs as a response to an electronic excitation (*e.g.* Photoemission Spectroscopy (**PES**)) on the defect. We label polarization energy P_n this second contribution that can be defined as the difference $P_n^{\text{GW/COHSEX}} = \Delta_n^{\text{GW/COHSEX}} - \Delta_n^{\text{KS}}$.

While Δ_n^{KS} can shift up or down energy levels, the second effect always stabilizes holes and electrons. Namely, this pushes occupied levels towards the vacuum level, while on the contrary empty levels go down in energy.

4.2.3 Technical details

The **KS-DFT** calculations are performed with the ORCA code [57] that is used to obtain relaxed geometries and generate the **KS** eigenstates used as an input for many-body *GW* corrections. Such many-body calculations are performed with our Gaussian basis *GW* code

BEDEFT. All occupied, including core states, and unoccupied energy levels are included in the construction of the susceptibility and self-energy. We also use the standard Coulomb-fitting Resolution of the Identity (RI)-V approach (see section 1.3.2.10 page 56). At that stage, we emphasize that the present all-electron finite-size calculations with Gaussian basis sets, not relying on the Bloch theorem nor on the use of pseudopotentials, provide energy levels directly referenced to the vacuum level.

Structural relaxations are performed at the triple-zeta plus polarization 6-311G(d) level [63]. We adopt the same basis set for the calculation of energy differences at the *GW* and static COHSEX level. While absolute *GW* energies are not converged with such a basis set, energy differences between the defected fragment and corresponding multilayer systems are very well captured. Such energy differences involve long-range polarization effects that converge very quickly with basis size, as further demonstrated below in our discussion on the basis-set dependence of the fragments dipolar response.

Our dynamical *GW* calculations are performed at the non-self-consistent G_0W_0 level starting with a PBEh(α) functional [45] with 40% of exact exchange ($\alpha = 0.4$). In the process of calculating polarization energies, input KS eigenstates enter indirectly through the construction of the χ_0 KS independent-electron susceptibility. Since we are interested in exploring the impact of the dielectric response of added layers on the defect, we adopt an α value close to an optimal one ($\alpha = 0.409$) found in Ref. [207]. This reproduces the monolayer long-range dielectric properties in an optimally tuned-functional approach. We emphasize however that KS eigenstates are used in the present case as an input starting guess to build the non-interacting susceptibility χ_0 and the *GW* self-energy. This *GW* correction dramatically reduces the impact of the chosen DFT functional on the final Quasiparticle (QP) energies.

Concerning the RI-V approach, we use the universal Coulomb fitting auxiliary basis set [111] in conjunction with the 6-311G(d) basis set. It is in such an auxiliary basis representation $\{P\}$ that the Dyson equations for the screened Coulomb potential W , or equivalently the one for the interacting susceptibility χ , are inverted. Reducing the dimension of this auxiliary basis set can quickly degrade the quality of correlated calculations. We have observed, however, that the static dipolar polarizability tensor $\alpha^{(I)}$, of a given fragment (I), is hardly affected by reducing significantly the dimension N_P of the auxiliary basis set. Denoting $\mathbf{X}_g^{(I)}(\omega)$ the matrix representation, in the auxiliary basis, of the gas phase interacting susceptibility of the fragment (I), the coefficients of $\alpha^{(I)}$ are given by

$$\left[\alpha^{(I)}\right]_{ij} = - \int d\mathbf{r} d\mathbf{r}' r_i \left(\sum_{P,Q}^{N_P} P(\mathbf{r}) \left[\mathbf{X}_g^{(I)}(\omega = 0) \right]_{PQ} Q(\mathbf{r}') \right) r'_j, \quad (4.3)$$

for $r_i \in \{x, y, z\}$. In the case of the *h*-BN fragments considered in this study, removing the (*d, f, g*)-character orbitals and the core (*s, p*) ones from the auxiliary basis set $\{P\}$ hardly changes this fragment static dipolar polarizability tensor, with error well below the percent. Such a reduction enables us to go from an auxiliary basis set of dimension $N_P = 3454$ to a more reduced one of dimension $N_P = 720$, for fragments of 86 atoms, as detailed below. We use such reduced auxiliary basis sets to expand the independent-electron susceptibility $\chi_0^{(I)}$ of fragments that are strictly beyond the first-nearest-neighbors of the central defected

fragment of interest. We do not attempt to reduce the dimension of the basis of nearest-neighbor fragments. As a result, the calculated polarization energies from the monolayer to the multilayer cases do not change by more than a very few meV. We interpret this favorable behavior by emphasizing that for long-range interactions, induced dipoles are the major contribution to the reaction field and polarization energy. As such, an approximation that preserves the calculated dipolar tensor of remote fragments may be very accurate, as we observe. In fact, it would have been possible to use the compression method detailed in section 2.2 pages 67 to 75, leading certainly to a much more reduced auxiliary basis set. However, the study of this chapter 4 was achieved at the beginning of my 3-year thesis, while the methods of the chapter 2 were developed during the second year. In practice, the success of this reduction in size “by hand” was one of the starting point of the development of more elaborated techniques.

4.2.4 Geometries of the fragments

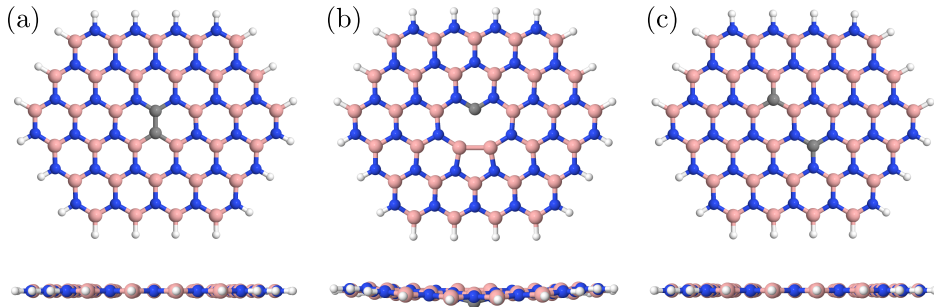


Figure 4.2: Ball-and-stick representation of the (a) carbon-dimer CC defect, (b) the nitrogen-vacancy $C_B V_N$ defect and (c) the carbon-dimer defect in the fourth nearest-neighbor configuration labeled $CC-\sqrt{7}$ [235]. Hydrogen, boron, carbon, and nitrogen atoms are in white, pink, gray, and blue, respectively. Defects are located at the center of a BN86 flake (or fragment). Edge atoms are passivated by hydrogen atoms. In the $C_B V_N$ defect, the carbon atom stands $\sim 0.5 \text{ \AA}$ below the average plane defining the defected layer (see text).

In this chapter, we study *h*-BN fragments containing 86, 138, 202 and 278 atoms with passivating hydrogens at the edge. These latter aim at repelling edge states away from the host gap, and they reduce the spurious contribution of edge polarization as compared to the bulk one. Such systems will be named BN86, BN138, etc. In the case of defected structures, the defect is located at the center of the fragment. I represent in FIGURE 4.2 the paradigmatic neutral carbon-dimer (labeled CC) defect and the so-called $CC-\sqrt{7}$ carbon-dimer variant [235]. I also show the $C_B V_N$ defect, where one boron atom B is substituted by a carbon atom C, and a nitrogen atom N by a vacancy. In the following, we will use *e.g.* the notation $CC@BN86$ for a CC defect at the center of a BN86 fragment (or flake). The CC defect in the BN138, BN202, and BN278 fragments are reproduced in FIGURE 4.3. This carbon-dimer defect has been proposed [211, 218] to be a likely candidate for the frequently observed 4.1 eV emission line, while the $C_B V_N$ defect has been associated with the $\sim 2 \text{ eV}$ emission line [215, 236]. The $CC-\sqrt{7}$ carbon-dimer defect, with carbon atoms in fourth-nearest-neighbor

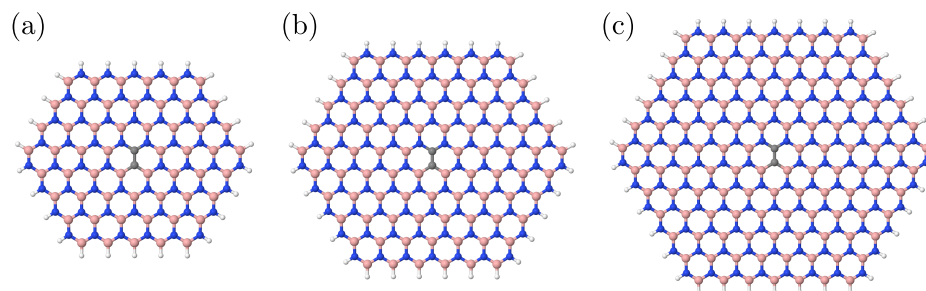


Figure 4.3: Representation of the (a) CC@BN138, (b) CC@BN202 and (c) CC@BN278 structures, with the same color code as the one used in FIGURE 4.2.

position, is less stable than the standard (nearest-neighbor) CC carbon-dimer defect [235]. However, it exhibits a larger spatial extension and a gap significantly smaller (by ~ 2.2 eV at the static COHSEX level for the infinite-size monolayer) than the standard carbon-dimer defect, allowing to show below that polarization (screening) effects are nearly independent of the geometrical and electronic properties of the defect of interest. All structures are relaxed at the PBE0 6-311G(d) level.

Except for the non-planar $C_B V_N$ defect, we do not attempt to relax multilayer systems. In the dilute limit, the energetics around the defect is not expected to govern the stacking properties of the *h*-BN layers. As a test, in the case of the carbon-dimer (CC) defect located in a BN86 fragment, we prepare a bilayer by adding an undefected BN86 fragment in an AA' stacking geometry with the experimental 3.33 Å interlayer spacing [237, 238]. Structural relaxation including D3 dispersion forces [239] preserves the AA' stacking geometry, with a slightly reduced 3.25 Å interlayer spacing in the relaxed bilayer. As such, even in the rather high-doping limit, planarity and stacking are preserved for the carbon-dimer defects. In what follows, we will thus relax individually the layers and stack them in an AA' fashion with the experimental 3.33 Å interlayer spacing.

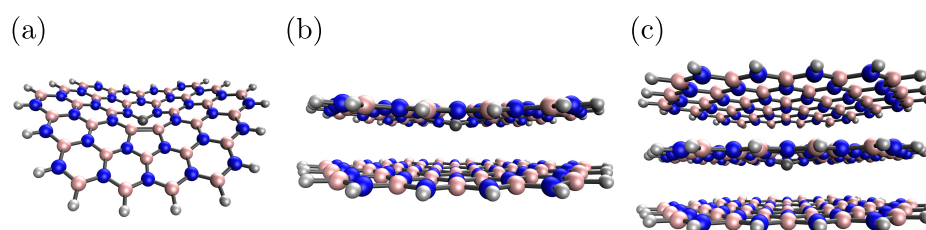


Figure 4.4: Representation of the $C_B V_N$ defect in (a) a BN86 monolayer, (b) a BN86 bilayer, and (c) a BN86 trilayer. Structures are not on scale.

The case of the $C_B V_N$ defect is more complicated, since the relaxation of a single-layer defected fragment leads to a highly non-planar system, as represented in FIGURE 4.4(a). This is due presumably to the tensile strain induced by forming a B-B bond across the missing N atom. However, adding a second undefected fragment in AA' stacking and relaxing with D3 dispersion corrections allows to dramatically restore planarity thanks to layer-layer interaction, as illustrated in FIGURE 4.4(b). Nevertheless, the C atom goes towards the

neighboring layer with an out-of-plane deviation of about 0.55 Å. The same result is obtained in a trilayer system where the defect is sandwiched between two undefected layers, as shown in FIGURE 4.4(c). The C atom remains 0.52 Å out of plane despite the restored symmetry of having one layer on each side of the defect. In what follows, we thus adopt the bilayer or trilayer geometry, for studying the surface and bulk limits, and add subsequent layers in an AA' stacking geometry and a 3.33 Å distance with respect to the nearest undefected layer.

4.3 Fragmentation of the monolayer

In a previous study [218] carried out in our group, the monolayer CC dimer defect was studied using the *GW* and Bethe–Salpeter Equation (BSE) formalisms within an approach based on one finite-size defected flake. The variations of the QP gap and optical excitation energies were followed as a function of the flake size. It was shown in particular that the defect electronic energy levels converge very slowly with system size following a $1/R_{2D}^2$ scaling law, with R_{2D} the average radius of the defected *h*-BN flake considered. As illustrated in section 2.3.4 page 87, or in Ref. [123], such a scaling law was shown to originate from long-range polarization, or screening, effects in a 2D system. To reach such an asymptotic regime, allowing to extrapolate to the infinite-size limit, *GW* calculations on systems with increasing sizes well above 200 atoms had to be considered. Such results are reproduced in FIGURE 4.5 at the present $G_0W_0@PBEh(0.4)$ (red dots) and static COHSEX@PBEh(0.4) (black dots) levels. The evolution of the gap, denoted ΔGap following notations of section 4.2.2, of a CC defect at the center of BN138, BN202, and BN278 flakes are given, taking as a reference the smallest CC@BN86 system. The dashed lines with corresponding colors are a $(1/N_{\text{at}})$ affine fit of the data, with N_{at} the number of B/N atoms that is proportional to the squared radius of the flake. The smallest CC@BN86 system is excluded from these fits to obtain an improved affine behavior, indicating that large systems must be considered to enter the asymptotic regime.

The significant evolution of the gap is the signature of the influence of enhanced screening by additional B/N atoms. In the asymptotic infinite monolayer size limit, the defect gap is closing by 0.46 eV (G_0W_0) or 0.51 eV (static COHSEX) as compared to the smaller CC@BN86 system. A small contribution from the closing of the gap originates from the evolution of the KS-DFT gap that can be fitted with a $\Delta\text{Gap}^{\text{KS}} = [1.87/N_{\text{at}} - 0.05]$ eV law¹. This change in gap at the DFT level is an order of magnitude smaller than the evolution at the G_0W_0 level, indicating that long-range polarization effects are not captured at the KS-DFT level. The closing of the gap due to polarization only, subtracting the ground-state KS contribution, amounts to $(P_e - P_h) = -0.41$ eV at the *GW* level. This originates both from the stabilization of the defect occupied level ($P_h = 0.20$ eV) and of the unoccupied one ($P_e = -0.21$ eV), where the subscripts “h” and “e” stand for hole and electron, respectively. I show now that the same results can be obtained by fragmenting the monolayer in domains. This reproduces the same screening, or polarization, effects on the central defect, but at a dramatically reduced cost allowing us to reach much larger system sizes.

To rationalize this strategy, we plot in FIGURE 4.6 the three principal axes static po-

¹Such an affine law may be associated to quantum-confinement effects, scaling as $1/R_{2D}^2 \propto 1/N_{\text{at}}$.

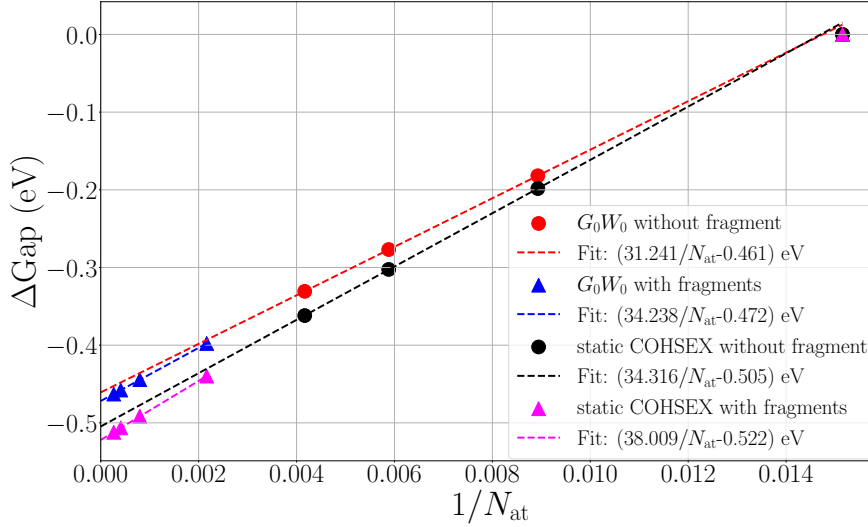


Figure 4.5: Evolution of the gap between the occupied and unoccupied CC defect energy levels with respect to the CC@BN86 fragment. ΔGap , in eV, is computed as a function of $1/N_{\text{at}}$. The red (black) dots are full G_0W_0 (static COHSEX) calculations for the CC@BN138, CC@BN202 and CC@BN278 fragments. The blue (pink) up-triangles represent fragment G_0W_0 (static COHSEX) calculations for a central defected CC@BN86 fragment surrounded by up to four shells of undefected BN86 fragments. Dashed lines are $[a/N_{\text{at}} + b]$ fits. The fragment made of 86 atoms ($\Delta\text{Gap} = 0.0$ eV) is excluded from the fits.

larizabilities (as defined in Eq.(4.3) page 126) of the pristine (undefected) BN58, BN86, BN138, BN202 and BN278 flakes in the RPA. It is such an approximation that is used to build the screened Coulomb potential W in standard GW calculations (see section 1.3.2.9 page 54). Such results show that the polarizability principal components follow accurately a linear relation with respect to the number of B/N atoms. As such, one can define a polarizability-per-atom that is independent of the size of the considered fragment. We believe that such a behavior is characteristic of insulating systems where charges cannot be displaced from one side of the system to another, and polarization proceeds rather by the creation of local dipoles. The consequence of such a behavior is that the effect on the central defect of polarizing a B/N atom located in an infinite monolayer, or at the same distance from the defect but in a finite-size fragment, are very similar. Such a finding allows us to set up a fully *ab initio* embedding scheme, with a central defected fragment embedded in rings of first, second, third, etc., undefected neighbor fragments. This approach, illustrated in the FIGURE 4.7, enables us to reproduce the effect of a continuous layer at a dramatically reduced cost. As emphasized in section 4.2, instead of calculating the independent-electron susceptibility χ_0 of a system with increasing size, with a quartic scaling evolution in terms of the number of operations to perform, the corresponding susceptibility matrix can be calculated fragment by fragment, in a block-diagonal fashion. Such a method is associated to a linear scaling. As highlighted in the zoom of the FIGURE 4.7b, the undefected fragments are put so that B/N atoms are located at the position they would occupy in an infinite-size monolayer. We avoid any vacuum between the different fragments, even if this leads to overlap between B/N and

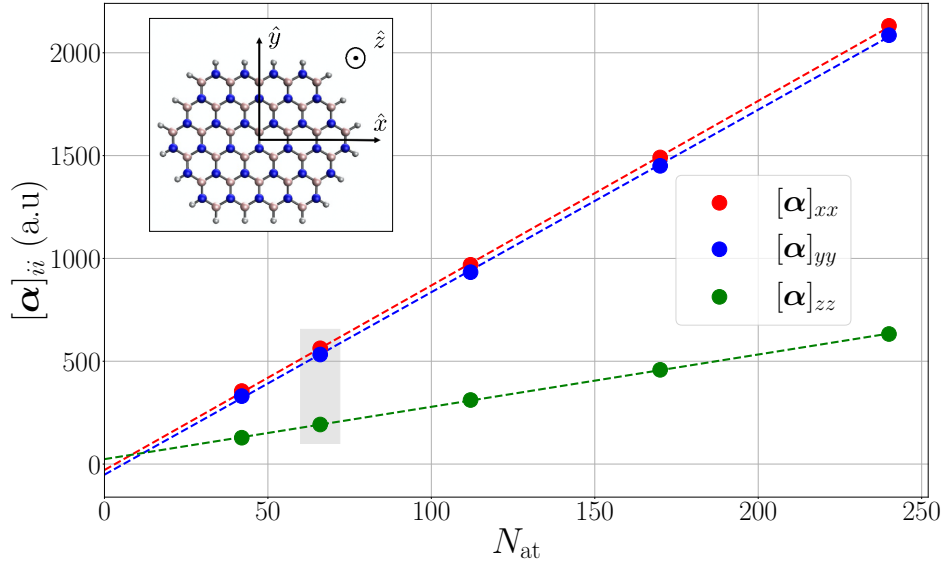


Figure 4.6: Evolution of the Random-Phase Approximation (RPA) static polarizability tensor components (in atomic units) of pristine *h*-BN flakes, as defined in Eq.(4.3) page 126. Components are computed with respect to increasing number N_{at} of B/N atoms. The three principal axes (as defined in the inset) polarizabilities are given. The smallest contribution indicates the out-of-plane polarizability. The shaded data indicates the BN86 flake (see inset) used to fragment/reconstruct extended monolayers in the following.

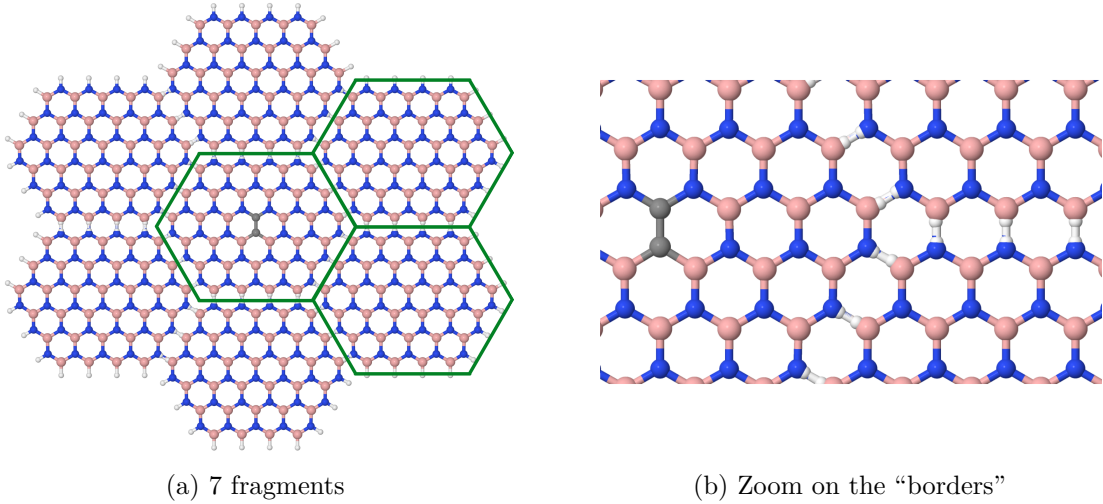


Figure 4.7: (a) Symbolic representation of the fragment approach to build the susceptibility χ_0 . The central CC@BN86 defected fragment is surrounded by 6 undefected pristine BN86 first-nearest-neighbor fragments, highlighted by green hexagons. Larger systems can be reconstructed by adding second-, third-, etc. nearest-neighbor fragments (not represented here). (b) Zoom on the “borders” between different fragments, at the junction between the three green hexagons of FIGURE (a). Since the hydrogen atoms hardly contribute to the fragment polarizability, their overlap in real-space hardly matters.

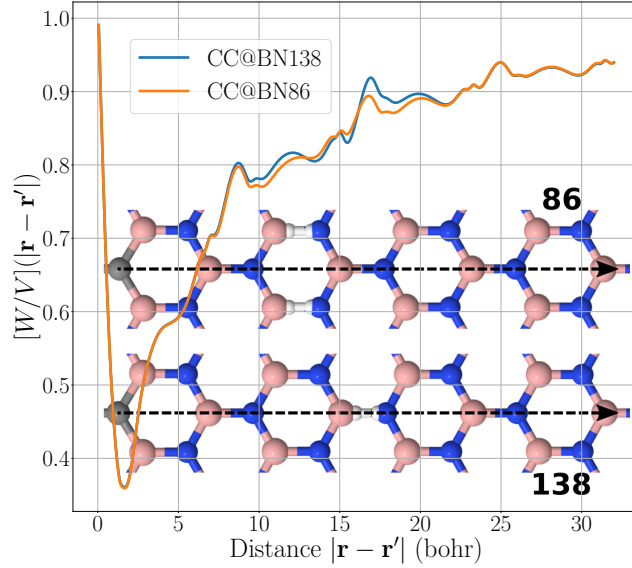


Figure 4.8: Ratio of the statically screened Coulomb potential $W(\mathbf{r}; \mathbf{r}'; \omega = 0)$ divided by the bare Coulomb potential $V(\mathbf{r}, \mathbf{r}')$, with \mathbf{r} fixed at the center of the CC bond and \mathbf{r}' varying along the direction indicated by the horizontal black dashed lines in the inset. The case of a defected monolayer reconstructed with BN86 fragments (orange plot) or larger BN138 fragments (blue plot) are compared. Inset: schematic representation of the atoms along the direction in which is translated \mathbf{r}' , for a monolayer reconstructed by BN86 (at the top) or BN138 (at the bottom) fragments.

H atoms. These H atoms hardly contribute to the fragment polarizability. As such, their overlap in real-space hardly matters.

To further confirm the preservation of long-range screening upon fragmenting the monolayer, I plot in FIGURE 4.8 the ratio of the statically screened Coulomb potential $W(\mathbf{r}, \mathbf{r}'; \omega = 0)$ over the bare Coulomb potential $V(\mathbf{r}, \mathbf{r}')$, with the susceptibility χ_0 built within the fragment approximation from the gas phase χ_0^{defect} and χ_0^{pristine} susceptibilities. The \mathbf{r} point is fixed to the CC bond center while \mathbf{r}' varies radially in a specific direction, represented by horizontal black dashed lines in the inset of FIGURE 4.8. One can see that we measure the potentials close to H atoms when reforming the monolayer with BN86 fragments, and across H atoms when reconstructing the monolayer with larger BN138 fragments. The $[W/V](|\mathbf{r} - \mathbf{r}'|)$ ratio is very similar in both cases, with small differences when crossing or coming close to H atoms. In the vicinity of the CC bond, where the defect states are localized, the W/V ratio for the two systems is indistinguishable. As such, changing the size of the fragments, that is changing the ratio of H atoms to B/N ones, hardly affects the screening properties. As expected for a 2D system, the W/V ratio converges to unity in the long-range limit [232, 240–242], at odds with the $1/\epsilon_M$ limit in 3D systems, where ϵ_M is the macroscopic dielectric constant. This is a clear indication that long-range screening properties in 2D or 3D systems cannot be reproduced within DFT by the same functional.

A plot of the W/V ratio, for a monolayer reconstructed by BN86 fragments and for \mathbf{r}'

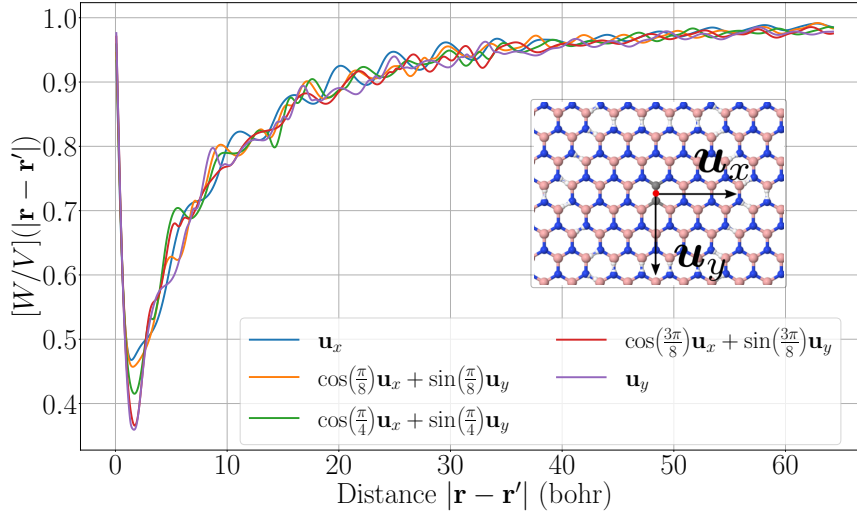


Figure 4.9: Representation of the ratio of the static screened Coulomb potential $W(\mathbf{r}, \mathbf{r}'; \omega = 0)$ divided by the bare Coulomb potential $V(\mathbf{r}, \mathbf{r}')$ along several directions for \mathbf{r}' , for a monolayer reconstructed by BN86 fragments. The position \mathbf{r} is fixed to the center of the defect CC bond, as represented by the red dot in the inset. This latter represents also the orientation of the considered axes \mathbf{u}_x and \mathbf{u}_y .

going in several directions, is provided in the FIGURE 4.9. While in the FIGURE 4.8, such a ratio was computed only along the \mathbf{u}_y direction (see inset of the FIGURE 4.9), 4 others ones are now probed. In all directions, smooth evolutions of the ratio can be noticed when \mathbf{r}' goes from a fragment to another one. Moreover, the small variations for a given $|\mathbf{r} - \mathbf{r}'|$ distance indicate the magnitude of local field effects that fade away at large distance.

I now compare the G_0W_0 and static COHSEX calculations performed for the CC@BNX systems, with X varying from 86 to 278, to the results within the fragment approach. In this latter, the monolayer is fragmented into BN86 defected (center) and undefected fragments, as represented in FIGURE 4.7. Since the fragment approach can only account for polarization effects at the GW /static COHSEX level, the small $\Delta\text{Gap}^{\text{KS}} = [1.87/N_{\text{at}} - 0.05]$ eV (see above) evolution of the KS-DFT gap with system size beyond the 86-atoms system is added perturbatively to the polarization correction. As emphasized above, such a perturbative approach is justified by the order-of-magnitude difference between gap changes at the KS-DFT and many-body levels. As a result, the FIGURE 4.5 shows that extrapolations from the full (unfragmented) calculations (red and black dotted lines) and from the much cheaper fragment approach (up-triangles and corresponding fit) differ by no more than 11 meV (17 meV) in the G_0W_0 (static COHSEX) calculations, respectively. As can be seen from the graph, the system including the fourth shell of nearest-neighbor fragments, amounting to 57 flakes of 86 atoms each, (see *e.g.* blue up-triangle at the G_0W_0 level) is already very close to the asymptotic infinite limit.

I have also performed the very same exercise by reconstructing the infinite monolayer with larger BN138 fragments. Adopting bigger fragments allows reducing the possible effects of edge H atoms polarizability. The results are represented in FIGURE 4.10. Since we start

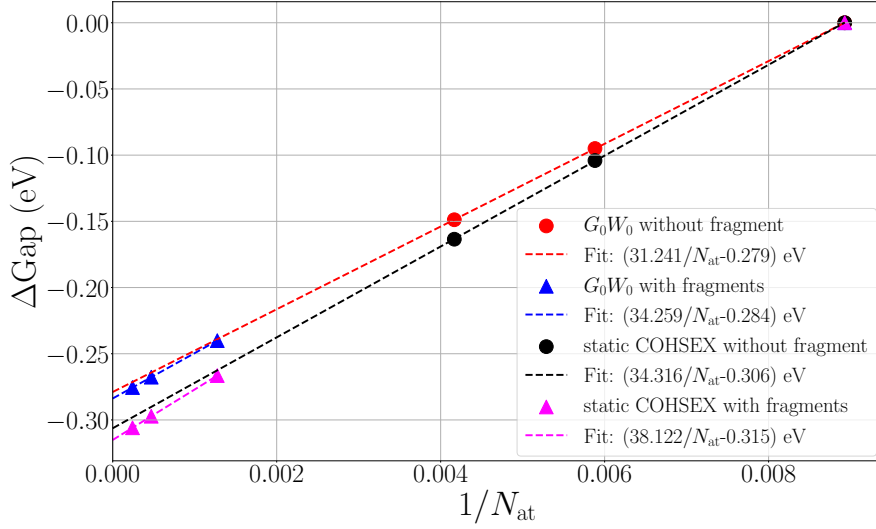


Figure 4.10: Same study as the one of the FIGURE 4.5, with the same notations, but using BN138 fragments instead of BN86 ones. The reference here ($\Delta\text{Gap} = 0.0\text{ eV}$) is computed for a CC@BN138 fragment, and is not excluded from the affine fits without fragment.

from a larger system, the infinite-size correction is smaller. The extrapolated value using the fragment approach falls within 5 meV (9 meV) of the extrapolated value obtained without any fragment approximation at the G_0W_0 (static COHSEX) level, respectively. As such, fragmenting the monolayer with small BN86 flakes or larger BN138 ones leads to very close results, confirming that edge effects (*e.g.* hydrogen polarization) are negligible.

For further validation, we explored even larger systems using an efficient classical induced-dipole model of polarizable points [123, 149], with site polarizabilities fitted to reproduce the results of FIGURE 4.6. Such a microelectrostatic model allows us to reach systems more than one order of magnitude larger than the one we can afford at the *ab initio* level with the fragment approach. The outcome of these model calculations is that extrapolating the evolution of the gap to the infinite monolayer, on the basis of data acquired with much larger systems, does not change by more than a meV the extrapolated value obtained with systems of the size we study *ab initio* in the present fragments scheme. This is reported in more details in our corresponding article [181].

Coming back to the distinction between static and dynamical GW calculations, we observe at that stage that the static COHSEX approximation leads to polarization energies that are overestimated by about 10% as compared to G_0W_0 calculations. This is in a fair agreement with results of the chapter 3. The static COHSEX approximation slightly overestimates the closing of the gap due to enhanced dielectric screening.

4.4 Fragmentation of the multilayers

I now study the effect of layering on the defect energy levels, considering first the carbon-dimer CC defect. I start this exploration by providing in FIGURE 4.11 the evolution of the defect

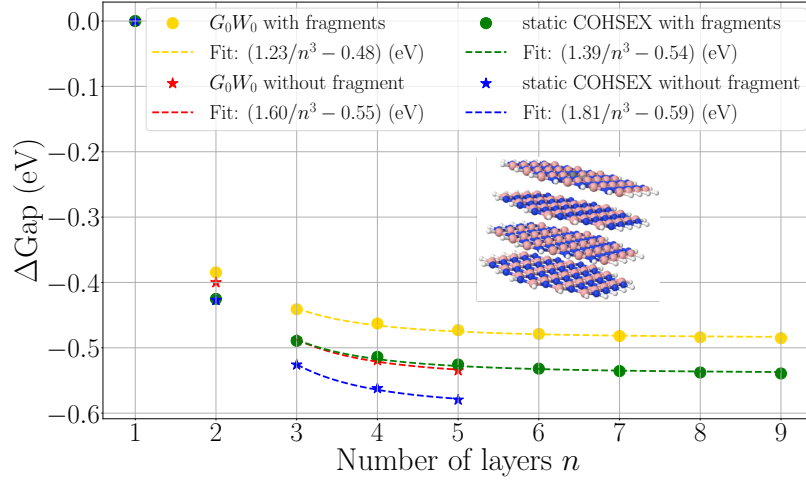


Figure 4.11: Evolution as a function of the number of layers of the defect gap of a defected CC@BN86 fragment located at the surface of a stack of BN86 undefected fragments in an AA' geometry. The reference is taken to be the monolayer CC@BN86 fragment. Full G_0W_0 (red stars) and static COHSEX (blue stars) are compared to fragment G_0W_0 (yellow dots) and static COHSEX (green dots). Energies are in eV. Dashed lines are $[a/n^3 + b]$ fits. Inset: schematic representation of the ($n = 4$) system.

G_0W_0 (red stars) and static COHSEX (blue stars) gaps from the monolayer to n -layer systems in an 86-atoms finite size layered geometry. Namely, I here do not stack infinite layers but create a “cylinder” of stacked 86-atoms flakes. I put a surface defected CC@BN86 fragment deposited on top of undefected BN86 fragments in an AA' stacking fashion with 3.33 Å separation between layers (see schematic inset FIGURE 4.11). We start with full G_0W_0 and static COHSEX calculations, without any fragment approximation, stopping at five layers, representing already 430 atoms.

As expected, interlayer screening reduces the gap associated with the defect. At the G_0W_0 level in this 86-atoms stack geometry, the gap closes by as much as 0.4 eV upon adding a second layer, 0.49 eV with a third layer, etc. Such a correction can be compared to the 0.106 eV closing of the gap at the KS-DFT level originating from the addition of a second layer, the difference between the pentalayer and the bilayer being reduced to 4 meV. This illustrates again that KS-DFT cannot reproduce long-range screening unless a strategy is adopted to readjust the functional for each number of layers in order to mimic increased screening with increasing number of layers [207]. Concerning many-body approaches, we observe again that the static COHSEX approximation overestimates the effect of screening. This “cylinder” being a one dimensional system, we can use the formula (2.35) page 87 for $D = 1$ to extrapolate ΔGap in the infinite number of layers limit. In the present situation, $R \propto n$ leads to an asymptotic affine relation $\Delta\text{Gap} = a/n^3 + b$ with respect to $1/n^3$. This is what we can observe in FIGURE 4.11, where such fits, starting from $n = 3$, are represented by dashed lines. In the infinite number of layers limit, the static COHSEX approximation overestimates the closing of the gap by 0.05 eV with respect to the G_0W_0 approach, to be compared to a total correction of 0.55 eV, namely an error not larger than 9%.

In a second step, I adopt a fragment approach, namely decoupling the wavefunctions at the **KS-DFT** level between adjacent layers, constructing the independent-electron susceptibility in a block-diagonal fashion from the susceptibility of the isolated layers. Such an approach has been used in several previous studies devoted to exploring the properties of stacked **2D** systems (intercalating *e.g.* *h*-BN, graphene, dichalcogenides) [146, 147]. As done in the previous section for reaching the infinite monolayer limit, the small **KS-DFT** shift between monolayer and multilayer systems is added perturbatively to the fragment *GW* and static **COHSEX** calculations to allow comparisons with the full (unfragmented) calculations.

The present decoupling scheme is shown in **FIGURE 4.11** to underestimate the impact of screening on the defect gap beyond the bilayer system (compare the yellow dots to the red stars at the G_0W_0 level and the green dots to the blue stars at the static **COHSEX** level). The error is however of the order of 60 meV at most, to be compared to a total closing of the gap of 0.4 – 0.6 eV. This relatively small error certainly confirms the success of the fragment approach in the **2D**-genomics studies.

We further observe that this error is comparable in magnitude with that induced by the static **COHSEX** approximation, but with an opposite sign. As a result, and up to the five-layers system for which full reference G_0W_0 calculations were possible, there is a significant cancellation of errors between the static **COHSEX** approximation, that overestimates the effect of screening, and the fragment approximation that underestimates it. We conclude from these tests that the fragment plus static **COHSEX** approximation reproduces with a limited error full G_0W_0 calculations, thanks to a cancellation of error between the static and the fragment approximations. This cancellation reduces the 30 – 60 meV errors associated with each separate approximation to significantly lower values. For example, in the infinite number of layers limit, the G_0W_0 approach without fragment, and the static **COHSEX** one with fragments differ by less than 10 meV. While such a cancellation is certainly fortuitous, since both errors are of different nature, this latter approach is adopted in the following.

4.5 Point defects in the surface and bulk limit

I now explore within the fragment static **COHSEX** scheme the evolution of the correction upon increasing the size of the layers, namely trying to converge towards the stacking of infinite-size layers. I first study in **FIGURE 4.12a** the effect of stacking 138-atoms (red squares) and 202-atoms (blue pluses) flakes beyond the 86-atoms (green up triangles) systems studied in **FIGURE 4.11**. The defect is here again localized on the surface layer. Clearly, as expected, increasing the size of each layer leads to increasing the polarization energy.

Enlarging further the size of each layer becomes prohibitively expensive. I thus adopt the strategy of section 4.3 page 129 consisting into increasing the in-plane lateral size by patching undefected BN86 fragments around each CC@BN86 (defected layer) or BN86 (undefected layers) central fragment. Adding first-, second-, third- and fourth-nearest-neighbor flakes allows reaching much larger layers. These systems are large enough to extrapolate to infinite-size layers for each (n) value. This is again carefully checked with the semi-empirical model of polarizable points (see the corresponding article [181]). Reaching the asymptotic regime is shown to be more difficult upon increasing the number of layers, suggesting that convergence

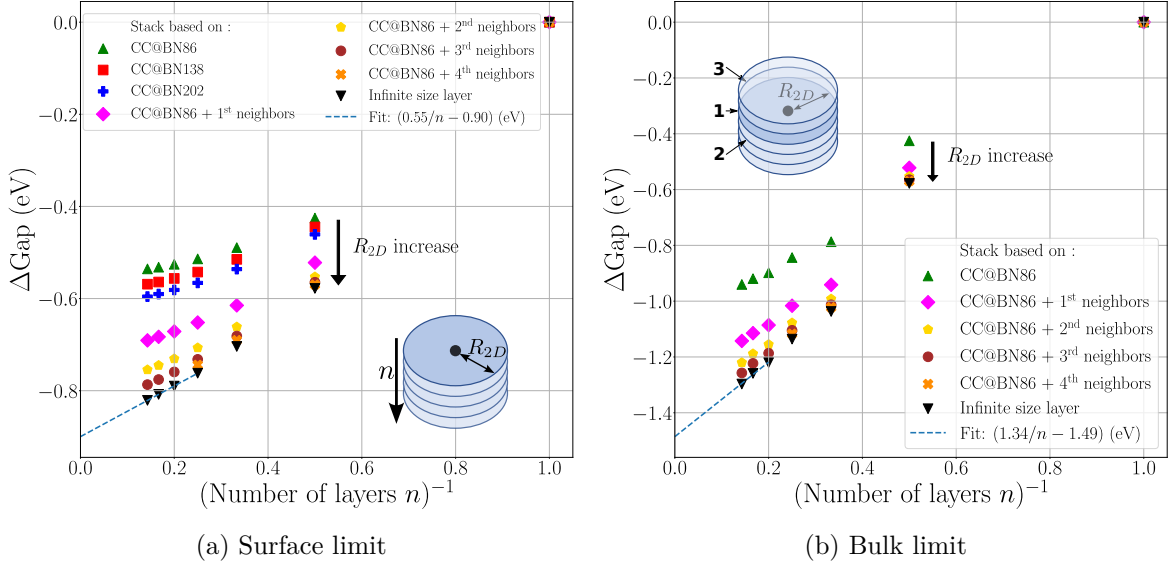


Figure 4.12: Evolution of the defect gap (with respect to the monolayer) as a function of the inverse of the number of layers (n) and the size of each layer. In (a) the defect is on the surface layer, as represented by the black dot in the inset, while in (b) it is in the bulk with layers added alternatively on each side of the defect. The black down triangles are extrapolations to the infinite layers size for a given (n) value. Extrapolated data points can be nicely fitted by a $[0.55/n - 0.90]$ eV functional form for the defect at the surface and $[1.34/n - 1.49]$ eV for the defect in the bulk. Data obtained at the fragment ΔCOHSEX level.

criteria are related to the aspect ratio of the systems.

The closing of the gap extrapolated to the infinite layer size for each (n) value are represented by black down triangles. Following the formulas (2.36) page 89, polarization energies should scale as $(1/n)$ as a function of the number (n) of layers in the limit of infinite-size layers. This is what we observe in FIGURE 4.12a with an affine fit of the $n = 4$ to 7 layers extrapolated values by a $[0.55/n - 0.90]$ eV functional form. I turn now to the bulk case in FIGURE 4.12b, adding additional layers alternatively on one side and the other of the defected layer. One obtains an asymptotic evolution of the gap from the monolayer to the bulk that scales as $[1.34/n - 1.49]$ eV, when fitting the $n = 5$ to 7 layers data. The functional form yields a gap closing by 1.04 eV and 1.16 eV for $n = 3$ and $n = 4$, respectively, in close agreement with the 1.04 eV and 1.14 eV explicit values. This indicates that the asymptotic regime is already quite accurate for very few layers. The $n = 2$ case, very far from the asymptotic limit, can be much better estimated by the “surface” fit that yields -0.63 eV, within 0.05 eV of the explicit $\Delta\text{Gap} = -0.58$ eV value. This rapid recovery of the $(1/n)$ asymptotic behavior of the polarization energy, with respect to the number of layers, was again confirmed with the semi-empirical micro-electrostatic model presented in the corresponding article [181].

As expected, the closing of the gap by 1.49 eV in the bulk limit as compared to the monolayer is significantly larger than the 0.90 eV value found for a defect at the surface. We observe that for ($n = 3$) the polarization energy correction accounts for $\sim 70\%$ (1.04 eV

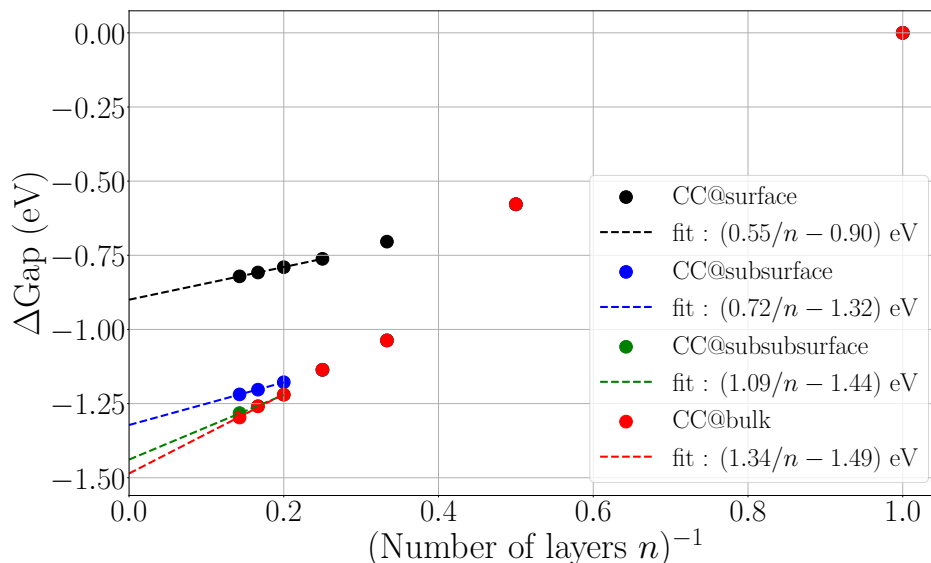


Figure 4.13: Evolution of the defect gap (with respect to the monolayer) as a function of the inverse of the number of layers (n), for CC dimer defect at the surface, subsurface, subsurface and bulk position. For each value of (n) and each configuration, ΔGap is extrapolated to the infinite size limit ($R_{2D} \rightarrow \infty$ in insets of FIGURE 4.12).

instead of 1.49 eV) of the ($n \rightarrow \infty$) limit. This means that the nearest layers contribute significantly to the screening, but that the true bulk limit requires additional layers. Using the obtained functional form, 90% of the closing of the gap is obtained for eight additional layers, that is four layers on each side of the defected layer.

I also provide in FIGURE 4.13 the evolution of the defect gap for the CC dimer defect from the monolayer to a n -layer system with the defect in surface, subsurface, subsurface and bulk positions. In the subsurface case, the ($n = 2$) layer is added on one side of the defected layer, while all the other layers for ($n > 2$) are added on the other side. In the subsurface case, the layers are added alternatively on each side of the defected layer up to $n = 5$ (2 layers on each side) and then added subsequently only on one side. The asymptotic closings of the gap show a rapid convergence with respect to the depth of the defect. For example, the computed value for the CC dimer in the subsurface (-1.32 eV) is closer to the bulk value (difference of 0.16 eV) than the surface one (difference of 0.42 eV).

I present in FIGURE 4.14 the evolution of the QP gap of another point defect in h -BN, namely the $C_B V_N$ one. Taking as a reference the monolayer, its gap is also computed with respect to the inverse of the number of layers n , in a bulk configuration. Layers are added on each side alternatively of the central defected layer, respecting AA' stacking. In the fragment approach, the evolution of this gap properly contains the perturbatively added -40 meV and -57 meV evolution (closing) at the KS-DFT level from the monolayer to the bi- and trilayers, respectively. Additional layers hardly change the KS gap value. As such, both ground-state electrostatic and hybridization effects, together with polarization (screening) effects at the many-body level, are accounted for. This graph shows that the closing of the gap from the monolayer to the bulk amounts to 1.45 eV, very close to the 1.49 eV value obtained before

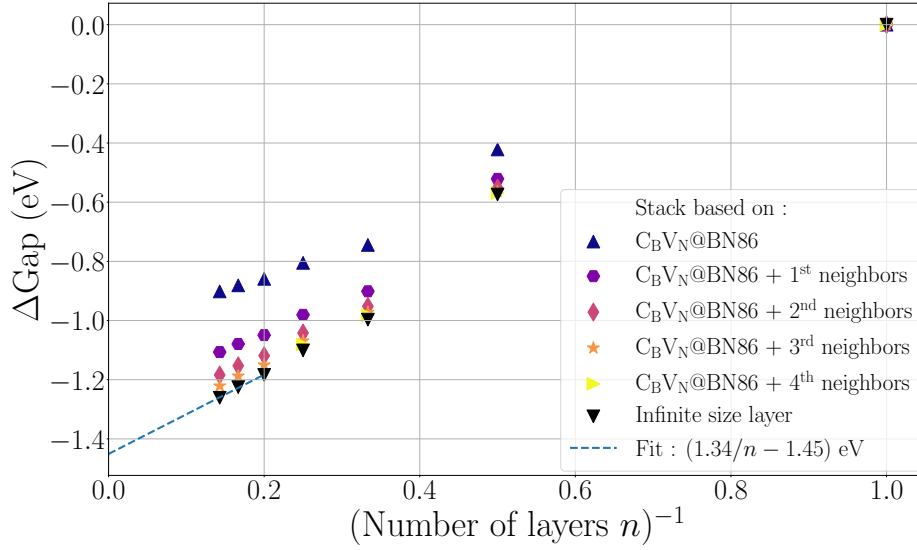


Figure 4.14: Evolution of the QP gap as a function of the inverse of the number of layers n and as compared to the monolayer, for the C_BV_N defect in the bulk geometry (layers successively added on both side of the defect). The black down triangles are extrapolations to the infinite layers size for a given (n) value. The dashed line corresponds to an affine fit $[1.34/n - 1.45]$ eV of these extrapolated data points.

for the CC defect. These values are consistent with the 1.27 eV, 1.31 eV and 1.49 eV gap variations obtained for the C_B, C_N and C_BV_N defects within KS-DFT using Koopman’s-type conditions to adjust the fraction of exact exchange upon changing the number of layers [207]. Such an agreement is remarkable given that the two techniques are significantly different.

We observe thus that the energy shift from the monolayer to the bulk is very weakly defect-dependent. The KS-DFT energy shifts between the monolayer and the multilayer systems is expected to change from one defect to another, depending on the local chemistry (hybridization, ionicity, etc.). Considering, *e.g.*, the C_BV_N defect, the PBEh(0.4) KS-DFT gap is shown to close by about 60 meV from the monolayer to the three-layer system on the basis of the stack of BN86 fragments. This value can be compared to the 0.19 eV closing in the carbon-dimer CC defect case. These two shifts are very different in percentage but small in absolute value. In the following section, the stability of the much larger polarization energy induced by long-range screening from one defect to another is thus explored.

4.6 Universality of the polarization energies among the different defects

I now compare the evolution with layers number of the QP energy levels for several defects, focusing on the CC carbon-dimer defect in its most stable first-nearest-neighbor conformation and its “CC- $\sqrt{7}$ ” fourth-nearest-neighbor geometry, together with the much studied C_BV_N defect. As discussed above, the evolution of the energy levels can be partitioned into a

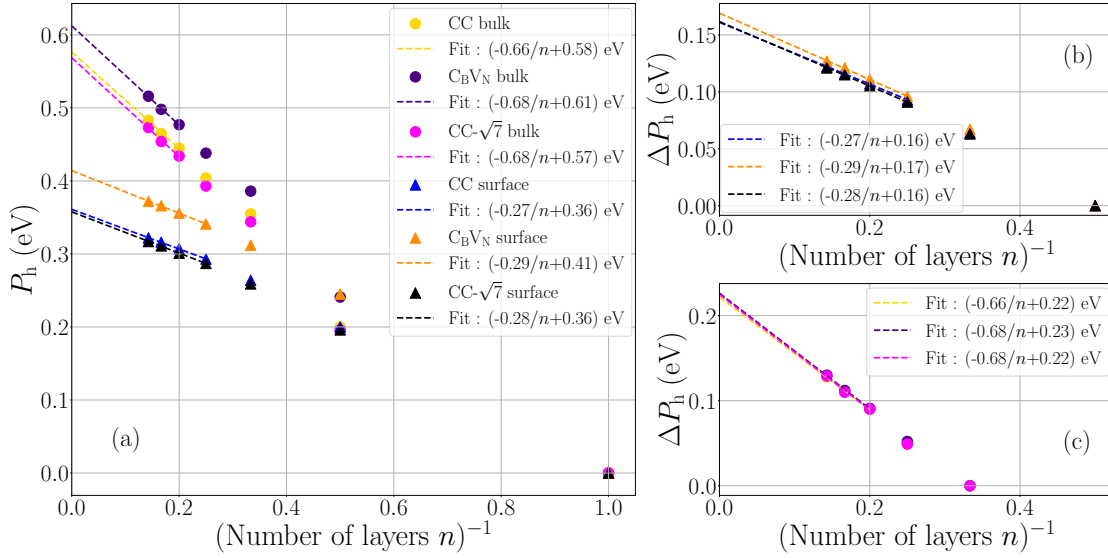


Figure 4.15: Polarization energy, in eV, as a function of the inverse of the number of layers n for the CC, $C_B V_N$ and CC- $\sqrt{7}$ defect-associated occupied level in the surface and bulk limits. In (a) the polarization energy P_h is taken with respect to the monolayer, while in (b) it is taken with respect to the bilayer for surface defects and in (c) with respect to the trilayer (one layer on each side of the defected layer) for the bulk ones. For each given number of layers n , P_h is computed for systems in the infinite size layers limit (namely, $R_{2D} \rightarrow \infty$ in the insets of FIGURE 4.12 page 137). The asymptotic affine fits $[a/n + b]$ are provided.

KS-DFT correction and the long-range polarization energies. While the **KS-DFT** correction has been shown to be short-range, involving mainly nearest-neighbor layers interactions, and rather small in magnitude, we now show that the larger polarization energy is very much universal, namely system independent.

I plot in FIGURE 4.15(a) the evolution, from the monolayer to the n -layer case, of the defect occupied energy level polarization energy (P_h) with respect to $1/n$. I consider both cases of the defected layer in the bulk or at the surface. In the bulk limit, the polarization energies from one defect to another range from 0.57 eV to 0.61 eV, namely a variation around the mean value of about 3%. Further, the prefactors governing the $(1/n)$ evolution are remarkably close, comparing the evolution to the bulk limit and separately the evolution to the surface limit. The $C_B V_N$ defect is associated with the largest polarization energy. We attribute this to the $C_B V_N$ geometry, with the carbon atom coming closer to its neighbor layer by $\sim 0.5 \text{ \AA}$, inducing a larger reaction field from this layer. The two other carbon-dimer defects are planar and, even though showing different in-plane extension and electronic properties, lead to very similar polarization energies.

To further analyze the small differences from one defect to another, I provide in FIGURE 4.15(b) the evolution of the polarization energy for the defect at the surface, taking the bilayer system as reference. As such, this removes the evolution from the monolayer to the bilayer. Clearly, the various defects are characterized by residual polarization energies that are now within a very few meV. In the case of the bulk, I reproduce the same exercise

in FIGURE 4.15(c) but starting from the three-layer case (one layer on each side of the defected one). Again, the evolution beyond the nearest-neighbor layers is very much defect independent, with variations within 5 meV in the bulk limit. Such results confirm that the small differences observed in FIGURE 4.15(a) between defects originate mainly from the response of the nearest-neighbor layers. The response of other layers is nearly completely independent of the defect chemical nature.

To conclude this section, one should notice that polarization energies, originating from environmental screening, are very much universal. Namely, they depend on the host dielectric properties and on the defect location (surface or bulk), but hardly on the defect chemical nature. Indeed, even though the studied defects showed different chemical composition and band gap, variations of the polarization energies from the monolayer to the bulk are within a very few percent of their mean value. In practice, they are even smaller if the defects do not break the planarity of the defected layer. To better rationalize this universal behavior, we emphasize that the surrounding medium reacts to a localized added charge of which the exact spatial distribution, defect and level dependent, only affects its environment through higher-order (dipolar, quadrupolar, etc.) contributions.

The small observed differences originate nearly entirely from the effects of the nearest-neighbor layers. Further, the universal $(1/n)$ long-range behavior, with n the number of layers, starts being valid for a very small number of added layers. In practice, this really means that KS-DFT calculations may be required for a specific defect in the bilayer and trilayer geometries, to capture short-range ground-state crystal field and hybridization effects. Concerning the long-range polarization effects beyond the monolayer case, they can be accurately accounted for on the basis of the simple scaling laws provided in this chapter. As such, expensive *GW* calculations beyond the monolayer limit may be spared when exploring a large zoology of defects in their neutral state.

4.7 Defect levels with respect to *h*-BN valence band edge

All-electron finite-size Gaussian basis sets calculations provide energy levels directly related to the vacuum level. Locating defect levels with respect to the host semiconductor band edge may also be an important issue when it comes to discuss, *e.g.*, the evolution with the number of layers of the stability of defect charged states [212]. Contrary to localized states, addressing the energy of extended Bloch states from a finite size fragment calculation is a difficult task as compared to periodic boundary calculations. The flakes to be considered for extrapolating to infinity are much larger than a standard unit cell of the pristine semiconductor, and the physical interpretation in terms of \mathbf{k} -points is lost. However, we try in the following to apply the fragment approach to study the evolution of defect energy levels with respect to the *h*-BN valence band edge. Such a procedure is certainly not optimal to achieve such an objective, but this may provide guidance for this problem.

In our defected flake calculations, the levels lying below the defect occupied level are delocalized *h*-BN states. As such, the scheme presented here above can be used as well to extrapolate to the bulk limit not only the defects localized states, but further the highest occupied *h*-BN states representative of the *h*-BN top of the valence band. The results are

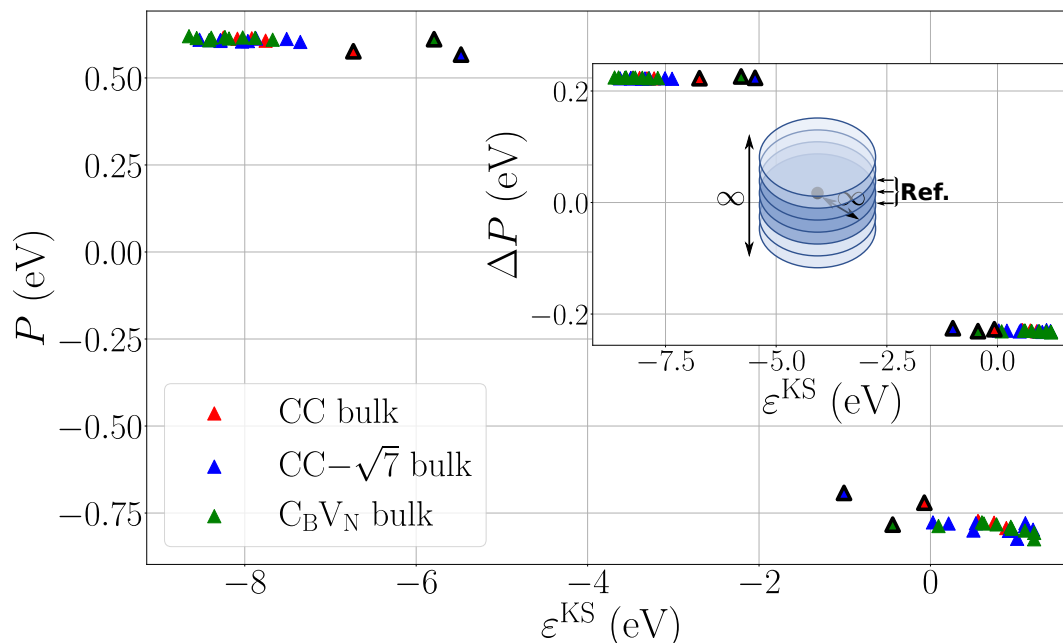


Figure 4.16: Polarization energies P , in eV, from the monolayer to the bulk for a larger set of occupied and unoccupied states, including defect and h -BN delocalized states, as a function of KS-DFT energy ε^{KS} with respect to the vacuum level. Data corresponding to defect states present black bold edges. Most unoccupied states are unbound. Inset: evolution of the polarization energies from the 3-layer system (one undefected layer on each side of the defected one) to the bulk, as represented in the schematic cylinder.

represented in FIGURE 4.16 which reports the bulk polarization energy, as compared to the monolayer, for a large set of states around the gap in the case of the CC, $\text{CC}-\sqrt{7}$ and C_BV_N defects. The states are ordered according to their KS-DFT energy. The data corresponding to defect states are emphasized by black bold edges.

The salient result is that polarization energies for the occupied states at the top of the h -BN occupied states manifold are very stable around $P_h \sim 0.6 \text{ eV}$, to be compared to the $0.57 - 0.61 \text{ eV}$ shift obtained for the localized defect levels (see FIGURE 4.15). As such, screening by additional layers hardly affects the difference of energy between localized defect levels and delocalized h -BN states at the top of the valence bands.

An additional analysis via the FIGURE 4.17, considering larger fragments, confirms that the polarization energy is hardly dependent on the in-plane localization of the considered states. In such a graph, we evaluate the evolution of the polarization energy associated with the highest occupied h -BN delocalized states as a function of the fragment size. Since in our approach the h -BN states are confined to the central fragment, varying the size of such a fragment, from BN86 to BN138, allows us to assess the influence of the in-plane spatial extension. More particularly, in FIGURE 4.17, we compare the polarization energies obtained for the HOMO of pure (undefected) central BN86 and BN138 flakes, surrounded by fragments of the same size in the same layer or in surrounding layers. We also look at the evolution of

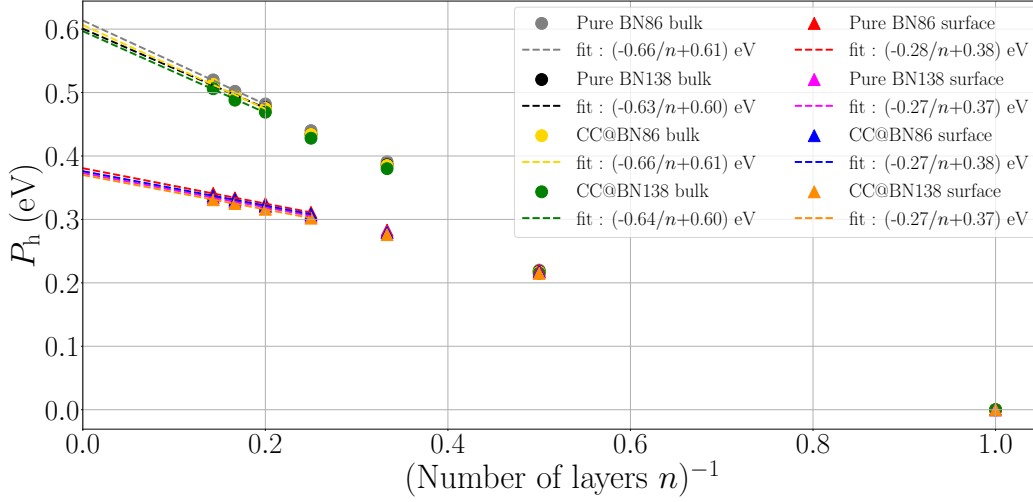


Figure 4.17: Polarization energies P_h from the monolayer to a n -layer system for the highest occupied h -BN state delocalized over a central fragment with size BN86 or BN138. P_h is computed with respect to $1/n$. Both the Highest Occupied Molecular Orbital (HOMO) orbital of a pristine (pure) central BN86 or BN138 fragments, and the highest-but-one (HOMO $- 1$) orbital of defected CC@BN86 or CC@BN138 fragments, are studied in the bulk and surface limits.

the HOMO $- 1$ of defected central CC@BN86 and CC@BN138 fragments. Both the surface and bulk limits are considered. For a given surface or bulk configuration, with a given size of the considered fragments, the energy level of the HOMO of the pure central BN fragment or the HOMO $- 1$ of the defected one follow globally the same evolution. This indicates that the states with energy levels below the defect occupied one can be associated to delocalized h -BN states. When the number of atoms in the flakes is increased, variations of the order of 10 meV are observed on the polarization energy, *e.g.* from $P_h \simeq 0.60$ eV to $P_h \simeq 0.61$ eV in the bulk limit. This tends to confirm the stability of the obtained polarization energies for extended h -BN Bloch states as a function of fragment size.

These different results leave hybridization and electrostatic effects in the ground state as the only source able to modify significantly the position of the occupied defect energy levels with respect to the h -BN Valence Band Maximum (VBM). Here again, polarization energies, difficult to obtain at the KS-DFT level, are very much universal. Defect-dependent shifts with respect both to the vacuum level, but also the VBM, can be obtained at the much cheaper (as compared to GW) KS-DFT level.

As discussed above, the effect of stacking layers in a bulk configuration moves the defect occupied level towards the vacuum level (reduced Ionization Potential (IP)) by about 0.19 eV and 0.11 eV, respectively, at the KS-DFT ground-state level for the CC and $C_B V_N$ defects. This correction is nearly entirely due to the interaction with the nearest layers. Concerning h -BN, it has been shown and analyzed in several papers that the top of the valence band at the high-symmetry point K is very weakly dispersive in the AA' stacking configuration [243–245]. Namely, from the monolayer to the bulk, the top of the valence band remains

degenerate, dispersion growing slowly away from the K -point. Taking the vacuum level as a reference, the top of the valence band at K was shown to go down in energy by about 0.08 eV [244] at the **KS-DFT** level with the HSE hybrid functional [246, 247], demonstrating both weak electrostatic and hybridization effects. A similar value of 0.06 eV was found in Ref. [212] at the PBE level [42], confirming the stability of the **VBM** at the **KS-DFT** ground-state level, namely in the absence of polarization effects between the monolayer and the bulk. Adding the ~ -0.1 eV shift of the h -BN **VBM** and the $\sim +0.1$ eV to $\sim +0.2$ eV shift upward of the occupied defect levels in the CC and $C_B V_N$ cases, one finds that the energy spacing between the occupied defect levels and the **VBM** increases by a limited 0.2 eV to 0.3 eV from the monolayer to the bulk limit. Such an effect is mostly related to electrostatic and hybridization effects accounted for at the **KS-DFT** level.

We finally address the challenging case of unoccupied states. Focusing first on the defect states, we observe in FIGURE 4.16 that their polarization energy P_e is larger (in absolute value) as compared to the one associated with occupied defect levels. Unoccupied defect states are approaching the vacuum level, being weakly bound to the atomic layer. As such, the associated wavefunctions start delocalizing away from the atomic layer, inducing an enhanced polarization response from neighboring layers. The study of the charge density accumulated within a distance z of a CC@BN86 defected system for selected states highlights such a behavior. Namely, defining the z -axis as the normal one to the plane of the flake, we can define a charge density $\rho(z)$ along this axis, associated to a given wavefunction $\phi(\mathbf{r})$, such that

$$\rho(z) = \int dx dy |\phi(x, y, z)|^2. \quad (4.4)$$

In the FIGURE 4.18, focusing on the charge localized only on one side of the fragment, I compute

$$\int_0^z dz' \rho(z') \quad (4.5)$$

with respect to z . Namely, taking the reference $z = 0$ in the plane of the CC@BN86 fragment, I calculate the charge density contained within a height z . This graph evidences the delocalization away from the atomic plane with increasing **KS-DFT** energy. This can be used as a mean to better understand the increase of polarization energies (in absolute value) for unoccupied states with increasing energies in FIGURE 4.16.

However, such a delocalization phenomenon affects mainly the polarization response from the nearest-neighbor layers. If we calculate the polarization energy from the 3-layer system to the bulk, as illustrated in the inset of FIGURE 4.16, one observes that the effect of screening becomes much more state-independent and symmetric between holes and electrons. This is an indication that delocalization away from the defected layer remains small, at least for states close to the conduction edge, affecting mostly the response of the nearest layers but not beyond. This is similar to what was observed for the $C_B V_N$ defect, with the out-of-plane C atom polarizing more strongly (as compared to the in-plane CC defect) the nearest layers. This overscreening effect due to loosely bound charges spilling out the BN layer vanishes quickly for the response of layers located farther away. As a result, polarization effects stabilize unoccupied defect levels by an energy $|P_e| \sim 0.7 - 0.8$ eV, or an energy $|P_e - P_h| \sim 1.3 - 1.4$ eV as compared to the h -BN **VBM**.

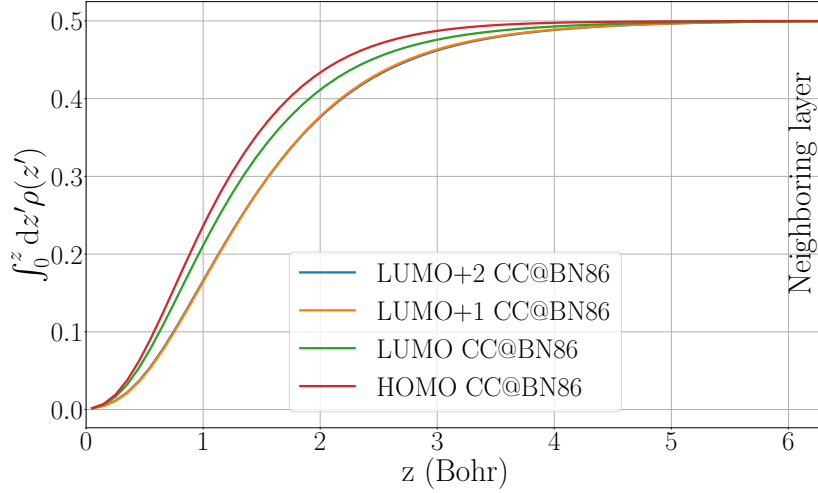


Figure 4.18: Integrated charge (see Eq.(4.4)) accumulated within a distance z of a CC@BN86 defected fragment for various states. The z -axis is perpendicular to the plane of the fragment. HOMO indicates the highest occupied orbital, while Lowest Unoccupied Molecular Orbital (LUMO), (LUMO+1) and (LUMO+2) indicate the lowest, lowest-plus-one and lowest-plus-two unoccupied ones. The vertical dashed line indicates the position of the neighboring layer.

We will not attempt here to discuss the position of the h -BN Conduction Band Minimum (CBM). As shown in FIGURE 4.16, states above the unoccupied defect levels lie above the vacuum with a positive KS-DFT energy. As such, delocalized nearly-free-electron states are expected to be present at the CBM of h -BN as documented in early studies on h -BN [245, 248]. The difficulties associated with describing unbound states with localized basis sets, and the much larger dispersion of h -BN states upon stacking at the CBM [244, 245], are serious limitations for the present localized-basis fragments calculations. The reader is reported to previous periodic-boundary GW and Quantum Monte Carlo (QMC) studies of the evolution of the electronic properties of pristine h -BN from the monolayer to the bulk [207, 213, 245, 249].

4.8 Conclusion

In this chapter, our fragment GW approach has been applied and validated for the study of defects in h -BN multilayer systems, where individual layers are fragmented in domains with non-overlapping wave functions. The resulting interacting susceptibility and screened Coulomb potential are shown to accurately describe the screening properties of infinite monolayers in the vicinity of the dopant, reproducing at the few meV level the extrapolation of QP energies in the infinite layer size limit. Such a divide-and-conquer scheme allows us to study at the many-body level systems containing thousands of atoms, dramatically facilitating the study of dilute defects in monolayer, few-layers, surface, or bulk h -BN systems.

The success of the fragmentation scheme for the block diagonalization of the independent-electron susceptibility is associated with the large ionic gap character of the h -BN substrate.

For such systems, the response to a perturbation proceeds by the creation of very localized induced dipoles, rather than the displacement of electrons over large distances. This can be restated by saying that the susceptibility $\chi_0(\mathbf{r}, \mathbf{r}'; \omega)$ is very short-ranged, with an exponential decay in real-space in the case of insulators [182]. Along that line, exploring the robustness of this approach for other 2D systems with smaller gap (*e.g.*, dichalcogenides) would be an interesting direction. In the present case, we find that our results are rather insensitive to fragment size and shape, provided that the fragments are large enough (around 100 atoms in the present study). As an additional ingredient, passivation of edge atoms, by repelling edge states away from the host gap, reduces the spurious contribution of edge polarization as compared to the bulk one. We do not exclude more efficient passivation strategies.

As a first application, we have studied the evolution of the paradigmatic carbon-dimer and $C_B V_N$ defects energy levels from the monolayer to n -layer systems, including the surface and bulk limits. The polarization energy, namely, the evolution of the *GW* electronic energy levels as a function of increased screening upon the inclusion of additional layers, is shown to follow a nearly-universal $(P_0/n + P_\infty)$ law with the number n of layers. The slope P_0 and the asymptotic value P_∞ depend on the defect location (bulk or surface) but hardly on the defect type. Such an approach rationalizes the evolution of defect energy levels as a function of the number of layers and allows us to easily extrapolate data obtained for the monolayer or very-few-layer systems to the bulk.

This universal behavior can be rationalized by emphasizing that the surrounding polarizable substrate reacts basically to an added charge associated with the photoemission process used to measure electron addition or removal energies. As such, the exact spatial distribution of this added charge, that depends on the defect type and chosen energy level, only contributes to higher order (dipolar, quadrupolar, etc.) terms to the perturbation felt by the polarizable substrate. While such arguments allow to rationalize asymptotic behaviors, it is remarkable that they start applying to the reaction of second-, and even first-, nearest-neighbor layers. While the present scheme ideally applies to localized defect states, our results suggest that similar polarization energies can be obtained for extended *h*-BN Bloch states, leaving aside conduction band edge states that start delocalizing away from the plane of atoms. Special care should probably be taken with defects inducing large elastic deformations, requiring potentially larger fragments.

Together with the fragmentation scheme, we have shown that the neglect of neighboring layer wavefunction overlap, a common approximation in the 2D-genomics approach, leads to underestimating screening effects by up to 10%. This error is, however, very largely canceled by neglecting the frequency dependence of the dielectric response in the calculation of the QP energy difference between the monolayer and n -layer systems. This approximation takes the form of the well-known static COHSEX approximation in the *GW* framework. This static Δ COHSEX scheme for calculating the increase in polarization energy upon adding layers, leads to overestimating polarization energies. It significantly reduces the error introduced by decoupling wave function overlaps between layers.

We further explored a multipole-like expansion of the long-range susceptibility, with a dramatic reduction of the auxiliary basis size used to express density variations in the long-range. Together with fragmentation, this approach also contributed significantly to reducing the cost of performing many-body calculations. For the sake of indication, static COHSEX

calculations on $\sim 10^5$ electrons, as encountered for seven-layer systems, were conducted with a typical cost of 1600 CPU hours in the present fragment approach. While done here in a somehow *ad hoc* fashion by removing high-angular momentum channels in the auxiliary basis, such a scheme can certainly be improved by using the susceptibility compression scheme developed in the chapter 2.

Conclusion (version française)

Ce travail doctoral a ouvert la voie aux calculs GW sur des environnements extrêmement grands et de plus en plus réalistes, contenant des centaines de milliers d'atomes. Ceci a été rendu possible grâce à l'utilisation d'approches quantiques dites « environnées », dans lesquelles le système total est partitionné en un sous-système « central » ou « actif », et son environnement. Alors que le formalisme *ab initio* GW était jusqu'à présent majoritairement associé à des approches semi-empiriques pour la prise en compte des effets de l'environnement, cette thèse a été l'occasion de développer une description totalement *ab initio* de ce dernier.

Les différents travaux présentés dans ce manuscrit reposent tous sur l'approximation fragment. Celle-ci consiste à négliger le recouvrement orbitalaire entre les différents sous-systèmes, permettant d'obtenir une susceptibilité électronique non-interagissante χ_0 diagonale par blocs. La complexité globale d'un calcul GW passe alors de quartique à cubique. Afin de pouvoir étudier des systèmes de très grande taille, il est également nécessaire de réduire le préfacteur associé à l'inversion de l'équation de Dyson du potentiel de Coulomb écranté W . Pour ce faire, nous avons développé un algorithme de compression de l'opérateur susceptibilité, nous permettant ainsi de réduire de façon drastique la taille des blocs associés aux fragments de l'environnement. Lors de la validation de notre approche sur des cristaux de fullerènes en surface ou volume, nous avons ainsi pu étudier des systèmes contenant jusqu'à près de 200 000 atomes, en moins de 10 000 heures CPU.

Traditionnellement, les méthodes semi-empiriques multi-échelles, pour la description d'un milieu environnant polarisable, reposent sur une description statique de l'environnement. Afin de mieux caractériser notre approche « environnée », et en s'appuyant sur le caractère dynamique par nature du formalisme GW , nous avons cherché à quantifier l'erreur induite par une telle approximation. Nous avons donc réalisé des comparaisons explicites, sur une surface de fullerènes et une molécule d'eau dans un nanotube de carbone métallique, entre deux approches statiques d'une part et une description totalement dynamique de la réponse diélectrique de l'environnement d'autre part. Notre nouvelle approche QM_{GW}/QM_{COHSEX} , permettant d'allier dans le même calcul une description dynamique de la partie « active » à celle statique $COHSEX$ pour le milieu polarisable, s'avère la plus précise. Elle mène à des erreurs sur l'énergie de polarisation inférieure à 10%.

Au-delà de ces travaux de développement, l'approche fragment a également été appliquée à l'étude des niveaux d'énergie de défauts ponctuels dans du nitrure de bore hexagonal (h -BN). Plus précisément, la fragmentation est utilisée entre les couches de h -BN, mais aussi à l'intérieur de celles-ci. En repoussant suffisamment la limite sur la taille des systèmes étudiables, nous avons pu calculer la renormalisation de ces niveaux dans la vraie limite diluée, à l'aide de lois d'échelle sur le nombre de couches de h -BN considérées. Cette étude met également en avant un caractère universel pour l'énergie de polarisation correspondante, qui ne dépend pas du type exact de défaut analysé.

Perspectives

Concernant la méthode fragment à proprement parler, une possibilité d'amélioration consisterait à la coupler avec des méthodes scindant le système total en plusieurs sous-systèmes au niveau DFT [169, 250, 251]. Ceci permettrait d'améliorer les états propres Kohn-Sham, en prenant en compte les effets créés par les densités électroniques (gelées) de l'ensemble des fragments. En particulier, le champ électrostatique généré dans l'état fondamental, d'une grande importance dans les milieux organiques présentant un dipôle, quadrupôle, etc., permanents [3, 123, 149, 166, 252], pourrait être pris en compte au niveau DFT.

De plus, la méthode fragment semble pouvoir être améliorée au niveau GW en prenant en compte des corrections associées à des dimères de fragments [140]. Une autre solution pourrait être de conserver les effets de la susceptibilité de fragments totalement interagissants, mais en se restreignant uniquement à un faible nombre d'états vides ou occupés [170, 253].

Concernant l'étude des défauts ponctuels dans du h -BN, celle-ci a mis avant la possibilité de fragmenter des systèmes covalents isolants. Ceci ouvre la voie à l'étude au niveau GW de divers systèmes désordonnés. Il peut s'agir de structures composées d'un empilement de couches, de différentes natures ou tournées les unes par rapport aux autres, entraînant un effet de Moiré [254]. L'étude d'interfaces désordonnées [4], particulièrement utile pour le photovoltaïque organique, ou celle de monocouches également désordonnées telles le h -BCN, composé d'une juxtaposition de domaines de graphène et de h -BN [255, 256], semblent être des sujets propices à l'utilisation de la méthode fragment.

De manière plus générale, une extension naturelle des travaux réalisés au cours de ces trois dernières années consisterait à utiliser nos résultats comme points de départ pour des calculs BSE (*Bethe-Salpeter Equation*), afin de pouvoir calculer des excitations neutres, ou autrement dit l'absorption optique. Une fois les énergies de quasiparticules et le potentiel de Coulomb écranté W du système d'intérêt renormalisés par les effets de l'environnement, les calculs BSE peuvent être menés comme d'habitude, sur la partie « active » isolée. Toutes les informations nécessaires concernant les effets de l'environnement sont déjà pris en compte au niveau sous-jacent GW [7]. D'autre part, l'approche standard BSE « adiabatique » néglige la dépendance en fréquence de W . Les subtilités sur le traitement statique ou dynamique des effets de l'environnement ne sont donc plus pertinentes à ce niveau. Au-delà des énergies d'absorption, l'impact de l'environnement sur le couplage exciton-exciton pour les transferts d'énergie au niveau BSE pourrait également être étudié. De même, toujours en lien avec les travaux en cours dans notre groupe au CNRS et au CEA, l'influence du milieu environnant sur les gradients BSE et les propriétés du système (distribution de charge, géométrie, etc.) dans l'état excité, sont de possibles extensions aux développements réalisés durant cette thèse.

Finalement, durant mes trois années de thèse, la majeure partie de mon temps a été consacrée aux développements mathématiques, et par-dessus tout, à l'implémentation efficace des différentes équations dans notre code massivement parallèle Beyond Density-Functional Theory (BEDEFT) (C++/MPI/OpenMP). Ceci peut s'apparenter à la mise en place, pendant plusieurs années, d'un vaste système expérimental par nos collègues expérimentateurs. Par conséquent, peu d'applications ont été réalisées au cours des trois dernières années. Nos exemples ont servi essentiellement à illustrer notre méthodologie, plutôt qu'à répondre à des questions spécifiques sur un matériau ou un phénomène donné. Cependant, l'étude de

l'évolution des niveaux de quasiparticules pour un défaut dans du *h*-BN, en fonction du nombre de couches considérées, fait quelque peu exception. Cette étude transmet un véritable message physique à la communauté. Les simples lois asymptotiques mises en valeur, en lien avec les effets d'écrantage à longue portée, sont des résultats quelquefois mal compris par la communauté, notamment celle de la DFT. Il n'en demeure pas moins que les nouvelles fonctionnalités du code BEDEFT devraient permettre bien plus d'applications. Bien que notre groupe s'intéresse avant tout au développement méthodologique, l'ouverture prochaine du code à tous devrait s'accompagner, je l'espère, de nouvelles applications intéressantes.

Conclusion (English version)

These doctoral studies have paved the way to perform GW calculations in very large-scale and more realistic environments, containing up to hundreds of thousands of atoms. This has been made possible thanks to “embedded” quantum approaches, where the total system is divided into an “active” or “central” subsystem, and its environment. Until now, the *ab initio* GW formalism has essentially been merged with semi-empirical methods to describe the effects of the environment. To go further, this thesis has been dedicated to the development of an *ab initio* description of this latter.

All the different studies presented in this manuscript are based on the fragment approximation. It consists into neglecting the wavefunction overlap between the different subsystems, resulting in a block-diagonal non-interacting electron susceptibility χ_0 . The global complexity of a GW calculation goes from quartic to cubic. To study very large-scale systems, one should also decrease the prefactor associated to the Dyson equation of the screened Coulomb potential W . To do so, we have developed a compression algorithm under constraints of the susceptibility operator. This enables us to drastically reduce the size of the blocks associated to fragments within the environment. We have been able to tackle systems containing up to 200 000 atoms, within less than 10 000 CPU hours, during the validation of our approach on surface and bulk fullerene crystals.

Traditionally, the multiscale semi-empirical methods, used for the description of a polarizable environment, are based on a static description of this latter. To better characterize our “embedded” scheme, and based on the dynamical nature of the GW formalism, we have tried to quantify the error induced by such an approximation. We have explicitly compared, through the examples of a fullerene surface and a water molecule inside a metallic carbon nanotube, two static approaches to a fully dynamical description of the dielectric response of the environment. Our new QM_{GW}/QM_{COHSEX} approach, which enables us to describe, in the same calculation, the “active” part at the fully dynamical level and the environment at the static COHSEX level, is the most accurate method. It leads to errors on polarization energies below 10%.

Beyond these development parts, the fragment approximation has also been applied to the study of energy levels of point defects in hexagonal Boron Nitride (*h-BN*). More exactly, the fragmentation has been used between the *h-BN* layers, but also inside each of them. By pushing enough the boundaries of the size of affordable systems, we have been able to compute the renormalizations of these energy levels in the true dilute limit. This has been possible thanks to scaling laws on the number of layers of *h-BN*. This study also highlights a universal behavior of the corresponding polarization energy, which does not depend on the exact type of defect under study.

Perspectives

The fragment approach could be improved by merging it with subsystem-Density-Functional Theory (DFT) techniques [169, 250, 251]. It may enhance the input Kohn-Sham eigenstates,

by taking into account the effects created by the frozen density of every fragment. More specifically, the electrostatic field generated by the environment in the ground state, of crucial importance in organic media made of molecules with a permanent dipole, quadrupole, etc. [3, 123, 149, 166, 252], could be further accounted for at the DFT level.

Moreover, the fragment method could also be improved at the *GW* level by taking into account fragments-dimer corrections [140]. Another possibility would be to conserve the effects created by the interacting susceptibility of the full system, but restricted to a small subset of occupied or unoccupied states [170, 253].

Concerning the study of point defects in *h*-BN, this application illustrates the possibility to apply the fragment approach to covalent insulators. This paves the way to study, at the *GW* level, diverse disordered systems. This includes the stacking of layers of different chemical nature, or systems made of rotated layers with Moiré patterns [254]. Disordered interfaces [4], particularly useful for organic photovoltaic cells, or disordered monolayers such as *h*-BCN with the formation of segregated *h*-BN and graphene domains [255, 256], seem to be relevant systems for the fragment approach

More generally, an obvious extension of the present studies is the possibility to perform Bethe–Salpeter Equation (BSE) calculations for the study of neutral excitations, namely optical absorption. As a matter of fact, once the Quasiparticle (QP) energies and screened Coulomb potential are renormalized by the environment, BSE calculations can be performed as usual, that is as a standard calculation in the gas phase. All needed information about the effect of the environment are already available as outputs of the preceding *GW* calculations. Furthermore, in the standard “adiabatic” BSE approach that neglects the frequency-dependence of the screened Coulomb potential, the subtleties of whether one should consider a static or dynamical environment become irrelevant. Beyond absorption energies, the impact of the environment on the exciton-exciton coupling for energy transfers at the BSE level can be straightforwardly considered. Similarly, still in relation with ongoing studies in our groups at CNRS and CEA, the influence of the environment on BSE excited-state gradients, and on the related excited states properties (charge distribution, geometries, etc.), may stand as future extension made possible by the present developments.

During the three years devoted to my doctoral studies, much time was spent in mathematical developments and, most of all, in implementing all related equations efficiently in the massively parallel Beyond Density-Functional Theory (BEDEFT) code (C++/MPI/OpenMP). This is very much like building for many years a big experimental setup for our experimentalist colleagues. As such, the applications we considered were relatively scarce, with the purpose to illustrate the methodology rather than answering some specific questions about a given material and phenomenon. As an exception, the change in QP energies for defects levels in *h*-BN, as a function of the number of layers, was a real physical message to the community. The simple laws we could illustrate, in relation with long-range screening, are results not so commonly understood by the community, and in particular by the DFT community. It remains that the novel functionalities of the BEDEFT code should allow much more applications. While our group is mostly involved in methodology, the upcoming distribution of the BEDEFT package should, I hope, foster interesting applications.

Appendices

Constrained compression of the fragment susceptibility

This appendix is dedicated to some algebraic developments for the constrained compression of the gas phase susceptibility of the different fragments, as presented in section 2.2 page 67.

A.1 Computation of $\widetilde{\mathbf{X}}_g$

In this section, I present algebraic details to go from Eq.(2.22) page 73, to Eq.(2.26), via the equations (2.25).

In practice, all matrices appearing in Eq.(2.25) are real. In this context, it can be shown [257, 258] that¹

$$\frac{\partial \text{Tr}(\mathbf{A}\mathbf{X}\mathbf{B})}{\partial \mathbf{X}} = \frac{\partial \text{Tr}(\mathbf{B}^\dagger \mathbf{X}^\dagger \mathbf{A}^\dagger)}{\partial \mathbf{X}} = \mathbf{A}^\dagger \mathbf{B}^\dagger \quad (\text{A.1a})$$

$$\frac{\partial \text{Tr}(\mathbf{X}^\dagger \mathbf{A}\mathbf{X}\mathbf{B})}{\partial \mathbf{X}} = \mathbf{A}\mathbf{X}\mathbf{B} + \mathbf{A}^\dagger \mathbf{X}\mathbf{B}^\dagger. \quad (\text{A.1b})$$

Using these formulas, the cyclic property of the trace and the fact that \mathbf{A}_1 is symmetric, this leads to [259]

$$\mathbf{K}^\dagger \Gamma \left[\mathbf{Z} - \Gamma^\dagger \left(\mathbf{U}_R \mathbf{C} \mathbf{U}_R^\dagger + \mathbf{K} \mathbf{A}_1 \mathbf{K}^\dagger + \mathbf{U}_R \mathbf{A}_2 \mathbf{K}^\dagger + \mathbf{K} \mathbf{A}_2^\dagger \mathbf{U}_R^\dagger \right) \Gamma \right] \Gamma^\dagger \mathbf{K} = \mathbf{0} \quad (\text{A.2a})$$

$$\mathbf{U}_R^\dagger \Gamma \left[\mathbf{Z} - \Gamma^\dagger \left(\mathbf{U}_R \mathbf{C} \mathbf{U}_R^\dagger + \mathbf{K} \mathbf{A}_1 \mathbf{K}^\dagger + \mathbf{U}_R \mathbf{A}_2 \mathbf{K}^\dagger + \mathbf{K} \mathbf{A}_2^\dagger \mathbf{U}_R^\dagger \right) \Gamma \right] \Gamma^\dagger \mathbf{K} = \mathbf{0}. \quad (\text{A.2b})$$

\mathbf{K} and \mathbf{U}_R being orthogonal matrices spanning supplementary subspaces, it comes that

$$\mathbf{K} \mathbf{K}^\dagger + \mathbf{U}_R \mathbf{U}_R^\dagger = \mathbf{I}_{N_\gamma}, \quad (\text{A.3})$$

with \mathbf{I}_{N_γ} the identity matrix of size N_γ . Thus, the two equations (A.2) lead to

$$\Gamma \left[\mathbf{Z} - \Gamma^\dagger \left(\mathbf{U}_R \mathbf{C} \mathbf{U}_R^\dagger + \mathbf{K} \mathbf{A}_1 \mathbf{K}^\dagger + \mathbf{U}_R \mathbf{A}_2 \mathbf{K}^\dagger + \mathbf{K} \mathbf{A}_2^\dagger \mathbf{U}_R^\dagger \right) \Gamma \right] \Gamma^\dagger \mathbf{K} = \mathbf{0}. \quad (\text{A.4})$$

Assuming that $\Gamma \Gamma^\dagger$ is invertible², such an equation is equivalent to

$$\left(\mathbf{K} \mathbf{A}_1 \mathbf{K}^\dagger + \mathbf{U}_R \mathbf{A}_2 \mathbf{K}^\dagger + \mathbf{K} \mathbf{A}_2^\dagger \mathbf{U}_R^\dagger \right) \Gamma \Gamma^\dagger \mathbf{K} = \left[\left(\Gamma \Gamma^\dagger \right)^{-1} \Gamma \mathbf{Z} - \mathbf{U}_R \mathbf{C} \mathbf{U}_R^\dagger \Gamma \right] \Gamma^\dagger \mathbf{K}. \quad (\text{A.5})$$

¹Namely, the same symbol can be used for the transpose \mathbf{A}^\top and the conjugate transpose \mathbf{A}^\dagger of the matrix \mathbf{A} , which simplifies the equations in this section.

²In practice, the dimension N_γ of polarization basis $\{\gamma\}$ is much smaller than the one N_t of the test basis $\{t\}$. In the following subsections, $N_\gamma \sim 60$, while $N_t \sim 8000$ and the basis set are such that this hypothesis is valid.

It should be noticed that $\mathbf{K}^\dagger \mathbf{\Gamma} \mathbf{\Gamma}^\dagger \mathbf{K}$, which is the Gram matrix³ of the columns of \mathbf{K} , is also invertible. Multiplying Eq.(A.5) on the left by \mathbf{U}_R^\dagger leads to

$$\mathbf{A}_2 = \mathbf{U}_R^\dagger \left[(\mathbf{\Gamma} \mathbf{\Gamma}^\dagger)^{-1} \mathbf{\Gamma} \mathbf{Z} - \mathbf{U}_R \mathbf{C} \mathbf{U}_R^\dagger \mathbf{\Gamma} \right] \mathbf{\Gamma}^\dagger \mathbf{K} (\mathbf{K}^\dagger \mathbf{\Gamma} \mathbf{\Gamma}^\dagger \mathbf{K})^{-1}. \quad (\text{A.6})$$

Once \mathbf{A}_2 is computed, multiplying Eq.(A.5) on the left by \mathbf{K}^\dagger leads to \mathbf{A}_1 such that

$$\mathbf{A}_1 = \left(\mathbf{K}^\dagger \left[(\mathbf{\Gamma} \mathbf{\Gamma}^\dagger)^{-1} \mathbf{\Gamma} \mathbf{Z} \right] - \mathbf{A}_2^\dagger \mathbf{U}_R^\dagger \mathbf{\Gamma} \right) \mathbf{\Gamma}^\dagger \mathbf{K} (\mathbf{K}^\dagger \mathbf{\Gamma} \mathbf{\Gamma}^\dagger \mathbf{K})^{-1}. \quad (\text{A.7})$$

To simplify formulas of \mathbf{A}_1 and \mathbf{A}_2 , one can introduce

$$\mathbf{J} = \mathbf{K}^\dagger \mathbf{\Gamma}. \quad (\text{A.8})$$

Still assuming that $\mathbf{J} \mathbf{J}^\dagger$ and $\mathbf{\Gamma} \mathbf{\Gamma}^\dagger$ are invertible, \mathbf{U}_Γ and \mathbf{U}_J are thus square orthonormal matrices. In particular, using the compact Singular Value Decomposition (SVD) leads to

$$(\mathbf{\Gamma} \mathbf{\Gamma}^\dagger)^{-1} \mathbf{\Gamma} = \mathbf{U}_\Gamma \mathbf{\Sigma}_\Gamma^{-1} \mathbf{V}_\Gamma^\dagger = (\mathbf{\Gamma}^\oplus)^\dagger \quad (\text{A.9a})$$

$$(\mathbf{K}^\dagger \mathbf{\Gamma} \mathbf{\Gamma}^\dagger \mathbf{K})^{-1} \mathbf{K}^\dagger \mathbf{\Gamma} = \mathbf{U}_J \mathbf{\Sigma}_J^{-1} \mathbf{V}_J^\dagger = (\mathbf{J}^\oplus)^\dagger, \quad (\text{A.9b})$$

where \mathbf{M}^\oplus is the pseudo-inverse of \mathbf{M} (see definition (2.18) page 72). Equations (A.6) and (A.7) can be rewritten

$$\mathbf{A}_2 = \mathbf{U}_R^\dagger \left[(\mathbf{\Gamma}^\oplus)^\dagger \mathbf{Z} - \mathbf{U}_R \mathbf{C} \mathbf{U}_R^\dagger \mathbf{\Gamma} \right] \mathbf{J}^\oplus \quad (\text{A.10a})$$

$$\mathbf{A}_1 = \left[\mathbf{K}^\dagger (\mathbf{\Gamma}^\oplus)^\dagger \mathbf{Z} - \mathbf{A}_2^\dagger \mathbf{U}_R^\dagger \mathbf{\Gamma} \right] \mathbf{J}^\oplus \quad (\text{A.10b})$$

Introducing \mathbf{P} the matrix such that

$$\mathbf{P} = \mathbf{J}^\oplus \mathbf{K}^\dagger, \quad (\text{A.11})$$

and using Eq.(A.3), the equations (A.10) lead to

$$\mathbf{U}_R \mathbf{A}_2 \mathbf{K}^\dagger = (\mathbf{\Gamma}^\oplus)^\dagger \mathbf{Z} \mathbf{P} - \mathbf{K} \mathbf{K}^\dagger (\mathbf{\Gamma}^\oplus)^\dagger \mathbf{Z} \mathbf{P} - \mathbf{U}_R \mathbf{C} \mathbf{U}_R^\dagger \mathbf{\Gamma} \mathbf{P} \quad (\text{A.12a})$$

$$\mathbf{K} \mathbf{A}_1 \mathbf{K}^\dagger = \mathbf{K} \mathbf{K}^\dagger (\mathbf{\Gamma}^\oplus)^\dagger \mathbf{Z} \mathbf{P} - \mathbf{K} \mathbf{A}_2^\dagger \mathbf{U}_R^\dagger \mathbf{\Gamma} \mathbf{P}. \quad (\text{A.12b})$$

It follows that

$$\mathbf{K} \mathbf{A}_1 \mathbf{K}^\dagger + \mathbf{U}_R \mathbf{A}_2 \mathbf{K}^\dagger + \mathbf{K} \mathbf{A}_2^\dagger \mathbf{U}_R^\dagger = (\mathbf{\Gamma}^\oplus)^\dagger \mathbf{Z} \mathbf{P} - \mathbf{U}_R \mathbf{C} \mathbf{U}_R^\dagger \mathbf{\Gamma} \mathbf{P} + \mathbf{K} \mathbf{A}_2^\dagger \mathbf{U}_R^\dagger (\mathbf{I}_{N_\gamma} - \mathbf{\Gamma} \mathbf{P}). \quad (\text{A.13})$$

The last term can be rewritten

$$\mathbf{K} \mathbf{A}_2^\dagger \mathbf{U}_R^\dagger (\mathbf{I}_{N_\gamma} - \mathbf{\Gamma} \mathbf{P}) = \left[\mathbf{P}^\dagger \mathbf{Z} (\mathbf{\Gamma}^\oplus) - \mathbf{P}^\dagger \mathbf{Z} (\mathbf{\Gamma}^\oplus) \mathbf{K} \mathbf{K}^\dagger - \mathbf{P}^\dagger \mathbf{\Gamma}^\dagger \mathbf{U}_R \mathbf{C} \mathbf{U}_R^\dagger \right] (\mathbf{I}_{N_\gamma} - \mathbf{\Gamma} \mathbf{P}) \quad (\text{A.14a})$$

$$\begin{aligned} &= -\mathbf{P}^\dagger \mathbf{\Gamma}^\dagger \mathbf{U}_R \mathbf{C} \mathbf{U}_R^\dagger (\mathbf{I}_{N_\gamma} - \mathbf{\Gamma} \mathbf{P}) \\ &\quad + \mathbf{P}^\dagger \mathbf{Z} (\mathbf{\Gamma}^\oplus) (\mathbf{I}_{N_\gamma} - \mathbf{\Gamma} \mathbf{P} - \mathbf{K} \mathbf{K}^\dagger + \mathbf{K} \mathbf{K}^\dagger \mathbf{\Gamma} \mathbf{P}) \end{aligned} \quad (\text{A.14b})$$

$$\begin{aligned} &= -\mathbf{P}^\dagger \mathbf{\Gamma}^\dagger \mathbf{U}_R \mathbf{C} \mathbf{U}_R^\dagger (\mathbf{I}_{N_\gamma} - \mathbf{\Gamma} \mathbf{P}) \\ &\quad + \mathbf{P}^\dagger \mathbf{Z} (\mathbf{\Gamma}^\oplus) (\mathbf{I}_{N_\gamma} - \mathbf{\Gamma} \mathbf{P} - \mathbf{K} \mathbf{K}^\dagger + \mathbf{K} \mathbf{J} \mathbf{J}^\oplus \mathbf{K}^\dagger) \end{aligned} \quad (\text{A.14c})$$

$$= -\mathbf{P}^\dagger \mathbf{\Gamma}^\dagger \mathbf{U}_R \mathbf{C} \mathbf{U}_R^\dagger (\mathbf{I}_{N_\gamma} - \mathbf{\Gamma} \mathbf{P}) + \mathbf{P}^\dagger \mathbf{Z} (\mathbf{\Gamma}^\oplus - \mathbf{P}). \quad (\text{A.14d})$$

³For the scalar product defined by the symmetric positive definite matrix $\mathbf{\Gamma} \mathbf{\Gamma}^\dagger$.

To go from Eq.(A.14c) to Eq.(A.14d), I use the hypothesis that \mathbf{U}_J is a square orthonormal matrix, leading to $\mathbf{J}\mathbf{J}^\oplus = \mathbf{I}$, and the fact that

$$\mathbf{\Gamma}^\oplus \mathbf{\Gamma} \mathbf{P} = \mathbf{\Gamma}^\dagger (\mathbf{\Gamma} \mathbf{\Gamma}^\dagger)^{-1} \mathbf{\Gamma} \mathbf{\Gamma}^\dagger \mathbf{K} (\mathbf{K}^\dagger \mathbf{\Gamma} \mathbf{\Gamma}^\dagger \mathbf{K})^{-1} \mathbf{K}^\dagger \quad (\text{A.15a})$$

$$= \mathbf{\Gamma}^\dagger \mathbf{K} (\mathbf{K}^\dagger \mathbf{\Gamma} \mathbf{\Gamma}^\dagger \mathbf{K})^{-1} \mathbf{K}^\dagger \quad (\text{A.15b})$$

$$= \mathbf{J}^\oplus \mathbf{K}^\dagger \quad (\text{A.15c})$$

$$= \mathbf{P}, \quad (\text{A.15d})$$

thanks to Eq.(A.9). Defining the matrix \mathbf{L} such that $\mathbf{L} = \mathbf{R}^\oplus [\mathbf{I}_N - \mathbf{\Gamma} \mathbf{P}]$, the optimal solution $\tilde{\mathbf{X}}_g$ is given by

$$\tilde{\mathbf{X}}_g = \mathbf{L}^\dagger \mathbf{O} \mathbf{L} + \mathbf{P}^\dagger \mathbf{Z} \mathbf{\Gamma}^\oplus + (\mathbf{\Gamma}^\oplus)^\dagger \mathbf{Z} \mathbf{P} - \mathbf{P}^\dagger \mathbf{Z} \mathbf{P}. \quad (\text{A.16})$$

The absence of constraints is similar to the case where $\mathbf{R} = \mathbf{0}$, $\mathbf{L} = \mathbf{0}$, $\mathbf{K} = \mathbf{I}_{N_\gamma}$ and $\mathbf{P} = \mathbf{\Gamma}^\oplus$. The formula (A.16) simplifies thus into

$$\tilde{\mathbf{X}}_g = (\mathbf{\Gamma}^\oplus)^\dagger \mathbf{Z} \mathbf{\Gamma}^\oplus. \quad (\text{A.17})$$

A.2 Computation of the polarization basis $\{\gamma\}$

This section explains our method to compute the polarization basis set $\{\gamma\}$, of dimension N_γ , via the Eq.(2.28) page 74. $\tilde{\mathbf{X}}_g^{(1)}(\omega)$ is computed in such a basis set. Following the previous sections, for the sake of compactness the exponent (I) and the frequency index ω are now dropped. More exactly, in this section, we develop our method to compute the $\{C_{\gamma P}\}$ coefficient set of Eq.(2.29). An exact solution being too difficult to calculate, we start from the equation (2.22) page 73 and we compute an approximation of these coefficients through two sub-problems. Still, in this section, all the matrices are real.

A.2.1 Optimization for $N_\gamma = N_{\text{cstr}}$

Keeping the same notation as in section 2.2.3 pages 71 to 74, we start by studying the specific problem of $N_\gamma = N_{\text{cstr}}$, with a initial choice of the polarization basis set $\{\gamma_0\} = \{P\}$. Namely, this corresponds to a polarization basis set which is the same as the auxiliary one. To be more explicit, we re-index by 0 all matrices depending directly on $\{\gamma_0\}$. \mathbf{C}_0 being invertible, with $\text{rank}(\mathbf{C}_0) = N_{\text{cstr}}$, there is a matrix \mathbf{S} such that $\mathbf{A}_1 = \mathbf{S} \mathbf{C}_0 \mathbf{S}^\dagger$, and $\mathbf{A}_2 = \mathbf{C}_0 \mathbf{S}^\dagger$. Following the equation (2.15), we search for $\mathbf{S}_{\text{opt}}^{(1)}$ such that

$$\mathbf{S}_{\text{opt}}^{(1)} = \underset{\mathbf{S}}{\text{argmin}} \left\| \mathbf{Z} - \mathbf{\Gamma}_0^\dagger (\mathbf{U}_{\mathbf{R}_0} + \mathbf{K}_0 \mathbf{S}) \mathbf{C}_0 (\mathbf{U}_{\mathbf{R}_0} + \mathbf{K}_0 \mathbf{S})^\dagger \mathbf{\Gamma}_0 \right\|^2. \quad (\text{A.18})$$

The solution $\mathbf{S}_{\text{opt}}^{(1)}$ of this non-linear optimization problem is computed by a gradient descent algorithm, thanks to the gradient $\mathbf{G}(\mathbf{S})$ such that⁴

$$\mathbf{G}(\mathbf{S}) = \frac{\partial}{\partial \mathbf{S}} \left\| \mathbf{Z} - \Gamma_0^\dagger (\mathbf{U}_{\mathbf{R}_0} + \mathbf{K}_0 \mathbf{S}) \mathbf{C}_0 (\mathbf{U}_{\mathbf{R}_0} + \mathbf{K}_0 \mathbf{S})^\dagger \Gamma_0 \right\|^2 \quad (\text{A.19a})$$

$$= -4 \mathbf{K}_0^\dagger \Gamma_0 \left[\mathbf{Z} - \Gamma_0^\dagger (\mathbf{U}_{\mathbf{R}_0} + \mathbf{K}_0 \mathbf{S}) \mathbf{C}_0 (\mathbf{U}_{\mathbf{R}_0} + \mathbf{K}_0 \mathbf{S})^\dagger \Gamma_0 \right] \Gamma_0^\dagger (\mathbf{U}_{\mathbf{R}_0} + \mathbf{K}_0 \mathbf{S}) \mathbf{C}_0. \quad (\text{A.19b})$$

We keep $\mathbf{U}_{\mathbf{R}} = \mathbf{U}_{\mathbf{R}_0} + \mathbf{K}_0 \mathbf{S}_{\text{opt}}^{(1)}$ as a subset of the researched optimal directions $\{\gamma\}$. More exactly, the i^{th} column of $\mathbf{U}_{\mathbf{R}}$ corresponds to the coefficients $\{C_{\gamma P}\}$ of the i^{th} vector of the required basis set $\{\gamma\}$.

A.2.2 Optimization problem for $\mathbf{A}_2 = \mathbf{0}$

To find the other coefficients $\{C_{\gamma P}\}$, we use a greedy strategy. We consider only the first and second terms of the right-hand side of the equation (2.22), so namely $\mathbf{A}_2 = \mathbf{0}$. We also write the factorized form of the general symmetric matrix $\mathbf{A}_1 = \mathbf{S} \mathbf{\Delta} \mathbf{S}^\dagger$, with $\mathbf{\Delta}$ a diagonal matrix. Independently of $\mathbf{\Delta}$, the required coefficients $\{C_{\gamma P}\}$ defining the optimal directions are only determined by the \mathbf{S} matrix⁵. Using the N_{cstr} first directions previously found, given $\mathbf{Z}_{\text{cstr}} = \mathbf{Z} - \Gamma_0^\dagger \mathbf{U}_{\mathbf{R}} \mathbf{C}_0 \mathbf{U}_{\mathbf{R}}^\dagger \Gamma_0$, and $m = \max(0, N_\gamma - N_{\text{cstr}})$, we thus search for solutions $\mathbf{S}_{\text{opt}}^{(2)}$ of the low rank sub-problem

$$\mathbf{S}_{\text{opt}}^{(2)} = \underset{\mathbf{S}, \mathbf{\Delta} / \text{rank}(\mathbf{S}) \leq m}{\text{argmin}} \left\| \mathbf{Z}_{\text{cstr}} - \Gamma_0^\dagger \mathbf{K}_0 \mathbf{S} \mathbf{\Delta} \mathbf{S}^\dagger \mathbf{K}_0^\dagger \Gamma_0 \right\|^2. \quad (\text{A.20})$$

Defining $\mathbf{J}_0 = \mathbf{K}_0^\dagger \Gamma_0$, and using its compact SVD $\mathbf{J}_0 = \mathbf{U}_{\mathbf{J}_0} \mathbf{\Sigma}_{\mathbf{J}_0} \mathbf{V}_{\mathbf{J}_0}^\dagger$, this problem is equivalent to

$$\mathbf{S}_{\text{opt}}^{(2)} = \underset{\mathbf{S}, \mathbf{\Delta} / \text{rank}(\mathbf{S}) \leq m}{\text{argmin}} \left\| \mathbf{V}_{\mathbf{J}_0}^\dagger \mathbf{Z}_{\text{cstr}} \mathbf{V}_{\mathbf{J}_0} - \mathbf{\Sigma}_{\mathbf{J}_0} \mathbf{U}_{\mathbf{J}_0}^\dagger \mathbf{S} \mathbf{\Delta} \mathbf{S}^\dagger \mathbf{U}_{\mathbf{J}_0} \mathbf{\Sigma}_{\mathbf{J}_0} \right\|^2. \quad (\text{A.21})$$

Indeed, even if $\mathbf{V}_{\mathbf{J}_0}$ is not a square orthonormal matrix, we can consider the nullspace of $\mathbf{V}_{\mathbf{J}_0}^\dagger$, of which we write an orthonormal basis as the column of the matrix \mathbf{W} , such that $\mathbf{V}_{\mathbf{J}_0}^\dagger \mathbf{W} = \mathbf{0}$. In particular, $\mathbf{W} \mathbf{W}^\dagger + \mathbf{V}_{\mathbf{J}_0} \mathbf{V}_{\mathbf{J}_0}^\dagger = \mathbf{I}$, with \mathbf{I} the identity matrix, leading for every matrix \mathbf{A} to

$$\|\mathbf{A}\|^2 = \left\| \left(\mathbf{W} \mathbf{W}^\dagger + \mathbf{V}_{\mathbf{J}_0} \mathbf{V}_{\mathbf{J}_0}^\dagger \right) \mathbf{A} \right\|^2 \quad (\text{A.22a})$$

$$= \left\| \mathbf{W} \mathbf{W}^\dagger \mathbf{A} \right\|^2 + \left\| \mathbf{V}_{\mathbf{J}_0} \mathbf{V}_{\mathbf{J}_0}^\dagger \mathbf{A} \right\|^2. \quad (\text{A.22b})$$

The last formula comes from the fact that $\mathbf{V}_{\mathbf{J}_0}$ and \mathbf{W} are orthonormal matrices, spanning orthogonal subspaces. Then, using the fact that $\mathbf{V}_{\mathbf{J}_0}^\dagger \mathbf{V}_{\mathbf{J}_0} = \mathbf{I}$, $\mathbf{W}^\dagger \mathbf{W} = \mathbf{I}$ and $\|\mathbf{B}\|^2 = \text{Tr}(\mathbf{B}^\dagger \mathbf{B})$ for every matrix \mathbf{B} , Eq.(A.22b) becomes

$$\|\mathbf{A}\|^2 = \left\| \mathbf{W}^\dagger \mathbf{A} \right\|^2 + \left\| \mathbf{V}_{\mathbf{J}_0}^\dagger \mathbf{A} \right\|^2. \quad (\text{A.23})$$

⁴The formula (A.19b) can be computed thanks to the definition (2.24) page 73, or in a faster way thanks to this online matrix calculus tool: <https://www.matrixcalculus.org/>.

⁵Each direction is defined only modulo a multiplicative factor.

Following the same methods for $\|\mathbf{B}\|^2 = \left\| \mathbf{B}(\mathbf{W}\mathbf{W}^\dagger + \mathbf{V}_{\mathbf{J}_0}\mathbf{V}_{\mathbf{J}_0}^\dagger) \right\|^2$ leads to

$$\|\mathbf{A}\|^2 = \left\| \mathbf{W}^\dagger \mathbf{A} \mathbf{W} \right\|^2 + \left\| \mathbf{W}^\dagger \mathbf{A} \mathbf{V}_{\mathbf{J}_0} \right\|^2 + \left\| \mathbf{V}_{\mathbf{J}_0}^\dagger \mathbf{A} \mathbf{W} \right\|^2 + \left\| \mathbf{V}_{\mathbf{J}_0}^\dagger \mathbf{A} \mathbf{V}_{\mathbf{J}_0} \right\|^2. \quad (\text{A.24})$$

In the specific situation of $\mathbf{A} = \mathbf{Z}_{\text{cstr}} - \mathbf{\Gamma}_0^\dagger \mathbf{K}_0 \mathbf{S} \mathbf{\Delta} \mathbf{S}^\dagger \mathbf{K}_0^\dagger \mathbf{\Gamma}_0$, Eq.(A.24) becomes

$$\begin{aligned} \left\| \mathbf{Z}_{\text{cstr}} - \mathbf{\Gamma}_0^\dagger \mathbf{K}_0 \mathbf{S} \mathbf{\Delta} \mathbf{S}^\dagger \mathbf{K}_0^\dagger \mathbf{\Gamma}_0 \right\|^2 &= \left\| \mathbf{W}^\dagger \mathbf{Z}_{\text{cstr}} \mathbf{W} \right\|^2 + \left\| \mathbf{W}^\dagger \mathbf{Z}_{\text{cstr}} \mathbf{V}_{\mathbf{J}_0} \right\|^2 + \left\| \mathbf{V}_{\mathbf{J}_0}^\dagger \mathbf{Z}_{\text{cstr}} \mathbf{W} \right\|^2 \\ &+ \left\| \mathbf{V}_{\mathbf{J}_0}^\dagger (\mathbf{Z}_{\text{cstr}} - \mathbf{\Gamma}_0^\dagger \mathbf{K}_0 \mathbf{S} \mathbf{\Delta} \mathbf{S}^\dagger \mathbf{K}_0^\dagger \mathbf{\Gamma}_0) \mathbf{V}_{\mathbf{J}_0} \right\|^2, \end{aligned} \quad (\text{A.25})$$

thanks to the relation $\mathbf{V}_{\mathbf{J}_0}^\dagger \mathbf{W} = \mathbf{0}$. The first three terms being constant with respect to \mathbf{S} , the minimization can be performed only on the last term, leading to Eq.(A.21).

One can define the SVD of $\mathbf{V}_{\mathbf{J}_0}^\dagger \mathbf{Z}_{\text{cstr}} \mathbf{V}_{\mathbf{J}_0} = \mathbf{U}_1 \mathbf{\Sigma}_1 \mathbf{V}_1^\dagger$ and $\mathbf{\Sigma}_1^{(m)}$ the $m \times m$ diagonal matrix made of the first m singular values of $\mathbf{\Sigma}_1$. Defining $\mathbf{U}_1^{(m)}$ (respectively $\mathbf{V}_1^{(m)}$) the submatrix made of the first m columns of \mathbf{U}_1 (respectively \mathbf{V}_1), the Eckart–Young–Mirsky theorem leads to a solution $\mathbf{S}_{\text{opt}}^{(2)}$ of Eq.(A.21) such that

$$\mathbf{S}_{\text{opt}}^{(2)} = \left[\sqrt{\mathbf{\Sigma}_1^{(m)}} (\mathbf{V}_1^{(m)})^\dagger \mathbf{\Sigma}_{\mathbf{J}_0}^{-1} \mathbf{U}_{\mathbf{J}_0}^\dagger \right]^\dagger, \quad \mathbf{\Delta} = (\mathbf{V}_1^{(m)})^\dagger \mathbf{U}_1^{(m)}.$$

The required coefficients $\{C_{\gamma P}\}$ are given by the columns of $\mathbf{K}_0 \mathbf{S}_{\text{opt}}^{(2)}$.

At the end of the process, the coordinates of the N_γ polarization vectors $\{\gamma\}$ in the auxiliary basis $\{P\}$, corresponding to the $\{C_{\gamma P}\}$ coefficients, are given by the columns of $\mathbf{U}_{\mathbf{R}}$ and of $\mathbf{K}_0 \mathbf{S}_{\text{opt}}^{(2)}$. In the specific case where no constraints are enforced, \mathbf{R}_0 is not defined, nor $\mathbf{U}_{\mathbf{R}_0}$, and \mathbf{K}_0 is the identity matrix. So the basis $\{\gamma\}$ is given by the columns of $\mathbf{S}_{\text{opt}}^{(2)}$, with $\mathbf{Z}_{\text{cstr}} = \mathbf{Z}$ and $\mathbf{J}_0 = \mathbf{\Gamma}_0$.

We emphasize that such a method can be easily adapted to another choice of the first guess $\{\gamma_0\}$, different of the auxiliary basis set.

The QM_{GW}/QM_{COHSEX} approach: interchange of limit and integral

This appendix is totally inspired of our work published in *Journal of Chemical Theory and Computation* [260].

B.1 Introduction

This appendix gives more details on how to go from Eq.(3.26a) to Eq.(3.26b) page 102. In this section, and for the sake of compactness, we remove the space variables.

Taking the limit $\lambda \rightarrow \infty$ in Eq.(3.26a) is not *a priori* a simple task, because of the non-trivial dependency of $\tilde{\chi}^{(A)}(\omega, \lambda)$ with respect to λ . However, to tackle this limit, we can first remark that the integral along a closed complex contour \mathcal{C} enclosing the two poles Ω_1 and Ω_2 of the following product

$$\int_{\mathcal{C}} d\omega \frac{1}{\omega - \Omega_1} \frac{1}{\omega - \Omega_2} = \frac{2i\pi}{\Omega_2 - \Omega_1} + \frac{2i\pi}{\Omega_1 - \Omega_2} = 0, \quad (\text{B.1})$$

is always null. This property will be useful to rewrite the correlation-only self-energy $\Sigma_{(A)}^{\text{C}}$ integral by considering only the residues taken at the poles of $G^{(A)}$. Once we have such an expression, it becomes possible to take the limit value of these residues when $\lambda \rightarrow \infty$. Finally, we can revert the expression by casting the sum over limit values of the residues as an integral of the form $G^{(A)}(\varepsilon + \omega)[\tilde{V}(\omega = 0) \cdot \tilde{\chi}^{(A)}(\omega, \lambda \rightarrow \infty) \cdot \tilde{V}(\omega = 0)]$.

B.2 Demonstration

To start our demonstration, it should be noticed that

$$W(\omega, \lambda) - V = V_{\text{reac}}(\omega, \lambda) + [\tilde{V} \cdot \tilde{\chi}^{(A)} \cdot \tilde{V}](\omega, \lambda) \quad (\text{B.2})$$

has simple poles, thanks to its general spectral decomposition (1.124) page 52. Thanks to the definition of the reaction field (3.12), and the definition of the model susceptibility of the environment (3.15), $V_{\text{reac}}(\omega, \lambda)$ has also simple poles. By linearity, it follows that $[\tilde{V} \cdot \tilde{\chi}^{(A)} \cdot \tilde{V}](\omega, \lambda)$ is also a sum of simple poles.

We can thus rewrite this formula as

$$[\tilde{V} \cdot \tilde{\chi}^{(A)} \cdot \tilde{V}](\omega, \lambda) = [\Delta^{(+)} + \Delta^{(-)}](\omega, \lambda), \quad (\text{B.3})$$

where $\Delta^{(+)}$ regroup all its poles within the complex upper-plane (such that $\text{Im}(\omega) > 0$), while $\Delta^{(-)}$ holds all its poles within the complex lower-plane (such that $\text{Im}(\omega) < 0$). Similarly, using the spectral decomposition of the Green's function given by the equation (1.70) page 43, we split $G^{(A)}$ into $G_{\text{occ}}^{(A)}$ and $G_{\text{vir}}^{(A)}$ with poles occupying also respectively the upper-plane and the lower-plane. This leads to

$$\frac{i}{2\pi} \int_{-\infty}^{+\infty} d\omega e^{i\eta\omega} G^{(A)}(\varepsilon + \omega) [\tilde{V} \cdot \tilde{\chi}^{(A)} \cdot \tilde{V}](\omega, \lambda) \quad (\text{B.4a})$$

$$= \frac{i}{2\pi} \int_{-\infty}^{+\infty} d\omega e^{i\eta\omega} \left(G_{\text{occ}}^{(A)}(\varepsilon + \omega) + G_{\text{vir}}^{(A)}(\varepsilon + \omega) \right) \left(\Delta^{(+)}(\omega, \lambda) + \Delta^{(-)}(\omega, \lambda) \right). \quad (\text{B.4b})$$

We insist on the fact that all these sub-quantities have a $1/\omega$ asymptotic behavior, with no constant terms, as they are sums of simple poles. Thus, expression (B.4b) is clearly an integral over products of simple poles. Using Eq.(B.1) as selection rule for which of these product residues to keep after integration over a semicircle enclosing all the upper-plane (as represented in FIGURE 1.10 page 52), with an infinite radius, we can now express Eq.(B.4a) as

$$\frac{i}{2\pi} \int_{-\infty}^{+\infty} d\omega e^{i\eta\omega} G^{(A)}(\varepsilon + \omega) [\tilde{V} \cdot \tilde{\chi}^{(A)} \cdot \tilde{V}](\omega, \lambda) \quad (\text{B.5a})$$

$$= -\sum_i \text{Res}(G_{\text{occ}}^{(A)}, \varepsilon_i) \Delta^{(-)}(\varepsilon_i - \varepsilon, \lambda) - \sum_k G_{\text{vir}}^{(A)}(\varepsilon + \Omega_k) \text{Res}(\Delta^{(+)}, \Omega_k), \quad (\text{B.5b})$$

where the sum over (i) runs over occupied states, while the sum over (k) runs over the poles of $\Delta^{(+)}$. $\text{Res}(f, x)$ corresponds to the residue of the function f , associated to its pole x . We can use again Eq.(B.1) on a closed complex contour enclosing all the poles of $G_{\text{vir}}^{(A)}$ and $\Delta^{(+)}$. By linearity of the spectral decomposition with respect to the simple poles functions, we can rewrite the sum over (k) as another one over the empty states (a) such that

$$\sum_k G_{\text{vir}}^{(A)}(\varepsilon + \Omega_k) \text{Res}(\Delta^{(+)}, \Omega_k) = \sum_k \sum_a \frac{\text{Res}(G_{\text{vir}}^{(A)}, \varepsilon_a)}{\varepsilon + \Omega_k - \varepsilon_a} \text{Res}(\Delta^{(+)}, \Omega_k) \quad (\text{B.6a})$$

$$= -\sum_a \sum_k \text{Res}(G_{\text{vir}}^{(A)}, \varepsilon_a) \frac{\text{Res}(\Delta^{(+)}, \Omega_k)}{\varepsilon_a - \varepsilon - \Omega_k} \quad (\text{B.6b})$$

$$= -\sum_a \text{Res}(G_{\text{vir}}^{(A)}, \varepsilon_a) \Delta^{(+)}(\varepsilon_a - \varepsilon, \lambda). \quad (\text{B.6c})$$

In particular, it leads to an expression of (B.4a) that involves only residues taken at the poles of $G^{(A)}$:

$$\frac{i}{2\pi} \int_{-\infty}^{+\infty} d\omega e^{i\eta\omega} G^{(A)}(\varepsilon + \omega) [\tilde{V} \cdot \tilde{\chi}^{(A)} \cdot \tilde{V}](\omega, \lambda) \quad (\text{B.7a})$$

$$= -\sum_i \text{Res}(G_{\text{occ}}^{(A)}, \varepsilon_i) \Delta^{(-)}(\varepsilon_i - \varepsilon, \lambda) + \sum_a \text{Res}(G_{\text{vir}}^{(A)}, \varepsilon_a) \Delta^{(+)}(\varepsilon_a - \varepsilon, \lambda). \quad (\text{B.7b})$$

Now that we have an expression that requires only evaluation of $\Delta^{(+)}$ and $\Delta^{(-)}$ at finite values of ω , we can explore their limit when $\lambda \rightarrow \infty$. Using the fact that for all ω

$$\lim_{\lambda \rightarrow \infty} \chi_{g,\lambda}^{(B)}(\omega) \stackrel{\text{DEF}}{=} \chi_{g,\infty}^{(B)}(\omega) \quad (\text{B.8a})$$

$$= \chi_g^{(B)}(0), \quad (\text{B.8b})$$

thanks to the definition (3.15), where $\chi_g^{(B)}(0)$ is the correct (without model) static susceptibility of (B) , it follows that

$$\lim_{\lambda \rightarrow \infty} \tilde{V}(\omega, \lambda) = \lim_{\lambda \rightarrow \infty} \left(V + V \cdot \chi_{g,\lambda}^{(B)}(\omega) \cdot V \right) \quad (\text{B.9a})$$

$$= V + V \cdot \chi_g^{(B)}(0) \cdot V \quad (\text{B.9b})$$

$$\stackrel{\text{DEF}}{=} \tilde{V}(0), \quad (\text{B.9c})$$

where $\tilde{V}(0)$ is also the correct (without model susceptibility) static value of this potential. Then, using the definition (3.14), it comes that

$$\lim_{\lambda \rightarrow \infty} \left[\tilde{\chi}^{(A)}(\omega, \lambda) \right]^{-1} = \lim_{\lambda \rightarrow \infty} \left(\left[\chi_0^{(A)}(\omega) \right]^{-1} - \tilde{V}(\omega, \lambda) \right) \quad (\text{B.10a})$$

$$= \left[\chi_0^{(A)}(\omega) \right]^{-1} - \tilde{V}(0) \quad (\text{B.10b})$$

$$\stackrel{\text{DEF}}{=} \left[\tilde{\chi}_{\text{stat-env}}^{(A)}(\omega) \right]^{-1}. \quad (\text{B.10c})$$

$\tilde{\chi}_{\text{stat-env}}^{(A)}(\omega)$ corresponds to the interacting susceptibility of the subsystem (A) , when its Coulomb interactions are renormalized by the static reaction field created by the environment (B) .

Thus, for any finite value ω , these different results lead to

$$\lim_{\lambda \rightarrow \infty} \left(\tilde{V}(\omega, \lambda) \cdot \tilde{\chi}^{(A)}(\omega, \lambda) \cdot \tilde{V}(\omega, \lambda) \right) = \tilde{V}(0) \cdot \tilde{\chi}_{\text{stat-env}}^{(A)}(\omega) \cdot \tilde{V}(0). \quad (\text{B.11})$$

We can then proceed as previously by separating

$$\tilde{V}(0) \cdot \tilde{\chi}_{\text{stat-env}}^{(A)}(\omega) \cdot \tilde{V}(0) = \tilde{\Delta}^{(+)}(\omega) + \tilde{\Delta}^{(-)}(\omega) \quad (\text{B.12})$$

into contributions of the upper-plane and lower-plane poles. The equation (B.11) being true for all finite ω , this implies that we now can make the identification

$$\lim_{\lambda \rightarrow \infty} \Delta^{(+/-)}(\omega, \lambda) = \tilde{\Delta}^{(+/-)}(\omega). \quad (\text{B.13})$$

The limit values of $\Delta^{(+/-)}(\omega, \lambda)$ can be re-injected into the finite sums of (B.7), leading to

$$\lim_{\lambda \rightarrow \infty} \frac{i}{2\pi} \int_{-\infty}^{+\infty} d\omega e^{i\eta\omega} G^{(A)}(\varepsilon + \omega) \left[\tilde{V} \cdot \tilde{\chi}^{(A)} \cdot \tilde{V} \right](\omega, \lambda) \quad (\text{B.14a})$$

$$= -\sum_i \text{Res}(G_{\text{occ}}^{(A)}, \varepsilon_i) \tilde{\Delta}^{(-)}(\varepsilon_i - \varepsilon) + \sum_a \text{Res}(G_{\text{vir}}^{(A)}, \varepsilon_a) \tilde{\Delta}^{(+)}(\varepsilon_a - \varepsilon). \quad (\text{B.14b})$$

Finally, it is now possible to revert the derivation starting from Eq.(B.14) and rewinding the steps Eq.(B.7) back to Eq.(B.4) to finally obtain that

$$\lim_{\lambda \rightarrow \infty} \frac{i}{2\pi} \int_{-\infty}^{+\infty} d\omega e^{i\eta\omega} G^{(A)}(\varepsilon + \omega) \left[\tilde{V} \cdot \tilde{\chi}^{(A)} \cdot \tilde{V} \right](\omega, \lambda) \quad (\text{B.15a})$$

$$= \frac{i}{2\pi} \int_{-\infty}^{+\infty} d\omega e^{i\eta\omega} G^{(A)}(\varepsilon + \omega) \left(\tilde{V}(0) \cdot \tilde{\chi}_{\text{stat-env}}^{(A)}(\omega) \cdot \tilde{V}(0) \right). \quad (\text{B.15b})$$

Typical input file of beDefT

This appendix presents below a typical input file to run a *GW* calculation with our code [BEDEF T](#). Such a script is written in Lua, enabling us to use all the functions and methods of this language. More information will be available in the user manual distributed with the code.

```
1 -----
2 -- 1) Instanciation of fragments from atomic positions
3 -----
4 mol = Fragment.new( [[
5     <system name="H2O">
6         <fragment name="H2O">
7             <atoms unit="angstrom">
8                 O  0.0000 0.0000 0.0000
9                 H  0.7571 0.5861 0.0000
10                H -0.7571 0.5861 0.0000
11            </atoms>
12        </fragment>
13    </system>
14    ]] )
15
16
17 mol2 = Fragment.new( [[
18     <system test>
19         <fragment name="H2">
20             <atoms unit="angstrom">
21                 H   0.    3.3   0.
22                 H   0.    3.3   0.741
23            </atoms>
24        </fragment>
25    </system>
26    ]] )
27
28
29 -----
30 -- 2) Set species in use
31 -----
32
33 mol:setKohnShamSpecies("*","def2-tzvp")
34 mol:setAuxiliarySpecies("*","def2-tzvp-ri")
35 mol:setRealspaceSpecies("*","def2-tzvp-rs")
36
37 mol2:setKohnShamSpecies("*","def2-qzvp")
38 mol2:setAuxiliarySpecies("*","def2-qzvp-ri")
39
```

```
40
41
42 -----
43 -- 3) Compute KS DFT wave functions with Orca
44 -----
45
46 mol:OrcaDysonOrbitals([[
47     ! PBE0 TightSCF
48     ]])
49
50 mol2:OrcaDysonOrbitals([[
51     ! PBE0 TightSCF
52     ]])
53
54
55 -----
56 -- 4) Set RI methods
57 -----
58
59 mol:setRealspaceRI()           -- set Real Space RI for mol
60 mol:setLTMode("LTMode::precise") -- set Laplace Transform for mol
61
62 lmax_RV      = 6                -- we ask for RI-V
63 lmax_constraint = -1           -- do not constrain exact
64     density charge and dipoles
65 mol2:setStandardRI(lmax_RV,lmax_constraint) -- set standard coulomb RI
66     method for mol2
67
68 -----
69 -- 5) Set number of corrected occupied and virtual states
70 -- for the fragment of interest
71 -----
72 nocc = 3
73 nvir = 2
74
75
76 -----
77 -- 6) Creation of new references of fragments
78 -----
79
80 -- Lua tables to store the initial fragment, the number of corrected
81 -- occupied states, and the number of corrected virtual states
82
83 table_frag={mol}
84 table_nocc={nocc}
85 table_nvir={nvir}
86
87 for k = 1,2 do
88     -- rotation angle
89     theta=k*math.pi/4
90
91
```

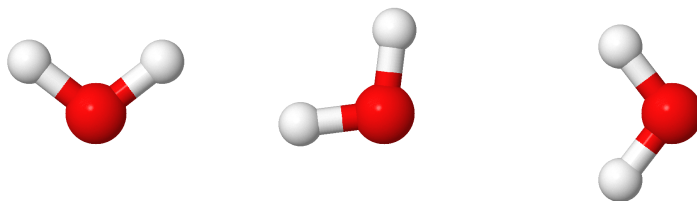
```
92 -- define new axis coordinates
93 new_x = { math.cos(theta), math.sin(theta), 0.0 }
94 new_y = { -1.0*math.sin(theta), math.cos(theta), 0.0}
95 new_z = { 0.0 , 0.0 , 1.0 }
96
97 -- creation of the rotation
98 transformation = RigidMotion:new()
99 transformation = transformation:rotate(new_x,new_y,new_z)
100
101 -- add translation on top of the rotation
102 transformation = transformation:translate({ k*6.2 , 0.0 , 0.0 })
103
104 -- insertion of the new fragment reference (the translated/rotated one)
105 -- into table_frag
106 table.insert(table_frag,mol:transform( transformation ))
107
108 -- we do not correct at the GW level these fragments, so we correct 0
109 -- states for them
110 table.insert(table_nocc,0)
111 table.insert(table_nvir,0)
112
113 end
114
115 -----
116 -- 7) Creation of a FragmentList. It is an object which regroups different
117 -- fragments, and which presents specific methods for group of fragments
118 -----
119 L_interest=FragmentList.new(table_frag,"H2Os")
120
121 -- Creation of a file.xyz with the structure of the 3 water molecules
122 L_interest:xyz("H2Os")
123
124 -----
125 -- 8) perform one GW iteration, with 12 pure imaginary
126 -- axis integration points
127 -- static COHSEX : set 12 to 0 (no calculation along the imaginary axis)
128 -----
129
130 for i=1,1 do
131     evGW(L_interest,12,table_nocc,table_nvir)
132 end
133
134 -----
135 -- 9) Creation of another FragmentList for the environment, to use the
136 -- QM_{GW}/QM_{COHSEX} method on one water molecule
137 -----
138
139 -- Parameters for the compression method for the susceptibility of fragment
140 -- in the environment
141 mol2:dysonOrbitalsEpol(mol2:dysonOrbitalsEqp())
142 mol2:setConstraintsSpecies("fragment","lmax=1")
```

```

143 mol2:setModelSpecies("*","def2-qzvp-ri")
144
145 -- We keep only 10 directions for the polarization basis set
146 mol2:nmodelChi(10)
147
148 L_QM_COHSEX=FragmentList.new({mol2},"Environment")
149
150 -----
151 -- 10) QM_{GW}/QM_{COHSEX} method on one H2O molecule
152 -----
153
154 L_QM_GW=FragmentList.new({mol},"H2O_alone")
155 L_QM_COHSEX:embed(L_QM_GW)
156
157 -- evGW method on the part of interest, with 6 iterations.
158 -- We decide to correct only the HOMO and LUMO of the water molecule
159
160 for i=1,6 do
161     evGW(L_QM_GW,12,1,1)
162 end

```

- As already commented in the input file, section 1) is dedicated to the definition of the atomic positions of the different `Fragment`s (here a H_2O molecule, and a H_2 one), as defined in chapter 2 page 63.
- Section 2) aims at defining the different required basis sets, as the Kohn-Sham (**KS**)-**DFT** one, or the auxiliary one. For the first type of fragment `mol`, we also define a basis set for the Real Space (**RS**)-Resolution of the Identity (**RI**) method.
- Section 3) indicates to **BEDEFT** to run **KS-DFT** calculations with the ORCA package.
- The following section 4) defines the **RI** methods used for the different fragments.
- Starting from the initial fragment `mol`, we duplicate this latter, through rotations and translations, in section 6). At the end of the process, starting from the fragment on the left in the picture below, we generate the two other ones:



- Section 7) defines a `FragmentList` containing the three fragments presented before. A `FragmentList` is an object made of fragments, with specific methods applying to all its subsystems.
- In section 8), we perform a G_0W_0 calculation on this `FragmentList`.

- Section 9) defines the parameters for a typical fragment in the environment of an embedded calculation. The gas phase susceptibility of the fragment `mo12` is compressed under the constraint $l_{\max} = 1$ (see section 2.2.2 page 69).
- Finally, in section 10), the `QMGW/QMCOHSEX` method (see section 3.2.3 page 99) is used via the `embed` method. The fragment `mo12` (via its corresponding `FragmentList`) is described at the `QMCOHSEX` level, while the fragment `mo1` (here alone) is described at the `QMGW` level. An *evGW* calculation, with 6 iterations, is then performed on this fragment. Contrary to its first *GW* calculation done before, with 2 other water molecules, these *evGW* iterations do not start from `KS-DFT` eigenvalues. Each fragment stores the results of previous computations. Therefore, these *evGW* calculations rather start from results of line 130.

Scientific production

Articles

- David Amblard, Gabriele D’Avino, Ivan Duchemin, and Xavier Blase. “Universal polarization energies for defects in monolayer, surface, and bulk hexagonal boron nitride: A finite-size fragments *GW* approach”. In: *Phys. Rev. Mater.* 6 (6 June 2022), p. 064008
- David Amblard, Xavier Blase, and Ivan Duchemin. “Many-body *GW* calculations with very large scale polarizable environments made affordable: A fully ab initio QM/QM approach”. In: *J. Chem. Phys.* 159.16 (Oct. 2023), p. 164107
- David Amblard, Xavier Blase, and Ivan Duchemin. “Static versus dynamically polarizable environments within the many-body *GW* formalism”. In: *J. Chem. Phys.* 160.15 (Apr. 2024), p. 154104
- Ivan Duchemin, David Amblard, and Xavier Blase. “Polarizable Continuum Models and Green’s Function *GW* Formalism: On the Dynamics of the Solvent Electrons”. In: *J. Chem. Theory Comput.* 10.1021/acs.jctc.4c00745 (As Soon As Publishable). PMID: 39226212

Conferences and workshops

- Poster presentation “*Optimal representation for electronic susceptibility*” in EMERGING EXCITED-STATE METHODS IN ELECTRONIC STRUCTURE workshop (April 2023), Toulouse, France
- Poster presentation “*Recent developments in embedded many-body *GW* perturbation theory*” in ACCELERATING THEORETICAL SPECTROSCOPY FOR COMPLEX MULTISCALE MATERIALS workshop (March 2023), Leiden, the Netherlands
- Contributed talk “*Dynamical versus static embedding in QM/QM many-body *GW* formalisms*” in C π C-12 symposium (May 2022), Grenoble, France

Bibliography

- [1] Lars Hedin. “New Method for Calculating the One-Particle Green’s Function with Application to the Electron-Gas Problem”. In: *Phys. Rev.* 139 (3A Aug. 1965), A796–A823 (cit. on pp. [13](#), [17](#), [48–50](#), [53](#), [100](#)).
- [2] Fabien Bruneval, Nike Dattani, and Michiel J. van Setten. “The GW Miracle in Many-Body Perturbation Theory for the Ionization Potential of Molecules”. In: *Frontiers in Chemistry* 9 (2021) (cit. on pp. [13](#), [17](#)).
- [3] Jing Li, Ivan Duchemin, Otello Maria Roscioni, Pascal Friederich, Marie Anderson, Enrico Da Como, Gabriele Kociok-Köhn, Wolfgang Wenzel, Claudio Zannoni, David Beljonne, Xavier Blase, and Gabriele D’Avino. “Host dependence of the electron affinity of molecular dopants”. In: *Mater. Horiz.* 6 (1 2019), pp. 107–114 (cit. on pp. [14](#), [18](#), [150](#), [154](#)).
- [4] Gabriele D’Avino, Sébastien Mothy, Luca Muccioli, Claudio Zannoni, Linjun Wang, Jérôme Cornil, David Beljonne, and Frédéric Castet. “Energetics of Electron–Hole Separation at P3HT/PCBM Heterojunctions”. In: *The Journal of Physical Chemistry C* 117.25 (2013), pp. 12981–12990 (cit. on pp. [14](#), [18](#), [150](#), [154](#)).
- [5] Toan Trong Tran, Christopher Elbadawi, Daniel Totonjian, Charlene J. Lobo, Gabriele Grosso, Hyowon Moon, Dirk R. Englund, Michael J. Ford, Igor Aharonovich, and Milos Toth. “Robust Multicolor Single Photon Emission from Point Defects in Hexagonal Boron Nitride”. In: *ACS Nano* 10.8 (2016). PMID: 27399936, pp. 7331–7338 (cit. on pp. [14](#), [18](#), [122](#)).
- [6] Ivan Duchemin, Denis Jacquemin, and Xavier Blase. “Combining the GW formalism with the polarizable continuum model: A state-specific non-equilibrium approach”. In: *J. Chem. Phys.* 144.16 (2016), p. 164106 (cit. on pp. [14](#), [18](#), [62](#), [96](#), [98](#), [125](#)).
- [7] Ivan Duchemin, Ciro A. Guido, Denis Jacquemin, and Xavier Blase. “The Bethe–Salpeter formalism with polarisable continuum embedding: reconciling linear-response and state-specific features”. In: *Chem. Sci.* 9 (19 2018), pp. 4430–4443 (cit. on pp. [14](#), [18](#), [56](#), [96](#), [125](#), [150](#)).
- [8] Jacob M. Clary, Mauro Del Ben, Ravishankar Sundararaman, and Derek Vigil-Fowler. “Impact of solvation on the GW quasiparticle spectra of molecules”. In: *J. Appl. Phys.* 134.8 (Aug. 2023), p. 085001 (cit. on pp. [14](#), [18](#), [62](#), [96](#)).
- [9] Björn Baumeier, Michael Rohlfing, and Denis Andrienko. “Electronic Excitations in Push–Pull Oligomers and Their Complexes with Fullerene from Many-Body Green’s Functions Theory with Polarizable Embedding”. In: *J. Chem. Theory Comput.* 10.8 (2014). PMID: 26588281, pp. 3104–3110 (cit. on pp. [14](#), [18](#), [62](#), [96](#)).
- [10] Jing Li, Gabriele D’Avino, Ivan Duchemin, David Beljonne, and Xavier Blase. “Combining the Many-Body GW Formalism with Classical Polarizable Models: Insights on the Electronic Structure of Molecular Solids”. In: *The Journal of Physical Chemistry Letters* 7.14 (2016). PMID: 27388926, pp. 2814–2820 (cit. on pp. [14](#), [18](#), [27](#), [56](#), [62](#), [75](#), [96](#), [98](#)).
- [11] Jing Li, Gabriele D’Avino, Ivan Duchemin, David Beljonne, and Xavier Blase. “Accurate description of charged excitations in molecular solids from embedded many-body perturbation theory”. In: *Phys. Rev. B* 97 (3 Jan. 2018), p. 035108 (cit. on pp. [14](#), [18](#), [26](#), [62](#), [75](#), [96](#), [98](#)).
- [12] Jens Wehner, Lothar Brombacher, Joshua Brown, Christoph Junghans, Onur Çaylak, Yuriy Khalak, Pranav Madhikar, Gianluca Tirimbò, and Björn Baumeier. “Electronic Excitations in Complex Molecular Environments: Many-Body Green’s Functions Theory in VOTCA-XTP”. In: *J. Chem. Theory Comput.* 14.12 (2018). PMID: 30404449, pp. 6253–6268 (cit. on pp. [14](#), [18](#), [62](#), [96](#)).

- [13] G. Tirimbò, V. Sundaram, O. Çaylak, W. Scharpach, J. Sijen, C. Junghans, J. Brown, F. Zapata Ruiz, N. Renaud, J. Wehner, and B. Baumeier. “Excited-state electronic structure of molecules using many-body Green’s functions: Quasiparticles and electron–hole excitations with VOTCA-XTP”. In: *J. Chem. Phys.* 152.11 (Mar. 2020), p. 114103 (cit. on pp. 14, 18, 62, 96).
- [14] Dorothea Golze, Marc Dvorak, and Patrick Rinke. “The GW Compendium: A Practical Guide to Theoretical Photoemission Spectroscopy”. In: *Frontiers in Chemistry* 7 (2019) (cit. on pp. 25, 45, 46, 50–52, 54, 55, 57, 60, 61).
- [15] S. Hüfner. *Photoelectron Spectroscopy: Principles and Applications*. Advanced Texts in Physics. Springer, 2003 (cit. on p. 25).
- [16] D. E. Aspnes and A. A. Studna. “Dielectric functions and optical parameters of Si, Ge, GaP, GaAs, GaSb, InP, InAs, and InSb from 1.5 to 6.0 eV”. In: *Phys. Rev. B* 27 (2 Jan. 1983), pp. 985–1009 (cit. on p. 27).
- [17] J. B. Neaton, Mark S. Hybertsen, and Steven G. Louie. “Renormalization of Molecular Electronic Levels at Metal-Molecule Interfaces”. In: *Phys. Rev. Lett.* 97 (21 Nov. 2006), p. 216405 (cit. on pp. 28, 67, 76, 98, 107, 110, 112, 125).
- [18] X. Blase, C. Attaccalite, and V. Olevano. “First-principles GW calculations for fullerenes, porphyrins, phtalocyanine, and other molecules of interest for organic photovoltaic applications”. In: *Phys. Rev. B* 83 (11 Mar. 2011), p. 115103 (cit. on pp. 29, 55, 56).
- [19] Sivan Refaely-Abramson, Roi Baer, and Leeor Kronik. “Fundamental and excitation gaps in molecules of relevance for organic photovoltaics from an optimally tuned range-separated hybrid functional”. In: *Phys. Rev. B* 84 (7 Aug. 2011), p. 075144 (cit. on p. 29).
- [20] Jacopo Tomasi, Benedetta Mennucci, and Roberto Cammi. “Quantum Mechanical Continuum Solvation Models”. In: *Chemical Reviews* 105.8 (2005). PMID: 16092826, pp. 2999–3094 (cit. on p. 29).
- [21] Sahar Sharifzadeh, Ariel Biller, Leeor Kronik, and Jeffrey B. Neaton. “Quasiparticle and optical spectroscopy of the organic semiconductors pentacene and PTCDA from first principles”. In: *Phys. Rev. B* 85 (12 Mar. 2012), p. 125307 (cit. on p. 29).
- [22] Kikujiro Ishii, Minoru Kinoshita, and Haruo Kuroda. “Dielectric Constant Measurement on Organic Crystalline Powder”. In: *Bulletin of the Chemical Society of Japan* 46.11 (1973), pp. 3385–3391 (cit. on p. 29).
- [23] Paul Winget, Derek Dolney, David Giesen, Christopher Cramer, and Donald Truhlar. “Minnesota Solvent Descriptor Database”. In: (Jan. 1999) (cit. on p. 29).
- [24] M. Born and R. Oppenheimer. “Zur Quantentheorie der Molekeln”. In: *Annalen der Physik* 389.20 (1927), pp. 457–484 (cit. on p. 30).
- [25] E. Engel and R.M. Dreizler. *Density Functional Theory: An Advanced Course*. Theoretical and Mathematical Physics. Springer Berlin Heidelberg, 2011 (cit. on pp. 31–34, 36, 48).
- [26] P. Hohenberg and W. Kohn. “Inhomogeneous Electron Gas”. In: *Phys. Rev.* 136 (3B Nov. 1964), B864–B871 (cit. on pp. 31, 35).
- [27] Richard M. Martin. *Electronic Structure: Basic Theory and Practical Methods*. Cambridge University Press, 2004 (cit. on p. 31).
- [28] Mel Levy. “Universal variational functionals of electron densities, first-order density matrices, and natural spin-orbitals and solution of the v-representability problem”. In: *Proceedings of the National Academy of Sciences* 76.12 (1979), pp. 6062–6065 (cit. on p. 32).

- [29] W. Kohn. *Highlights of condensed-matter theory*. Proceedings of the International School of Physics "Enrico Fermi" ; course 89. 1985 (cit. on p. 32).
- [30] W. Kohn and L. J. Sham. "Self-Consistent Equations Including Exchange and Correlation Effects". In: *Phys. Rev.* 140 (4A Nov. 1965), A1133–A1138 (cit. on p. 33).
- [31] D. M. Ceperley and B. J. Alder. "Ground State of the Electron Gas by a Stochastic Method". In: *Phys. Rev. Lett.* 45 (7 Aug. 1980), pp. 566–569 (cit. on p. 35).
- [32] P. A. M. Dirac. "Note on Exchange Phenomena in the Thomas Atom". In: *Mathematical Proceedings of the Cambridge Philosophical Society* 26.3 (1930), pp. 376–385 (cit. on p. 35).
- [33] S. H. Vosko, L. Wilk, and M. Nusair. "Accurate spin-dependent electron liquid correlation energies for local spin density calculations: a critical analysis". In: *Canadian Journal of Physics* 58.8 (1980), pp. 1200–1211 (cit. on pp. 35, 115).
- [34] J. P. Perdew and Alex Zunger. "Self-interaction correction to density-functional approximations for many-electron systems". In: *Phys. Rev. B* 23 (10 May 1981), pp. 5048–5079 (cit. on p. 35).
- [35] John P. Perdew and Yue Wang. "Accurate and simple analytic representation of the electron-gas correlation energy". In: *Phys. Rev. B* 45 (23 June 1992), pp. 13244–13249 (cit. on p. 35).
- [36] Gábor I. Csonka, John P. Perdew, Adrienn Ruzsinszky, Pier H. T. Philipsen, Sébastien Lebègue, Joachim Paier, Oleg A. Vydrov, and János G. Ángyán. "Assessing the performance of recent density functionals for bulk solids". In: *Phys. Rev. B* 79 (15 Apr. 2009), p. 155107 (cit. on p. 35).
- [37] Fabien Bruneval, Nathalie Vast, and Lucia Reining. "Effect of self-consistency on quasiparticles in solids". In: *Phys. Rev. B* 74 (4 July 2006), p. 045102 (cit. on pp. 35, 53, 100, 107).
- [38] A. D. Becke. "Density-functional exchange-energy approximation with correct asymptotic behavior". In: *Phys. Rev. A* 38 (6 Sept. 1988), pp. 3098–3100 (cit. on p. 35).
- [39] Chengteh Lee, Weitao Yang, and Robert G. Parr. "Development of the Colle-Salvetti correlation-energy formula into a functional of the electron density". In: *Phys. Rev. B* 37 (2 Jan. 1988), pp. 785–789 (cit. on p. 35).
- [40] John P. Perdew, P. Ziesche, and H. Eschrig. *Electronic structure of solids' 91*. 1991 (cit. on p. 35).
- [41] John P. Perdew, J. A. Chevary, S. H. Vosko, Koblar A. Jackson, Mark R. Pederson, D. J. Singh, and Carlos Fiolhais. "Atoms, molecules, solids, and surfaces: Applications of the generalized gradient approximation for exchange and correlation". In: *Phys. Rev. B* 46 (11 Sept. 1992), pp. 6671–6687 (cit. on p. 35).
- [42] John P. Perdew, Kieron Burke, and Matthias Ernzerhof. "Generalized Gradient Approximation Made Simple". In: *Phys. Rev. Lett.* 77 (18 Oct. 1996), pp. 3865–3868 (cit. on pp. 35, 144).
- [43] Eva Pavarini, Erik Koch, and Schiwei Zhang, eds. *Many-Body Methods for Real Materials*. Vol. 9. Schriften des Forschungszentrums Jülich. Modeling and Simulation. Autumn School on Correlated Electrons, Jülich (Germany), 16 Sep 2019 - 20 Sep 2019. Jülich: Forschungszentrum Jülich GmbH Zentralbibliothek, Verlag, Sept. 16, 2019, getr. Zählung (cit. on pp. 35, 36).
- [44] Axel D. Becke. "Density-functional thermochemistry. III. The role of exact exchange". In: *The Journal of Chemical Physics* 98.7 (Apr. 1993), pp. 5648–5652 (cit. on p. 36).
- [45] John P. Perdew, Matthias Ernzerhof, and Kieron Burke. "Rationale for mixing exact exchange with density functional approximations". In: *J. Chem. Phys.* 105.22 (1996), pp. 9982–9985 (cit. on pp. 36, 75, 104, 126).

- [46] Carlo Adamo and Vincenzo Barone. “Toward reliable density functional methods without adjustable parameters: The PBE0 model”. In: *J. Chem. Phys.* 110 (Apr. 1999) (cit. on pp. 36, 75, 104).
- [47] Michael G. Medvedev, Ivan S. Bushmarinov, Jianwei Sun, John P. Perdew, and Konstantin A. Lyssenko. “Density functional theory is straying from the path toward the exact functional”. In: *Science* 355.6320 (2017), pp. 49–52 (cit. on p. 36).
- [48] Lars Hedin. “On correlation effects in electron spectroscopies and the GW approximation”. In: *Journal of Physics: Condensed Matter* 11.42 (Oct. 1999), R489 (cit. on pp. 37, 52, 54, 61).
- [49] J. F. Janak. “Proof that $\frac{\partial E}{\partial n_i} = \epsilon$ in density-functional theory”. In: *Phys. Rev. B* 18 (12 Dec. 1978), pp. 7165–7168 (cit. on p. 37).
- [50] John P. Perdew, Robert G. Parr, Mel Levy, and Jose L. Balduz. “Density-Functional Theory for Fractional Particle Number: Derivative Discontinuities of the Energy”. In: *Phys. Rev. Lett.* 49 (23 Dec. 1982), pp. 1691–1694 (cit. on p. 37).
- [51] John P. Perdew and Mel Levy. “Comment on “Significance of the highest occupied Kohn-Sham eigenvalue””. In: *Phys. Rev. B* 56 (24 Dec. 1997), pp. 16021–16028 (cit. on p. 37).
- [52] Mel Levy, John P. Perdew, and Virajt Sahni. “Exact differential equation for the density and ionization energy of a many-particle system”. In: *Phys. Rev. A* 30 (5 Nov. 1984), pp. 2745–2748 (cit. on p. 37).
- [53] C.-O. Almbladh and U. von Barth. “Exact results for the charge and spin densities, exchange-correlation potentials, and density-functional eigenvalues”. In: *Phys. Rev. B* 31 (6 Mar. 1985), pp. 3231–3244 (cit. on p. 37).
- [54] Aron J. Cohen, Paula Mori-Sánchez, and Weitao Yang. “Fractional charge perspective on the band gap in density-functional theory”. In: *Phys. Rev. B* 77 (11 Mar. 2008), p. 115123 (cit. on p. 38).
- [55] Massimiliano Comin. “Multiscale modeling of charge transfer and release in doped organic semiconductors”. 2022GRALY022. PhD thesis. 2022 (cit. on p. 38).
- [56] Chen Li and Weitao Yang. “On the piecewise convex or concave nature of ground state energy as a function of fractional number of electrons for approximate density functionals”. In: *The Journal of Chemical Physics* 146.7 (Feb. 2017), p. 074107 (cit. on p. 38).
- [57] Frank Neese, Frank Wennmohs, Ute Becker, and Christoph Riplinger. “The ORCA quantum chemistry program package”. In: *J. Chem. Phys.* 152.22 (2020), p. 224108 (cit. on pp. 39, 75, 104, 125).
- [58] Frank Neese. “Software update: The ORCA program system—Version 5.0”. In: *WIREs Comput. Mol. Sci.* 12.5 (2022), e1606 (cit. on pp. 39, 75, 104).
- [59] S. F. Boys and Alfred Charles Egerton. “Electronic wave functions - I. A general method of calculation for the stationary states of any molecular system”. In: *Proceedings of the Royal Society of London. Series A. Mathematical and Physical Sciences* 200.1063 (1950), pp. 542–554 (cit. on p. 39).
- [60] B.J. Alder, S. Fernbach, and M. Rotenberg. *Methods in Computational Physics: Advances in Research and Applications. Volume 2: Quantum Mechanics*. vol. 2. Academic Press, 1963 (cit. on p. 39).
- [61] Benjamin P. Pritchard, Doaa Altarawy, Brett Didier, Tara D. Gibson, and Theresa L. Windus. “New Basis Set Exchange: An Open, Up-to-Date Resource for the Molecular Sciences Community”. In: *Journal of Chemical Information and Modeling* 59.11 (2019). PMID: 31600445, pp. 4814–4820 (cit. on pp. 40, 57).

- [62] R. Ditchfield, W. J. Hehre, and J. A. Pople. “Self-Consistent Molecular-Orbital Methods. IX. An Extended Gaussian-Type Basis for Molecular-Orbital Studies of Organic Molecules”. In: *The Journal of Chemical Physics* 54.2 (Sept. 1971), pp. 724–728 (cit. on p. 40).
- [63] R. Krishnan, J. S. Binkley, R. Seeger, and J. A. Pople. “Self-consistent molecular orbital methods. XX. A basis set for correlated wave functions”. In: *J. Chem. Phys.* 72.1 (1980), pp. 650–654 (cit. on pp. 40, 126).
- [64] Florian Weigend and Reinhart Ahlrichs. “Balanced basis sets of split valence, triple zeta valence and quadruple zeta valence quality for H to Rn: Design and assessment of accuracy”. In: *Phys. Chem. Chem. Phys.* 7 (18 2005), pp. 3297–3305 (cit. on pp. 40, 104).
- [65] Alexander Fetter and John Walecka. *Quantum Theory of Many-Particle System*. Vol. 25. Jan. 2003 (cit. on p. 41).
- [66] E.K.U. Gross, E. Runge, and O. Heinonen. *Many-Particle Theory*. Taylor & Francis, 1991 (cit. on pp. 41, 44, 45, 47).
- [67] F. Bruneval. “Echange et Corrélacion dans la Structure Electronique des Solides, du Silicium à l’Oxyde Cuivreux: Approximation GW et au-delà”. Theses. Ecole Polytechnique X, Oct. 2005 (cit. on pp. 41, 46, 47, 52, 53, 100).
- [68] Viktor Mikhailovich Galitskii and Arkadii Beinusovich Migdal. “Application of quantum field theory methods to the many body problem”. In: *Sov. Phys. JETP* 7.96 (1958), p. 18 (cit. on p. 42).
- [69] Julien Toulouse. *Introduction to many-body Green-function theory*. URL: https://www.lct.jussieu.fr/pagesperso/toulouse/enseignement/introduction_green.pdf. Last visited on 2023/12/20. 2019 (cit. on pp. 43, 45–47).
- [70] Carl-Olof Almbladh and Lars Hedin. “Handbook of Synchrotron Radiation vol. 1b, ed. by E.-E. Koch”. In: North-Holland Compagny, July 1983. Chap. 8 Beyond the One-Electron Model. Many-Body Effects in Atoms, Molecules, and Solids, pp. 607–904 (cit. on pp. 43, 52, 96).
- [71] W. Appel and E. Kowalski. *Mathematics for Physics and Physicists*. Mathematical notes. Princeton University Press, 2007 (cit. on pp. 44, 52, 53, 101).
- [72] Giancarlo Strinati. “Application of the Green’s functions method to the study of the optical properties of semiconductors”. In: *La Rivista del Nuovo Cimento* 11 (Dec. 1988), pp. 1–86 (cit. on pp. 45, 47, 55).
- [73] Xavier Blase. *An Introduction to the GW Green’s function many-body perturbation theory*. URL: <http://perso.neel.cnrs.fr/xavier.blase/LECTURES/gw-intro-Raproche-Blase.pdf>. Last visited on 2024/01/05. 2019 (cit. on p. 46).
- [74] Paul C. Martin and Julian Schwinger. “Theory of Many-Particle Systems. I”. In: *Phys. Rev.* 115 (6 Sept. 1959), pp. 1342–1373 (cit. on p. 47).
- [75] M. J. van Setten, F. Weigend, and F. Evers. “The GW-Method for Quantum Chemistry Applications: Theory and Implementation”. In: *Journal of Chemical Theory and Computation* 9.1 (2013). PMID: 26589026, pp. 232–246 (cit. on p. 52).
- [76] Christof Holzer, Andrew M. Teale, Florian Hampe, Stella Stopkowicz, Trygve Helgaker, and Wim Klopper. “GW quasiparticle energies of atoms in strong magnetic fields”. In: *The Journal of Chemical Physics* 150.21 (June 2019), p. 214112 (cit. on p. 52).
- [77] Christof Holzer, Andrew M. Teale, Florian Hampe, Stella Stopkowicz, Trygve Helgaker, and Wim Klopper. “Erratum: “GW quasiparticle energies of atoms in strong magnetic fields” [J. Chem. Phys. 150, 214112 (2019)]”. In: *The Journal of Chemical Physics* 151.6 (Aug. 2019), p. 069902 (cit. on p. 52).

- [78] Ivan Duchemin and Xavier Blase. “Robust Analytic-Continuation Approach to Many-Body GW Calculations”. In: *Journal of Chemical Theory and Computation* 16.3 (2020). PMID: 32023052, pp. 1742–1756 (cit. on pp. 52, 56–58, 60, 61).
- [79] Mark S. Hybertsen and Steven G. Louie. “Electron correlation in semiconductors and insulators: Band gaps and quasiparticle energies”. In: *Phys. Rev. B* 34 (8 Oct. 1986), pp. 5390–5413 (cit. on pp. 53, 54, 125).
- [80] J. Arjan Berger, Pierre-François Loos, and Pina Romaniello. “Potential Energy Surfaces without Unphysical Discontinuities: The Coulomb Hole Plus Screened Exchange Approach”. In: *J. Chem. Theory Comput.* 17.1 (2021). PMID: 33306908, pp. 191–200 (cit. on p. 53).
- [81] C. Faber, P. Boulanger, I. Duchemin, C. Attaccalite, and X. Blase. “Many-body Green’s function GW and Bethe-Salpeter study of the optical excitations in a paradigmatic model dipeptide”. In: *The Journal of Chemical Physics* 139.19 (Nov. 2013), p. 194308 (cit. on p. 54).
- [82] F Aryasetiawan and O Gunnarsson. “The GW method”. In: *Reports on Progress in Physics* 61.3 (Mar. 1998), p. 237 (cit. on pp. 54, 61).
- [83] Richard M. Martin, Lucia Reining, and David M. Ceperley. *Interacting Electrons: Theory and Computational Approaches*. Cambridge University Press, 2016 (cit. on pp. 54, 55).
- [84] Stephen L. Adler. “Quantum Theory of the Dielectric Constant in Real Solids”. In: *Phys. Rev.* 126 (2 Apr. 1962), pp. 413–420 (cit. on p. 54).
- [85] Nathan Wiser. “Dielectric Constant with Local Field Effects Included”. In: *Phys. Rev.* 129 (1 Jan. 1963), pp. 62–69 (cit. on p. 54).
- [86] The experimental values come from [<https://webbook.nist.gov/cgi/cbook.cgi?ID=C99685968&Units=SI&Mask=20#Refs>]. The experimental gap is computed as the difference between the ionization energy and the electron affinity. (cit. on pp. 55, 56, 88, 108).
- [87] M. van Schilfgaarde, Takao Kotani, and S. Faleev. “Quasiparticle Self-Consistent GW Theory”. In: *Phys. Rev. Lett.* 96 (22 June 2006), p. 226402 (cit. on p. 55).
- [88] A. Stan, N. E. Dahlen, and R. van Leeuwen. “Fully self-consistent GW calculations for atoms and molecules”. In: *Europhys. Lett.* 76.2 (Sept. 2006), p. 298 (cit. on p. 55).
- [89] C. Rostgaard, K. W. Jacobsen, and K. S. Thygesen. “Fully self-consistent GW calculations for molecules”. In: *Phys. Rev. B* 81 (8 Feb. 2010), p. 085103 (cit. on p. 55).
- [90] Noa Marom, Fabio Caruso, Xinguo Ren, Oliver T. Hofmann, Thomas Körzdörfer, James R. Chelikowsky, Angel Rubio, Matthias Scheffler, and Patrick Rinke. “Benchmark of GW methods for azabenzenes”. In: *Phys. Rev. B* 86 (24 Dec. 2012), p. 245127 (cit. on p. 55).
- [91] P. Koval, D. Foerster, and D. Sánchez-Portal. “Fully self-consistent GW and quasiparticle self-consistent GW for molecules”. In: *Phys. Rev. B* 89 (15 Apr. 2014), p. 155417 (cit. on p. 55).
- [92] F. Kaplan, M. E. Harding, C. Seiler, F. Weigend, F. Evers, and M. J. van Setten. “Quasi-Particle Self-Consistent GW for Molecules”. In: *J. Chem. Theory Comput.* 12.6 (2016). PMID: 27168352, pp. 2528–2541 (cit. on pp. 55, 76).
- [93] Joseph W. Knight, Xiaopeng Wang, Lukas Gallandi, Olga Dolgounitcheva, Xinguo Ren, J. Vincent Ortiz, Patrick Rinke, Thomas Körzdörfer, and Noa Marom. “Accurate Ionization Potentials and Electron Affinities of Acceptor Molecules III: A Benchmark of GW Methods”. In: *J. Chem. Theory Comput.* 12.2 (2016). PMID: 26731609, pp. 615–626 (cit. on p. 55).
- [94] Antoine Marie and Pierre-François Loos. “A Similarity Renormalization Group Approach to Green’s Function Methods”. In: *J. Chem. Theory Comput.* 19.13 (2023). PMID: 37311565, pp. 3943–3957 (cit. on p. 55).

- [95] Mickaël Véril, Pina Romaniello, J. A. Berger, and Pierre-François Loos. “Unphysical Discontinuities in GW Methods”. In: *J. Chem. Theory Comput.* 14.10 (2018). PMID: 30212627, pp. 5220–5228 (cit. on p. 55).
- [96] Enzo Monino and Pierre-François Loos. “Unphysical discontinuities, intruder states and regularization in GW methods”. In: *J. Chem. Phys.* 156.23 (June 2022), p. 231101 (cit. on p. 55).
- [97] M. Shishkin and G. Kresse. “Self-consistent GW calculations for semiconductors and insulators”. In: *Phys. Rev. B* 75 (23 June 2007), p. 235102 (cit. on p. 55).
- [98] Tonatiuh Rangel, Samia M. Hamed, Fabien Bruneval, and Jeffrey B. Neaton. “Evaluating the GW Approximation with CCSD(T) for Charged Excitations Across the Oligoacenes”. In: *J. Chem. Theory Comput.* 12.6 (2016). PMID: 27123935, pp. 2834–2842 (cit. on pp. 55, 76).
- [99] Xin Gui, Christof Holzer, and Wim Klopper. “Accuracy Assessment of GW Starting Points for Calculating Molecular Excitation Energies Using the Bethe–Salpeter Formalism”. In: *Journal of Chemical Theory and Computation* 14.4 (2018). PMID: 29499116, pp. 2127–2136 (cit. on p. 55).
- [100] Jan Wilhelm, Mauro Del Ben, and Jürg Hutter. “GW in the Gaussian and Plane Waves Scheme with Application to Linear Acenes”. In: *Journal of Chemical Theory and Computation* 12.8 (2016). PMID: 27348184, pp. 3623–3635 (cit. on p. 55).
- [101] Ivan Duchemin and Xavier Blase. “Cubic-Scaling All-Electron GW Calculations with a Separable Density-Fitting Space–Time Approach”. In: *Journal of Chemical Theory and Computation* 17.4 (2021). PMID: 33797245, pp. 2383–2393 (cit. on pp. 56, 58, 59, 66, 116).
- [102] Denis Jacquemin, Ivan Duchemin, and Xavier Blase. “Benchmarking the Bethe–Salpeter Formalism on a Standard Organic Molecular Set”. In: *Journal of Chemical Theory and Computation* 11.7 (2015). PMID: 26207104, pp. 3290–3304 (cit. on p. 56).
- [103] Denis Jacquemin, Ivan Duchemin, and Xavier Blase. “Is the Bethe–Salpeter Formalism Accurate for Excitation Energies? Comparisons with TD-DFT, CASPT2, and EOM-CCSD”. In: *The Journal of Physical Chemistry Letters* 8.7 (2017). PMID: 28301726, pp. 1524–1529 (cit. on p. 56).
- [104] O. Vahtras, J. Almlöf, and M.W. Feyereisen. “Integral approximations for LCAO-SCF calculations”. In: *Chemical Physics Letters* 213.5 (1993), pp. 514–518 (cit. on pp. 56, 75, 104).
- [105] Xinguo Ren, Patrick Rinke, Volker Blum, Jürgen Wieferink, Alexandre Tkatchenko, Andrea Sanfilippo, Karsten Reuter, and Matthias Scheffler. “Resolution-of-identity approach to Hartree-Fock, hybrid density functionals, RPA, MP2 and GW with numeric atom-centered orbital basis functions”. In: *New J. Phys.* 14.5 (May 2012), p. 053020 (cit. on p. 56).
- [106] Ivan Duchemin, Jing Li, and Xavier Blase. “Hybrid and Constrained Resolution-of-Identity Techniques for Coulomb Integrals”. In: *J. Chem. Theory Comput.* 13.3 (2017). PMID: 28094983, pp. 1199–1208 (cit. on pp. 56, 57, 75, 104).
- [107] J. L. Whitten. “Coulombic potential energy integrals and approximations”. In: *The Journal of Chemical Physics* 58.10 (May 1973), pp. 4496–4501 (cit. on p. 57).
- [108] Florian Weigend, Marco Häser, Holger Patzelt, and Reinhart Ahlrichs. “RI-MP2: optimized auxiliary basis sets and demonstration of efficiency”. In: *Chemical Physics Letters* 294.1 (1998), pp. 143–152 (cit. on pp. 57, 104).
- [109] Christof Hättig. “Optimization of auxiliary basis sets for RI-MP2 and RI-CC2 calculations: Core–valence and quintuple- ζ basis sets for H to Ar and QZVPP basis sets for Li to Kr”. In: *Phys. Chem. Chem. Phys.* 7 (1 2005), pp. 59–66 (cit. on p. 57).

- [110] Arnim Hellweg and Dmitrij Rappoport. “Development of new auxiliary basis functions of the Karlsruhe segmented contracted basis sets including diffuse basis functions (def2-SVPD, def2-TZVPPD, and def2-QVPPD) for RI-MP2 and RI-CC calculations”. In: *Phys. Chem. Chem. Phys.* 17 (2 2015), pp. 1010–1017 (cit. on p. 57).
- [111] Florian Weigend. “Accurate Coulomb-fitting basis sets for H to Rn”. In: *Phys. Chem. Chem. Phys.* 8 (9 2006), pp. 1057–1065 (cit. on pp. 57, 126).
- [112] Ramón L. Panadés-Barrueta and Dorothea Golze. “Accelerating Core-Level GW Calculations by Combining the Contour Deformation Approach with the Analytic Continuation of W”. In: *Journal of Chemical Theory and Computation* 19.16 (2023). PMID: 37566917, pp. 5450–5464 (cit. on p. 57).
- [113] Max Kehry, Wim Klopper, and Christof Holzer. “Robust relativistic many-body Green’s function based approaches for assessing core ionized and excited states”. In: *The Journal of Chemical Physics* 159.4 (July 2023), p. 044116 (cit. on p. 57).
- [114] Ivan Duchemin and Xavier Blase. “Separable resolution-of-the-identity with all-electron Gaussian bases: Application to cubic-scaling RPA”. In: *The Journal of Chemical Physics* 150.17 (May 2019), p. 174120 (cit. on pp. 58, 59, 116).
- [115] Jan Almlöf. “Elimination of energy denominators in Møller–Plesset perturbation theory by a Laplace transform approach”. In: *Chemical Physics Letters* 181.4 (1991), pp. 319–320 (cit. on p. 59).
- [116] Marco Häser and Jan Almlöf. “Laplace transform techniques in Møller–Plesset perturbation theory”. In: *The Journal of Chemical Physics* 96.1 (Jan. 1992), pp. 489–494 (cit. on p. 59).
- [117] S. Miertuš, E. Scrocco, and J. Tomasi. “Electrostatic interaction of a solute with a continuum. A direct utilization of AB initio molecular potentials for the prevision of solvent effects”. In: *Chem. Phys.* 55.1 (1981), pp. 117–129 (cit. on p. 62).
- [118] E. Cancès, B. Mennucci, and J. Tomasi. “A new integral equation formalism for the polarizable continuum model: Theoretical background and applications to isotropic and anisotropic dielectrics”. In: *J. Chem. Phys.* 107.8 (1997), pp. 3032–3041 (cit. on p. 62).
- [119] Mark A. Thompson and Gregory K. Schenter. “Excited States of the Bacteriochlorophyll b Dimer of Rhodospseudomonas viridis: A QM/MM Study of the Photosynthetic Reaction Center That Includes MM Polarization”. In: *J. Phys. Chem.* 99.17 (1995), pp. 6374–6386 (cit. on p. 62).
- [120] Anders Osted, Jacob Kongsted, Kurt V. Mikkelsen, Per-Olof Åstrand, and Ove Christiansen. “Statistical mechanically averaged molecular properties of liquid water calculated using the combined coupled cluster/molecular dynamics method”. In: *J. Chem. Phys.* 124.12 (Mar. 2006), p. 124503 (cit. on p. 62).
- [121] Lin and Jiali Gao. “Solvatochromic Shifts of the $n \rightarrow \pi^*$ Transition of Acetone from Steam Vapor to Ambient Aqueous Solution: A Combined Configuration Interaction QM/MM Simulation Study Incorporating Solvent Polarization”. In: *J Chem. Theory Comput.* 3.4 (2007). PMID: 26633219, pp. 1484–1493 (cit. on p. 62).
- [122] Carles Curutchet, Aurora Muñoz-Losa, Susanna Monti, Jacob Kongsted, Gregory D. Scholes, and Benedetta Mennucci. “Electronic Energy Transfer in Condensed Phase Studied by a Polarizable QM/MM Model”. In: *J. Chem. Theory Comput.* 5.7 (2009). PMID: 26610008, pp. 1838–1848 (cit. on p. 62).

- [123] Gabriele D'Avino, Luca Muccioli, Frédéric Castet, Carl Poelking, Denis Andrienko, Zoltán G Soos, Jérôme Cornil, and David Beljonne. “Electrostatic phenomena in organic semiconductors: fundamentals and implications for photovoltaics”. In: *Journal of Physics: Condensed Matter* 28.43 (Sept. 2016), p. 433002 (cit. on pp. 62, 86, 96, 129, 134, 150, 154).
- [124] Mattia Bondanza, Michele Nottoli, Lorenzo Cupellini, Filippo Lipparini, and Benedetta Men-
nucci. “Polarizable embedding QM/MM: the future gold standard for complex (bio)systems?”
In: *Phys. Chem. Chem. Phys.* 22 (26 2020), pp. 14433–14448 (cit. on pp. 62, 96).
- [125] Daniele Loco, Louis Lagardère, Olivier Adjoua, and Jean-Philip Piquemal. “Atomistic Polar-
izable Embeddings: Energy, Dynamics, Spectroscopy, and Reactivity”. In: *Acc. Chem. Res.*
54.13 (2021). PMID: 33961401, pp. 2812–2822 (cit. on p. 62).
- [126] David Amblard, Xavier Blase, and Ivan Duchemin. “Many-body *GW* calculations with very
large scale polarizable environments made affordable: A fully ab initio QM/QM approach”. In:
J. Chem. Phys. 159.16 (Oct. 2023), p. 164107 (cit. on pp. 63, 173).
- [127] H. N. Rojas, R. W. Godby, and R. J. Needs. “Space-Time Method for Ab Initio Calculations
of Self-Energies and Dielectric Response Functions of Solids”. In: *Phys. Rev. Lett.* 74 (10 Mar.
1995), pp. 1827–1830 (cit. on p. 66).
- [128] D. Foerster, P. Koval, and D. Sánchez-Portal. “An $O(N^3)$ Implementation of Hedins *GW*
Approximation for Molecules”. In: *J. Chem. Phys.* 135 (2011), p. 074105 (cit. on p. 66).
- [129] Daniel Neuhauser, Yi Gao, Christopher Arntsen, Cyrus Karshenas, Eran Rabani, and Roi Baer.
“Breaking the Theoretical Scaling Limit for Predicting Quasiparticle Energies: The Stochastic
GW Approach”. In: *Phys. Rev. Lett.* 113 (7 Aug. 2014), p. 076402 (cit. on p. 66).
- [130] Peitao Liu, Merzuk Kaltak, Jiří Klimeš, and Georg Kresse. “Cubic scaling *GW*: Towards fast
quasiparticle calculations”. In: *Phys. Rev. B* 94 (16 Oct. 2016), p. 165109 (cit. on p. 66).
- [131] Vojtěch Vlček, Eran Rabani, Daniel Neuhauser, and Roi Baer. “Stochastic *GW* Calculations
for Molecules”. In: *J. Chem. Theory Comput.* 13.10 (2017). PMID: 28876912, pp. 4997–5003
(cit. on p. 66).
- [132] Vojtěch Vlček, Wenfei Li, Roi Baer, Eran Rabani, and Daniel Neuhauser. “Swift *GW* beyond
10,000 electrons using sparse stochastic compression”. In: *Phys. Rev. B* 98 (7 Aug. 2018),
p. 075107 (cit. on p. 66).
- [133] Jan Wilhelm, Dorothea Golze, Leopold Talirz, Jürg Hutter, and Carlo A. Pignedoli. “Toward
GW Calculations on Thousands of Atoms”. In: *J. Phys. Chem. Lett.* 9.2 (2018). PMID:
29280376, pp. 306–312 (cit. on p. 66).
- [134] Arno Förster and Lucas Visscher. “Low-Order Scaling G_0W_0 by Pair Atomic Density Fitting”.
In: *J. Chem. Theory Comput.* 16.12 (2020). PMID: 33174743, pp. 7381–7399 (cit. on p. 66).
- [135] Minjung Kim, Glenn J. Martyna, and Sohrab Ismail-Beigi. “Complex-time shredded propagator
method for large-scale *GW* calculations”. In: *Phys. Rev. B* 101 (3 Jan. 2020), p. 035139 (cit. on
p. 66).
- [136] A.L. Kutepov. “Self-consistent *GW* method: $O(N)$ algorithm for polarizability and self energy”.
In: *Comput. Phys. Commun.* 257 (2020), p. 107502 (cit. on p. 66).
- [137] Jan Wilhelm, Patrick Seewald, and Dorothea Golze. “Low-Scaling *GW* with Benchmark
Accuracy and Application to Phosphorene Nanosheets”. In: *J. Chem. Theory Comput.* 17.3
(2021). PMID: 33621085, pp. 1662–1677 (cit. on p. 66).
- [138] Takatoshi Fujita and Yoshifumi Noguchi. “Development of the fragment-based COHSEX
method for large and complex molecular systems”. In: *Phys. Rev. B* 98 (20 Nov. 2018),
p. 205140 (cit. on pp. 67, 75, 124).

- [139] Takatoshi Fujita, Yoshifumi Noguchi, and Takeo Hoshi. “Charge-transfer excited states in the donor/acceptor interface from large-scale GW calculations”. In: *J. Chem. Phys.* 151.11 (2019), p. 114109 (cit. on pp. 67, 75).
- [140] Takatoshi Fujita and Yoshifumi Noguchi. “Fragment-Based Excited-State Calculations Using the GW Approximation and the Bethe–Salpeter Equation”. In: *J. Phys. Chem. A* 125.49 (2021). PMID: 34871000, pp. 10580–10592 (cit. on pp. 67, 69, 75, 97, 150, 154).
- [141] Johannes Tölle, Thorsten Deilmann, Michael Rohlfing, and Johannes Neugebauer. “Subsystem-Based GW/Bethe–Salpeter Equation”. In: *J. Chem. Theory Comput.* 17.4 (2021). PMID: 33683119, pp. 2186–2199 (cit. on pp. 67, 75, 124, 125).
- [142] Guorong Weng and Vojtěch Vlček. “Efficient treatment of molecular excitations in the liquid phase environment via stochastic many-body theory”. In: *J. Chem. Phys.* 155.5 (Aug. 2021), p. 054104 (cit. on p. 67).
- [143] Guorong Weng, Amanda Pang, and Vojtěch Vlček. “Spatial Decay and Limits of Quantum Solute–Solvent Interactions”. In: *J. Phys. Chem. Lett.* 14.10 (2023). PMID: 36867592, pp. 2473–2480 (cit. on p. 67).
- [144] Zhen-Fei Liu, Felipe H. da Jornada, Steven G. Louie, and Jeffrey B. Neaton. “Accelerating GW-Based Energy Level Alignment Calculations for Molecule–Metal Interfaces Using a Substrate Screening Approach”. In: *J. Chem. Theory Comput.* 15.7 (2019). PMID: 31194538, pp. 4218–4227 (cit. on pp. 67, 98).
- [145] Zhen-Fei Liu. “Dielectric embedding GW for weakly coupled molecule-metal interfaces”. In: *J. Chem. Phys.* 152.5 (Feb. 2020), p. 054103 (cit. on p. 67).
- [146] Fengyuan Xuan, Yifeng Chen, and Su Ying Quek. “Quasiparticle Levels at Large Interface Systems from Many-Body Perturbation Theory: The XAF-GW Method”. In: *J. Chem. Theory Comput.* 15.6 (2019). PMID: 31084031, pp. 3824–3835 (cit. on pp. 67, 124, 136).
- [147] Kirsten Andersen, Simone Latini, and Kristian S. Thygesen. “Dielectric Genome of van der Waals Heterostructures”. In: *Nano Letters* 15.7 (2015). PMID: 26047386, pp. 4616–4621 (cit. on pp. 67, 124, 136).
- [148] Kirsten T. Winther and Kristian S. Thygesen. “Band structure engineering in van der Waals heterostructures via dielectric screening: the $G\Delta W$ method”. In: *2D Mater.* 4.2 (Mar. 2017), p. 025059 (cit. on pp. 67, 124).
- [149] Gabriele D’Avino, Luca Muccioli, Claudio Zannoni, David Beljonne, and Zoltán G. Soos. “Electronic Polarization in Organic Crystals: A Comparative Study of Induced Dipoles and Intramolecular Charge Redistribution Schemes”. In: *J. Chem. Theory Comput.* 10.11 (2014). PMID: 26584380, pp. 4959–4971 (cit. on pp. 70, 76, 134, 150, 154).
- [150] Mi-Song Dupuy. *Notes de cours pour la minischool du GDR NBODY*. URL: https://wiki.lct.jussieu.fr/gdrnbody/images/8/84/Lecture_notes_dupuy_2023.pdf. Last visited on 2024/02/12. 2023 (cit. on p. 72).
- [151] Johannes Traa. *Matrix Calculus - Notes on the Derivative of a Trace*. URL: <https://paulklein.ca/newsite/teaching/matrixcalculus.pdf>. Last visited on 2024/02/12 (cit. on p. 73).
- [152] L. S. Blackford, J. Choi, A. Cleary, E. D’Azevedo, J. Demmel, I. Dhillon, J. Dongarra, S. Hammarling, G. Henry, A. Petitet, K. Stanley, D. Walker, and R. C. Whaley. *ScaLAPACK Users’ Guide*. Philadelphia, PA: Society for Industrial and Applied Mathematics, 1997 (cit. on p. 74).

- [153] Hugh F. Wilson, François Gygi, and Giulia Galli. “Efficient iterative method for calculations of dielectric matrices”. In: *Phys. Rev. B* 78 (11 Sept. 2008), p. 113303 (cit. on pp. 74, 98).
- [154] Marco Govoni and Giulia Galli. “Large Scale GW Calculations”. In: *J. Chem. Theory Comput.* 11.6 (2015). PMID: 26575564, pp. 2680–2696 (cit. on pp. 74, 98).
- [155] Paul A. Heiney, John E. Fischer, Andrew R. McGhie, William J. Romanow, Arnold M. Denenstien, John P. McCauley Jr., Amos B. Smith, and David E. Cox. “Orientational ordering transition in solid C₆₀”. In: *Phys. Rev. Lett.* 66 (22 June 1991), pp. 2911–2914 (cit. on pp. 75, 105).
- [156] Fabien Bruneval and Miguel A. L. Marques. “Benchmarking the Starting Points of the GW Approximation for Molecules”. In: *J. Chem. Theory Comput.* 9.1 (2013). PMID: 26589035, pp. 324–329 (cit. on p. 76).
- [157] Frank Jensen. “Polarization consistent basis sets. III. The importance of diffuse functions”. In: *J. Chem. Phys.* 117.20 (Nov. 2002), pp. 9234–9240 (cit. on p. 81).
- [158] Dmitriy Rappoport and Filipp Furche. “Property-optimized Gaussian basis sets for molecular response calculations”. In: *J. Chem. Phys.* 133.13 (Oct. 2010), p. 134105 (cit. on p. 81).
- [159] Eric L. Shirley and Steven G. Louie. “Electron excitations in solid C₆₀: Energy gap, band dispersions, and effects of orientational disorder”. In: *Phys. Rev. Lett.* 71 (1 July 1993), pp. 133–136 (cit. on p. 88).
- [160] B. Reihl. “Geometric and Electronic Structure of Fullerene Film Growth as a Function of Coverage”. In: *Mater Res Soc Symp Proc* 359 (1994), p. 377 (cit. on pp. 88, 105, 107).
- [161] J.H. Weaver. “Electronic structures of C₆₀, C₇₀ and the fullerides: Photoemission and inverse photoemission studies”. In: *J. Phys. Chem. Solids* 53.11 (1992), pp. 1433–1447 (cit. on pp. 88, 105, 107).
- [162] P. J. Benning, D. M. Poirier, T. R. Ohno, Y. Chen, M. B. Jost, F. Stepniak, G. H. Kroll, J. H. Weaver, J. Fure, and R. E. Smalley. “C₆₀ and C₇₀ fullerenes and potassium fullerides”. In: *Phys. Rev. B* 45 (12 Mar. 1992), pp. 6899–6913 (cit. on pp. 88, 105, 107).
- [163] R. W. Lof, M. A. van Veenendaal, B. Koopmans, H. T. Jonkman, and G. A. Sawatzky. “Band gap, excitons, and Coulomb interaction in solid C₆₀”. In: *Phys. Rev. Lett.* 68 (26 June 1992), pp. 3924–3927 (cit. on pp. 88, 105, 107).
- [164] T. Takahashi, S. Suzuki, T. Morikawa, H. Katayama-Yoshida, S. Hasegawa, H. Inokuchi, K. Seki, K. Kikuchi, S. Suzuki, K. Ikemoto, and Y. Achiba. “Pseudo-gap at the Fermi level in K₃C₆₀ observed by photoemission and inverse photoemission”. In: *Phys. Rev. Lett.* 68 (8 Feb. 1992), pp. 1232–1235 (cit. on pp. 88, 105, 107).
- [165] David Amblard, Xavier Blase, and Ivan Duchemin. “Static versus dynamically polarizable environments within the many-body GW formalism”. In: *J. Chem. Phys.* 160.15 (Apr. 2024), p. 154104 (cit. on pp. 93, 173).
- [166] Daniele Varsano, Emanuele Cocchia, Olivia Pulci, Adriano Mosca Conte, and Leonardo Guidoni. “Ground state structures and electronic excitations of biological chromophores at Quantum Monte Carlo / Many Body Green’s Function Theory level”. In: *Comput. Theor. Chem.* 1040-1041 (2014), pp. 338–346 (cit. on pp. 96, 150, 154).
- [167] B.T. Thole. “Molecular polarizabilities calculated with a modified dipole interaction”. In: *Chem. Phys.* 59.3 (1981), pp. 341–350 (cit. on p. 96).
- [168] D. K. Andrea Phan Huu, Rama Dhali, Carlotta Pieroni, Francesco Di Maiolo, Cristina Sissa, Francesca Terenziani, and Anna Painelli. “Antidiabatic View of Fast Environmental Effects on Optical Spectra”. In: *Phys. Rev. Lett.* 124 (10 Mar. 2020), p. 107401 (cit. on p. 96).

- [169] Christoph R. Jacob and Johannes Neugebauer. “Subsystem density-functional theory”. In: *WIREs Comput. Mol. Sci.* 4.4 (2014), pp. 325–362 (cit. on pp. 97, 150, 153).
- [170] Nicholas Lin Quan Cheng, Fengyuan Xuan, Catalin D. Spataru, and Su Ying Quek. “Charge Transfer Screening and Energy Level Alignment at Complex Organic–Inorganic Interfaces: A Tractable Ab Initio GW Approach”. In: *J. Phys. Chem. Lett.* 12.36 (2021). PMID: 34492190, pp. 8841–8846 (cit. on pp. 97, 150, 154).
- [171] Michael Rohlfing, Peter Krüger, and Johannes Pollmann. “Efficient scheme for GW quasiparticle band-structure calculations with applications to bulk Si and to the Si(001)-(2×1) surface”. In: *Phys. Rev. B* 52 (3 July 1995), pp. 1905–1917 (cit. on p. 98).
- [172] Mauro Del Ben, Felipe H. da Jornada, Gabriel Antonius, Tonatiuh Rangel, Steven G. Louie, Jack Deslippe, and Andrew Canning. “Static subspace approximation for the evaluation of G_0W_0 quasiparticle energies within a sum-over-bands approach”. In: *Phys. Rev. B* 99 (12 Mar. 2019), p. 125128 (cit. on p. 98).
- [173] Jie Ma, Angelos Michaelides, Dario Alfè, Laurids Schimka, Georg Kresse, and Enge Wang. “Adsorption and diffusion of water on graphene from first principles”. In: *Phys. Rev. B* 84 (3 July 2011), p. 033402 (cit. on p. 115).
- [174] Kerstin Falk, Felix Sedlmeier, Laurent Joly, Roland R. Netz, and Lydéric Bocquet. “Molecular Origin of Fast Water Transport in Carbon Nanotube Membranes: Superlubricity versus Curvature Dependent Friction”. In: *Nano Lett.* 10.10 (2010). PMID: 20845964, pp. 4067–4073 (cit. on p. 115).
- [175] Shigeki Inukai, Rodolfo Cruz-Silva, Josue Ortiz-Medina, Aaron Morelos-Gomez, Kenji Takeuchi, Takuya Hayashi, Akihiko Tanioka, Takumi Araki, Syogo Tejima, Toru Noguchi, Mauricio Terrones, and Morinobu Endo. “High-performance multi-functional reverse osmosis membranes obtained by carbon nanotube · polyamide nanocomposite”. In: *Scientific Reports* 5.1 (Sept. 2015), p. 13562 (cit. on p. 115).
- [176] Kunzhou Li, Byeongho Lee, and Yonghyup Kim. “High performance reverse osmosis membrane with carbon nanotube support layer”. In: *Journal of Membrane Science* 592 (2019), p. 117358 (cit. on p. 115).
- [177] José M Soler, Emilio Artacho, Julian D Gale, Alberto García, Javier Junquera, Pablo Ordejón, and Daniel Sánchez-Portal. “The SIESTA method for ab initio order-N materials simulation”. In: *J. Phys.: Cond. Matt.* 14.11 (Mar. 2002), p. 2745 (cit. on p. 115).
- [178] M. Dion, H. Rydberg, E. Schröder, D. C. Langreth, and B. I. Lundqvist. “Van der Waals Density Functional for General Geometries”. In: *Phys. Rev. Lett.* 92 (24 June 2004), p. 246401 (cit. on p. 115).
- [179] Guillermo Román-Pérez and José M. Soler. “Efficient Implementation of a van der Waals Density Functional: Application to Double-Wall Carbon Nanotubes”. In: *Phys. Rev. Lett.* 103 (9 Aug. 2009), p. 096102 (cit. on p. 115).
- [180] Calculation performed on 2304 cores of the TGCC-Irene French supercomputer with Intel Skylake processors (2.70 GHz, 4Gb RAM/core). (cit. on p. 116).
- [181] David Amblard, Gabriele D’Avino, Ivan Duchemin, and Xavier Blase. “Universal polarization energies for defects in monolayer, surface, and bulk hexagonal boron nitride: A finite-size fragments GW approach”. In: *Phys. Rev. Mater.* 6 (6 June 2022), p. 064008 (cit. on pp. 119, 134, 136, 137, 173).
- [182] Arno Schindlmayr. “Decay properties of the one-particle Green function in real space and imaginary time”. In: *Phys. Rev. B* 62 (19 Nov. 2000), pp. 12573–12576 (cit. on pp. 122, 146).

- [183] A. Katzir, J. T. Suss, A. Zunger, and A. Halperin. “Point defects in hexagonal boron nitride. I. EPR, thermoluminescence, and thermally-stimulated-current measurements”. In: *Phys. Rev. B* 11 (6 Mar. 1975), pp. 2370–2377 (cit. on p. 122).
- [184] Koh Era, Fujio Minami, and Takashi Kuzuba. “Fast luminescence from carbon-related defects of hexagonal boron nitride”. In: *J. Lumin.* 24-25 (1981), pp. 71–74 (cit. on p. 122).
- [185] M. G. Silly, P. Jaffrennou, J. Barjon, J.-S. Lauret, F. Ducastelle, A. Loiseau, E. Obraztsova, B. Attal-Tretout, and E. Rosencher. “Luminescence properties of hexagonal boron nitride: Cathodoluminescence and photoluminescence spectroscopy measurements”. In: *Phys. Rev. B* 75 (8 Feb. 2007), p. 085205 (cit. on p. 122).
- [186] Luc Museur, Eduard Feldbach, and Andrei Kanaev. “Defect-related photoluminescence of hexagonal boron nitride”. In: *Phys. Rev. B* 78 (15 Oct. 2008), p. 155204 (cit. on p. 122).
- [187] S. Meuret, L. H. G. Tizei, T. Cazimajou, R. Bourrellier, H. C. Chang, F. Treussart, and M. Kociak. “Photon Bunching in Cathodoluminescence”. In: *Phys. Rev. Lett.* 114 (19 May 2015), p. 197401 (cit. on p. 122).
- [188] Dillon Wong, Jairo Velasco, Long Ju, Juwon Lee, Salman Kahn, Hsin-Zon Tsai, Chad Germany, Takashi Taniguchi, Kenji Watanabe, Alex Zettl, Feng Wang, and Michael F. Crommie. “Characterization and manipulation of individual defects in insulating hexagonal boron nitride using scanning tunnelling microscopy”. In: *Nature Nanotech.* 10 (2015) (cit. on p. 122).
- [189] T.T. Tran, K. Bray, M.J. Ford, M. Toth, and I. Aharonovich. “Quantum emission from hexagonal boron nitride monolayers”. In: *Nature Nanotech* 11 (2016), pp. 37–41 (cit. on p. 122).
- [190] Romain Bourrellier, Sophie Meuret, Anna Tararan, Odile Stéphan, Mathieu Kociak, Luiz H. G. Tizei, and Alberto Zobelli. “Bright UV Single Photon Emission at Point Defects in h-BN”. In: *Nano Lett.* 16.7 (2016). PMID: 27299915, pp. 4317–4321 (cit. on p. 122).
- [191] T. Q. P. Vuong, G. Cassabois, P. Valvin, A. Ouerghi, Y. Chassagneux, C. Voisin, and B. Gil. “Phonon-Photon Mapping in a Color Center in Hexagonal Boron Nitride”. In: *Phys. Rev. Lett.* 117 (9 Aug. 2016), p. 097402 (cit. on p. 122).
- [192] Nicholas R. Jungwirth, Brian Calderon, Yanxin Ji, Michael G. Spencer, Michael E. Flatté, and Gregory D. Fuchs. “Temperature Dependence of Wavelength Selectable Zero-Phonon Emission from Single Defects in Hexagonal Boron Nitride”. In: *Nano Lett.* 16.10 (2016). PMID: 27580074, pp. 6052–6057 (cit. on p. 122).
- [193] Andreas Gottscholl, Mehran Kianinia, Victor Soltamov, Sergei Orlinskii, Georgy Mamin, Carlo Bradac, Christian Kasper, Klaus Krambrock, Andreas Sperlich, Milos Toth, Igor Aharonovich, and Vladimir Dyakonov. “Initialization and read-out of intrinsic spin defects in a van der Waals crystal at room temperature”. In: *Nat. Mater.* 19 (2020), pp. 540–545 (cit. on p. 122).
- [194] Fariah Hayee, Leo Yu, Jingyuan Linda Zhang, Christopher J. Ciccarino, Minh Nguyen, Ann F Marshall, Igor Aharonovich, Jelena Vučković, Prineha Narang, Tony F Heinz, and Jennifer. A Dionne. “Revealing multiple classes of stable quantum emitters in hexagonal boron nitride with correlated optical and electron microscopy”. In: *Nat. Mater.* 19 (2020), pp. 534–539 (cit. on p. 122).
- [195] Noah Mendelson, Dipankar Chugh, Jeffrey R. Reimers, Tin S. Cheng, Andreas Gottscholl, Hu Long, Christopher J. Mellor, Alex Zettl, Vladimir Dyakonov, Peter H. Beton, Sergei V. Novikov, Chennupati Jagadish, Hark Hoe Tan, Michael J. Ford, Milos Toth, Carlo Bradac, and Igor Aharonovich. “Identifying carbon as the source of visible single-photon emission from hexagonal boron nitride”. In: *Nat. Mater.* 20 (2021), p. 321 (cit. on p. 122).

- [196] C. Attaccalite, M. Bockstedte, A. Marini, A. Rubio, and L. Wirtz. “Coupling of excitons and defect states in boron-nitride nanostructures”. In: *Phys. Rev. B* 83 (14 Apr. 2011), p. 144115 (cit. on pp. 122, 123).
- [197] C. Attaccalite, L. Wirtz, A. Marini, and A. Rubio. “Efficient Gate-tunable light-emitting device made of defective boron nitride nanotubes: from ultraviolet to the visible”. In: *Sci. Rep.* 3 (2013) (cit. on p. 122).
- [198] Natalia Berseneva, Andris Gulans, Arkady V. Krashennnikov, and Risto M. Nieminen. “Electronic structure of boron nitride sheets doped with carbon from first-principles calculations”. In: *Phys. Rev. B* 87 (3 Jan. 2013), p. 035404 (cit. on pp. 122, 123).
- [199] Feng Wu, Andrew Galatas, Ravishankar Sundararaman, Dario Rocca, and Yuan Ping. “First-principles engineering of charged defects for two-dimensional quantum technologies”. In: *Phys. Rev. Mater.* 1 (7 Dec. 2017), p. 071001 (cit. on pp. 122, 123).
- [200] Bing Huang and Hoonkyung Lee. “Defect and impurity properties of hexagonal boron nitride: A first-principles calculation”. In: *Phys. Rev. B* 86 (24 Dec. 2012), p. 245406 (cit. on p. 122).
- [201] Sherif Abdulkader Tawfik, Sajid Ali, Marco Fronzi, Mehran Kianinia, Toan Trong Tran, Catherine Stampfl, Igor Aharonovich, Milos Toth, and Michael J. Ford. “First-principles investigation of quantum emission from hBN defects”. In: *Nanoscale* 9 (36 2017), pp. 13575–13582 (cit. on p. 122).
- [202] G.D. Cheng, Y.G. Zhang, L. Yan, H.F. Huang, Q. Huang, Y.X. Song, Y. Chen, and Z. Tang. “A paramagnetic neutral $C_B V_N$ center in hexagonal boron nitride monolayer for spin qubit application”. In: *Comput. Mater. Sci.* 129 (2017), pp. 247–251 (cit. on p. 122).
- [203] Nicholas R. Jungwirth and Gregory D. Fuchs. “Optical Absorption and Emission Mechanisms of Single Defects in Hexagonal Boron Nitride”. In: *Phys. Rev. Lett.* 119 (5 July 2017), p. 057401 (cit. on p. 122).
- [204] Jeffrey R. Reimers, A. Sajid, Rika Kobayashi, and Michael J. Ford. “Understanding and Calibrating Density-Functional-Theory Calculations Describing the Energy and Spectroscopy of Defect Sites in Hexagonal Boron Nitride”. In: *J. Chem. Theory Comput.* 14.3 (2018). PMID: 29412670, pp. 1602–1613 (cit. on p. 122).
- [205] Mehdi Abdi, Jyh-Pin Chou, Adam Gali, and Martin B. Plenio. “Color Centers in Hexagonal Boron Nitride Monolayers: A Group Theory and Ab Initio Analysis”. In: *ACS Photonics* 5.5 (2018), pp. 1967–1976 (cit. on p. 122).
- [206] L. Weston, D. Wickramaratne, M. Mackoït, A. Alkauskas, and C. G. Van de Walle. “Native point defects and impurities in hexagonal boron nitride”. In: *Phys. Rev. B* 97 (21 June 2018), p. 214104 (cit. on p. 122).
- [207] Tyler J. Smart, Feng Wu, Marco Govoni, and Yuan Ping. “Fundamental principles for calculating charged defect ionization energies in ultrathin two-dimensional materials”. In: *Phys. Rev. Mater.* 2 (12 Dec. 2018), p. 124002 (cit. on pp. 122, 123, 126, 135, 139, 145).
- [208] A. Sajid, Jeffrey R. Reimers, and Michael J. Ford. “Defect states in hexagonal boron nitride: Assignments of observed properties and prediction of properties relevant to quantum computation”. In: *Phys. Rev. B* 97 (6 Feb. 2018), p. 064101 (cit. on p. 122).
- [209] Mark E. Turiansky, Audrius Alkauskas, Lee C. Bassett, and Chris G. Van de Walle. “Dangling Bonds in Hexagonal Boron Nitride as Single-Photon Emitters”. In: *Phys. Rev. Lett.* 123 (12 Sept. 2019), p. 127401 (cit. on p. 122).
- [210] Tatiana Korona and Michał B. Chojecki. “Exploring point defects in hexagonal boron-nitrogen monolayers”. In: *Int. J. Quant. Chem.* 119.14 (2019), e25925 (cit. on p. 122).

- [211] M. Mackoit-Sinkevičienė, M. Maciaszek, C. G. Van de Walle, and A. Alkauskas. “Carbon dimer defect as a source of the 4.1 eV luminescence in hexagonal boron nitride”. In: *Appl. Phys. Lett.* 115.21 (2019), p. 212101 (cit. on pp. 122, 127).
- [212] Dan Wang and Ravishankar Sundararaman. “Layer dependence of defect charge transition levels in two-dimensional materials”. In: *Phys. Rev. B* 101 (5 Feb. 2020), p. 054103 (cit. on pp. 122, 141, 144).
- [213] Yifeng Chen and Su Ying Quek. “Photophysical Characteristics of Boron Vacancy-Derived Defect Centers in Hexagonal Boron Nitride”. In: *J. Phys. Chem. C* 125.39 (2021), pp. 21791–21802 (cit. on pp. 122, 123, 145).
- [214] Jeffrey R. Reimers, Jun Shen, Mehran Kianinia, Carlo Bradac, Igor Aharonovich, Michael J. Ford, and Piotr Piecuch. “Photoluminescence, photophysics, and photochemistry of the V_B^- defect in hexagonal boron nitride”. In: *Phys. Rev. B* 102 (14 Oct. 2020), p. 144105 (cit. on p. 122).
- [215] A Sajjid and Kristian S Thygesen. “ $V_N C_B$ defect as source of single photon emission from hexagonal boron nitride”. In: *2D Mater.* 7.3 (June 2020), p. 031007 (cit. on pp. 122, 127).
- [216] Jooyong Bhang, He Ma, Donggyu Yim, Giulia Galli, and Hosung Seo. “First-Principles Predictions of Out-of-Plane Group IV and V Dimers as High-Symmetry, High-Spin Defects in Hexagonal Boron Nitride”. In: *ACS Appl. Mater. Interfaces* 13.38 (2021). PMID: 34541839, pp. 45768–45777 (cit. on p. 122).
- [217] Cesar Jara, Tomáš Rauch, Silvana Botti, Miguel A. L. Marques, Ariel Norambuena, Raul Coto, J. E. Castellanos-Águila, Jeronimo R. Maze, and Francisco Munoz. “First-Principles Identification of Single Photon Emitters Based on Carbon Clusters in Hexagonal Boron Nitride”. In: *J. Phys. Chem. A* 125.6 (2021). PMID: 33554602, pp. 1325–1335 (cit. on p. 122).
- [218] Michael Winter, Manon H. E. Bousquet, Denis Jacquemin, Ivan Duchemin, and Xavier Blase. “Photoluminescent properties of the carbon-dimer defect in hexagonal boron-nitride: A many-body finite-size cluster approach”. In: *Phys. Rev. Mater.* 5 (9 Sept. 2021), p. 095201 (cit. on pp. 122, 123, 127, 129).
- [219] Shiyuan Gao, Hsiao-Yi Chen, and Marco Bernardi. “Radiative properties of quantum emitters in boron nitride from excited state calculations and Bayesian analysis”. In: *npj Comput. Mater.* 7 (2021), p. 85 (cit. on pp. 122, 123).
- [220] Francesco Libbi, Pedro Miguel M. C. de Melo, Zeila Zanolli, Matthieu Jean Verstraete, and Nicola Marzari. “Phonon-Assisted Luminescence in Defect Centers from Many-Body Perturbation Theory”. In: *Phys. Rev. Lett.* 128 (16 Apr. 2022), p. 167401 (cit. on pp. 122, 123).
- [221] Alexander Kirchhoff, Thorsten Deilmann, Peter Krüger, and Michael Rohlfing. “Electronic and optical properties of a hexagonal boron nitride monolayer in its pristine form and with point defects from first principles”. In: *Phys. Rev. B* 106 (4 July 2022), p. 045118 (cit. on pp. 122, 123).
- [222] Christoph Freysoldt, Blazej Grabowski, Tilmann Hickel, Jörg Neugebauer, Georg Kresse, Anderson Janotti, and Chris G. Van de Walle. “First-principles calculations for point defects in solids”. In: *Rev. Mod. Phys.* 86 (1 Mar. 2014), pp. 253–305 (cit. on p. 122).
- [223] Giacomo Miceli, Wei Chen, Igor Reshetnyak, and Alfredo Pasquarello. “Nonempirical hybrid functionals for band gaps and polaronic distortions in solids”. In: *Phys. Rev. B* 97 (12 Mar. 2018), p. 121112 (cit. on p. 122).
- [224] Michael P. Surh, Hélio Chacham, and Steven G. Louie. “Quasiparticle excitation energies for the F-center defect in LiCl”. In: *Phys. Rev. B* 51 (12 Mar. 1995), pp. 7464–7470 (cit. on p. 122).

- [225] Magnus Hedström, Arno Schindlmayr, Günther Schwarz, and Matthias Scheffler. “Quasiparticle Corrections to the Electronic Properties of Anion Vacancies at GaAs(110) and InP(110)”. In: *Phys. Rev. Lett.* 97 (22 Nov. 2006), p. 226401 (cit. on p. 122).
- [226] Patrick Rinke, Anderson Janotti, Matthias Scheffler, and Chris G. Van de Walle. “Defect Formation Energies without the Band-Gap Problem: Combining Density-Functional Theory and the *GW* Approach for the Silicon Self-Interstitial”. In: *Phys. Rev. Lett.* 102 (2 Jan. 2009), p. 026402 (cit. on p. 122).
- [227] L. Martin-Samos, G. Roma, P. Rinke, and Y. Limoge. “Charged Oxygen Defects in SiO₂: Going beyond Local and Semilocal Approximations to Density Functional Theory”. In: *Phys. Rev. Lett.* 104 (7 Feb. 2010), p. 075502 (cit. on p. 122).
- [228] Manish Jain, James R. Chelikowsky, and Steven G. Louie. “Quasiparticle Excitations and Charge Transition Levels of Oxygen Vacancies in Hafnia”. In: *Phys. Rev. Lett.* 107 (21 Nov. 2011), p. 216803 (cit. on p. 122).
- [229] Wei Chen and Alfredo Pasquarello. “Correspondence of defect energy levels in hybrid density functional theory and many-body perturbation theory”. In: *Phys. Rev. B* 88 (11 Sept. 2013), p. 115104 (cit. on p. 122).
- [230] Anna Tararan, Stefano di Sabatino, Matteo Gatti, Takashi Taniguchi, Kenji Watanabe, Lucia Reining, Luiz H. G. Tizei, Mathieu Kociak, and Alberto Zobelli. “Optical gap and optically active intragap defects in cubic BN”. In: *Phys. Rev. B* 98 (9 Sept. 2018), p. 094106 (cit. on p. 122).
- [231] Carlo A. Rozzi, Daniele Varsano, Andrea Marini, Eberhard K. U. Gross, and Angel Rubio. “Exact Coulomb cutoff technique for supercell calculations”. In: *Phys. Rev. B* 73 (20 May 2006), p. 205119 (cit. on p. 123).
- [232] Falco Hüser, Thomas Olsen, and Kristian S. Thygesen. “How dielectric screening in two-dimensional crystals affects the convergence of excited-state calculations: Monolayer MoS₂”. In: *Phys. Rev. B* 88 (24 Dec. 2013), p. 245309 (cit. on pp. 123, 132).
- [233] Catalin D. Spataru. “Electronic and optical gap renormalization in carbon nanotubes near a metallic surface”. In: *Phys. Rev. B* 88 (12 Sept. 2013), p. 125412 (cit. on p. 124).
- [234] Matthias Drüppel, Thorsten Deilmann, Jonathan Noky, Philipp Marauhn, Peter Krüger, and Michael Rohlfing. “Electronic excitations in transition metal dichalcogenide monolayers from an LDA + *GdW* approach”. In: *Phys. Rev. B* 98 (15 Oct. 2018), p. 155433 (cit. on p. 124).
- [235] Philipp Auburger and Adam Gali. “Towards ab initio identification of paramagnetic substitutional carbon defects in hexagonal boron nitride acting as quantum bits”. In: *Phys. Rev. B* 104 (7 Aug. 2021), p. 075410 (cit. on pp. 127, 128).
- [236] A Sajid, Michael J Ford, and Jeffrey R Reimers. “Single-photon emitters in hexagonal boron nitride: a review of progress”. In: *Rep. Prog. Phys.* 83.4 (Mar. 2020), p. 044501 (cit. on p. 127).
- [237] V.L Solozhenko, G Will, and F Elf. “Isothermal compression of hexagonal graphite-like boron nitride up to 12 GPa”. In: *Solid State Commun.* 96.1 (1995), pp. 1–3 (cit. on p. 128).
- [238] W. Paszkowicz, J. Pelka, M. Knapp, T. Szyszko, and S. Podsiadlo. “Lattice parameters and anisotropic thermal expansion of hexagonal boron nitride in the 10-297.5 K temperature range”. In: *Appl. Phys. A* 75 (2002), pp. 431–435 (cit. on p. 128).
- [239] Stefan Grimme, Jens Antony, Stephan Ehrlich, and Helge Krieg. “A consistent and accurate ab initio parametrization of density functional dispersion correction (DFT-D) for the 94 elements H-Pu”. In: *J. Chem. Phys.* 132.15 (2010), p. 154104 (cit. on p. 128).

- [240] Pierluigi Cudazzo, Claudio Attaccalite, Ilya V. Tokatly, and Angel Rubio. “Strong Charge-Transfer Excitonic Effects and the Bose-Einstein Exciton Condensate in Graphane”. In: *Phys. Rev. Lett.* 104 (22 June 2010), p. 226804 (cit. on p. 132).
- [241] Pierluigi Cudazzo, Ilya V. Tokatly, and Angel Rubio. “Dielectric screening in two-dimensional insulators: Implications for excitonic and impurity states in graphane”. In: *Phys. Rev. B* 84 (8 Aug. 2011), p. 085406 (cit. on p. 132).
- [242] S. Latini, T. Olsen, and K. S. Thygesen. “Excitons in van der Waals heterostructures: The important role of dielectric screening”. In: *Phys. Rev. B* 92 (24 Dec. 2015), p. 245123 (cit. on p. 132).
- [243] R. M. Ribeiro and N. M. R. Peres. “Stability of boron nitride bilayers: Ground-state energies, interlayer distances, and tight-binding description”. In: *Phys. Rev. B* 83 (23 June 2011), p. 235312 (cit. on p. 143).
- [244] Darshana Wickramaratne, Leigh Weston, and Chris G. Van de Walle. “Monolayer to Bulk Properties of Hexagonal Boron Nitride”. In: *J. Phys. Chem. C* 122.44 (2018), pp. 25524–25529 (cit. on pp. 143–145).
- [245] Fulvio Paleari, Thomas Galvani, Hakim Amara, François Ducastelle, Alejandro Molina-Sánchez, and Ludger Wirtz. “Excitons in few-layer hexagonal boron nitride: Davydov splitting and surface localization”. In: *2D Mater.* 5.4 (Aug. 2018), p. 045017 (cit. on pp. 143, 145).
- [246] Jochen Heyd, Gustavo E. Scuseria, and Matthias Ernzerhof. “Hybrid functionals based on a screened Coulomb potential”. In: *The Journal of Chemical Physics* 118.18 (May 2003), pp. 8207–8215 (cit. on p. 144).
- [247] Jochen Heyd, Gustavo E. Scuseria, and Matthias Ernzerhof. “Erratum: “Hybrid functionals based on a screened Coulomb potential” [J. Chem. Phys. 118, 8207 (2003)]”. In: *The Journal of Chemical Physics* 124.21 (June 2006), p. 219906 (cit. on p. 144).
- [248] X Blase, A Rubio, S. G Louie, and M. L Cohen. “Stability and Band Gap Constancy of Boron Nitride Nanotubes”. In: *Europhys. Lett.* 28.5 (Nov. 1994), pp. 335–340 (cit. on p. 145).
- [249] R. J. Hunt, B. Monserrat, V. Zólyomi, and N. D. Drummond. “Diffusion quantum Monte Carlo and *GW* study of the electronic properties of monolayer and bulk hexagonal boron nitride”. In: *Phys. Rev. B* 101 (20 May 2020), p. 205115 (cit. on p. 145).
- [250] Laura E. Ratcliff, William Dawson, Giuseppe Fisicaro, Damien Caliste, Stephan Mohr, Augustin Degomme, Brice Videau, Viviana Cristiglio, Martina Stella, Marco D’Alessandro, Stefan Goedecker, Takahito Nakajima, Thierry Deutsch, and Luigi Genovese. “Flexibilities of wavelets as a computational basis set for large-scale electronic structure calculations”. In: *J. Chem. Phys.* 152.19 (May 2020), p. 194110 (cit. on pp. 150, 153).
- [251] William Dawson, Stephan Mohr, Laura E. Ratcliff, Takahito Nakajima, and Luigi Genovese. “Complexity Reduction in Density Functional Theory Calculations of Large Systems: System Partitioning and Fragment Embedding”. In: *J. Chem. Theory Comput.* 16.5 (2020). PMID: 32216343, pp. 2952–2964 (cit. on pp. 150, 153).
- [252] C. Poelking, M. Tietze, C. Elschner, Selina Olthof, Dirk Hertel, Björn Baumeier, Frank Würthner, Klaus Meerholz, K. Leo, and D. Andrienko. “Impact of mesoscale order on open-circuit voltage in organic solar cells”. In: *Nat. Mater* 14 (2015), pp. 434–439 (cit. on pp. 150, 154).
- [253] Du Li, Zhen-Fei Liu, and Li Yang. “Accelerating *GW* Calculations of Point Defects with the Defect-Patched Screening Approximation”. In: *J. Chem. Theory Comput.* 19.24 (2023). PMID: 38059814, pp. 9435–9444 (cit. on pp. 150, 154).

- [254] Evgeny M. Alexeev, David A. Ruiz-Tijerina, Mark Danovich, Matthew J. Hamer, Daniel J. Terry, Pramoda K. Nayak, Seongjoon Ahn, Sangyeon Pak, Juwon Lee, Jung Inn Sohn, Maciej R. Molas, Maciej Koperski, Kenji Watanabe, Takashi Taniguchi, Kostya S. Novoselov, Roman V. Gorbachev, Hyeon Suk Shin, Vladimir I. Fal'ko, and Alexander I. Tartakovskii. “Resonantly hybridized excitons in moiré superlattices in van der Waals heterostructures”. In: *Nature* 567 (2019), pp. 81–86 (cit. on pp. [150](#), [154](#)).
- [255] Marco Bernardi, Maurizia Palummo, and Jeffrey C. Grossman. “Optoelectronic Properties in Monolayers of Hybridized Graphene and Hexagonal Boron Nitride”. In: *Phys. Rev. Lett.* 108 (22 June 2012), p. 226805 (cit. on pp. [150](#), [154](#)).
- [256] Marco Bernardi, Maurizia Palummo, and Jeffrey C. Grossman. “Semiconducting Monolayer Materials as a Tunable Platform for Excitonic Solar Cells”. In: *ACS Nano* 6.11 (2012). PMID: 23062107, pp. 10082–10089 (cit. on pp. [150](#), [154](#)).
- [257] Peter H. Schonemann. “On the Formal Differentiation of Traces and Determinants”. In: *Multivariate Behavioral Research* 20.2 (1985). PMID: 26771405, pp. 113–139 (cit. on p. [157](#)).
- [258] K. B. Petersen and M. S. Pedersen. *The Matrix Cookbook*. Version 20121115. Nov. 2012 (cit. on p. [157](#)).
- [259] Shriram Srinivasan and Nishant Panda. “What is the gradient of a scalar function of a symmetric matrix?” In: *Indian Journal of Pure and Applied Mathematics* 54.3 (Sept. 2023), pp. 907–919 (cit. on p. [157](#)).
- [260] Ivan Duchemin, David Amblard, and Xavier Blase. “Polarizable Continuum Models and Green’s Function GW Formalism: On the Dynamics of the Solvent Electrons”. In: *J. Chem. Theory Comput.* 10.1021/acs.jctc.4c00745 (As Soon As Publishable). PMID: 39226212 (cit. on pp. [163](#), [173](#)).